

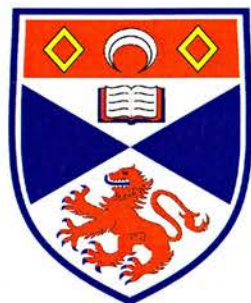
University of St Andrews



Full metadata for this thesis is available in
St Andrews Research Repository
at:

<http://research-repository.st-andrews.ac.uk/>

This thesis is protected by original copyright



STRUCTURE AND CATALYTIC
PROPERTIES OF MICROPOROUS
ALUMINOPHOSPHATES

A thesis presented for the degree of

Doctor of Philosophy

in the Faculty of Science of the University of St Andrews

by Martin J. Maple, BSc, MPhil, MRSC

May 2003

School of Chemistry

St Andrews



TL
E 430.

Declarations

I, Martin J. Maple, hereby certify that this thesis, which is approximately 64 000 words in length, has been written by me, that that it is the record of work carried out by me and that it has not been submitted in any previous application for a higher degree.

I was admitted as a research student in September 1999 and as a candidate for the degree of Doctor of Philosophy in September 2000; the higher study for which this is a record was carried out in the University of St Andrews between 1999 and 2003.

In submitting this thesis to the University of St Andrews I understand that I am giving permission for it to be made available for use in accordance with the regulations of the University Library for the time being in force, subject to any copyright vested in the work not being affected thereby. I also understand that the title and abstract will be published, and that a copy of the work may be made available and supplied to any *bona fide* library or research worker.

Martin J. Maple (Candidate)

I hereby certify that the candidate has fulfilled the conditions of the Resolution and Regulations appropriate for the degree of Doctor of Philosophy in the University of St Andrews and that the candidate is qualified to submit this thesis in application for that degree.

Paul ~~X~~. Wright (Supervisor)

Abstract

Crystalline microporous solids were synthesised from aluminophosphate gels treated hydrothermally under autogeneous pressure. Catalytic properties are conferred on these materials by the inclusion of Mg^{II} , Si^{IV} , Mn^{II} , Fe^{II} , Co^{II} , Ni^{II} or Zn^{II} cations in the synthesis gels. Organic amine and quaternary ammonium salts are used as structure directing agents, or templates, during synthesis. Novel materials were prepared and characterised.

The azamacrocyclic 1,4,8,11-tetramethyl-1,4,8,11-tetraazacyclotetradecane templates either STA-6 or the novel phase STA-7. Uniquely, the framework that crystallises is *controlled* by the substituting metal cations present in the gel, Mg^{II} , Si^{IV} , Mn^{II} , Fe^{II} or Ni^{II} giving STA-6, Co^{II} or Zn^{II} , STA-7. The structure of STA-6 is known and that of STA-7 has been solved by single crystal X-ray diffraction. Co-STA-7, $[(\text{C}_{14}\text{H}_{34}\text{N}_4)_{2.3}(\text{H}_2\text{O})_9] [\text{Co}_{0.8}\text{Al}_{19.2}\text{P}_{24}\text{O}_{96}]$, is tetragonal ($P4/n$, $a = 18.740(5) \text{ \AA}$, $c = 9.439(7) \text{ \AA}$). It is the first zeolitic material known to possess two distinct and fully interconnected small pore channel systems; its structure contains double 6-rings and is related to the **CHA**, **AEI** and **KFI** frameworks. STA-6 and STA-7 were given the IUPAC framework type codes **SAS** and **SAV**, respectively.

Layered materials in which 1,4,8,11-tetraazacyclotetradecane becomes incorporated into the structure, and a framework in which it remains unbound, were synthesised depending upon the metal cations present in the gel. Aluminophosphate materials were prepared with poly[4-(1,4-diazabicyclo[2.2.2]oct-1-ylmethyl)benzyl] cations and 1,5-diaminopentane/18-crown-6 with structures that remain unsolved.

The aluminophosphate STA-2 was synthesised with varying degrees of metal substitution. The structural chemistry of the $\text{AlPO}_4(\text{F})$ and MgAPO

forms were studied by solid state NMR spectroscopy and Rietveld X-ray profile refinement.

Substituted aluminophosphates were evaluated as acid catalysts for the conversion of methanol to olefins (MTO) in a plug-flow reactor. The acidity of selected catalysts was studied with a probe reaction (*n*-butane cracking) and by TPD of *n*-butylamine. Activity and selectivity in the MTO reaction is discussed with respect to acidity and pore structure. Si-STA-7 is the most promising novel solid acid catalyst studied.

Selected CoAPOs were studied as catalysts for the terminal oxidation of *n*-alkanes.

Acknowledgments

I would first like to offer my supervisors, Drs Paul Wright and Richard Oldroyd, my sincerest thanks for allowing me to work with them and for their guidance throughout the project.

I must also acknowledge the help I have received from others during this work: Drs Phil Lightfoot and Alex Slawin for single crystal diffractometry, Dr David Apperley for collecting the solid state NMR spectra and Dr Paul Cox for supplying the results of his template simulations. Others are mentioned in the text.

So too must I acknowledge all the departmental technical staff for their help, but particular thanks must go to Bobby Cathcart and Brian Walker of the mechanical and electrical workshops respectively, for their expertise.

I should also like to thank all the colleagues (too numerous to mention individually) from whom I have learned so much, but especially to those with whom I have had the pleasure of sharing laboratory and office space. A special thank you to Humphrey Yiu, Tim Coombs and Raquel García.

I would also like to thank my parents, and especially Zoe, for their support and continuing interest in my work.

Lastly I would like to acknowledge the financial support I have received from BP and the EPSRC through their award of a CASE studentship.

*Oor universe is like an e'e
Turned in, man's benmaist hert to see,
And swamped in subjectivity.*

*But whether it can use its sicht
To bring what lies withoot to licht
To answer's still ayont my micht.*

From "A Drunk Man Looks at the Thistle",
by Hugh MacDiarmid, 1926

Contents

Abstract	ii
Acknowledgments	iv
1 Introduction	1
1.1 Microporous solids	1
1.1.1 Nomenclature	1
1.1.2 Historical development	3
1.1.3 Aims of the work	6
1.2 The bulk structure of crystals	6
1.2.1 Geometry and symmetry in crystals	7
1.2.2 Diffraction of X-rays by crystals	12
1.2.3 Solving crystal structures	15
1.2.4 The Rietveld method	17
1.2.5 Synchrotron radiation	20
1.3 Local structure in crystals	22
1.3.1 NMR spectroscopy	22
1.3.2 Pauling's rules	30
1.3.3 Loewenstein's rules	32
1.3.4 Dempsey's rule	34
1.3.5 Flanigen's rules	34
1.4 Synthesis of microporous solids	36
1.4.1 The concept of templating	37
1.4.2 Mechanisms of crystallisation	39
1.5 Physicochemical properties	41

1.5.1	Catalysis	41
2	The search for new materials	48
2.1	Introduction	48
2.1.1	Recent developments	49
2.1.2	Characterising new materials	62
2.2	Experimental	65
2.2.1	Synthesis	65
2.2.2	Crystallography	67
2.2.3	NMR spectroscopy	69
2.2.4	Chemical analysis	69
2.2.5	Molecular modelling	70
2.3	Results	70
2.3.1	Tmtact as a template	70
2.3.2	Cyclam as a “template”	73
2.3.3	Tmtacn as a template	76
2.3.4	K222 as a template	78
2.3.5	18-crown-6 as an additive	80
2.3.6	Tmhht as a template	85
2.3.7	Hhpp as a template	87
2.3.8	Hhmpp as a template	87
2.3.9	Peabcoa as a template	90
2.3.10	Troger’s base as a template	91
2.3.11	Spiro templates	91
2.3.12	Pbcomb polymer as a template	92
2.3.13	Phosphazine base templates	92
2.4	Discussion	94
2.5	Conclusion	96
3	Structural chemistry of STA-2	98
3.1	Introduction	98
3.2	Experimental	99
3.2.1	Synthesis	99

3.2.2	Chemical analysis	99
3.2.3	Crystallography	100
3.2.4	NMR spectroscopy	100
3.3	Results	101
3.3.1	Synthesis	101
3.3.2	NMR spectroscopy	108
3.3.3	Crystallography	111
3.4	Discussion	114
3.5	Conclusion	121
4	Structural chemistry of STA-6 and STA-7	122
4.1	Introduction	122
4.2	Experimental	122
4.2.1	Synthesis	122
4.2.2	Chemical analysis	123
4.2.3	Crystallography	123
4.2.4	NMR spectroscopy	124
4.2.5	Molecular modelling	125
4.2.6	Electron microscopy	125
4.3	Results	125
4.3.1	Synthesis	125
4.3.2	Crystallography	128
4.3.3	NMR spectroscopy	139
4.3.4	Molecular modelling	143
4.3.5	Electron microscopy	143
4.3.6	Chemical analysis	145
4.3.7	Thermal stability and porosity	148
4.4	Discussion	151
4.5	Conclusion	157
5	Catalytic properties of STA-2, STA-6 and STA-7	158
5.1	Introduction	158
5.2	Conversion of methanol to olefins	159

5.2.1	Experimental	162
5.2.2	Results	166
5.2.3	Discussion	178
5.2.4	Conclusion	179
5.3	<i>n</i> -Butane cracking	180
5.3.1	Experimental	184
5.3.2	Results	184
5.3.3	Discussion	190
5.3.4	Conclusion	193
5.4	Oxidation catalysis	193
5.4.1	Experimental	198
5.4.2	Results	201
5.4.3	Discussion	205
5.4.4	Conclusion	206
	Epilogue	207
	A Single crystal XRD data	209
	B Rietveld refinement data	243
	C Publications	272
	References	273

List of Tables

1.1	A chronology of early discoveries	5
1.2	The seven crystal systems	8
1.3	The thirty-two crystal classes	9
1.4	Space group symmetry elements and their symbols	10
1.5	Parameters for refinement during Rietveld analysis	20
1.6	²⁹ Si NMR chemical shift assignments for zeolites	34
1.7	Flanigen's rules for substitution in aluminophosphates	36
2.1	Classification of zeolitic materials by pore size	49
2.2	6-ring stacking sequences in zeolitic materials	57
2.3	Inorganic reagents used in this work	67
2.4	Results of syntheses with tmtact	71
2.5	Results of syntheses with hhmpp	91
2.6	Results of syntheses with spiro templates	91
4.1	Results of syntheses with tmtact	126
4.2	Fit parameters of EXAFS data for Ni-STA-6	142
4.3	Non-bonded energy of tmtact within the pores of STA-6 and STA-7	143
5.1	Composition data for catalysts used in the MTO reaction	166
5.2	Results of MTO reactions catalysed by SAPO-34, NiSAPO-34, Si-STA-6, NiSi-STA-6 and Co-STA-7	171
5.3	Results of MTO reactions catalysed by SAPO-34, SAPO-56, Si-STA-2, NiSi-STA-2, Si-STA-6 and Mg-STA-6	176
5.4	Results of MTO reactions catalysed by Si-STA-7	177

5.5	Intermediates formed during <i>n</i> -butane cracking	182
5.6	Conversion and product distribution data for <i>n</i> -butane cracking by SAPO-34	186
5.7	Conversion and product distribution data for <i>n</i> -butane cracking by SAPO-56	187
5.8	Conversion and product distribution data for <i>n</i> -butane cracking by Mg-STA-2	188
5.9	Conversion and product distribution data for <i>n</i> -butane cracking by Si-STA-3	189
5.10	Results of <i>n</i> -alkane oxidation reactions by MAPOs	197
5.11	Qualitative results of <i>n</i> -hexane oxidations in the Parr reactor .	202
5.12	Qualitative results of <i>n</i> -hexane oxidations in the glass reactor	202
5.13	Quantitative results of <i>n</i> -hexane oxidations	203
5.14	Quantitative results of <i>n</i> -octane oxidations	204
5.15	Results of <i>n</i> -alkane oxidation reactions by MAPOs	206
A.1	Atomic coordinates and thermal parameters for STA-2	210
A.2	Atomic coordinates and thermal parameters for Mg-STA-6 . .	211
A.3	Atomic coordinates and thermal parameters for Co-STA-7 . .	212
A.4	Selected bond distances for Co-STA-7	213
A.5	Selected bond angles for Co-STA-7	214
A.6	Atomic coordinates and thermal parameters for Zn-STA-7 . .	216
A.7	Selected bond distances for Zn-STA-7	217
A.8	Selected bond angles for Zn-STA-7	218
A.9	Atomic coordinates and thermal parameters for CoAPO- cyclam-1	220
A.10	Atomic coordinates and thermal parameters for MgAPO-18 (cy- clam)	222
A.11	Selected bond distances for MgAPO-18 (cyclam)	223
A.12	Selected bond angles for MgAPO-18 (cyclam)	224
A.13	Atomic coordinates and thermal parameters for MgAPO-18 (tmtacn)	226
A.14	Selected bond distances for MgAPO-18 (tmtacn)	227

A.15 Selected bond angles for MgAPO-18 (tmtacn)	228
A.16 Atomic coordinates and thermal parameters for ZnAPO-42 . .	230
A.17 Selected bond distances for ZnAPO-42	231
A.18 Selected bond angles for ZnAPO-42	231
A.19 Atomic coordinates and thermal parameters for Co-UCSB-6 .	232
A.20 Selected bond distances for Co-UCSB-6	233
A.21 Selected bond angles for Co-UCSB-6	235
A.22 Atomic coordinates and thermal parameters for AlPO ₄ -21 . .	239
A.23 Selected bond distances for AlPO ₄ -21	240
A.24 Selected bond angles for AlPO ₄ -21	241
B.1 Atomic coordinates and thermal parameters for NiAPO- cyclam-1	244
B.2 Selected bond distances for NiAPO-cyclam-1	245
B.3 Selected bond angles for NiAPO-cyclam-1	246
B.4 Atomic coordinates and thermal parameters for as-prepared AlPO ₄ (F)-STA-2	248
B.5 Selected bond distances for as-prepared AlPO ₄ (F)-STA-2 . . .	249
B.6 Selected bond angles for as-prepared AlPO ₄ (F)-STA-2	249
B.7 Atomic coordinates and thermal parameters for calcined AlPO ₄ (F)-STA-2	251
B.8 Selected bond distances for calcined AlPO ₄ (F)-STA-2	251
B.9 Selected bond angles for calcined AlPO ₄ (F)-STA-2	252
B.10 Atomic coordinates and thermal parameters for as-prepared Mg-STA-2	253
B.11 Selected bond distances for as-prepared Mg-STA-2	254
B.12 Selected bond angles for as-prepared Mg-STA-2	254
B.13 Atomic coordinates and thermal parameters for calcined Mg- STA-2	256
B.14 Selected bond distances for calcined Mg-STA-2	257
B.15 Selected bond angles for calcined Mg-STA-2	257
B.16 Atomic coordinates and thermal parameters for Co-STA-7 . .	259
B.17 Selected bond distances for Co-STA-7	260

B.18 Selected bond angles for Co-STA-7	261
B.19 Atomic coordinates and thermal parameters for Zn-STA-7	262
B.20 Selected bond distances for Zn-STA-7	263
B.21 Selected bond angles for Zn-STA-7	264
B.22 Atomic coordinates and thermal parameters for Mn-STA-6	266
B.23 Selected bond distances for Mn-STA-6	267
B.24 Selected bond angles for Mn-STA-6	267
B.25 Atomic coordinates and thermal parameters for Ni-STA-6	268
B.26 Selected bond distances for Ni-STA-6	269
B.27 Selected bond angles for Ni-STA-6	269
B.28 Atomic coordinates and thermal parameters for Co-STA-6	270
B.29 Selected bond distances for Co-STA-6	270
B.30 Selected bond angles for Co-STA-6	271

List of Figures

1.1	The sodalite, or β , cage and four zeolites constructed from it	4
1.2	The fourteen Bravais lattices	11
1.3	The Bragg construction for diffraction by a 3-D crystal	14
1.4	The Synchrotron Radiation Source at Daresbury, UK	21
1.5	Energy level diagram for a spin- $\frac{1}{2}$ nucleus in a magnetic field	23
1.6	Equilibrium position of the bulk magnetisation in a magnetic field	25
1.7	The bulk magnetisation after perturbation by an r.f. pulse	25
1.8	The linear field oscillation generated in the xy plane	26
1.9	Orientations of the bulk magnetisation, its xy component and the rotating field	27
1.10	A caesium aluminophosphate containing Al–O–Al linkages	35
1.11	Scheme illustrating tri-quat	39
1.12	Schemes of zeolites showing extra-framework cations	43
1.13	Scheme illustrating Brønsted and Lewis acid sites in zeolites	43
1.14	Shape selective catalysis by zeolites	45
2.1	Projection of the mineral cacoxenite	50
2.2	Projection of the high silica zeolite CIT-1	51
2.3	Projection of the magnesioaluminophosphate DAF-1	52
2.4	Projection of the aluminophosphate STA-1	52
2.5	Projection of the aluminophosphate UCSB-6	54
2.6	Diagrams showing two cancrinite, or ϵ , cages linking across a double 6-ring	55
2.7	Projections of the aluminophosphate UCSB-8	55

2.8	Projections of the aluminophosphate STA-2	56
2.9	Projections of the aluminophosphate STA-6	58
2.10	“Designer” templates used in the synthesis of zeolitic materials	59
2.11	Flexible templates used in the synthesis of zeolitic materials	62
2.12	“Designer” templates used in this work	66
2.13	Powder XRD patterns of materials synthesised with tmtact	72
2.14	Projections of the aluminophosphate CoAPO–cyclam-1	74
2.15	Rietveld plot of NiAPO–cyclam-1 XRD data	75
2.16	Powder XRD pattern of MgAPO-18 (cyclam)	76
2.17	Powder XRD pattern of MgAPO-18 (tmtacn)	77
2.18	Stereoview of the tmtacn template in AlPO ₄ -18	78
2.19	Powder XRD patterns of MAPO-42 materials	79
2.20	Powder XRD patterns of CoAPO-42 synthesised with varying Co/P ratios	81
2.21	Powder XRD pattern of CoAPO-42 collected with synchrotron radiation	82
2.22	Powder XRD patterns of CoAPO-21 and ZnAPO-41	83
2.23	Micrograph of CoAPO-21 crystallites	83
2.24	Powder XRD patterns of MgAPO-21 and MgAPO-25	84
2.25	Powder XRD pattern of an unidentified CoAPO synthesised with 1,5-diaminopentane and 18-crown-6	84
2.26	Micrographs of Co–UCSB-6 and CoAPO-34 crystallites	86
2.27	Powder XRD pattern of Zn–UCSB-6	87
2.28	Solid state ²⁷ Al and ³¹ P NMR spectra of Zn–UCSB-6	88
2.29	Solid state ¹³ C NMR spectrum of Zn–UCSB-6	89
2.30	Powder XRD pattern of MgAPO-21	90
2.31	Powder XRD pattern of mixed phase MgAPO-34–MgAPO-21	92
2.32	Powder XRD pattern of Mg–STA-4	93
3.1	Scheme illustrating babob and babop	100
3.2	Powder XRD patterns of STA-2 aluminophosphates synthesised with babob	102

3.3	Powder XRD patterns of STA-2 aluminophosphates synthesised with babop	103
3.4	Powder XRD pattern of Mg–STA-2 synthesised with babob . .	104
3.5	Powder XRD pattern of Co–STA-2 synthesised with babob . .	104
3.6	Powder XRD pattern of Zn–STA-2 synthesised with babop . .	105
3.7	Powder XRD patterns of Mg–STA-2 synthesised with various Mg/P ratios and babob	106
3.8	Powder XRD pattern of Si–STA-2 synthesised with babob . .	106
3.9	Powder XRD patterns of Si–STA-2 synthesised with various Si/Al ratios and babob	107
3.10	Solid state ^{27}Al and ^{31}P NMR spectra of $\text{AlPO}_4(\text{F})$ –STA-2 . .	109
3.11	Solid state ^{19}F and ^{13}C NMR spectra of $\text{AlPO}_4(\text{F})$ –STA-2 . .	109
3.12	Solid state ^{27}Al MQ NMR spectrum of $\text{AlPO}_4(\text{F})$ –STA-2 . . .	110
3.13	Solid state ^{27}Al NMR spectrum of Mg–STA-2	111
3.14	Solid state ^{27}Al MQ NMR spectrum of Mg–STA-2	112
3.15	Solid state ^{31}P NMR spectra of Mg–STA-2	113
3.16	Solid state ^{13}C NMR spectrum of Mg–STA-2	113
3.17	Rietveld plot of as-prepared $\text{AlPO}_4(\text{F})$ –STA-2 XRD data . . .	115
3.18	Rietveld plot of calcined $\text{AlPO}_4(\text{F})$ –STA-2 XRD data	115
3.19	Rietveld plot of as-prepared Mg–STA-2 XRD data	116
3.20	Rietveld plot of calcined Mg–STA-2 XRD data	116
3.21	The cavities in as-prepared and calcined $\text{AlPO}_4(\text{F})$ –STA-2 . .	117
3.22	The cavities in as-prepared and calcined Mg–STA-2	117
3.23	Possible sites of F^- or OH^- anions in $\text{AlPO}_4(\text{F})$ –STA-2 . . .	119
3.24	The cavities in AlPO_4 -17, STA-2 and AlPO_4 -56	121
4.1	Scheme illustrating tmtact	123
4.2	Powder XRD patterns of materials synthesised with tmtact at various temperatures	127
4.3	Powder XRD patterns of materials synthesised with tmtact after various times	129
4.4	Scheme illustrating dmtabch and hmhaco	130
4.5	Projection of the aluminophosphate STA-6	130

4.6	Stereoviews of the aluminophosphate STA-6	131
4.7	Projections of the aluminophosphate AlPO ₄ -21	133
4.8	Projection of the aluminophosphate STA-7	134
4.9	Stereoviews of the aluminophosphate STA-7	135
4.10	Rietveld plot of Co-STA-7 XRD data	136
4.11	Rietveld plot of Zn-STA-7 XRD data	137
4.12	Rietveld plot of Mn-STA-6 XRD data	138
4.13	Rietveld plot of Ni-STA-6 XRD data	140
4.14	Ni K-edge EXAFS spectrum of Ni-STA-6	141
4.15	Solid state ¹³ C NMR spectra of Mg-STA-6 and Zn-STA-7	142
4.16	Stereoview of tmtact in STA-6	144
4.17	Stereoview of tmtact in STA-7	144
4.18	Illustrative diagram of STA-7 showing the template location	145
4.19	Micrograph of STA-6 and STA-7 crystallites	146
4.20	Transmission electron micrograph of STA-7	147
4.21	Powder XRD pattern of Co-STA-6	149
4.22	Rietveld plot of Co-STA-6 XRD data	150
4.23	The cavities in AlPO ₄ -18, AlPO ₄ -42, STA-6 and STA-7	152
4.24	The CHA , AEI , KFI and SAV frameworks	153
4.25	Conformers of complexes of tetraaza macrocycles	155
5.1	The CRD plug flow reactor system	164
5.2	Plot of product stream composition with time for the MTO reaction catalysed by SAPO-34	167
5.3	Plot of product stream composition with time for the MTO reaction catalysed by SAPO-34	168
5.4	Plot of product stream composition with time for the MTO reaction catalysed by NiSAPO-34	168
5.5	Plot of product stream composition with time for the MTO reaction catalysed by Si-STA-6	169
5.6	Plot of product stream composition with time for the MTO reaction catalysed by Si-STA-6	169

5.7	Plot of product stream composition with time for the MTO reaction catalysed by NiSi-STA-6	170
5.8	Plot of product stream composition with time for the MTO reaction catalysed by Co-STA-7	170
5.9	Total hydrocarbon and DME production during the MTO reaction catalysed by SAPO-34, NiSAPO-34, Si-STA-6, NiSi-STA-6 and Co-STA-7	172
5.10	Plot of product stream composition with time for the MTO reaction catalysed by SAPO-34	172
5.11	Plot of product stream composition with time for the MTO reaction catalysed by SAPO-56	173
5.12	Plot of product stream composition with time for the MTO reaction catalysed by Si-STA-2	173
5.13	Plot of product stream composition with time for the MTO reaction catalysed by NiSi-STA-2	174
5.14	Plot of product stream composition with time for the MTO reaction catalysed by Si-STA-6	174
5.15	Plot of product stream composition with time for the MTO reaction catalysed by Mg-STA-6	175
5.16	Powder XRD pattern of Si-STA-7	178
5.17	Arrhenius plots for <i>n</i> -butane cracking with SAPO-34, SAPO-56, Mg-STA-2 and Si-STA-3	185
5.18	Total hydrocarbon production during <i>n</i> -butane cracking catalysed by SAPO-34, SAPO-56, Mg-STA-2 and Si-STA-3	190
5.19	TGA plots of SAPO-34, SAPO-56, Si-STA-6, Si-STA-2 and Si-STA-3	191
5.20	Photograph of as-prepared and calcined CoAPO catalysts . . .	199
5.21	The Parr stainless steel reactor system	200

Chapter 1

Introduction

1.1 Microporous solids

Microporous solids are materials that contain channels and cavities of diameter 2.5–20 Å. [1] There are many classes including amorphous carbons and crystalline silicate and phosphate materials. The first family of crystalline microporous materials to be discovered were aluminosilicate minerals called zeolites. Their open structure may reversibly sorb and desorb water and it was the observation of intumescence (the evolution of water from the crystal when heated in a blowpipe) that led the Swedish mineralogist Axel F. Cronstedt to name them after the Greek, ζεῖν—boil and λίθος—stone. [2]

In the work described here only crystalline solids are considered whose frameworks are comprised of pure or substituted aluminophosphate. This family of materials was discovered by workers at Union Carbide who reported in 1982. [3] These materials have framework topologies that may also be found as aluminosilicates or which are entirely novel. In describing the general structural chemistry and physicochemical properties of aluminophosphates reference will be made first in this chapter to the zeolite materials.

1.1.1 Nomenclature

Before we begin, a word about nomenclature. [4] The term “zeolite” is used inconsistently in the chemical literature to describe a range of materials with

either ion-exchange or adsorption properties or both. Mineralogists have a loose yet consistent definition, articulated by J. V. Smith [5] thus:

“a zeolite is an aluminosilicate with a framework structure enclosing cavities occupied by large ions and water molecules, both of which have considerable freedom of movement, permitting ion-exchange and reversible dehydration.”

Later, owing to the imprecision of the word “framework”, Smith amended his definition [6] to specify that:

“the Al and Si atoms occupy 4-connected vertices of a three-dimensional net, and the oxygen atoms occupy 2-connected positions between the 4-connected vertices.”

Thus, he makes a distinction between aluminosilicates that are 4;2-connected (zeolites) and others where oxygen atoms are bound either to one tetrahedral (T) atom and a hydrogen or three T atoms, or frameworks where T atoms connect to five or six oxygen neighbours.

Chemists tend to define *zeolite* more broadly to include silica polymorphs such as silicalite, clathrasils such as sodalite, interrupted frameworks where one or more oxygens are bonded to only one T atom (such as in cloverite), and materials whose framework composition comprises elements other than aluminium, silicon and oxygen.

Aluminophosphates where $\text{Al/P} = 1$, and certainly after the removal by calcination of occluded organic cations, do not obey the mineralogical definition of a zeolite, however some have the same framework topology as aluminosilicate zeolites. Metal-substituted aluminophosphates, especially the silicoaluminophosphates have an even more complex relationship to the zeolites.

In this work the term *zeolitic* will be applied to any “inorganic, three-dimensional host structure composed of fully-linked, corner-sharing tetrahedra”, [4] while *zeolite* will be reserved for silicates not containing phosphate.

Microporous framework structures may be called *hosts* and it is this that defines the pore structure that may additionally contain *guest* species. If information about the chemical composition of the host is removed the underlying

framework structure represents the *topology*. Hosts may have a dimensionality of zero (finite), one (chain), two (layer), or three (framework). When the topology is of the form of a 4;2-connected regular 3-D net the International Zeolite Association (IZA) will assign a three-letter code and include a type material in the *Atlas of Zeolite Framework Types*. [7]

The structures of zeolitic materials can be described in terms of composite building units (CBUs); the basic building units (BBUs) are the TO_4 tetrahedra. Rings are described by the number of tetrahedral atoms they contain (*e.g.* 4-ring, 6-ring) while pairs of rings are called double n -rings (*e.g.* double 6-ring, D6R). Polyhedra may also be identified as CBUs and described by the notation $[n_i^{m_i}]$, where m is the number of n -rings defining the polyhedron and $\sum m_i$ is the total number of faces (for example, a D6R would be described thus: $[4^6, 6^2]$). Some polyhedra have, however, been given additional names such as the sodalite, or β , cage (Figure 1.1), the cancrinite, or ε , cage and the α -cavity. In a polyhedron the n -rings are known as *windows*; polyhedra with windows too small to admit molecules larger than water (*i.e.* containing only 6-rings or smaller) are called *cages* and others *cavities*. If a cavity is infinitely extended and permits guest species to diffuse along its length it is called a *channel*.

1.1.2 Historical development

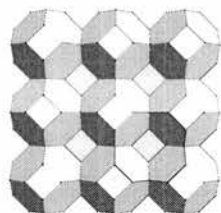
While zeolites were first observed in nature as early as 1756 it was 1862 before the first attempts to synthesise them were made. [8] These first attempts applied high temperatures and pressures to the synthesis ($T > 200^\circ\text{C}$, $P > 100\text{ bar}$) as these were believed to be required for natural zeolite formation. The first novel zeolite framework was not produced until 1948. [9] But it was not until 1982, as has been said, that the aluminophosphate [3] zeolite-analogues were synthesised, followed closely by metal-substituted frameworks. [10]

Table 1.1 summarises some of the important early discoveries that have been made in the field.

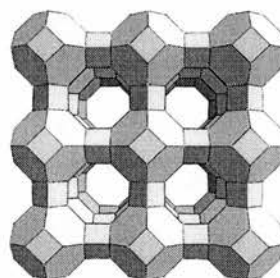
Figure 1.1: The sodalite, or β , cage is a composite building unit (CBU) seen in several zeolite frameworks. Four examples are shown below. In sodalite itself the cages are linked *via* fused 4-rings leaving only 6-ring windows. If double 4-ring (D4R) units are placed between the cages, 8-ring windows and voids called α -cavities are created, as in zeolite A. The cages may equally well be linked through the 6-rings, two known framework types, that of (cubic) faujasite and hexagonal faujasite, are then formed.



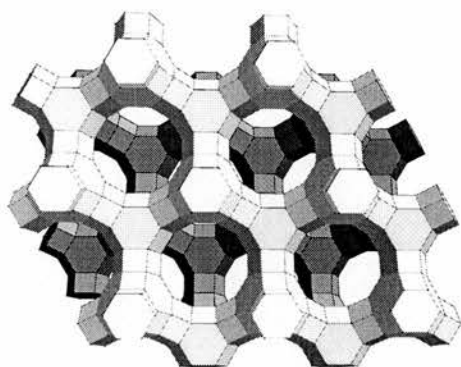
The sodalite cage



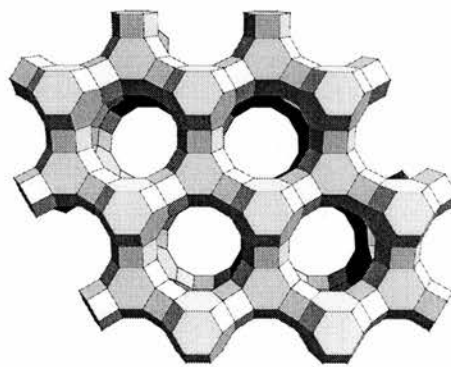
Sodalite (SOD)



Zeolite A (LTA)



Faujasite (FAU)



Hexagonal faujasite (EMT)

Table 1.1: A chronology of early discoveries in the field of microporous materials beginning with Cronstedt's identification of stilbite and ending with Flanigen and co-workers' report of the first microporous aluminophosphates.

1756	Cronstedt discovers stilbite and coins the term "zeolite" [2]
1758	Natrolite becomes the second zeolite to be discovered [11]
1772	Chabazite discovered [11]
1840	Reversible dehydration without loss of structural integrity observed in zeolites [12]
1858	Reversible ion-exchange observed in chabazite and natrolite [13]
1862	The first zeolite synthesis reported by de Sainte Claire-Deville [8] (Levynite from aqueous K and Na silicate heated in a glass tube at 170 °C)
1896	Adsorption of liquids (alcohol, benzene and chloroform) observed and an open, sponge-like, framework structure proposed for zeolites [14]
1909	Adsorption of gases observed (ammonia in chabazite) [15]
1925	Molecular sieving first observed by Weigel and Steinhoff who saw that dehydrated chabazite would adsorb water, methanol, ethanol and formic acid but not acetone, ether or benzene [16]
1930	The first zeolite structure is determined (analcine) by Taylor [17]
1932	McBain coins the term "molecular sieve" to describe microporous carbons and zeolites [18]
1948	Barrer synthesises the first zeolite with no natural counterpart (zeolite P with the ZK-5 framework) [9]
1949	Barrer [19] reports the first preparation of a H-zeolite <i>via</i> the NH ₄ -form
1956	Synthesis, properties [20] and structure [21] of zeolite A revealed
1961	The first direct synthesis of zeolites in the absence of inorganic bases reported [22]
1962	Mobil introduces the first zeolite-based cracking catalyst
1967	Ultra-stabilised zeolite Y prepared
1971	Silicon-rich ZSM-5 described
1982	Microporous aluminophosphate materials reported by Flanigen <i>et al</i> of Union Carbide [3]

1.1.3 Aims of the work

The aims of this work are threefold. Firstly to synthesise aluminophosphate-based solids, secondly to study the structural chemistry of selected materials, and thirdly to evaluate some metal-substituted materials' potential as catalysts.

The thesis presented in the subsequent chapters is ordered as follows: Chapter 1 surveys the field in broad terms, with reference to its development historically and to the theoretical and practical background of certain analytical techniques; in the chapters that follow the state-of-the-art is first reviewed before the results of this work are given and discussed. Specifically, Chapters 2 to 4 will deal with research of a synthetic and structural nature, including the search for new materials, their bulk structure and some results of an investigation of local structural features in selected materials. Results from experiments using the previously discussed materials in acid and oxidation catalysis are given in the last chapter, before suggestions for further work are made.

1.2 The bulk structure of crystals

Aluminosilicate zeolites possess the general formula $[M_{x/m}^{m+}(H_2O)_n][Si_{1-x}Al_xO_2]$ where M is typically a metal cation of valence m . The framework is anionic and consists of $[SiO_4]^{4-}$ and $[AlO_4]^{5-}$ tetrahedra. The overall charge on the framework is equal to the number of tetrahedral aluminium atoms and a corresponding number of cations are required for charge balance. These cations have access to the pore system and are incorporated into the structure at synthesis, yet can be exchanged later. The last structural element is the sorbed molecule, either water or an organic, which can play an important role in the synthesis of the particular phase. Following crystallisation this species may be removed to leave the framework structure intact.

Similarly aluminophosphate materials can be represented with the formula

$[(R)_y(H_2O)_n][AlPO_4]$. The framework is tetrahedrally connected and nominally composed of $[AlO_2]^-$ and $[PO_2]^+$ units. Aluminophosphates can be substituted by a range of heteroatoms M to form MAPOs or by silicon (SAPOs) or both (MAPSOs).

The framework structure of all these microporous solids is most easily determined by single crystal X-ray diffraction. This though is often hampered by the lack of crystallites of sufficient size for conventional diffractometers, although with the advent of image plate/CCD detectors and synchrotron X-ray sources the solution of materials' structures where only microcrystals ($10 \times 10 \times 10 \mu\text{m}$) are available is increasingly becoming routine. [23]

1.2.1 Geometry and symmetry in crystals

It has been said that the materials of interest here are crystalline. The beauty of these materials, and one of their most engaging properties, lies in their ordered structure, the architecture of which may readily be described with reference to symmetry. The symmetry of crystals will now be discussed, before the principal method of structure solution, X-ray crystallography, is outlined.

The seven crystal systems

René Haüy first proposed the idea of a polyhedral “structural subunit” or *molécules intégrantes* in 1784 after examining the cleavage of calcite. [24] In doing so he built upon Robert Hooke’s speculation (1665) that the regular form of crystals is derived from the regular packing of spherical particles within them. It seemed reasonable to Haüy that the symmetry of the crystal as a whole would be connected to the symmetry of some smaller subunit within it. By successively cleaving calcite crystals Haüy obtained rhomboid crystallites, reflecting the triad axis of symmetry within the complete crystal. From this he hypothesised that if the cleavage were to be repeated many times eventually all that would be left was an indivisible structural subunit that would have the same triad axis as the original crystal.

There are seven distinct types of subunit associated with the seven *crystal systems*. All the subunits are parallelepipeds whose shapes may be defined by

Table 1.2: The seven crystal systems.

System	Unit cell	Essential symmetry of crystal
Triclinic	No special relationships	None
Monoclinic	$a \neq b \neq c$ $\alpha = \gamma = 90^\circ \neq \beta$	Twofold axis or mirror plane (inverse twofold axis)
Orthorhombic	$a \neq b \neq c$ $\alpha = \beta = \gamma = 90^\circ$	Three orthogonal twofold or inverse twofold axes
Tetragonal	$a = b \neq c$ $\alpha = \beta = \gamma = 90^\circ$	One fourfold or inverse four- fold axis
Trigonal	$a = b = c$ $\alpha = \beta = \gamma \neq 90^\circ$	One threefold or inverse three- fold axis
Hexagonal	$a = b \neq c$ $\alpha = \beta = 90^\circ, \gamma = 120^\circ$	One sixfold or inverse sixfold axis
Cubic	$a = b = c$ $\alpha = \beta = \gamma = 90^\circ$	Four threefold axes

the lengths a, b, c and the angles α, β, γ , see Table 1.2. All crystals may be described in terms of subunits that exhibit the same essential symmetry as the crystal itself, even if, in some cases, the crystal as a whole exhibits less symmetry than the subunit. For example, a cubic subunit may yield a cube or tetrahedron-shaped crystal. The former has a centre of symmetry, nine mirror planes, six twofold axes, four threefold axes and three fourfold axes; the later has six mirror planes, three inverse fourfold axes and four threefold axes. So although the tetrahedron possesses less symmetry than the cube they both contain four triad axes: the essential characteristic of the cube.

The subunit, which when close-packed in three-dimensions gives the crystal, is called the *unit cell*. Although it may not be uniquely defined it is customary to choose a unit cell that contains the highest possible symmetry so that the underlying symmetry of the structure may be more clearly indicated.

The thirty-two crystal classes

Each of the seven crystal systems may be further subdivided depending upon the *symmetry elements* present. The collection of symmetry elements is called

Table 1.3: The thirty-two crystal classes.

System	Crystal classes (point groups)	
	Non-centrosymmetric	Centrosymmetric
Triclinic	1	$\bar{1}$
Monoclinic	2, m ($= \bar{2}$)	$2/m$
Orthorhombic	222, $2mm$	mmm
Tetragonal	4, $\bar{4}$	$4/m$
	422, $4mm$, $\bar{4}2m$	$4/mmm$
Trigonal	3	$\bar{3}$
	32, $3m$	$\bar{3}m$
Hexagonal	6, $\bar{6}$	$6/m$
	622, $6mm$, $\bar{6}2m$	$6/mmm$
Cubic	23	$m\bar{3}$
	432, $\bar{4}3m$	$m\bar{3}m$

the *point group*; in 1830 Hessel listed the thirty-two crystallographic point groups or *crystal classes*. For example, a triclinic crystal may or may not have a centre of symmetry, thus yielding two classes $\bar{1}$ and 1, the former representing a centre of symmetry and the latter representing a onefold axis, *i.e.* no symmetry at all. Table 1.3 lists all the crystal classes.

A note on the symbols: the combination $3m$ implies that the mirror plane *contains* the threefold axis and the trigonal symmetry demands that a set of three mirror planes exists. For the class $3/m$ (or 6) the mirror plane is perpendicular to the threefold axis. Redundant information is not always stated so that in the class $2mm$ the symmetry associated with the third axis is not stated because the two orthogonal mirror planes automatically generate a twofold axis along the line of the intersection, the alternative name is $2m$ or mm .

Miller indices and Bravais lattices

Planes drawn through a crystal intercept the unit cell edges at $\frac{a}{h}$, $\frac{b}{k}$, $\frac{c}{l}$, where hkl are integers, are called *Miller indices* after W. H. Miller who was first to propose the system in 1839. Those planes that are parallel to the crystal's

Table 1.4: Space group symmetry elements and their symbols.

Symmetry element	Symbols
Centre of symmetry	$\bar{1}$
Mirror plane	$m (\equiv \bar{2})$
Glide plane	a, b, c, n, d
Rotation axes	2, 3, 4, 6
Screw axes	$2_1, 3_1, 3_2, 4_1, 4_2, 4_3, 6_1, 6_2, 6_3, 6_4, 6_5$
Inversion axes	$\bar{3}, \bar{4}, \bar{6}$

faces may be used to name each face.

Moreover, it is possible to relate the repeating motif of atoms in the crystal to a *space lattice* of points, without reference to the actual unit cell contents. Only fourteen space lattices are required for three-dimensional systems and these are called *Bravais lattices* (see Figure 1.2). There are seven simple (primitive) lattices based on the seven crystal systems, each of which contains one lattice point. The other seven lattices contain more than one lattice point and are called “centred”.

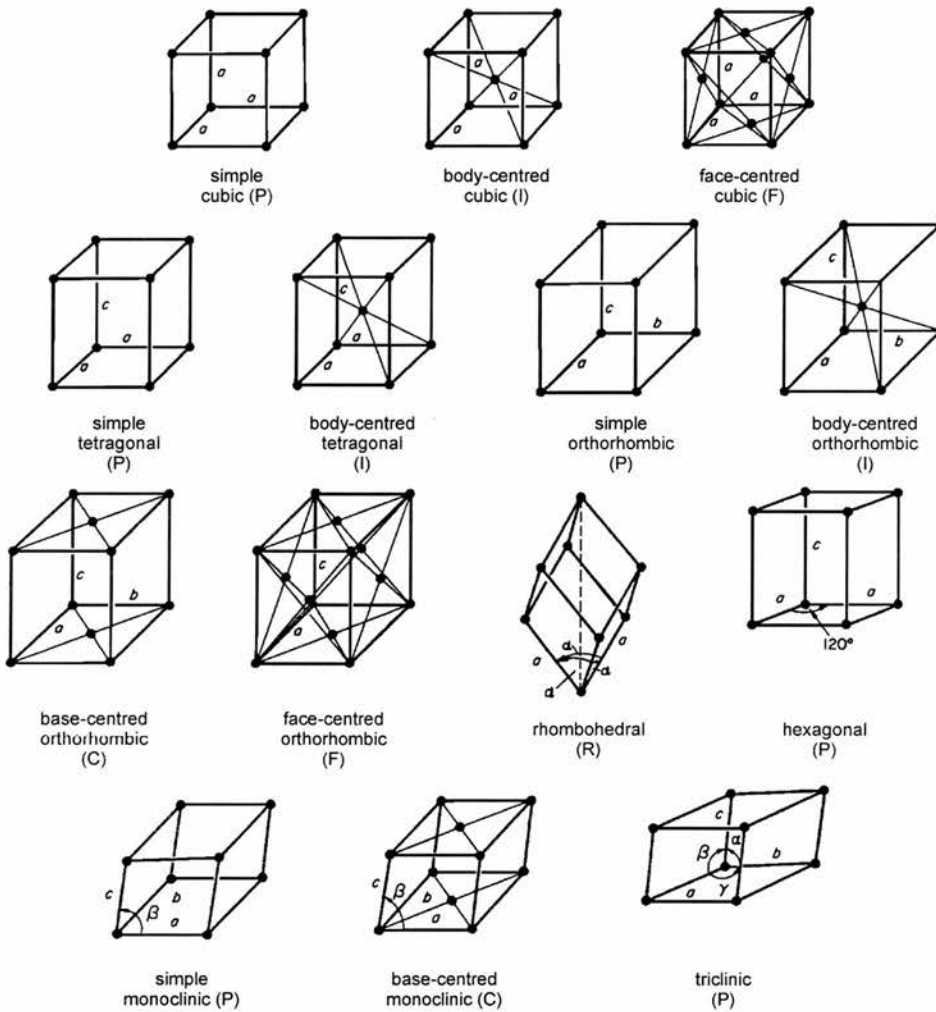
For each lattice many unit cells are possible. Conventionally, in the absence of rotation or reflection symmetry in the structure (see below) the unit cell has sides that are as short as possible, $a \leq b$, and an angle as close as possible to 90° . The presence of rotation or reflection symmetry imposes restrictions on the unit cell (*e.g.* in 2-Ds fourfold rotation demands a square unit cell).

Symmetry elements and space groups

If the atoms within the unit cell are considered further symmetry elements must be used, in addition to those seen in the thirty-two point groups, to define the relationships between them. These are outlined in Table 1.4. In addition to the symmetry elements found in two dimensions, crystals can possess other symmetry elements in which rotation or reflection are combined with translation to give *screw axes* and *glide planes*, respectively.

In a crystal there are 230 possible combinations of symmetry elements

Figure 1.2: The 14 Bravais lattices with lines connecting the points to clarify the relationships between them. [25]



(point group and rotation/reflection symmetry) and Bravais lattices; such arrangements are called *space groups*.

1.2.2 Diffraction of X-rays by crystals

In 1912 Max von Laue proposed that X-rays were composed of such short wavelength radiation that successive layers in a crystal might form an effective diffraction grating. At this time the nature of X-rays (particle or wave) was unknown; also the structure of crystals being regular arrangements of atoms was not undisputed. The experiment to test Laue's conjecture was carried out the same year by Walter Friedrich and Paul Knipping, who directed a beam of X-rays at a large crystal of copper sulfate and produced the first Laue diagram—the regular pattern of spots on a photographic plate.

The scattering of X-rays

The scattering process in crystals may be envisaged as the absorption of incident radiation with subsequent re-emission in all directions. It is the electrons within the atoms that are the scatterers in X-ray diffraction, the process occurring through two mechanisms. The first, called Thomson scattering, is the scattering of electromagnetic waves by (free) electrons. The theory states that when an electromagnetic wave impinges on an electron, the alternating electric-field vector imparts an alternating acceleration which causes it to emit electromagnetic radiation. This is a coherent scattering process, that is to say there is a phase relationship between the incident and scattered radiation, while the wavelength is unchanged. The second scattering process, known as Compton scattering, is incoherent and the wavelength of the scattered radiation is longer than that of the incident beam, the difference being dependent on the angle of the scatter.

In atoms however, the electrons are bound into defined energy states. Thomson scattering will therefore correspond to a zero change in energy of the electron, while Compton scattering must yield a quantised change of energy so that the electron might go from one bound state to another, or be ejected from the atom completely.

The diffraction of X-rays

Atoms within a crystal form a 3-D array which can be defined in terms of three vectors \mathbf{a} , \mathbf{b} and \mathbf{c} . All atoms scatter the X-ray beam *in phase* in some direction. This can be broken down into three conditions, (i) that the radiation scattered by the atoms of separation \mathbf{a} will constructively interfere, (ii) that the radiation scattered by the atoms of separation \mathbf{b} will constructively interfere and, (iii) that the radiation scattered by the atoms of separation \mathbf{c} will constructively interfere. This leads to three equations, first defined by Laue, that describe the conditions under which *diffraction* can occur

$$\begin{aligned}\mathbf{a} \cdot \mathbf{s} &= h \\ \mathbf{b} \cdot \mathbf{s} &= k \\ \mathbf{c} \cdot \mathbf{s} &= l\end{aligned}\tag{1.1}$$

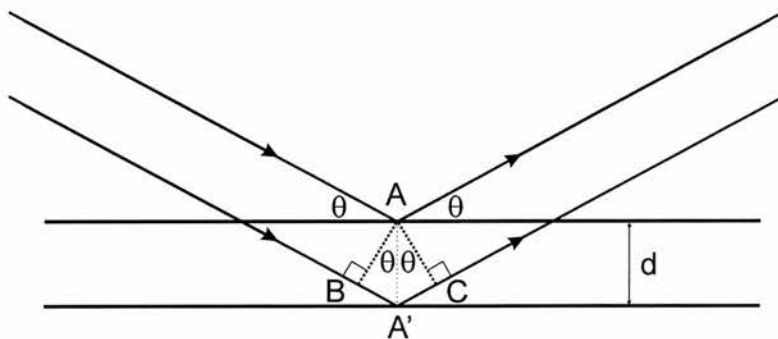
The problem of finding the scattering vectors \mathbf{s} which satisfy these relationships for a given set of integers (hkl) is mathematically complex and will not be considered here (the full treatment is given by, for example, Woolfson in his textbook [25]). Instead the Bragg construction will be used.

Bragg's law

In 1913 W. Laurence Bragg, having observed that X-rays were diffracted only at specific orientations of the crystal with respect to the source and detector, formulated the first mathematical explanation for the observed positions of the diffraction spots. Together with his father, William H. Bragg, he had refined the experimental technique studying sodium chloride, with monochromatic radiation in place of the "white" radiation used in the Laue method.

The theory can be described by considering a 3-D array of scatterers and a set of equally-spaced parallel lines, drawn through these points at a variety of orientations. One such set of "planes" is shown in Figure 1.3. These planes act as partial "reflectors" of X-rays so that when a parallel beam of X-rays fall on a plane any two points will yield rays in the reflected beam which are in phase.

Figure 1.3: The Bragg construction for diffraction by a 3-D crystal (one set of lattice planes is seen edge on).



To explain why diffraction occurs only at specific angles the effect of the distance between parallel reflecting planes must be considered. For reflections from points on two planes to interfere constructively they must be in phase. For the points A and A' separated by the distance d this reinforcement condition is given by

$$BA' + A'C = n\lambda \quad (1.2)$$

where n is an integer. When $n = 1$, for example, and from Figure 1.3

$$BA' = A'C = d \sin \theta \quad (1.3)$$

and so

$$2d \sin \theta = n\lambda \quad (1.4)$$

This is the expression of Bragg's law, giving the allowed angles of reflection θ in terms of λ , and the interplane spacing d . It is mathematically commensurate with the Laue equations.

The structure factor

If the detail of the crystal structure is again examined it can be seen that it comprises a close packed 3-D array of unit cells, each of which contains atoms. Each atom can be thought of as a point in a separate array comprising all

atoms at the same relative position in each unit cell. The non-zero diffracted X-ray beams from each of these arrays of atoms (according to the Laue equations) forms part of the observed diffracted beam from the whole crystal. The scattering from any one atom A , with respect to an electron at the centre of the unit cell at a distance \mathbf{r}_A , will be $f_A \exp(2\pi i \mathbf{r}_A \cdot \mathbf{s})$ so that the total scattering amplitude from the crystal is the *sum* of these factors for each atom. If there are N atoms in the unit cell this leads to

$$F_{hkl} = \sum_{j=1}^N f_j \exp(2\pi i \mathbf{r}_j \cdot \mathbf{s}) \quad (1.5)$$

where F_{hkl} is the *structure factor* and hkl are the *indices of reflection*.

1.2.3 Solving crystal structures

If a single crystal of adequate size and of sufficient quality is available it is routine to solve the material's structure. [26] After a dataset (hkl and intensity, error) has been collected on a single crystal diffractometer, the lattice parameters and crystal system may be found, and the space group determined by analysis of *systematic absences*. These are absences in the observed values of hkl and occur because of destructive interference if a crystal has a centred Bravais lattice or translational symmetry elements. Since $I_{hkl} \propto |F_{hkl}|^2$ the "phase problem" remains for determining the absolute value of the F_{hkl} for calculating electron density according to the equation

$$\rho(xyz) = \frac{1}{V} \sum_h \sum_k \sum_l F_{hkl} \cos 2\pi(hx + ky + lz) \quad (1.6)$$

Here it is most useful to rewrite Equation 1.5 assuming $\mathbf{r} = x\mathbf{a} + y\mathbf{b} + z\mathbf{c}$ where x, y, z are the atomic coordinates within a cell whose edges are the vectors $\mathbf{a}, \mathbf{b}, \mathbf{c}$ as it is the structure factors for each reflection (hkl) we wish to calculate from known atomic coordinates. So

$$F_{hkl} = \sum_{j=1}^N f_j \cos[2\pi(hx_j + ky_j + lz_j)] \quad (1.7)$$

There are two principal methods used for this solution that will now, briefly, be considered. (For further details see the textbooks by Clegg [27] and Giacobazzo. [28])

The Patterson function

In the Patterson, or heavy-atom, method [29] the following equation is used to generate a 3-D ‘‘Patterson’’ map

$$\rho(uvw) = \frac{1}{V} \sum_h \sum_k \sum_l |F_{hkl}|^2 \cos 2\pi(hu + kv + lw) \quad (1.8)$$

This map, instead of representing electron density, shows vectors between pairs of atoms in the unit cell. The height of the peaks is proportional to the product of the atomic numbers of the two atoms, making heavy atoms more prominent than lighter ones. It is their large X-ray scattering factor that makes their contribution to the structure factor summation (Equation 1.7) relatively great. If the structure factors are calculated using only the coordinates of the heavy atoms the magnitudes of the F_{hkl} will be only approximate but the phases are almost certainly correct. These phases can then be used with the observed $|F_{hkl}|$ values to calculate the electron density map with Equation 1.6 and locate the light atoms.

Direct methods

The Patterson method is less useful when all the atoms in the unit cell are of approximately the same atomic number. In this case direct methods, a statistical technique, is more useful for predicting the phase of the structure factors. [30] The technique works best when (a) all the atoms have the same X-ray scattering factor, and (b) that the distribution of atoms in the unit cell is quasi-random.

The phases of the normalised structure factors E_{hkl} are predicted by the Sayre probability relationship

$$S(hkl) \sim S(h'k'l') \cdot S(h - h', k - k', l - l') \quad (1.9)$$

where, in a centrosymmetric structure, $S(hkl)$ indicates the sign of the normalised structure factor. So for example, if E_{551} and E_{210} are both phase negative, E_{341} is likely to be positive. The probability that each relationship is correct may be calculated and a computer program used to determine the most self-consistent set of phases for all the observed reflections and from there obtain likely atomic positions.

Structure refinement

Once the basic structure has been determined it is refined by a least squares method to obtain the *best fit* of the model structure to the data. Depending on the computer program used either one of two sums are minimised, $\sum w(|F_o| - |F_c|)^2$ or $\sum w(F_o^2 - F_c^2)^2$, where F_o and F_c are the observed and calculated structure factors, respectively and w is a weighting factor. To assess the *goodness of fit* a number of residuals, or R -factors are calculated. For example

$$R = \frac{\sum || F_o | - | F_c ||}{\sum | F_o |} \quad (1.10)$$

The R -factor may also be weighted and calculated on F^2

$$wR^2 = \sqrt{\frac{\sum w(F_o^2 - F_c^2)^2}{\sum w(F_o^2)^2}} \quad (1.11)$$

1.2.4 The Rietveld method

Very often when studying the structure of zeolitic materials single crystals are not available. A powder X-ray diffraction profile can, however, be obtained from a sample containing many randomly orientated crystallites because at any angle 2θ there will be hkl planes in some crystallites that scatter X-rays according to the Bragg equation. Cones of scattering occur so that effectively the structural information contained within a 3-D single crystal dataset is compressed into two dimensions. Structure solution becomes non-trivial in these cases because of the difficulties inherent in indexing this data. Yet structural studies may still be carried out by analysing powder X-ray diffraction profiles by the Rietveld method where the basic structure is already known.

The basis of the technique

The Rietveld method [31] is an algorithm for the refinement of crystal structures from powder diffraction data. The most important feature of the method is that the parameters in the structural model, and the other sample and instrument effects, are refined with respect to the *whole* observed powder profile. Refinement stops when the *best fit* between these data and the whole calculated pattern is found. Another key feature is the feedback that is obtained during refinement. This increases knowledge of both the structure and the allocation of observed intensity to overlapping Bragg reflections. With the Rietveld method the observed intensity is not allocated to any particular Bragg reflections in advance, and no effort is made to resolve overlapping reflections. A good starting model is therefore required. Rietveld analysis is consequently a method of structure refinement, rather than structure solution *per se*.

During Rietveld profile refinement a least squares method is applied to minimise the residual

$$S_y = \sum_i w_i (y_i - y_{ci})^2 \quad (1.12)$$

where $w_i = \frac{1}{y_i}$, y_i is the observed intensity at the i th step, y_{ci} is the calculated intensity at the i th step, and the sum is over all data points.

The calculated intensities are determined from the square of the absolute structure factors $|F_K|^2$ that are in turn calculated from the structural model, *i.e.*

$$y_{ci} = S \sum_K L_K |F_K|^2 \phi(2\theta_i - 2\theta_K) P_K A + y_{bi} \quad (1.13)$$

where S is the scale factor, K is the Miller indices for a Bragg reflection, L_K contains the Lorentz polarisation and multiplicity factors, ϕ is the reflection profile, P_K the preferred orientation function, A the adsorption factor, F_K the structure factor for the K th Bragg reflection and y_{bi} is the background intensity at the i th step.

During the least squares minimisation procedure an $m \times m$ matrix is created where m is the number of parameters being refined. This is used to determine the derivatives of all the calculated intensities with respect to each adjustable

parameter. An iterative process must be applied because the residual function is non-linear. The procedure will either diverge or lead to a false minimum if the starting model is not close to the correct model (but this is a problem for all non-linear least squares refinements, not just Rietveld ones). Use of constraints or multiple datasets are two possible approaches to circumventing this difficulty.

Goodness of fit

Computer programs for Rietveld refinement give two possible methods to assess the goodness of fit of the model to the experimental data: those based on numerical R -factors and those applying graphics. Several numerical factors have been employed, however only the R -profile and R -weighted profile shall be considered here as these are implemented in the GSAS suite of programs [32] used in this work for Rietveld refinement

$$R_p = \frac{\sum |y_i(obs) - y_i(calc)|}{\sum y_i(obs)} \quad (1.14)$$

$$R_{wp} = \sqrt{\frac{\sum w_i(y_i(obs) - y_i(calc))^2}{\sum w_i(y_i(obs))^2}} \quad (1.15)$$

Mathematically R_{wp} is the most meaningful as the residual being minimised is included in the numerator. However R_{wp} may be inflated significantly by factors such as impurity phases that do not necessarily show an invalid structural model. Conversely R_{wp} may be lowered misleadingly if, for example, the refined background is high. To circumvent such problems with purely numerical criteria graphical tools such as the difference plot are used. Such plots may be used to immediately trace the source of problems such as errors in lattice parameters, zero point, impurity phases *etc.*

Strategy for refinement

Parameters that are refined during a Rietveld refinement may be divided into two classes: those specific to the (or each) phase present and those whose effect is global (see Table 1.5). The order in which parameters or groups of

Table 1.5: Parameters for refinement during Rietveld analysis. The order in which parameters are refined is important if false minima are to be avoided in the refinement.

Phase dependent	Global
x, y, z, U_{iso} , site occupancy	Zero point
Scale factor	Instrument profile
Profile parameters	Profile asymmetry
Lattice parameters	Background
Temperature factors	Absorption
Preferred orientation	
Extinction	

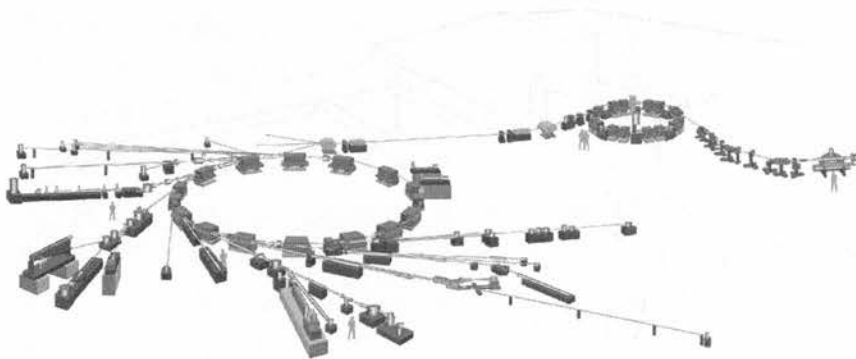
parameters are “turned on” (*i.e.* allowed to refine during the next cycle) can be critical if the global minimum is to be found and a stable refinement is to be obtained. In a typical refinement the scale factor and flat background parameters may be refined first before the zero point and lattice parameters are turned on. Further background coefficients may then be added and refinement of the profile parameters begun. Only once a reasonable fit to these parameters is obtained should refinement of the atomic parameters, thermal and site occupancies be attempted. At all stages a systematic, step-by-step, turn on sequence is important. Once an acceptable fit is obtained difference Fourier maps may be used to examine unallocated electron density.

Further explanation may be obtained from the monograph edited by Young. [33]

1.2.5 Synchrotron radiation

Diffraction studies of zeolitic materials, whether powder or single crystal, can benefit from the use of synchrotron light. This radiation is generated by accelerating electrons in a storage ring at close to the speed of light. High energy radiation is given off at wavelengths from the infra-red to hard X-rays, making the study of microcrystals (or weakly diffracting crystals) possible. Since

Figure 1.4: Diagram of the Synchrotron Radiation Source (SRS) at the CCLRC Daresbury Laboratory, Cheshire, UK. On the far right is the linear accelerator which injects electrons into the booster synchrotron and from there the main storage ring. Electrons travelling close to the speed of light produce synchrotron light. Beam lines are arranged at tangents around the storage ring to collect this for experiments.



the wavelength available for experiments is tunable, studies of materials containing elements that would normally fluoresce under the wavelengths used in laboratory diffractometers (*e.g.* Co with $\text{Cu-K}\alpha$ radiation) can be undertaken with ease. High resolution powder X-ray diffraction can also be carried out.

Experiments described in this work have been conducted at the Synchrotron Radiation Source (SRS) operated by the Central Laboratory of the Research Councils at Daresbury, Cheshire, UK. The SRS, built in 1980, was the first multi-user, high energy storage ring for research. It is 96 m in circumference with 16 large dipole magnets which steer the electron beam and three further insertion devices (wiggler or undulator magnets) which generate hard X-rays (see Figure 1.4).

1.3 Local structure in crystals

So by applying X-ray diffraction techniques the bulk structure of crystals can routinely be determined and through refinement of high quality powder diffraction data more detail may be discovered. This is clearly extremely important, but so too is obtaining a detailed understanding of the local structure around particular elements in zeolitic materials. This is necessary because the catalytic properties of these materials is determined by, and dependent upon, such local structure. For example, acid catalysis is dependent upon protons present in the material to charge balance, which are unlikely to be found directly by X-ray techniques.

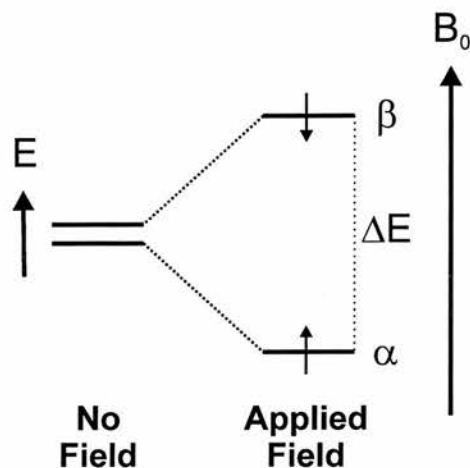
Local structure is studied with a variety of techniques including EXAFS, XANES, ESR and MAS NMR spectroscopies. [34] The principles of this last technique, which has been used in this work, shall now be considered.

1.3.1 NMR spectroscopy

In 1946 nuclear magnetic resonance (NMR) was measured independently by Edward Purcell and Felix Bloch in solids and liquids. NMR spectroscopy is the most powerful *spectroscopic* technique available to chemists for structural characterisation. In solids however, its application is less straightforward because the lack of rapid motion broadens the lines observed in the spectrum. Techniques have been developed to minimise this and consequentially today NMR is a useful tool for the characterisation of solids. The background theory of the technique will now be briefly outlined by describing some NMR experiments, with reference to the “vector model” (see below). A more rigorous mathematical treatment can be found in the monograph by Stejskal and Memory. [35]

Principles of nuclear magnetic resonance

Consider first the NMR experiment for a sample containing only one type of nucleus, the proton. The nuclear spin has an associated magnetic moment that will interact with an applied magnetic field. The proton has spin $I = \frac{1}{2}$ which

Figure 1.5: Energy level diagram for a nucleus ($I = \frac{1}{2}$) in a magnetic field B_0 .

splits into two $(2I+1)$ energy levels in a magnetic field called, using the nuclear spin quantum number, $m_I = +\frac{1}{2}$ and $m_I = -\frac{1}{2}$. This is the *Zeeman Effect*. [36] The former, lower energy state, corresponds to the nuclear magnetic moment being aligned parallel to the applied magnetic field B_0 and is called α . The other state β , is where the spin aligns antiparallel to the applied field (Figure 1.5). The difference in energy ΔE between these two states is dependent on the strength of the applied magnetic field in the following way

$$\Delta E = \frac{h\gamma B_0}{2\pi} \quad (1.16)$$

Here γ is the *magnetogyric ratio* which is the proportionality constant that relates the observation frequency for a particular nucleus to the applied field. The observation frequency can be expressed in terms of the magnetogyric ratio and the applied field

$$\omega = \gamma B_0, \quad \nu = \frac{\gamma B_0}{2\pi} \quad (1.17)$$

Where ω is the resonant frequency in rads^{-1} and ν is the resonance frequency in hertz. It is the difference in γ that lead to different observation frequencies on different spectrometers and so consequentially they are usually quoted,

relative to a standard, in terms of a fraction of the applied field (in ppm). So

$$\delta = \frac{\nu - \nu_{\text{std}} \text{ (Hz)}}{\text{operating frequency (MHz)}} \quad (1.18)$$

The two energy states, α and β , will differ in population depending on the applied field and the nucleus itself. The difference is very small, of the order of 1 in 10^5 but can be described by the Boltzmann equation

$$\frac{N_{\beta}}{N_{\alpha}} = \exp\left(\frac{-\Delta E}{kT}\right) \quad (1.19)$$

The sum of the magnetisation of the individual spins is termed the *bulk magnetisation* \mathbf{M} and its magnitude depends on the population of states.

The position of the bulk magnetisation during the NMR experiment can be visualised with vector diagrams (although a fully mathematical treatment is more rigorous). In the first instance the bulk magnetisation will be aligned with the applied magnetic field, in the z direction (Figure 1.6). If the magnetisation is moved off this axis then a force (torque) would be generated by B_0 on \mathbf{M} . This will cause \mathbf{M} to precess about B_0 at the particular frequency γB_0 (rads^{-1}) and is called *Larmor precession*. Because there is a component of the precessing magnetisation in the xy plane a coil wound round an axis in this plane will have an oscillating current induced in it. It is this current that forms the basis of the NMR signal.

Displacing the magnetisation

The precession frequency of the common nuclei, in the magnetic fields of today's spectrometers, are within the radio frequency (r.f.) band (*i.e.* 10s–100s MHz). The magnetic component of a radio frequency wave may be used to generate a second magnetic field B_1 which displaces the bulk magnetisation from the equilibrium position and causes precession (Figure 1.7). This second field is produced by a current in a coil wound perpendicular to B_0 (which could be the same one used to detect the NMR signal). If the coil is placed on the x axis a linear field oscillation is produced that is equivalent to two

Figure 1.6: Vector diagram illustrating the equilibrium position of the bulk magnetisation in a magnetic field.

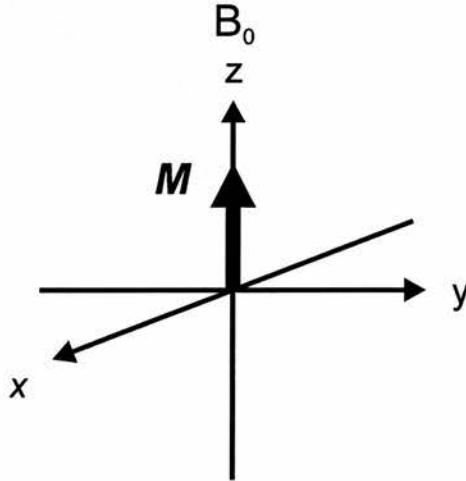


Figure 1.7: Vector diagram showing the behaviour of the bulk magnetisation after perturbation by a pulse of r.f. energy.

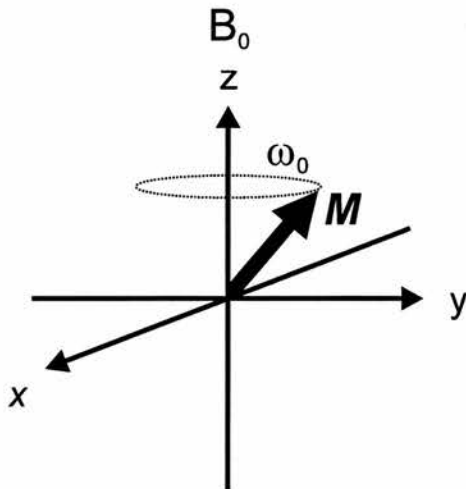
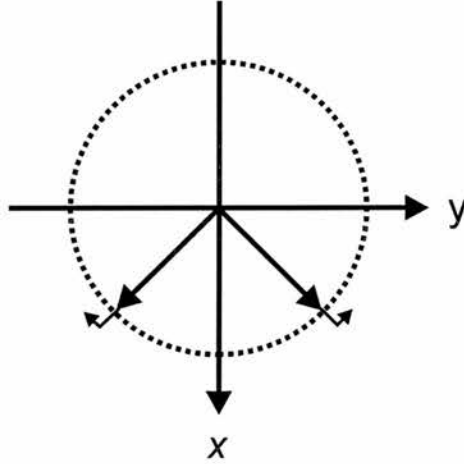


Figure 1.8: Illustrative diagram showing the linear field oscillation generated in the xy plane is equivalent to two rotating field vectors.



counter rotating field vectors in the xy plane (Figure 1.8). Consider one of these, B_1 with an excitation frequency exactly equal to the nuclear precession frequency: $\omega_1 = \omega_0 = \gamma B_0$. The field interacts with the magnetisation \mathbf{M} to produce a torque which moves it towards the xy plane. Since the precession frequency about the static field B_0 is equal to the rotating B_1 frequency, the magnetisation will remain perpendicular to the B_1 field component precessing around the r.f. field at an angular frequency γB_1 (*i.e.* nutation: precession around two axes simultaneously, Figure 1.9).

The final position of the magnetisation depends on the length of time the r.f. is applied. The tip angle θ is related to the pulse duration t_p in the following way

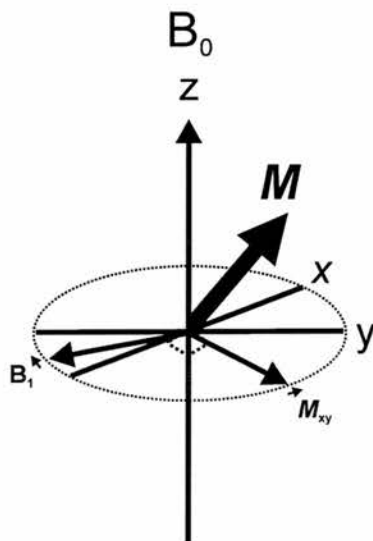
$$\theta = \gamma B_1 t_p \quad (1.20)$$

Thus the magnitude of B_1 is chosen to be large enough to tip the magnetisation from z axis to the xy plane in a few microseconds.

The rotating frame of reference

The explanation of the effect of pulses may be simplified by defining a rotating frame of reference (x', y', z') , rather than using a fixed frame. If the frame

Figure 1.9: The relative orientations of the magnetisation \mathbf{M} , its xy component \mathbf{M}_{xy} , and the rotating radio frequency field B_1 .



rotates at the angular frequency of the rotating component of B_1 , then the precession (about B_1) is simply a rotation of magnetisation in the $y'z'$ plane. The magnetisation will remain perpendicular to the B_1 field and a $\frac{\pi}{2}$ (90°) pulse will put the magnetisation along the y' axis. If the Larmor frequency and the pulse frequency are identical, then after the pulse, the magnetisation will remain fixed in the $x'y'$ plane, rotating at a frequency γB_0 in the laboratory xy plane.

Free induction decay

When the magnetisation is tipped from the z' axis to the y' axis it does not in fact remain indefinitely in the $x'y'$ plane. Instead it will return to equilibrium and the observed signal will diminish. This is the *free induction decay* (FID). Performing a Fourier transform on the FID yields the familiar NMR spectrum by transforming data in the time domain into the frequency domain. There are a number of processes occurring as the system regains equilibrium. These processes are called *relaxation* and are grouped into two classes (longitudinal relaxation T_1 , and transverse relaxation T_2) depending on how they effect the

magnetisation M .

Consider the aforementioned magnetisation after a $\frac{\pi}{2}$ pulse. With time it will relax back from the xy plane to be parallel with B_0 on the z axis. Energy is transferred during this process from the spin system to the lattice and is called the *spin-lattice relaxation*.

While this is happening transverse relaxation is also occurring. This happens because the spin systems experience slightly different effective magnetic fields (primarily because of field fluctuations due to nuclei and electrons in neighbouring parts of the lattice) that causes the nuclear magnetic moments to spread out from their positions on the y axis so that the magnetisation M_y decreases.

These two processes contribute principally to the observed FID.

NMR in solids

In nuclei with $I = 0$ or $\frac{1}{2}$ the predominant sources of line broadening are *dipolar broadening* and *chemical shift anisotropy* (CSA).

Dipolar broadening. In solids containing ^1H or ^{19}F the dominant broadening mechanism is dipole–dipole interactions. The local field B_{loc} at a nucleus I generated by a nucleus S is given by

$$B_{loc} = \pm\mu_S r_{IS}^{-3}(3\cos^2\theta_{IS} - 1) \quad (1.21)$$

where μ_S is the magnetic moment of S , r_{IS} is the internuclear distance and θ is the angle between the internuclear vector and the B_0 field.

Chemical shift anisotropy. The chemical shift is produced by electrons which shield the nucleus from the applied magnetic field. Since the distribution of electrons will not be uniform the chemical shift takes on a directional character too. However, like the dipole–dipole interactions the chemical shift depends on $(3\cos^2\theta_{IS} - 1)$.

Magic angle spinning (MAS)

In solution the dipole–dipole interactions and CSA are averaged to zero by rapid motion of the molecules yielding spectra with lines at the familiar isotropic chemical shift δ_{iso} . In solids this does not occur, but by spinning the sample rapidly at $\theta = 54^\circ 44'$ (the magic angle), $(3 \cos^2 \theta_{IS} - 1)$ becomes zero and such effects can be reduced significantly. The spinning speed must however be of the order of the CSA linewidth (kHz) to reduce the broadening caused by CSA significantly. In some cases it is not possible to spin fast enough to remove all the CSA, in these cases the resulting spectra will contain spinning sidebands. However dipolar broadening cannot yet be eliminated completely because the spinning speeds required are too great (10s kHz). To remove dipolar line broadening heteronuclear decoupling is applied instead by strong irradiation (100s W) of the coupling nucleus.

Nuclei with spin $> \frac{1}{2}$

Many nuclei have spin $I > \frac{1}{2}$ which results in a non-spherical charge distribution and electric quadrupole moment. In an electric field gradient this leads to two effects, (a) the NMR signals may be split into several components by the quadrupole interaction, and (b) the quadrupole interaction may provide an efficient relaxation mechanism.

For example, the ^{27}Al nucleus is quadrupolar ($I = \frac{5}{2}$); the quadrupole interaction alters the Zeeman splitting in a number of ways. The $+\frac{1}{2} \leftrightarrow -\frac{1}{2}$ transition is unaffected by the first order quadrupole interaction (both are shifted by the same amount in the same direction) while the other allowed transitions are usually too broad and shifted too far from resonance to be observed directly.

The line shape due to the $+\frac{1}{2} \leftrightarrow -\frac{1}{2}$ transition is distorted and shifted due to the second order quadrupole interaction. This may be minimised by working at high fields or by spinning the sample at more than one angle (which has been done either by switching the angle during the experiment or spinning at two angles simultaneously with a rotor-within-a-rotor [37]). These approaches to deriving solid state spectra of quadrupolar nuclei are highly demanding in

terms of spectrometer design. More recently a method utilising pulse sequences to obtain the same resolution has been devised, multiple quantum or MQMAS NMR.

MQMAS NMR

MQMAS NMR is a technique that enables separation of isotropic and anisotropic information in spectra of quadrupolar nuclei and was first proposed by Frydman and Harwood. [38] In the experiment transitions other than $+\frac{1}{2} \leftrightarrow -\frac{1}{2}$ are observed. A discussion of the mathematics behind this technique is beyond the scope of this thesis. However at the end of the multiple quantum experiment a set of FIDs is obtained, and after a Fourier transform and shearing transform are applied, a 2-D spectrum is obtained with isotropic axes parallel to F1 and F2 (see Chapter 3 for examples). A projection along F1 gives the isotropic spectrum while along F2 gives the quadrupolar frequencies.

One method for studying local structure in crystals has been presented. The discussion will now move on to consider some of the theories which describe local structure, for example, the distribution of cations in zeolitic frameworks. In this way a deeper understanding of the family of materials studied here may be obtained.

1.3.2 Pauling's rules

Although the bonding between metal and oxygen in zeolitic materials is largely covalent these solids may be imagined as being networks of tetrahedral species, $[\text{AlO}_4]^{5-}$, $[\text{PO}_4]^{3-}$, $[\text{SiO}_4]^{4-}$ etc. comprising large negative ions bonded to cations through ionic interactions. Formally the structure with the lowest free energy in any system is favoured. But in 1929 Pauling [39] wanted an explanation in terms of atoms or ions and their properties. This led him to give five principles that together determine the structure of complex ionic crystals:

“(i) a coördinated polyhedron of anions is formed about each cation, the cation–anion distance being determined by the radius sum and the coördination number of the cation by the radius ratio;

- (ii) in a stable coördination structure the electric charge of each anion tends to compensate the strength of the electrostatic valence bonds reaching to it from the cations at the centers of the polyhedra of which it forms a corner;
- (iii) the presence of shared edges, and particularly of shared faces, in a coördinated structure decreases its stability; this effect is large for cations with large valence and small coördination number, and especially large in case the radius ratio approaches the lower limit of stability of the polyhedron;
- (iv) in a crystal containing different cations those with large valence and small coördination number tend not to share polyhedron elements with each other;
- (v) the number of essentially different kinds of constituents in a crystal tends to be small.”

The first of these principles introduces the ionic radius and describes the geometry of anions surrounding each cation. The optimum cation–anion distance is the sum of the ionic radii, while the coordination number (CN) is governed by the ratio of cation/anion radius. If a great number of anions are grouped around one cation, the cation–cation repulsion becomes strong enough to prevent the anions from attaining optimum distance.

The second, “valence sum” rule essentially says the electrostatic balance is satisfied by the cations belonging to the primary coordination sphere. This is useful in distinguishing O^{2-} from OH^- and H_2O in complex crystal structures and computer programs have been developed for this purpose. [40]

The third rule summarises qualitatively the way in which the structure is affected by the way in which the polyhedra link. To minimise the energy of the system it is necessary that the distances between cations are as great as possible and that they are shielded from each other as much as possible. Cations are pushed increasingly close together when polyhedra share edges and particularly faces. Corner-sharing is favoured. Rule four is a corollary of this.

The final principle summarises the observation that most solids are crystalline rather than amorphous. [28]

1.3.3 Loewenstein's rules

Pauling's third rule, when applied to zeolitic materials, is known as *Loewenstein's rule*. Thus, while the framework composition may vary considerably depending on synthesis conditions, or from later modification, in zeolites the Si/Al ratio must always be greater than one (with a very few exceptions). This was rationalised by Loewenstein [41] in terms of an Al–O–Al avoidance rule:

“Whenever two tetrahedra are linked by one oxygen bridge, the center of only one of them can be occupied by aluminum; the other center must be occupied by silicon, or another small ion of electrovalence four or more, *e.g.* phosphorus.”

And in a second rule:

“... whenever two aluminum ions are neighbours to the same oxygen anion, at least one of them must have a coordination number larger than four, that is, five or six, towards oxygen”

on the basis that having adjacent $[\text{AlO}_2]^-$ units would mean having adjacent negative charges and so would be unfavourable. Recently, computational studies have led to the rule being rationalised in terms of energetics.

Bell *et al* [42] have studied the Si,Al ordering in zeolite A (Si/Al = 1) using a fully ionic model and applying lattice energy minimisation techniques. Calculations were performed on a 4:0 (*i.e.* Loewensteinian) framework and on a 3:1 framework where each Si is linked *via* an oxygen to 3Als and 1Si and necessarily each Al is linked *via* an oxygen to 3Si and 1Al thus creating an Al–O–Al group. In this second case two locations for the Al–O–Al bridge were used, (a) across the D4R, and (b) within the sodalite cage; three different Na^+ distributions were also applied. The results of these calculations showed that for each Na^+ distribution the Loewensteinian framework was favoured energetically. An energy penalty of 40 kJ mol^{-1} was found for the Al–O–Al linkage. This

though is not large and the authors suggest a weak thermodynamic preference at low temperatures for Al avoidance.

Ab initio and molecular mechanics calculations have also been performed by Catlow *et al* [43] on small fragments, rings and clusters, terminated by OH groups. The formation and condensation energies of a number of aluminate, aluminosilicate and silicate clusters were calculated. They found that hydration helps stabilise the fragments but that there is a substantial energy penalty (170–210 kJ mol⁻¹) for each Al–O–Al bridge. From this they conclude that although thermodynamic factors could be said to favour Loewensteinian distributions in the bulk crystal, it is more probably the unfavourable energetics in the formation of the precursor rings and clusters in solution which really underpins the rule. This would lead to a kinetic basis to Loewenstein’s rule in the hydrothermal synthesis of zeolites.

Similar calculations by Tossell [44] on the 4-ring Si₂Al₂O₄H₈²⁻ (using H termination to simplify the calculations) show similar results. The Loewensteinian anion is more stable by 63 kJ mol⁻¹ but this reduces to 22 kJ mol⁻¹ if Na⁺ are singly coordinated to the bridging O.

Solid state NMR spectroscopy has also been used to elucidate the Si ordering scheme in solids. Klinowski *et al* [45] studied five materials (losod, Li-A(BW), sodalite, cancrinite and eucryptite) all with Si/Al = 1 by ²⁹Si MAS NMR. In more dense materials, where the framework density (FD) is greater than 17.5 tetrahedra/1000 Å³ 4:0 ordering predominates. Yet in more open materials both 4:0 and 3:1 ordering were found. This led to the assignment of chemical shifts given in Table 1.6.

¹⁷O MQMAS NMR was used to study a natural sample of stilbite with Si/Al = 3 by Stebbins *et al*. [46] They assigned a peak at $\delta_{iso} = 21 \pm 3$ ppm to the oxygen in Al–O–Al and estimated that 0.5% of all O was present in such groups.

A number of non-Loewensteinian frameworks have been synthesised by applying non-hydrothermal methods. The classic example is sodalite where a purely aluminate material has been prepared by Depmeir. [47] And recently a caesium aluminophosphate was synthesised by Huang *et al* [48] *via* a high

Table 1.6: Klinowski's ^{29}Si MAS NMR chemical shift assignments revealing Al–O–Al groups in zeolites. [45]

	Si,Al scheme	Chemical shift from $(\text{CH}_3)_4\text{Si}$
Si(OAl ₄)	4:0	−80 to −87 ppm
Si(OAl ₃)(OSi)	3:1	−88 to −95 ppm
Si(OAl ₂)(OSi ₂)	2:2	−93 to −100 ppm
Si(OAl)(OSi ₃)	1:3	−97 to −106 ppm
Si(OSi ₄)	0:4	−102 to −113 ppm

temperature solid state reaction with caesium chloride flux. This material comprises $[\text{Al}_2\text{P}_2\text{O}_9]^{2-}$ layers held together by Cs^+ cations (see Figure 1.10). The layers are formed by chains of fused 4-rings linked by linear Al–O–Al units such that 6-rings are also present.

1.3.4 Dempsey's rule

Dempsey [49] has proposed a scheme for aluminium ordering at the next nearest neighbour level (specifically within the 6-rings of faujasite zeolites) so that Al–O–Si–O–Al linkages are avoided. Plots of Si/Al ratio with respect to lattice parameter appear to confirm this hypothesis as they reveal discontinuities where the ordering apparently changes. Sato *et al* [50] more recently extended the scope of Dempsey's rule by the use of ^{29}Si MAS NMR to include zeolites of framework type **PHI** and **MER**. However, Schröder *et al* [51] performed *ab initio* calculations on 6-ring units which are not in agreement with Dempsey's rule.

The ordering (or lack of it) of ions in zeolitic frameworks is an interesting problem but clearly still open to question, at least in hydrothermally prepared materials.

1.3.5 Flanigen's rules

Similarly in aluminophosphate materials the $[\text{AlO}_2]^-$ and $[\text{PO}_2]^+$ units of the framework must strictly alternate to give a neutral structure. This prohibits

Figure 1.10: Illustrative diagrams of the caesium aluminophosphate structure containing Al–O–Al linkages (highlighted with black bonds), with Cs as grey spheres, Al as hatched spheres, P as black spheres and O as white spheres. The projection down the a axis reveals the Cs in interlayer sites between the aluminophosphate sheets (a), with the Cs removed the aluminophosphate layers can be seen to be constructed from chains linked by Al–O–Al groups (b).

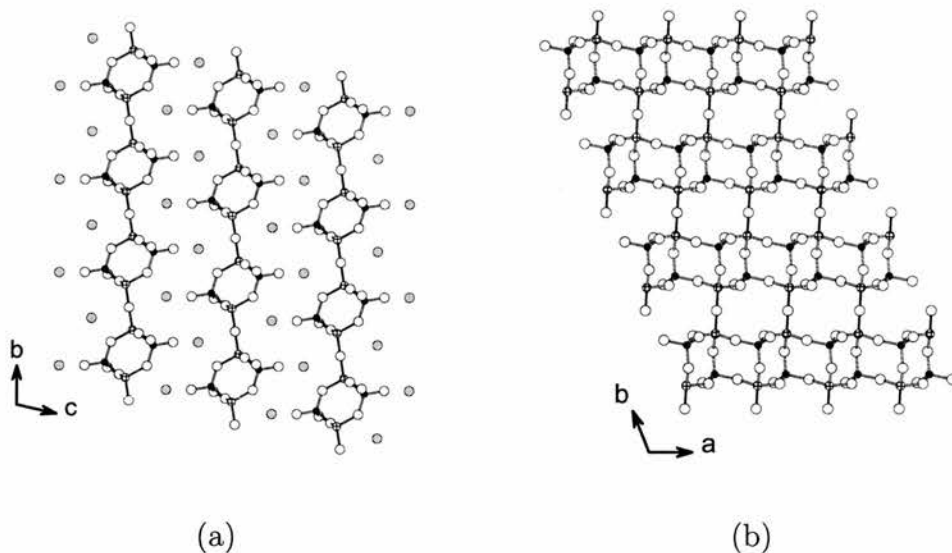


Table 1.7: Flanigen’s rules for the substitution of tetrahedral metal cations into aluminophosphates.

Observed	Not observed
Al–O–P	P–O–P
Si–O–Si	P–O–Si
Si–O–Al	Al–O–Al
Me–O–P	Me–O–Al
Me–O–P–O–Me	Me–O–Me

the formation of 5-rings although aluminium can, on occasion, adopt five or six-coordination (see [52] and references therein).

Flanigen has proposed a set of rules (see Table 1.7) to predict the relative locations of elements substituted into the aluminophosphate framework. The observed arrangements produce neutral or negatively charged frameworks in contrast to the other arrangements that lead to positively charged frameworks.

1.4 Synthesis of microporous solids

Having dealt with the structural aspects of zeolitic solids we should now move on to aspects of synthesis.

Lack of understanding of the mechanism of crystallisation means the synthesis of new materials must be carried out using empirical methods rather than being truly *engineered*. The organic template moiety is certainly the most important factor to be considered when attempting to synthesis new frameworks rationally, but the process still relies heavily on serendipity. Some attempt has been made to aid the process of discovering new materials or optimising the conditions of synthesis, by the use of computation [53] or high throughput techniques [54] and statistical experimental design [55] but these have to date not yielded a truly new framework type. The many variables (temperature, time, reactant source, *pH*, organic or inorganic cations in the gel, ageing, autoclave fill volume *etc.*) interact with each other to make for extremely complex systems.

Microporous solids are typically synthesised solvothermally under autogenous pressures and temperatures between 100–220 °C. A reactive gel, typically composed of hydrated alumina and aqueous phosphoric acid (in AlPO_4 preparations), is heated with an organic structure directing agent in a PTFE-lined stainless steel autoclave. The solvent becomes superheated and its solvation power is greatly increased which allows the gel to mix and dissolve more effectively than in an open system. The synthesis gel is a system with high entropy relative to the final product of crystallisation. Nevertheless zeolitic materials crystallise, the polymorph which does so first in any particular gel will therefore necessarily be the one with highest entropy. Microporous solids though are metastable and so may transform successively to increasingly thermodynamically stable phases. The process is encapsulated in *Ostwald's law of successive transformations* and is observed in numerous systems. For example, zeolite A will convert to the more stable sodalite in solutions of high alkalinity. [56] If the alkalinity is reduced zeolite P will crystallise between zeolite A and sodalite. Dense phases, such as quartz (or in aluminophosphate systems, berlinite or trydimite) may also form. The use of organic templates can inhibit the formation of dense phases by further stabilising the porous ones. And once separated from the mother liquor the metastable zeolite phase will remain unchanged indefinitely.

1.4.1 The concept of templating

The concept that the organic component of zeolitic gels is not simply acting to balance charge but also to *direct* the formation of particular framework structures was first put forward to account for the close relationship between the cavities and the organic moiety in some zeolites. Examples such as the tetramethyl ammonium cation occluded within the cages of sodalite at synthesis give weight to this idea: the cations are too large to enter the framework after crystallisation. [57] It was found that tetrapropyl ammonium cations lie in the intersection of the two pore systems in ZSM-5, the alkyl chains lying along the channels. [58] It has been suggested that these organic cations are acting as “templates”, arranging the oxide species in the gel around themselves to

crystallise particular frameworks.

Nevertheless, this is too simplistic: many zeolites may be prepared in the absence of organic templates, many templates will direct the formation of several frameworks and many frameworks may be synthesised with several templates some of which may have a poor correlation in shape to the shape of the materials' pores. Consequently some authors [59] have made a distinction between "templating", the process by which:

"a unique template leads to the formation of a unique structure which relates to the geometrical and electronic structure of the template"

and "structure direction", a more:

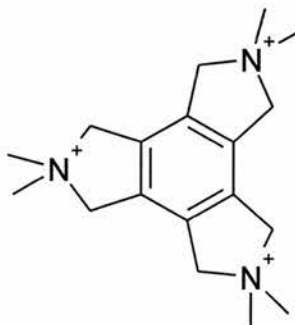
"subtle effect in which the use of a particular organic moiety leads to a preference for the synthesis of a particular structure *via* a combination of factors such as *pH* modification, solubility modification and electrostatic interactions with the solubilised silica, alumina and phosphate species in the reaction mixture."

Davis *et al* [60] distinguished three possible modes of action for the organic guest molecules, that is (i) as space fillers, (ii) as structure directing agents and (iii) as true templates.

Space fillers act only to exclude water from the molecular sieves' pores, thus helping to stabilise the growing framework. Examples may be found in the synthesis of zeolite ZSM-5 and $\text{AlPO}_4\text{-5}$ both of which can be made in the presence of numerous organic cations, the implication of which is that these organics are acting only as space fillers.

Examples of structure direction abound, but true templating is much less common. The preparation of ZSM-18 (**MEI**) with 2,2,5,5,8,8-hexamethyl-2,3,4,5,6,7,8,9-octahydro-1*H*-2,5,8-triazatrindene, "tri-quat" (Figure 1.11) is one case often quoted as the shape of the pores matches closely the shape of the organic molecule. [61] Energy minimisation by Davis and Lobo [60] indicates that the template is unable to rotate in the cage which has the same threefold symmetry as the tri-quat. Stevens *et al* [62] performed Monte Carlo

Figure 1.11: 2,2,5,5,8,8-hexamethyl-2,3,4,5,6,7,8,9-octahydro-1*H*-2,5,8-triazatrindene (tri-quat) used in the synthesis of zeolite ZSM-18 may be the only example of “true templating” known. [60]



simulated annealing calculations and found that the shape of the template plays a critical role in determining the location of the TO_4 tetrahedra that surround it—indicative of true templating.

1.4.2 Mechanisms of crystallisation

It has been hypothesised that microporous solids form *via* one of a two broad mechanisms: namely by transformation of the solid gel phase or by solution-phase nucleation and crystallisation. [63] More detailed mechanisms involving, for example, CBUs or chains have also been proposed based on examinations of known frameworks.

A plethora of techniques have been used to investigate the crystallisation of microporous solids. These include *in situ* X-ray and neutron diffraction, IR/Raman, EXAFS and NMR spectroscopies and optical/electron microscopy (see the review by Francis and O’Hare [64] and the references therein for further details). Nevertheless the autoclave largely remains a black box and a true, universal, mechanism has yet to be discovered. Theories abound however.

Solid hydrogel transformation mechanism

Here it is suggested that the solid gel phase may crystallise directly to form the observed zeolite. Evidence for this comes from both chemical analysis

and spectroscopy. It has been found, for example, that the composition of the final phase of many zeolites is the same as that of the parent sol-gel [65] and furthermore that gels known to form zeolite X would, when dried, slowly crystallise the desired phase under ambient conditions. [56]

Solution-mediated transport mechanism

Kerr [66] was the first to propose that soluble species play a major role in the crystallisation of zeolites. He suggested that an equilibrium exists between the solid gel and the solution which shifts towards the solution when nucleation occurs. Thus the gel dissolves continuously providing a feedstock to the growing crystals *via* the solution phase. Zeolites including A, B, Y, mordenite and ZSM-5 amongst others, will crystallise from clear solutions, providing evidence for this hypothesis (see for example, [67]).

Chain self-assembly model

Recently, Ozin *et al* [68] have augmented the solution-mediated transport mechanism for aluminophosphate materials. In their solvothermal preparations they observed that, (a) different structures are obtained in aqueous and non-aqueous syntheses and, (b) while many different templates have been used to direct the formation of chain and layer aluminophosphates the number of compositions seen in the inorganic component of in these materials is low. From this they developed a model based on the hydrolysis mediated transformation, *via* rotations and subsequent condensation, of a parent chain to explain the formation of 1-D, 2-D and 3-D framework structures.

So while these and other researchers have found explanations along similar lines to satisfactorily explain different features seen in microporous solids (such as the role of the fluoride ion in ordering the template during crystallisation of siliceous zeolites **IFR** and **STF** [69]) a full understanding of the mechanism has not been reached. A recent review by Cundy and Cox [70] explores aspects of the history and development of the hydrothermal method further.

1.5 Physicochemical properties

Now that both the long and short range order in zeolitic materials has been discussed some of their properties may be introduced. Porous solids are of interest because molecules, atoms and ions may diffuse into their frameworks and interact there. Zeolites (aluminosilicates) have long been used in ion-exchange (to selectively take-up ions to soften water or remove radioactive isotopes from waste streams), adsorption (to separate, for example, large from small molecules) and in catalysis (*e.g.* cracking). The composition of such materials is important as well as the structure. In molecular sieving a pure silica zeolite will, because it is hydrophobic, selectively adsorb organic molecules from water. Pure aluminophosphate has no ion-exchange capacity or catalytic potential, but the substituted aluminophosphates (MAPOs and SAPOs) do. The following section will concentrate on catalytic applications of these, rather than sorption or advanced material applications, but for a summary of the latter see Davis's recent review. [71]

1.5.1 Catalysis

Catalysis has a long history, but it was not until 1836 that the process was defined [72] by Jöns J. Berzelius:

“bodies. . .[which] have the property of exerting on other bodies an action which is very different from chemical affinity. By means of this action they produce decompositions in bodies, and form new compounds into the composition of which they do not enter. This new power, hitherto unknown, is common both in organic and inorganic nature. . .I shall. . .call it catalytic power. I shall also call catalysis the decomposition of bodies by this force.”

Berzelius's original definition [72] is still reasonable today, yet even before this time catalysts were in use. The first example of the commercial exploitation of heterogeneous catalysis came in 1823 with Döbereiner's lighter (or tinder box) which produced a flame from the oxidation of hydrogen, generated from the action of acid on zinc, over a finely divided platinum catalyst. By 1828

hundreds-of-thousands of Döbereiner's lighters had been produced and were still popular at the beginning of the first world war. [73]

Early landmarks in the evolution of industrial catalysis include processes by Haber (1909) for the synthesis of ammonia and Ostwald (1920) for the synthesis of nitric acid. Houdry's work (1930–40) on fixed-bed catalytic cracking of oils to fuel and Lewis and Gilleland's fluidised catalytic cracking reactor (1941) are also notable, as is the Fischer–Tropsch chemistry that enables almost all carbon sources to be converted, *via* syn-gas (CO and H₂), to alkanes, alkenes and alcohols (depending upon the catalyst). Further details and examples may be found in the extensive review by Thomas *et al.* [74]

Active sites

The Si/Al ratio may vary in zeolites. Ion-exchange capacity depends on the Al^{III} concentration, as does the strength of the acid sites (present when the counter ion is H⁺). Consider the schemes in Figure 1.12.

In zeolites the negative charge is not localised but distributed over the framework oxygens. The Brønsted acid form is represented as in Figure 1.12.c (although H is mobile). Where there is a low density of proton donor groups, the acid strength is high. Zeolites with low Al content are prepared by dealumination (*e.g.* by extraction with SiCl₄, or treatment with steam). Such materials are termed *ultrastable*. At very low Al content superacid sites are found which are, at high temperature, capable of protonating alkanes (*i.e.* cracking them). In reality a variety of acid site strengths are found even in the same material because the Al distribution is not necessarily homogeneous.

Other acid sites may be present also. Addition of water to acidic zeolites yields H₃O⁺ and cations such as La³⁺ react with water to form La–OH groups that are acidic.

When the proton form of a zeolite is heated, water is driven off and coordinatively unsaturated Al^{III} ions are formed. These are strong Lewis acids. From the scheme (Figure 1.13) it can be seen that one Lewis acid site is formed from two Brønsted acid sites. Aluminophosphates, like pure SiO₂, are neutral and so contain no acid sites. Yet if a metal cation M is incorporated into the

Figure 1.12: Illustrative schemes of the aluminosilicate zeolite framework. Each negative charge may be balanced by a monovalent cation (a), or a divalent cation may balance pairs of charges (b). If protons are present as the charge balancers the zeolite becomes a solid acid catalyst (c).

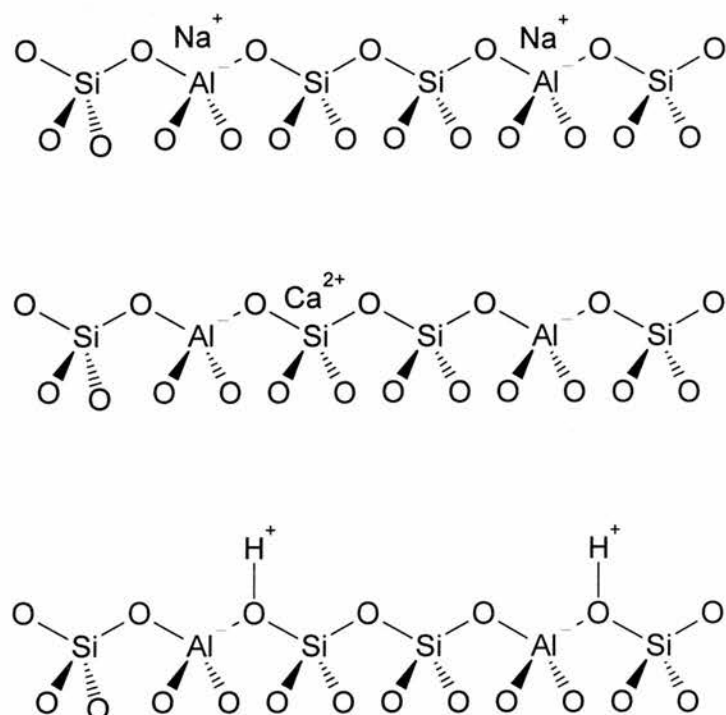
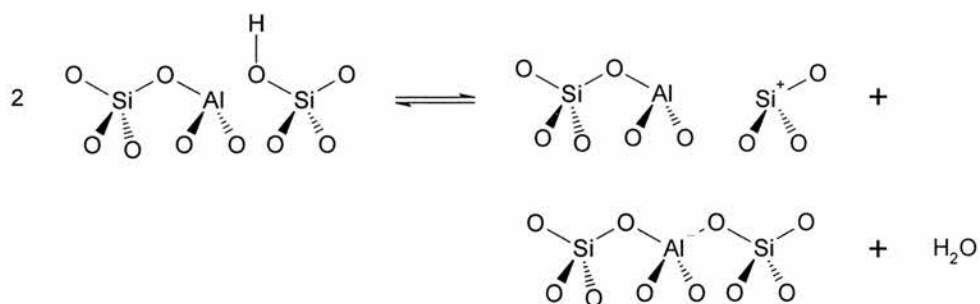


Figure 1.13: Scheme representing Brønsted acid sites in equilibrium with a Lewis acid site within the zeolite framework. When the H-form of a zeolite is heated at high temperature water is driven off and coordinately unsaturated Al^{III} ions are formed. These are strong Lewis acid sites.



framework aluminophosphate structure then an active catalytic site may be created. Brønsted acidity results from the substitution of a trivalent cation (Al^{III}) by a divalent one (*e.g.* Mg^{II}) since a proton is necessarily required to maintain electroneutrality. Alternatively P^{V} may be substituted by Si^{IV} .

In the same way if Mn^{II} , Fe^{II} or Co^{II} are substituted for aluminium then acid sites are created. Moreover, if the divalent ions are oxidised to their trivalent state, the Brønsted acidity disappears and redox properties are conferred. This occurs when the as-prepared material is calcined in oxygen (the organic template moiety is also driven off). It is possible to form a redox cycle while the ions remain in the framework in this way.

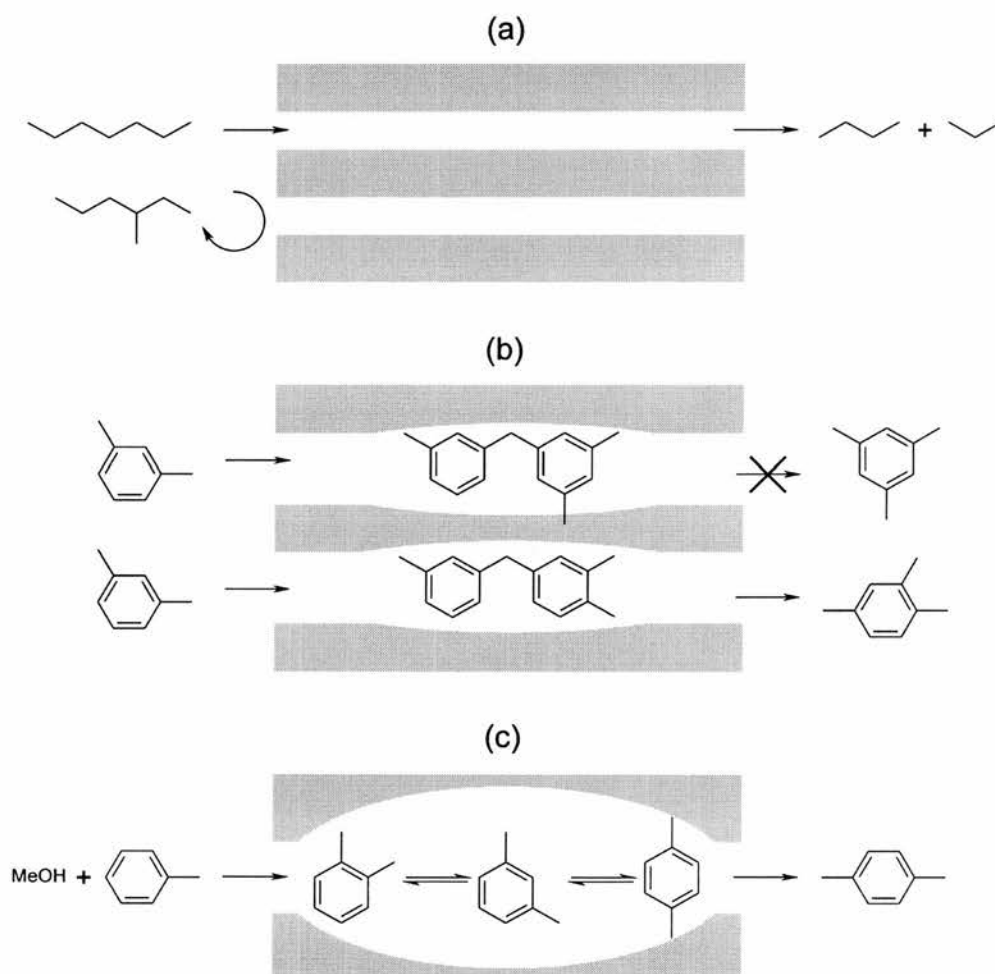
Activity and selectivity

A good catalyst must possess both high activity and long-term stability. These though can be issues of chemical engineering, from the academic perspective, selectivity (the ability to direct conversion of reactants along one path only) is the most interesting property.

The nature of the active site, its immediate environment and the geometry of the attached reactant (substrate) are of critical importance in determining the degree of selectivity offered by a catalyst. This is exemplified by enzymes which, due to advances in crystal structure determination, the technique of site-specific mutagenesis and the advent of sophisticated kinetic studies of tailored enzymes, are now well understood. For example, lysozyme, the first enzyme to have its structure solved (1965), is known to contain a cavity active site or cleft lined with amino acids that, while not binding the substrate too tightly, stabilise the transition state during the hydrolysis of glycosides. [75]

Shape selectivity is also a feature of zeolitic microporous solids since the dimensions of the pores of a particular material govern the shape of the reactant molecules that may enter it, the products that may leave it, and the nature of the intermediates that can form within it (see Figure 1.14).

Figure 1.14: Scheme showing three types of shape selective catalysis by zeolitic materials. The pore size determines for each reaction whether reactant (a), transition state (b), or product (c) selection occurs. [76]



Catalytic reactions

Catalysis is always preceded by adsorption. Adsorption is the accumulation of material on a surface, in contrast to absorption which is a bulk phenomenon where material is taken into the solid. The distinction becomes blurred with microporous solids as most of the surface lies within the solid. Moreover, two types of adsorption may be defined: physical adsorption and chemisorption. The former is a weak force of molecular interaction, whereas the latter involves the making and breaking of chemical bonds.

Heterogeneous catalysis proceeds *via* one of two basic mechanisms. In the Langmuir-Hinshelwood mechanism both reacting species are adsorbed on the surface, atomic reorganisation takes place in the adsorbed layer, and the product is formed. In the Eley-Rideal mechanism only one reactant is adsorbed, the product being formed when the other reactant impinges upon it from the surrounding pore volume. Further details may be obtained from Gates's monograph. [75]

Catalytic reactors

Having considered the catalysts themselves it will now be instructive to examine some of the main types of reactor used in these catalytic reactions. [77] The discussion will, however, be limited to laboratory reactors rather than industrial ones. Whether laboratory or industrial, reactors may be divided broadly into two types: *batch* and *continuous*.

Continuous reactors are open systems into which reactants constantly flow, while the products are removed. The catalyst usually forms a fixed bed in such reactors although flowing solids may sometimes be used if the catalyst deactivates rapidly. Laboratory reactors are typically of the *tubular* variety consisting simply of a straight tube containing the catalyst through which the reactant gas continuously flows. As the tube diameter increases so does the difficulty in obtaining a uniform temperature. If the conversion within the reactor is kept low (less than 5%) then maintaining isothermal conditions becomes easier. (Operating a reactor at low conversion is called "differential" mode.) In the differential tubular reactor gas passes through the catalyst

bed in plug flow, *i.e.* the radial velocity profile is uniform. The principal problem with operating laboratory reactors in this way is determining accurate chemical analysis of the multicomponent mixtures when conversion is so low. The tubular reactor is normally mounted vertically with the flow of gases moving downwards to avoid loss of solid material. The condition whereby channelling occurs within the solid bed, and the reactant stream is able to bypass the catalyst, must be avoided. Another problem is obtaining good distribution for vapour-liquid feeds within the catalyst bed.

When the tubular reactor is operated at higher conversions then it is said to be in “integral” mode. In narrow tubes isothermal conditions may be obtained without excessive difficulty. However, reactions that are even mildly exothermic are likely to cause loss of desired constant catalyst bed temperature. If isothermal conditions are maintained and plug flow remains an adequate description of the fluid mechanics then the same equations describing reactor performance can be used for both differential and integral modes (see the textbook by Thomas and Thomas for details [78]). This may not be adequate at high conversions because the concentration of reactant will decrease along the length of the catalyst bed. Diffusion effects within the catalyst particles may be avoided by using small particles, however if the particles are too small a large pressure drop over the catalyst bed may be induced that will invalidate the calculation of rate data.

Batch reactors are closed systems containing known quantities of reactant and catalyst. During the reaction the concentration of reactant is observed to diminish with time. Pressure and temperature are not serious constraints, but these reactors are unsuitable for studying fast exothermic reactions as changes in concentration and pressure are difficult to follow and a constant temperature is not easy to maintain. Batch reactors are usually used industrially only when small quantities of product are required.

Reactions involving continuous and batch reactors have been studied and the results are presented in Chapter 5 along with a detailed discussion of the literature.

Chapter 2

The search for new materials

2.1 Introduction

With each new zeolite structure comes potential for varied physicochemical properties and novel applications. The number of new framework topologies has increased dramatically in recent years. [79] Zeolite framework types are collated by the IZA Structure Commission and published in the *Atlas of Zeolite Framework Types*, [7] the first edition of which (1978) contained 38 topologies. The second edition (1988) listed 64, the third (1992) 85, the fourth (1996) 98 and the fifth (2001) 133. The desire of chemists to construct novel pore architectures is not simply driven by intellectual curiosity, but by the need to solve real problems in sorption and catalysis. Large pore frameworks have been synthesised to convert catalytically ever larger molecules. Chiral frameworks [80] show promise in the resolution of chiral molecules and may have capacity for asymmetric catalysis. [81] Small pore solids have potential as catalysts for the conversion of, for example, methanol to light alkenes or in the terminal oxidation of alkanes. (See Table 2.1 for definitions of pore size.)

In this chapter the discovery process of new aluminophosphate-based materials and their basic characterisation will be discussed. Firstly, though, some recently discovered and structurally interesting materials will be reviewed. No attempt is made to be exhaustive.

Table 2.1: Classification of zeolitic materials by pore size.

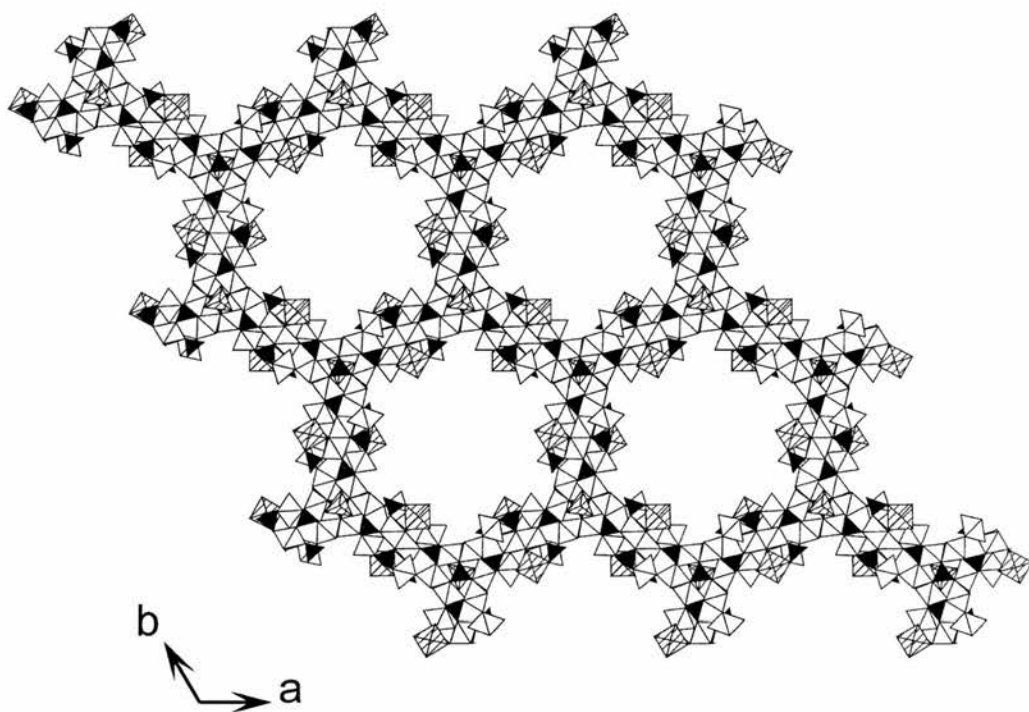
Class	Number of T atoms	Approximate size, Å
Ultra-large	14-ring	9.0
Large	12-ring	7.5
Medium	10-ring	6.0
Small	8-ring	4.5

2.1.1 Recent developments

The range of chemical compositions of porous crystalline solids is much broader today than aluminosilicate and aluminophosphate materials which have traditionally been investigated. Phosphates of gallium, indium, tin and many transition metals have been made. [82] Moreover, silicon and phosphorus have been replaced, expanding the family to include sulfides, selenides and nitrides. In addition, organic groups have been included covalently bound to phosphorus atoms (phosphonates) [83] and there has been work on open-frameworks with rigid organic links that utilise semi-ionic, covalent and hydrogen bonds to form novel materials. [84] Nevertheless, the need to be concise must limit discussion to silicate and phosphate-based materials here; for reference, a review of metal phosphate chemistry is available by Cheetham *et al* [82] and Férey has written another describing inorganic-organic hybrid structures. [85]

The synthesis of crystalline large pore materials is desirable but non-trivial. Although ordered mesoporous silica has been prepared with pores in excess of 20 Å (for example, the M41S family [86] comprising hexagonal MCM-41, cubic MCM-48 and layered MCM-50) these materials are not crystalline. Crystallinity is desirable not only for the elegance it confers on a material's structure, but also for the relative ease it affords a full structure determination. Crystallinity may also yield desirable properties such as increased mechanical stability *etc.* Nature has, of course, succeeded in forming enormous pores, exemplified by the mineral cacoenite, $[\text{Al}(\text{Al},\text{Fe})_3\text{Fe}_{21}\text{O}_6(\text{OH})_{12}(\text{PO}_4)_{17}(\text{H}_2\text{O})_{24}] \cdot \sim 51\text{H}_2\text{O}$ (Figure 2.1) which contains 14.2 Å channels. [87]

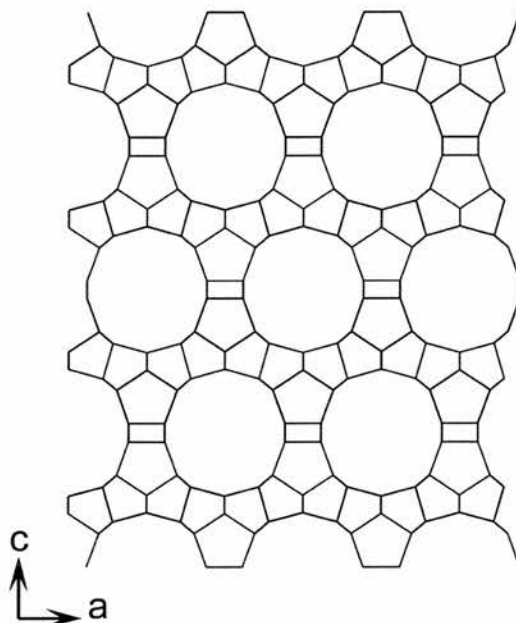
Figure 2.1: Illustrative diagram of the mineral cacoxenite, with Al as hatched trigonal bipyramids, Fe as white octahedra, and P as black tetrahedra. (For clarity, the water present in the channels, is not shown.) Projected down the c axis the enormous 14.2 Å channels are clearly visible.



Crystallising materials with similarly sized pores in the laboratory has not proved to be so easy.

The first ultra-large pore aluminophosphate, VPI-5, (**VFI** framework type) was reported by Davis *et al* [88] in 1988. This material contains 18-rings of diameter 12.7 Å. Others have followed such as the 14-ring AlPO_4 -8 (**AET**). [89] Yet such materials' potential as catalysts is doubtful because of their low thermal stability; only recently, with the discovery of UTD-1 (**DON**), has a high silica zeolite been made with ultra-large pores. [90] UTD-1 contains 1-D 14-ring channels (10×7.5 Å) and is an intergrowth of two or more polymorphs. [91] One polymorph has so far been prepared phase pure. [92] CIT-5 (**CFI**) is also a 14-ring silica zeolite. Figure 2.2 shows the 1-D channel system running parallel to the b axis. Other silicates such as SSZ-48 (**SFE**) [93] and SSZ-55

Figure 2.2: The [010] projection in CIT-5, a high silica zeolite with 1-D, 14-ring channels. Each vertex represents a tetrahedral atom, oxygens have been removed for clarity.



(ATS) [94] contain large 1-D 12-ring channels.

Materials with pores in more than one dimension are more desirable however as they generally deactivate more slowly during catalysis. Before the discovery of ITQ-7 (ISV) by Cambor *et al* [95] zeolite β had been the only known high silica 3-D 12-ring channel material. Unlike ITQ-7, β is a complex intergrowth of polymorphs. Intergrowths, because they contain stacking faults, are significant for catalysis because their presence can inhibit diffusion within the material. Very recently another siliceous zeolite, ITQ-21, has been discovered [96] with a 3-D 12-ring channel system. This is a promising material for commercialisation because unlike ITQ-7 or β its pore openings are larger than in zeolite Y, but unlike Y ITQ-21 would not require ultra-stabilisation before use.

Two novel large pore AlPO_4s are DAF-1 (DFO) and STA-1 (SAO), Figures 2.3 and 2.4, respectively. The former is only prepared as the metallo-

Figure 2.3: The $[001]$ projection of Mg-DAF-1 with 12-ring channels visible. Oxygen atoms removed for clarity.

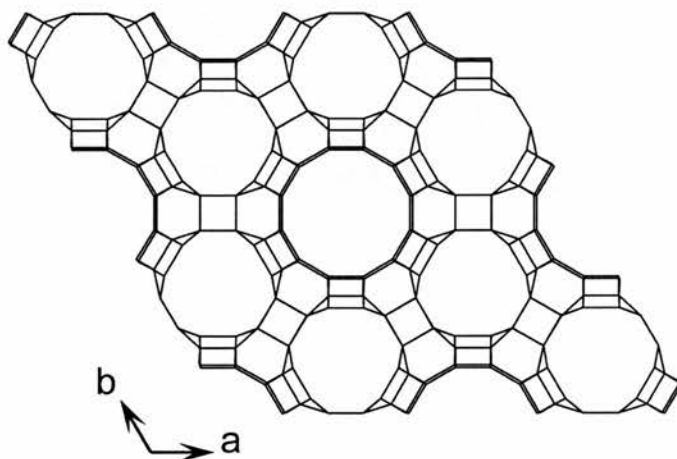
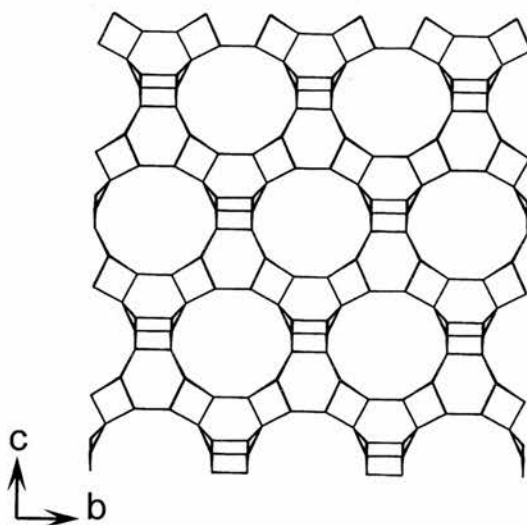


Figure 2.4: The $[100]$ projection of Mg-STA-1 with 12-ring channels running parallel to the a and b axes. Oxygen atoms removed for clarity.



aluminophosphate and contains two independent large pore channels systems. [97] STA-1, reported by Noble *et al* [98] in 1997, comprises channels bounded by 12-rings that run parallel to the a and b axes, but offset in the z direction. The channels are linked along z to form cavities.

Recently three new aluminophosphate (or gallophosphate) materials have been discovered with 3-D 12-ring pores containing cavities. [99] Prior to this only **FAU** and **EMT** were known in this class (see Figure 1.1, page 4). The three materials are called UCSB-6, -8 and -10 and have been assigned the topological codes **SBS**, **SBE** and **SBT** respectively. UCSB-6 and -10 share a similar structure, composed of two different cavities, illustrated in Figure 2.5. The difference lies in the way in which two cancrinite cages are linked across a double 6-ring. Such pairs of cages may be related to each other by either mirror symmetry (as in **LTL**) or by an inversion centre (as in **ERI** and STA-2, see below). The mirror linked unit is found in UCSB-6 (Figure 2.6.a), while the inversion-linked unit is found in UCSB-10 (Figure 2.6.b). The UCSB-8 framework (Figure 2.7) consists of a set of 12-ring channels in two-dimensions and an 8-ring channel in the third. These intersect to form very large (64 T atom) cavities which measure $20 \times 20 \times 15 \text{ \AA}$.

Small pore materials form the other extreme in zeolite channel size. Medium pore materials, such as the extensively studied ZSM-5 (**MFI**) will not be considered here specifically. There are a few examples of other ring numbers, for example, SSZ-23 (**STT**) [100] which contains 7-ring and 9-ring channels. The latter are puckered which reduces the effective pore size so that this material must be considered to be small pore.

Although much recent research has gone towards the creation of materials with ever larger pores the scope for producing new *small* pore materials has not diminished. Such materials are of industrial significance and are used extensively in, for example, cracking and molecular sieving applications.

The first example of a silica polymorph containing straight 2-D 8-ring channels is ITQ-3 (**ITE**). [101] In contrast the aluminophosphate APDAB200 has 2-D 8-ring zigzag channels. [102] Work in this laboratory has led to the discovery of novel aluminophosphate-based materials STA-2 (**SAT**) [98] which

Figure 2.5: Illustrative diagram of the UCSB-6 framework projected onto [001] reveal 12-ring channels and two types of cavities, A and B.

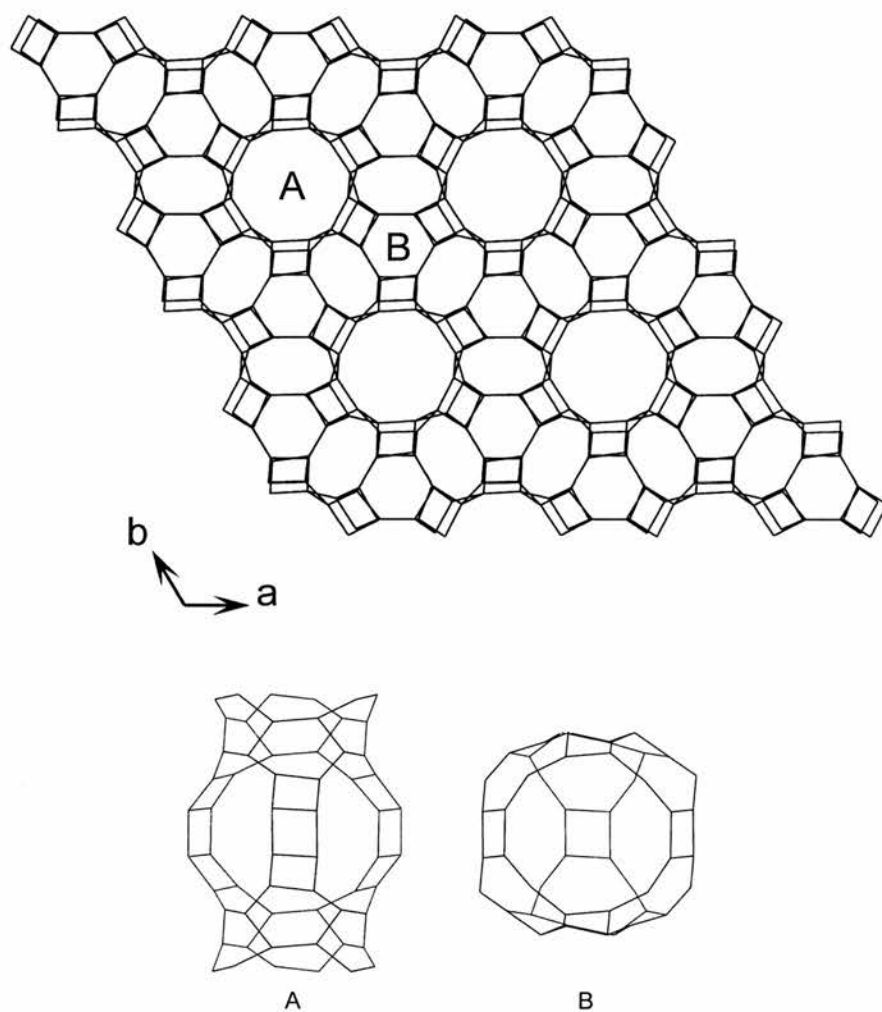


Figure 2.6: Diagrams illustrating the ways in which two cancrinite, or ϵ , cages may link across a double 6-ring. The two cages are related to each other either by mirror symmetry (a), or by an inversion centre (b). 4-rings are shown above and below the cancrinite cages, and selected rings have been shaded, to illustrate more clearly this difference. For clarity, O has been omitted.

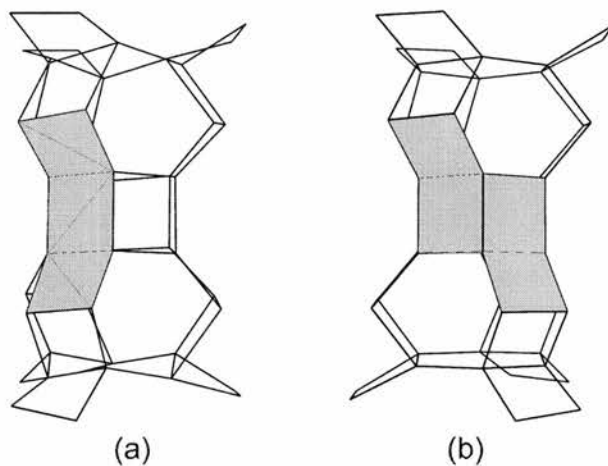


Figure 2.7: Illustrative diagrams of the UCSB-8 framework. UCSB-8 contains 12-ring channels in two dimensions and 8-ring channels in the third; where these intersect large ($20 \times 20 \times 15 \text{ \AA}$) cavities are formed.

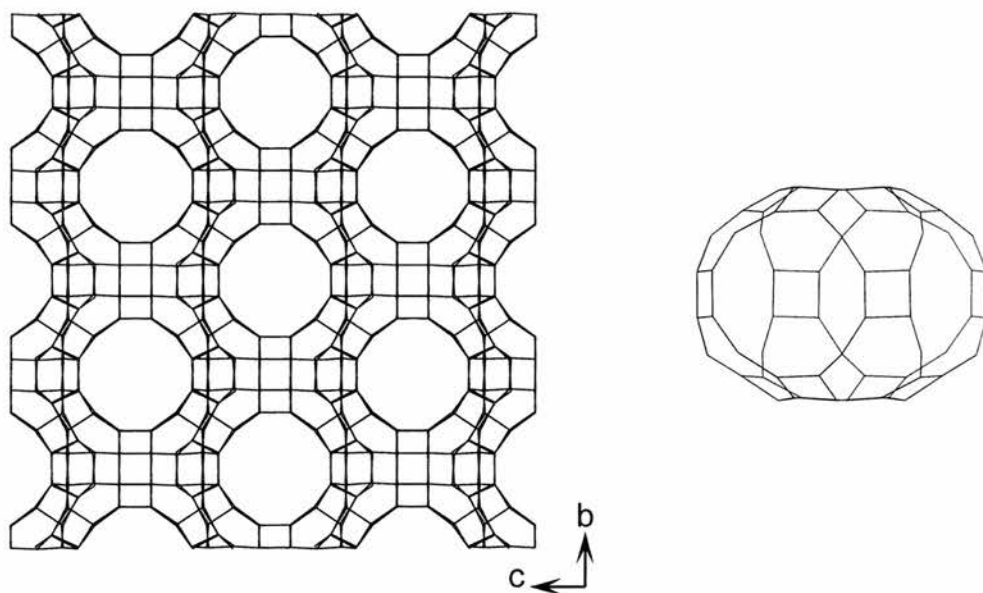
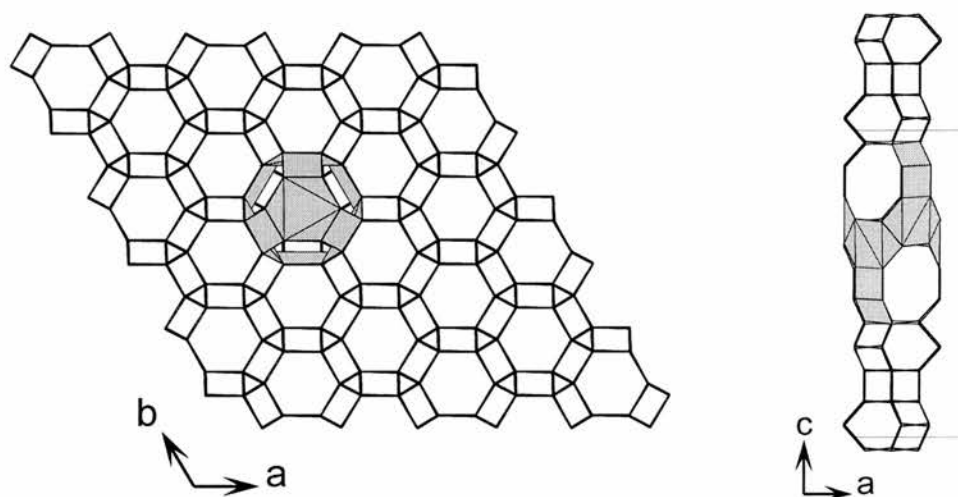


Figure 2.8: Illustrative diagrams of the STA-2 framework, in which the cavity has been highlighted with shading and O atoms have been removed for clarity. Projected onto [001] 8-ring channels may be seen running through the cavity. The structure is constructed by stacking 6-ring units, see text for further details.

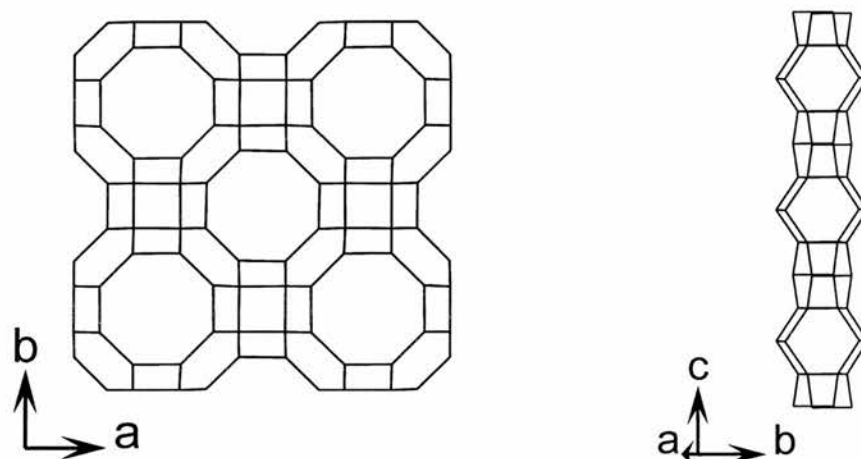


contains 3-D pores and STA-6 (**SAS**) [103] which contains 1-D pores. STA-2 is constructed from columns composed of a novel cavity *ca* 17 Å long (Figure 2.8). Above and below this unit in the *c* direction are two cancrinite cages rotated by 60° with respect to each other, and sandwiching a double 6-ring. The cancrinite cages are related by an inversion centre and this is the same unit seen in UCSB-10. The framework may be described in terms of stacked 6-rings whose centres are found only at (0, 0), ($\frac{1}{3}$, $\frac{1}{3}$) or ($\frac{2}{3}$, $\frac{2}{3}$) in the *ab* plane. If these positions are labelled A, B and C respectively, STA-2 can be said to have the stacking sequence ABAACACCBCBB (see Table 2.2). Similarly, the structure of STA-6 (Figure 2.9) is described as being constructed from chains of double 6-rings (D6Rs) running parallel to the *c* axis. Alternate D6Rs are rotated by 90° with respect to the chain axis and linked by face-sharing through 4-rings windows.

Table 2.2: 6-ring stacking sequences in zeolitic materials. The novel aluminophosphate STA-2, discovered in 1997, contains the most complicated regular 6-ring stacking sequence of any known zeolitic material. (Table reproduced from [98].)

Name	Layers in repeat	Sequence
Cancrinite	2	AB
Offretite	3	AAB
Sodalite	3	ABC
Gmelinite	4	AABB
Losod	4	ABAC
Chabazite	6	AABBCC
EAB	6	ABBACC
Erionite	6	AABAAC
Liottite	6	ABABAC
Afghanite	8	ABABACAC
AlPO ₄ -56	8	AABBCCBB
Levyne	9	AABCCABBC
AlPO ₄ -52	12	AABBCCAACCBB
STA-2	12	ABAACACCB

Figure 2.9: Illustrative diagrams of the STA-6 framework, in which the cavity has been highlighted with shading and O atoms have been removed for clarity. Projected onto $[001]$ 8-ring channels may be seen running through the cavity. The structure is constructed by stacking 6-ring units, see text for further details.

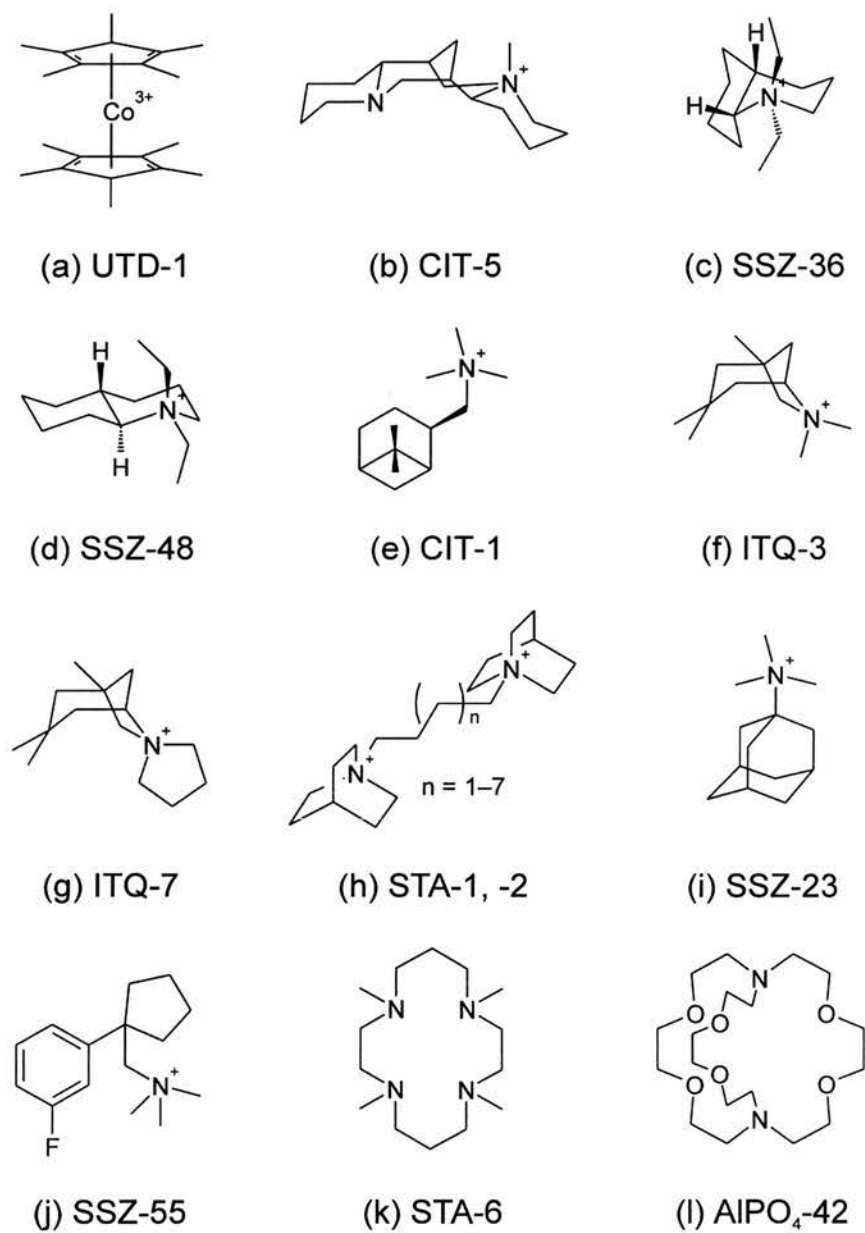


“Designer” templates

One method applied in this work for the discovery of new porous frameworks centres around the use of novel (“designer”) structure directing molecules. This approach is based on the premise that, (a) the organic cation present in the synthesis gel controls the phase which is crystallised and, (b) that only materials which require very specific structure direction remain to be discovered (although see below for examples showing this is not the case). The groups of Davis, Zones and Stucky in the USA and Cambor in Spain (see below for references) have pioneered use of this method. They have prepared a large number of conformationally rigid molecules, whose C/N ratio is within well defined limits, and have used these successfully to synthesis new materials. Illustrative examples of templates that have recently produced novel solids are given in Figure 2.10. Selected examples will be discussed in more detail now.

The silicate UTD-1 has been prepared as a mixture of polymorphs, [91]

Figure 2.10: “Designer” templates are extensively used in the synthesis of novel zeolitic materials. The framework name is given beneath the template molecule; see text for further details.



and one (polymorph C) as a pure phase when fluoride was included in the synthesis gel. [92] The organometallic complex bis(pentamethylcyclopentadienyl)cobalt(III) hydroxide, $[(\text{Cp}^*)_2\text{Co}]\text{OH}$, see Figure 2.10.a, was used as the template in both cases. Balancing the positive charge on the template with F^- is essential to prevent the faulted structures being produced. The template was found to be ordered with the fivefold axis parallel to the channel direction and with the Co located in the plane of alternate 14-rings. It could be removed by calcination and acid washing after synthesis to leave the pore system open. When the smaller bis(cyclopentadienyl)cobalt(III) $[(\text{Cp})_2\text{Co}]^+$ ion was used instead, clathrasil phases **NON**, **AST** and **DOH** were initially formed (although later UTD-12, a zeolite with accessible pores, was discovered). [104]

Synthesis of CIT-5 was achieved with *N*(16)-methylsparteinium hydroxide (see Figure 2.10.b). The authors suggest however that it is a weak directing agent for CIT-5, the optimal synthesis includes Li^+ which is thought to accelerate crystallisation of CIT-5 in preference to SSZ-24 (**AFI**). ITQ-21 is also made with *N*(16)-methylsparteinium cations.

There are abundant examples of subtleties in structure direction. Examples include the synthesis of zeolites SSZ-36 [105] and SSZ-48 [93] with the *trans* and *cis* isomers of *N,N*-diethyldecahydroquinolinium cations, respectively (Figure 2.10.c and 2.10.d). Or the synthesis of CIT-1, [106] a zeolite with intersecting 10- and 12-ring channels, where the (+)-isomer of *N,N,N,N*-trimethyl-(±)-*cis*-myrtanilammonium hydroxide (in which the methylene that links the trimethylammonium group to the rest of the molecule is pointing “up”) is required (Figure 2.10.e). And increasing the size of a template very slightly will transform the product from a small to large pore material, as in the different *N*-substitutions of 1,3,3-trimethyl-6-azoniabicyclo[3.2.1]octane, Figure 2.10.f and 2.10.g, or lengths of a methylene chain as in α,ω -bis(1-azoniabicyclo[2.2.2]octane)alkyl cations, Figure 2.10.h.

Use of 1,4-bis(1-azoniabicyclo[2.2.2]octane)butyl dihydroxide (Figure 2.10.h, $n = 1$) allowed the synthesis of pure silica SSZ-16 [107] which is isostructural with AlPO_4 -56 (**AFX**). [108] The following year AlPO_4 -STA-2 [109]

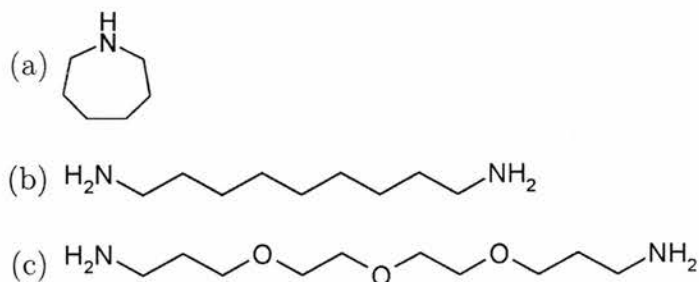
was reported—templated with the same organic as SSZ-16 (or with 1,5-bis-(1-azoniabicyclo[2.2.2]octane)pentyl dihydroxide) it has a different structure, although AlPO_4 -56 was sometimes observed as an impurity phase. Noble *et al* [98] also synthesised AlPO_4 -17 (**ERI**) when a similar template with a three-carbon methylene chain was employed. Molecular modelling revealed a close fit between the templates in these cases and the cavities in the **ERI**, **SAT** and **AFX** frameworks. [110]

N,N,N,N-trimethyl-1-adamantammonium and [1-(3-fluorophenyl)cyclopentyl)methyl]trimethylammonium cations (Figures 2.10.i and 2.10.j) direct the synthesis of SSZ-23 and SSZ-55, respectively. SSZ-23 has unusual 7- and 9-ring channels. [100] SSZ-55 is a borosilicate zeolite with the **ATS** topology. [94] This framework was known previously only in aluminophosphate form and to synthesise the silicate a very specific template was required.

The azamacrocycle 1,4,8,11-tetramethyl-1,4,8,11-tetraazacyclotetradecane (Figure 2.10.k) has been found to direct the synthesis of the novel material STA-6 from magnesianaluminophosphate gels, or AlPO_4 -21 from pure aluminophosphate systems. [103] The un-methylated macrocycle 1,4,8,11-tetraazacyclotetradecane forms part of a new inorganic–organic hybrid if included in a gallophosphate gel. [111] The azapolymacrocycle hexaoxa-4,7,13,16,21,24-diaza-1,10-bicyclo[8.8.8]hexacosane (Figure 2.10.l) has been found to direct the crystallisation of pure aluminophosphate materials with the **LTA** (zeolite A) structure. [112] Aza[poly]macrocyclic templates are a promising new class of structure directing agent which have not been extensively studied.

It is interesting to note, however, that materials such as UCSB-6, -8 and -10 [99] and MCM-35 [113] have been synthesised recently with cations of low rigidity, small size and low C/N ratio. The pure silica form of MCM-35 is made with hexamethyleneimine while the phosphates UCSB-6 and -8 are formed with 1,9-diaminononane and UCSB-10 with 4,7,10-trioxa-1,13-tridecanediamine (Figure 2.11). The novel aluminosilicate ERS-7 [114] has recently been made with the *N,N*-dimethylpiperidinium cation over a limited temperature and compositional range. By altering various synthesis parameters frameworks with the known topologies **LEV**, **MOR**, **MTW** and **NON**

Figure 2.11: Not all new microporous solids are templated with rigid molecules. Silica zeolite MCM-35 is synthesised with hexamethyleneimine (a), UCSB-6 and -8 are formed with 1,9-diaminononane (b), while UCSB-10 is directed by 4,7,10-trioxa-1,13-tridecanediamine (c).



were also produced. Gel chemistry is clearly more important, or template size, shape and hydrophobicity much less important, than proponents of the “designer” template approach would surmise. Clearly this makes the design of new materials with specific pore architectures much more difficult to rationalise *a priori*. Not only that, but when considering possible structure directing agents (once insoluble and uncharged molecules are discounted) the number that will apparently not template *something* is very small. There is therefore little scope for an “irrational” selection from the remainder. Although the preparation of “designer” templates is certainly the best approach available for the synthesis of microporous solids *by design* (since in many cases the organo-cation does have the greatest influence on the phase that is observed) the importance of gel chemistry must not be overlooked. The use of templates has not removed the need for hundreds of experiments to be performed before a new framework is discovered and so the idea of true framework *design* remains a distant prospect.

2.1.2 Characterising new materials

Some techniques for the characterisation of zeolitic materials have already been discussed in Chapter 1. Nevertheless, it will be useful to outline briefly here some steps in the process of screening organic molecules for activity as

templates of microporous solids. Also some techniques for discovering the materials' structure and basic properties will be mentioned.

Chemists are interested fundamentally in two things when discussing materials: their structure and composition. X-ray diffraction is by far the most powerful analytical technique for the elucidation of framework structure. Likewise NMR spectroscopy is useful in studying the occluded template and local structure of the host. This is the approach that has been applied in this work. Others (see, for example, [93] and [95]) have adopted a different approach, that of *model building*, whereby a model of the structure is obtained not from a single crystal diffraction study, but is developed by combining techniques such as high resolution transmission electron microscopy (HRTEM) and MASNMR spectroscopy with Rietveld refinement of powder X-ray diffraction data. This is a valid approach, particularly as many zeolitic materials form only as microcrystals, but is much more demanding of time. In the work described here the bulk structure of novel materials was always obtained from single crystal X-ray diffraction data, collected either on a laboratory diffractometer equipped with a CCD detector, or in the case where only microcrystals were available, on a similar system at a synchrotron source. [23]

Powder diffractometry was used in the first instance after a sample had been prepared, recovered, washed and dried, to establish whether it was of a known framework type. By comparison with the profiles of other zeolitic materials (from the *Collection of Simulated XRD Powder Patterns for Zeolites* [115]) the phase, if known, may be established. A larger database of inorganic structures is available in the *ICCD Powder Diffraction File* [116] which allows searching by intensity of recorded X-ray line. If the material is apparently novel, attempts to prepare crystals suitable for single crystal diffraction could be made. However, because of the complexity of powder patterns containing overlapping Bragg reflections the unambiguous confirmation of novelty is not always easy, particularly where a mixture of phases is present. In these cases, the determination of lattice parameters (most conveniently obtained from a single crystal) permits a search of the *Inorganic Crystal Structure Database* (ICSD), available through the EPSRC's Chemical Database Service

at Daresbury, [117] from which an almost unambiguous assessment may be made.

The next question to be answered is whether the structure directing agent is intact within the zeolite pore, or if it has broken down, and whether it may be removed to leave open pores. Solid state ^{13}C MAS NMR is invaluable in allowing the structure of the template to be determined within the zeolite pore, although if this technique is unavailable the inorganic component may be dissolved in acid and liquid state NMR carried out. The material may be calcined in oxygen at high temperature to remove the template. A powder X-ray pattern should be collected to check for structural integrity. If structure collapse has occurred the adsorption of *n*-hexane after calcination, during cooling, may stabilise the framework sufficiently (by excluding water) so that it remains intact. Dinitrogen adsorption (after removal of any *n*-hexane present) allows the pore volume to be measured (see [78] for details).

If the template is ordered within the zeolite pores its position may be obtained by X-ray diffraction. In cases where the template is disordered molecular modelling [62] may be the only way to establish the minimum energy conformation and likely position of the structure directing agent. Data obtained from such studies can be included in a model for Rietveld profile refinement and will result in a substantially better fit to data.

A number of techniques are available for the determination of composition of microporous solids. Inductively coupled plasma-atomic emission spectroscopy (ICP-AES), or energy dispersive analysis of emitted X-rays (EDX) may be used to ascertain the inorganic composition. Microanalysis is used to gauge the ratio of carbon-hydrogen-nitrogen (CHN) in the material which, combined with thermogravimetric analysis (TGA), will allow the amount of water and structure directing agent to be discovered.

Scanning electron microscopy is used to determine the crystal morphology and approximate size. This may prove useful in establishing the number of phases present in an unknown mixture too.

Microporous solids have been characterised in many other ways too, this list is not exhaustive. Some experiments will now be described and the results

discussed.

2.2 Experimental

2.2.1 Synthesis

Gels in a range of compositions were made up from mixtures of aluminium hydroxide hydrate, orthophosphoric acid, distilled water, a cation source (typically a metal acetate or fumed silica) and a template. Quaternary ammonium salt templates were converted from the halide to hydroxide form with silver(I) oxide. The salts were dissolved in water and a slurry formed with the silver(I) oxide which was stirred for 15 minutes before being filtered and excess water removed on a rotary evaporator. Further synthetic details are given in Table 2.3. In a typical synthesis a metal acetate was dissolved in a solution of orthophosphoric acid in water. A gel was prepared by the addition to this of aluminium hydroxide hydrate followed by an amine or quaternary ammonium hydroxide template. The mixture was stirred for 15 minutes after which the homogeneous gel was introduced into a PTFE-lined stainless steel autoclave and heated under autogeneous pressure and static conditions at either 160 or 190 °C for 48 hours. Silicoaluminophosphate materials were prepared in an analogous way. Fumed silica replaced the metal acetate and the gels were heated at 190 °C for 168–192 hours. On removal from the oven the autoclaves were immediately cooled under flowing water. Crystalline products were separated from the resulting mixtures by filtration, washed with distilled water and dried in air. If a mixture of phases was obtained (as determined with optical microscopy and XRD) the sample was suspended in water and treated in a sonic bath to allow separation by density.

In Figure 2.12 the templates used in this work are given. Secondary and tertiary amines, quaternary ammonium salts and phosphazines were employed as structure directing agents. Materials were purchased from either Aldrich or Fluka or synthesised *via* the Menschutkin reaction. [118] The spiro templates (Figure 2.12.k–2.12.m) were prepared in the laboratory of Dr R. A. Aitken (St Andrews) by Miss E. F. Philp.

Figure 2.12: Structure directing agents used in this work. (a) 1,4,8,11-tetramethyl-1,4,8,11-tetraazacyclotetradecane (tmtact), (b) 1,4,8,11-tetraazacyclotetradecane (cyclam), (c) 1,4,7-trimethyl-1,4,7-triazacyclononane (tm-tacn), (d) 4,7,13,16,21,24-hexaoxa-1,10-diazabicyclo[8.8.8]hexacosane (K222), (e) 1,4,7,10,13,16-hexaoxacyclooctadecane (18-crown-6), (f) 1,3,5-trimethyl-hexahydro-1,3,5-triazine (tmhht), (g) 1,3,4,6,7,8-hexahydro-2*H*-pyrimido[1,2-*a*]pyrimidine (hhpp), (h) 1,3,4,6,7,8-hexahydro-1-methyl-2*H*-pyrimido[1,2-*a*]pyrimidine (hhmpp), (i) [*R*-(*R*^{*},*S*^{*})-(-)-*N*-(1-phenylethyl)-1-azabicyclo[2.2.2]octan-3-amine (peabcoa), (j) 2,8-dimethyl-6*H*,12*H*-5,11-methanodibenzo[*b,f*][1,5]diazaoane (Troger's base), (k) 6-azoniaspiro[5.5]undecane (asu), (l) 8-oxa-5-azoniaspiro[4.5]decane (oasd), (m) benzotri(5-azonia[4.5]dec-2-ene (btad), (n) poly[4-(1,4-diazabicyclo[2.2.2]oct-1-ylmethyl)benzyl] (pbcomb), (o) phosphazine base P₁-*t*-Bu (p1), (p) phosphazine base P₁-*t*-Bu-tris(tetramethylene) (p2).

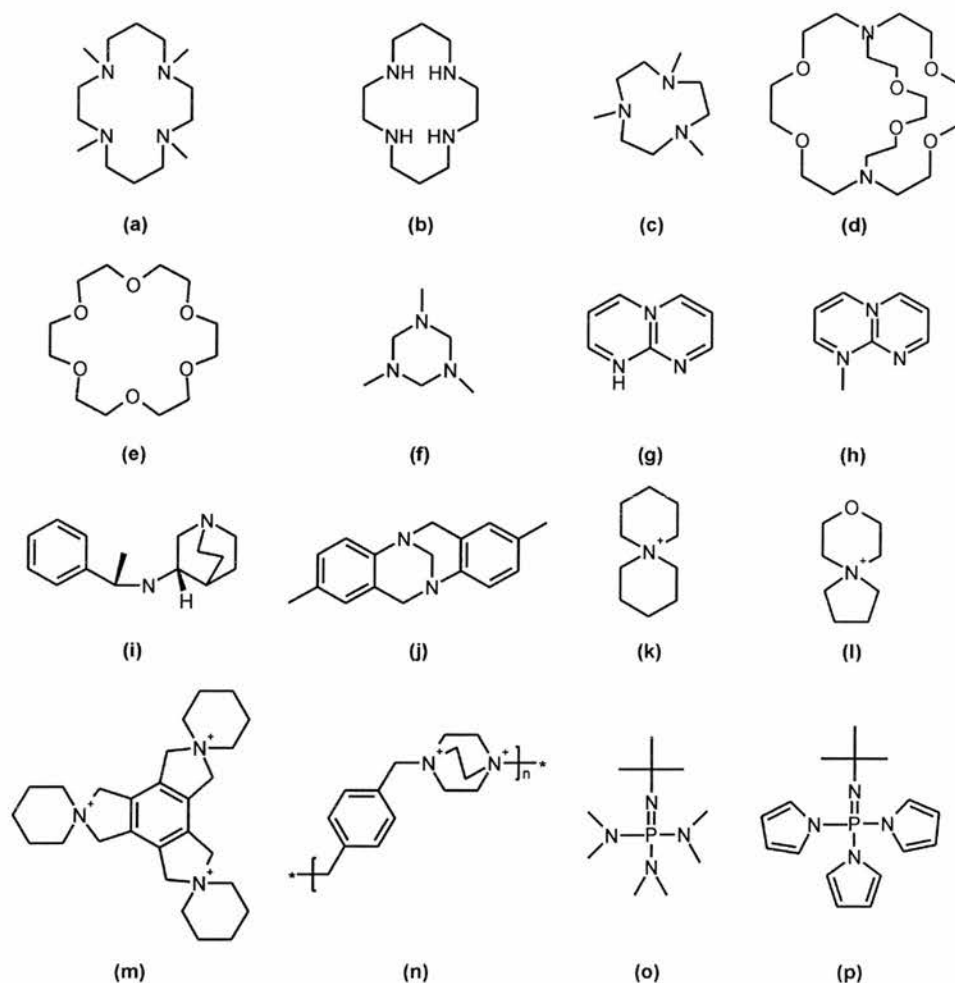


Table 2.3: Inorganic reagents used in this work, purity and supplier. All materials were used as supplied without further purification.

Reagent	Purity, %	Supplier
Aqueous hydrofluoric acid	40	Fluka
Magnesium(II) acetate tetrahydrate	99	Aldrich
Aluminium hydroxide hydrate	–	Aldrich
Silica, fumed	97	Fluka
Aqueous orthophosphoric acid	85	Prolabo
Scandium(III) acetate hydrate	99.9	Aldrich
Manganese(II) acetate tetrahydrate	98	Avocado
Iron(II) acetate	95	Aldrich
Cobalt(II) acetate tetrahydrate	98	Aldrich
Nickel(II) acetate tetrahydrate	98	BDH
Copper(II) acetate hydrate	98	GPR
Zinc(II) acetate dihydrate	98.5	BDH
Silver(I) oxide	97	Acros

The occluded organic template was removed from the framework by heating under dry flowing oxygen, in a tube furnace, at 550 °C (10 °C min⁻¹ from room temperature) for 5–10 h. The furnace was allowed to cool and when the temperature reached 150 °C the gas was switched to dry nitrogen which was passed first through a reservoir of *n*-hexane before entering the furnace. In this way *n*-hexane was adsorbed by the sample and water was excluded. This helps preserve the crystallinity of the calcined material. Selected samples were then loaded into 0.7 mm i.d. quartz glass capillaries, attached to a vacuum line and heated at 300 °C for 1 h in a vacuum of 10⁻³ mbar. This removed the *n*-hexane and any residual water. The capillaries were then separated from the vacuum line attachment and simultaneously sealed with a glassblowing torch.

2.2.2 Crystallography

X-ray powder diffraction patterns of all products were collected on one of two Philips X'Pert System diffractometers using Cu-K α radiation and operating

in reflectance mode (Bragg–Brentano geometry) with a secondary monochromator. Samples were placed on an aluminium plate sample holder and data typically collected in 45 minutes over the 2θ range $5\text{--}50^\circ$, with a 0.02° step. This enabled phase identification.

For structural analysis samples were loaded into 0.7 mm i.d. quartz glass capillaries and analysed on a Stoe STADIP diffractometer operating in transmission mode (Debye–Scherrer geometry) with primary monochromation and $\text{Cu-K}\alpha_1$ X-radiation. Data were typically collected over the range $4\text{--}70^\circ$ with a 0.01° step, in 14 hours. Alternatively, a similar diffractometer at Station 9.1 of the Synchrotron Radiation Source, CCLRC Daresbury Laboratory was used with monochromated synchrotron radiation ($\lambda = 0.99555(1)\text{ \AA}$). Data were collected between $3\text{--}60^\circ$ with a step of 0.01° . To improve counting statistics at higher 2θ angles data were collected with longer counting times in the range $20\text{--}60^\circ$. The program *PODSUM* was used subsequently at the SRS to normalise and join the resulting data files. For cobalt-containing samples, for example, the use of synchrotron radiation is preferable to the more widely available $\text{Cu-K}\alpha_1$ X-rays because there is no simultaneous fluorescence which would otherwise lead to a high background. The Philips diffractometers described previously overcome this difficulty with a secondary monochromator, but have poorer resolution and are unsuitable for structure refinement studies.

Selected crystals were examined by single crystal diffraction in St Andrews or at Station 9.8, at the SRS. In each case data were collected on a three-circle (fixed κ) Bruker diffractometer fitted with a Bruker SMART CCD detector equipped with sources of either $\text{Mo-K}\alpha$ or synchrotron radiation ($\lambda = 0.6942(1)\text{ \AA}$). Data were collected by stepwise variation in χ , with the detector 2θ and goniometer ϕ circles fixed, and this was repeated for reduced ω angular ranges at different ϕ values, to ensure a hemisphere of data was collected. Data reduction was carried out using the Bruker AXS *SAINTE* and *SADABS* packages. Structures were solved and refined either by Dr A. M. Z. Slawin or Dr P. Lightfoot; further details are given below.

2.2.3 NMR spectroscopy

To determine the condition of the occluded template moiety solid state ^{13}C CP-MAS NMR was performed at the EPSRC solid state NMR Facility in Durham. A Varian UNITY *Inova* spectrometer with a 7.05 T Oxford Instruments magnet was used with a Doty Scientific MAS probe with 7 mm o.d. rotors at ambient temperature. The frequency was 75.430 MHz and an acquisition time of 30.0 ms, relaxation delay of 5.0 s, CP contact time of 1.00 ms, and spin rate of 4.37 kHz were used. The shift reference sample was $(\text{CH}_3)_4\text{Si}$.

The coordination of Al and P within the framework was also examined by NMR on the same spectrometer. ^{27}Al DPMAS NMR spectra were collected with a Doty Scientific MAS probe at ambient temperature from samples in 5 mm o.d. rotors at a frequency of 78.157 MHz, using an acquisition time of 20.0 ms, relaxation delay of 0.2 s, pulse angle of 18.0° and spin rate of 10.2 kHz. Spectra were referenced to 1 M $\text{Al}(\text{H}_2\text{O})_6^{3+}$ (aq). Similarly, ^{31}P DPMAS NMR spectra were collected at a frequency of 121.421 MHz, using an acquisition time of 20.2 ms, relaxation delay of 300.0 s, pulse angle of 90.0° and spin rate of 9.97 kHz. Spectra were referenced to 85 % H_3PO_4 (aq).

2.2.4 Chemical analysis

Carbon–hydrogen–nitrogen (CHN) content of selected solids was determined by microanalysis in St Andrews on a CE Instruments EA 1110 analyser by Mrs S. Williamson. The amount of water and template included within the inorganic framework was inferred from thermogravimetric analysis plots recorded from 25–800 °C at a rate of $10^\circ\text{C min}^{-1}$ (under flowing oxygen, $100\text{ cm}^3\text{ min}^{-1}$) on a TA Instruments SDT 2960 simultaneous DTA–TGA furnace. To confirm the presence of metal cations within selected samples, single crystals were studied by energy dispersive analysis of emitted X-rays (EDX) (carried out on a Jeol JEM 2010 transmission electron microscope using an Oxford Instruments 6498 EDX detector) and powders were examined using inductively coupled plasma–atomic emission spectroscopy (ICP–AES) on samples dissolved in nitric acid.

2.2.5 Molecular modelling

The results of calculations were kindly supplied by Dr P. A. Cox of the University of Portsmouth who modelled the likely position of templates within microporous solids' pores. The conventional computational approach of combining Monte Carlo docking and subsequent Simulated Annealing was adopted using the *Constant Valence Forcefield* (CVFF) within the program *Discover*, [119] assuming that short-range interactions between the framework and the template molecules will determine the favoured locations, rather than Coulombic forces.

2.3 Results

2.3.1 Tmtact as a template

The results of selected syntheses with 1,4,8,11-tetramethyl-1,4,8,11-tetraazacyclotetradecane (tmtact, Figure 2.12.a) are given in Table 2.4. Corresponding powder X-ray diffraction patterns are shown in Figure 2.13. Notably the synthesis of STA-6 and a novel phase, STA-7 (**St Andrews-7**), only occurs in the presence of divalent cations. For the aluminophosphate gel composition AlPO_4 -21 is formed. The crystallisation of the STA-7 phase results from the presence of Co^{II} or Zn^{II} in the synthesis gel, whereas the presence of Mg^{II} , Mn^{II} , Fe^{II} , Ni^{II} results in the formation of STA-6. With iron in the gel the principal phase is STA-6, although a small number of STA-7 crystals (confirmed by single crystal XRD) are also present. The purest samples of Co-STA-7 and Zn-STA-7 are prepared from gels with $\text{M}^{\text{II}}/\text{P}$ ratios of 0.20. Higher or lower ratios of divalent cations result in crystalline impurities. In typical preparations using tmtact, yields of 50–60% on phosphorus were obtained for STA-7 prepared in the presence of cobalt and zinc. Much lower yields (a few percent) were obtained using magnesium as the divalent cation.

Attempts to prepare STA-6 or STA-7 with Sc^{III} , Ti^{IV} , Cu^{II} , or Cr^{II} cations were unsuccessful. For chromium and copper-containing gels the only crystalline phase to form is AlPO_4 -21. Scandium and titanium containing gels

Table 2.4: Selected gel compositions used in this work with tmtact. The product phases obtained from X-ray diffractometry after the hydrothermal treatment of these gels is reported.¹

Inorganic cation ratio in synthesis gel	Principal product (by XRD)
1.0Al : 1.0P	AlPO ₄ -21
0.2Mg : 0.8Al : 1.0P	Mg-STA-6
0.2Sc : 0.8Al : 1.0P	amorphous
0.2Ti : 0.8Al : 1.0P	AlPO ₄ -21 ²
0.2Cr : 0.8Al : 1.0P	AlPO ₄ -21
0.2Mn : 0.8Al : 1.0P	Mn-STA-6
0.2Fe : 0.8Al : 1.0P	Fe-STA-6 ³
0.2Co : 0.8Al : 1.0P	Co-STA-7
0.2Ni : 0.8Al : 1.0P	AlPO ₄ -21, Ni-STA-6 ⁴
0.2Cu : 0.8Al : 1.0P	AlPO ₄ -21
0.2Zn : 0.8Al : 1.0P	Zn-STA-7

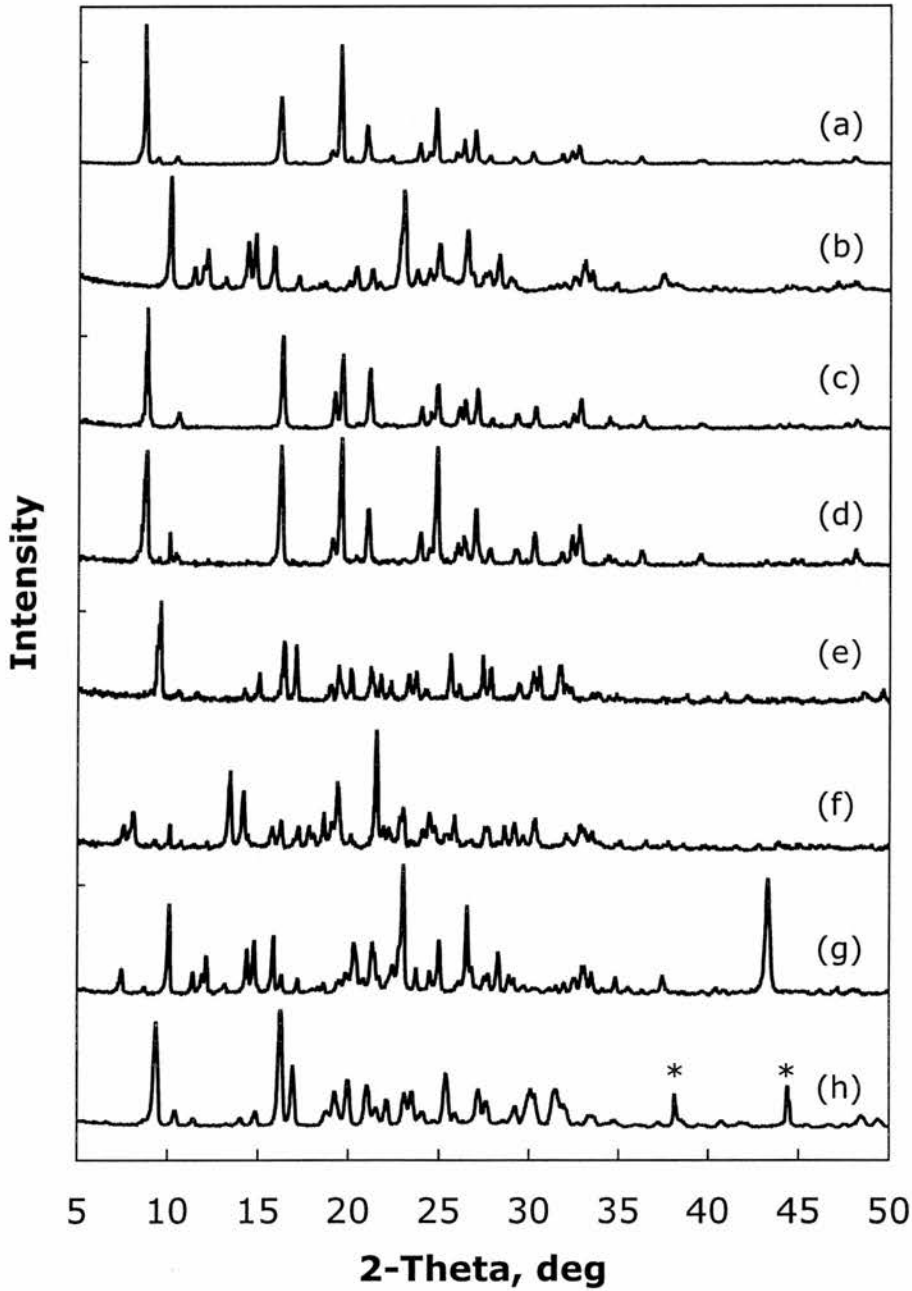
¹The ratio R/P varied from 0.34–0.63 so the initial gel pH was always 7; the typical gel composition is 0.2MOAc₂·4H₂O : 0.8Al(OH)₃·xH₂O : H₃PO₄ : 150H₂O : 0.5R.

²In the absence of H₂O₂ an amorphous phase forms.

³A very few crystals of Fe-STA-7 also form.

⁴Approximately 60/40 mixture

Figure 2.13: Powder X-ray diffraction patterns of solids crystallised from metalloaluminophosphates gels containing tmtact. $M = \text{Mg}^{\text{II}}$ (a), Ti^{IV} (b), Mn^{II} (c), Fe^{II} (d), Co^{II} (e), Ni^{II} (f), Cu^{II} (g), Zn^{II} (h). Sc^{III} , not shown, is amorphous. (Asterisked peaks correspond to Al from the sample holder.)



yielded amorphous products, however in the later case addition of H_2O_2 [120] enabled $\text{AlPO}_4\text{-21}$ to form.

When nickel is included in the synthesis gel two phases are produced, the principal one is $\text{AlPO}_4\text{-21}$. The minor phase may be separated by sonication and was identified as STA-6 (see Chapter 4 for details). All the nickel-containing products are bright pink which is indicative of Ni in square planar coordination, [121] and turn yellow on calcination. Further work has been carried out on Ni-containing materials by Miss R. García (St Andrews), see [122].

The structure of STA-7, and further characterisation, is described in Chapter 4.

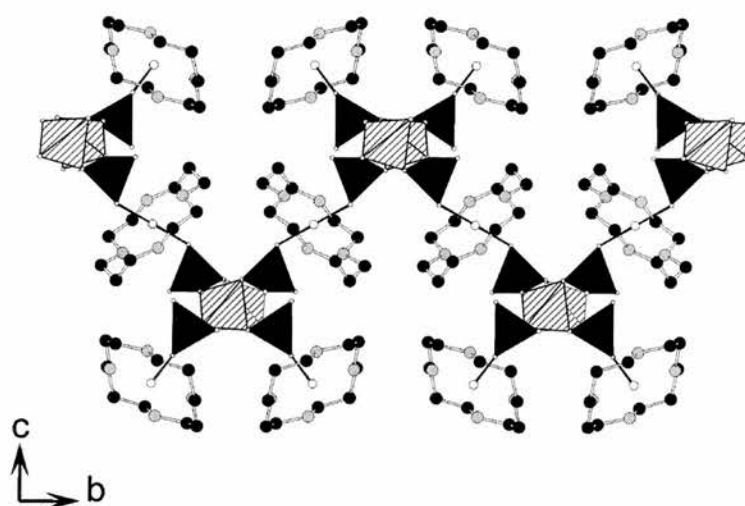
2.3.2 Cyclam as a “template”

Addition of 1,4,8,11-tetraazacyclotetradecane (cyclam, Figure 2.12.b) to a cobalt aluminophosphate preparation is known to yield crystals of a phase called CoAPO–cyclam-1. [123] The structure of this material is illustrated in Figure 2.14. It may best be described in terms of aluminophosphate chains, of stoichiometry $\text{AlP}_2\text{O}_8\text{H}$, which run parallel to the crystallographic a axis. These chains are connected to four others *via* P–O–Co–O–P linkages, with the octahedral cobalt being complexed also by cyclam. Within the chains, both aluminium and phosphorus atoms are tetrahedrally coordinated by oxygen. Of the four oxygens surrounding each of the two crystallographically-distinct phosphorus atoms, two form P–O–Al linkages, one a P–O–Co linkage, while the last is apparently a P–O single bond. In fact, two of these (and a proton) hydrogen-bond to each other (with an O–O distance of $2.50(1)$ Å) and to nitrogens of the cyclam units. Thus, the compound has the formula $\text{Co}^{\text{II}}(\text{C}_{10}\text{N}_4\text{H}_{24})\text{Al}(\text{PO}_4)\text{PO}_3(\text{OH})$.

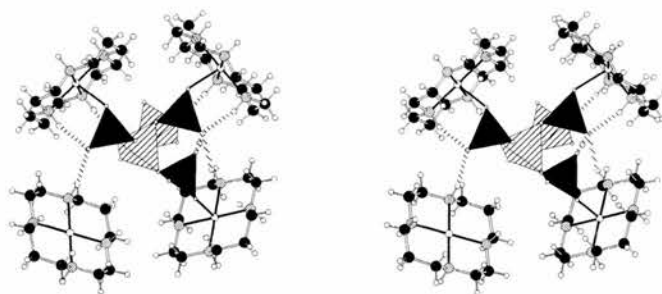
In this work, cyclam was added to AlPO_4 preparations in which 20% of the aluminium in the gel had been replaced with metal cations (Mg^{II} , Mn^{II} , Fe^{II} , Ni^{II} , Zn^{II}). A pure aluminophosphate gel was also prepared. In all but two cases, however, only amorphous products were obtained.

Adding nickel to the synthesis gel gave a purple solid which was thought to be isostructural with CoAPO–cyclam-1. Examination of a single crystal using

Figure 2.14: Views of CoAPO–cyclam-1. (a) Down the crystallographic a axis, along the $\text{AlP}_2\text{O}_8\text{H}$ chains, and (b) a stereoview of a section of the structure, showing the arrangement of Co–cyclam units linked *via* Co–O bonds to the phosphate oxygens of the aluminophosphate chains; also shown are the location of hydrogen bonds within the structure. C atoms are represented by black spheres, N atoms by grey spheres, Co by white spheres and AlO_4 and PO_4 tetrahedra are hatched and black, respectively.

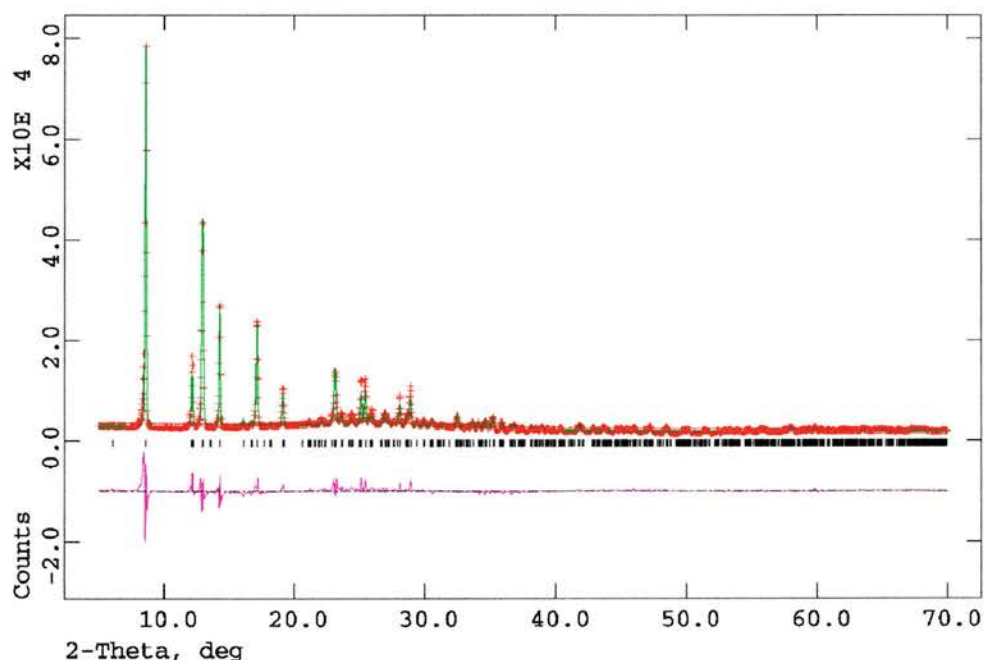


(a)



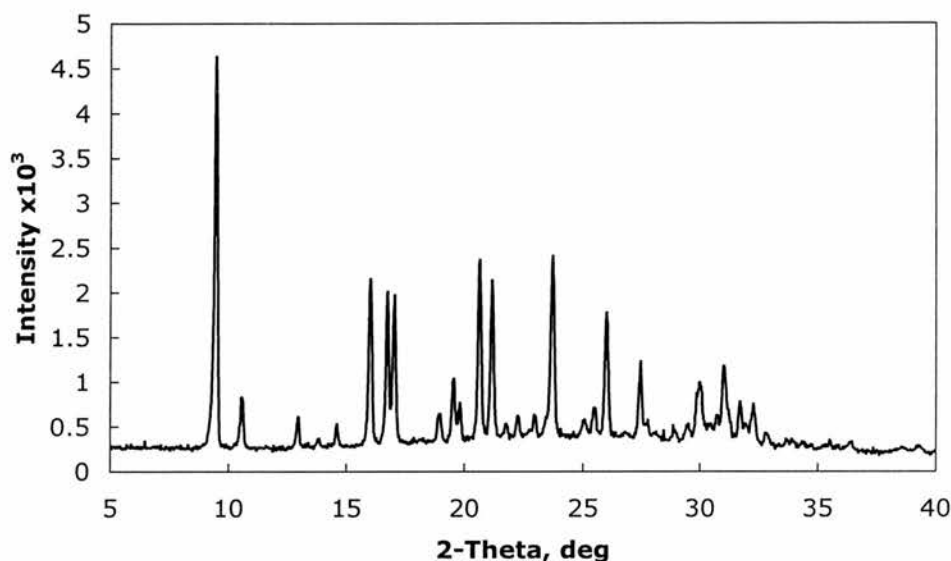
(b)

Figure 2.15: Rietveld refinement of X-ray powder diffraction profile of showing simulated pattern (line), experimental profile (crosses) and difference plot of NiAPO-cyclam-1, $\text{Ni}^{\text{II}}(\text{C}_{10}\text{N}_4\text{H}_{24})\text{Al}(\text{PO}_4)\text{PO}_3(\text{OH})$, collected using $\text{Cu-K}\alpha_1$ radiation ($P2_1/c$, $a = 14.862(2) \text{ \AA}$, $b = 14.627(2) \text{ \AA}$, $c = 8.4692(7) \text{ \AA}$, $\beta = 98.134(6)^\circ$, $R_{wp} = 11.1\%$ and $R_p = 7.9\%$).



X-ray diffraction in St Andrews revealed the lattice parameters to be similar (CoAPO-cyclam-1: $a = 14.9780(8) \text{ \AA}$, $b = 14.7200(8) \text{ \AA}$, $c = 8.4792(5) \text{ \AA}$, $\beta = 98.323(1)^\circ$, NiAPO-cyclam-1: $a = 14.849(8) \text{ \AA}$, $b = 14.623(7) \text{ \AA}$, $c = 8.464(6) \text{ \AA}$, $\beta = 98.09(5)^\circ$). To confirm this, and that the material was phase pure, the powder X-ray diffraction profile was Rietveld refined (Figure 2.15). The CoAPO-cyclam-1 structure (which was originally solved by single crystal X-ray diffraction) was used as a starting model and the lattice parameters, zero-point, background and peak shape refined. The fit was found to be satisfactory with $R_{wp} = 11.1\%$ and $R_p = 7.9\%$ and confirms that the structures are the same.

Figure 2.16: Powder X-ray diffraction pattern of MgAPO-18 synthesised with cyclam. (Preferred orientation may be seen.)



The presence of magnesium in the synthesis gel gives a different phase, identified as MgAPO-18 (**AEI**) by single crystal¹ and powder XRD (Figure 2.16). Calcining this material in flowing oxygen at 550 °C for 8 hours unexpectedly results in the material collapsing and becoming amorphous.

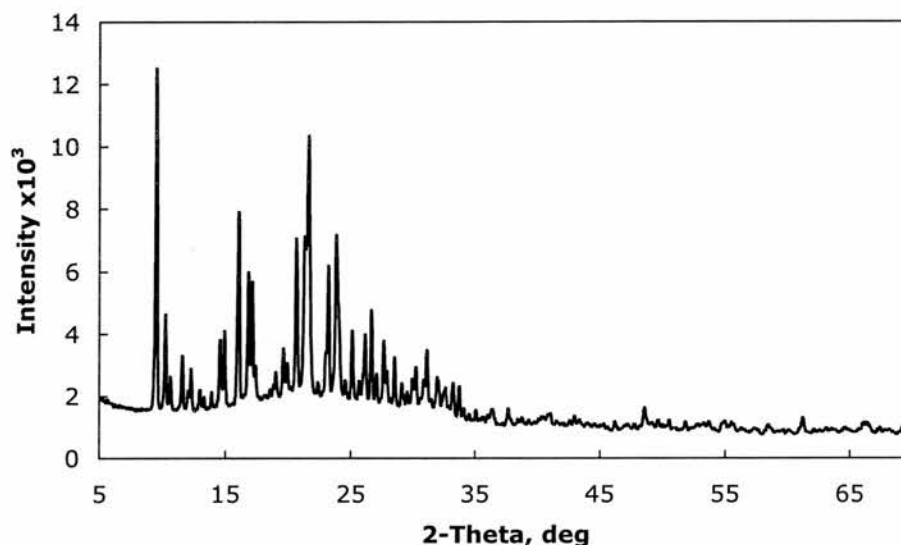
2.3.3 Tmtacn as a template

Addition of 1,4,7-trimethyl-1,4,7-triazacyclononane (tmtacn, Figure 2.12.c) to the reaction gel again results in the preparation of the MAPO-18 (**AEI**) framework. Crystals of MgAPO-18 ($60 \times 40 \times 35 \mu\text{m}$) of suitable quality for microcrystal diffraction were prepared. The powder X-ray pattern is given in Figure 2.17.

Selected single crystals were analysed by EDX and found to contain magnesium, with Mg/P ratio of *ca* 0.15; TGA showed there to be 2.6 tmtacn

¹MgAPO-18. $[(\text{Mg},\text{Al})_{24}\text{P}_{24}\text{O}_{96}]$, $M = 586.46$, orthorhombic, $a = 13.790(3) \text{ \AA}$, $b = 12.891(3) \text{ \AA}$, $c = 18.922(4) \text{ \AA}$, $V = 3364(1) \text{ \AA}^3$, $T = 293(2) \text{ K}$, space group $Cmc2_1$ (no. 36), $Z = 4$, $\mu(\text{Mo-K}\alpha) = 0.318 \text{ mm}^{-1}$, 6397 reflections measured, 2665 unique of which 1097 were observed. The final $R(\text{obs})$ was 0.2105 with $wR(F^2) = 0.4031$.

Figure 2.17: Powder X-ray diffraction pattern of MgAPO-18 synthesised with tmtacn.

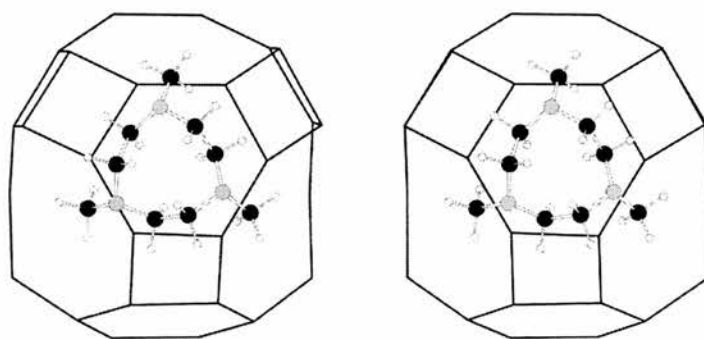


molecules per unit cell (an occupancy of 65%). MAPO-18 is a small pore structure that may be considered to possess a pore space made up entirely of cages. Molecular modelling reveals a strong preference of the uncharged tmtacn template for a site that possesses pseudo-threefold symmetry (Figure 2.18). Since it is possible that the macrocycle could be incorporated in a monoprotonated form to balance the negative charge imparted to the framework by the incorporation of magnesium, the modelling was also performed for this case. The final energy-minimised position is very close to that of the neutral amine. Inclusion of the template in this site at a refined occupancy level of 2.8 per 4 cages in the unit cell gives a marked improvement in the fit to the single crystal diffraction data.

Single microcrystals were examined on station 9.8 at the Daresbury synchrotron.² In each case the basic framework structure was solved using SIR92 and refined using the teXsan suite of programs, [124] and shown to possess the

²MgAPO-18. $[(C_9N_3H_{21})_{0.35}] [(Mg,Al)_3P_3O_{12}]$, $M = 139.47$, monoclinic, $a = 13.795(3) \text{ \AA}$, $b = 12.830(3) \text{ \AA}$, $c = 18.815(5) \text{ \AA}$, $\beta = 89.959(7)^\circ$, $V = 3330(1) \text{ \AA}^3$, $T = 150(2) \text{ K}$, space group $C2/c$ (no. 15), $Z = 24$, $\mu(0.6942 \text{ \AA}) = 0.567 \text{ mm}^{-1}$, 11252 reflections measured, 4501 unique of which 2535 were observed. The final $R(\text{obs})$ was 0.0837 with

Figure 2.18: Stereoview of the minimum energy position of tmtacn. The molecules threefold axis matches well with the pseudo-threefold axis of the portion of framework that makes up part of the AlPO_4 -18 cavity. For clarity only the position of tetrahedral atoms of the framework are shown.



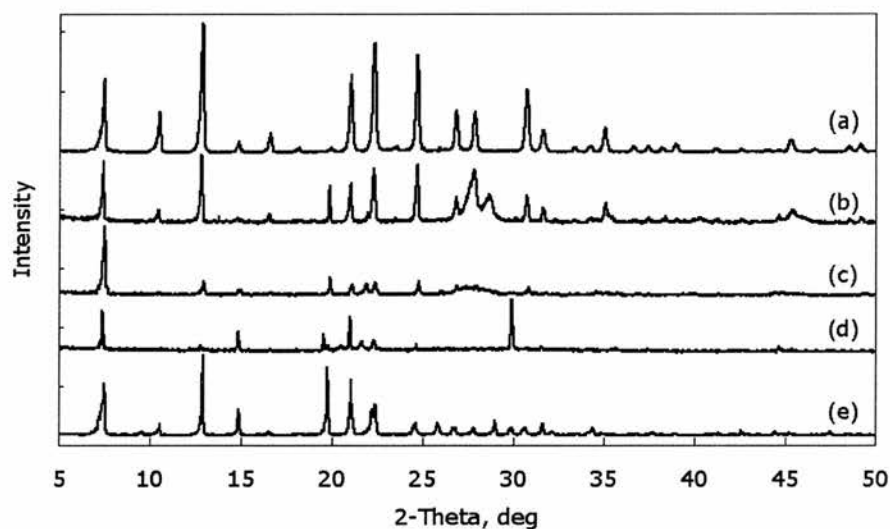
same space group and framework structure as reported previously for AlPO_4 -18 ($C2/c$). For MgAPO -18, input of the tmtacn template into the position suggested by modelling significantly improves the goodness of fit, $R(\text{obs})$ decreasing from 13.0 % to 8.4 %. In each case, average bond lengths and refined scattering on the “Al” sites indicate that divalent metal substitution has occurred into those sites. For MgAPO -18 the (Mg,Al)–O average bond length is 1.76(1) Å.

2.3.4 K222 as a template

If 20 % Mg^{II} , Mn^{II} or Fe^{II} cations are substituted for Al^{III} in a 4,7,13,16,21,24-hexaoxa-1,10-diazabicyclo[8.8.8]hexacosane–aluminophosphate gel (see Figure 2.12.d for the structure of K222), MAPO-42 (**LTA**) is formed. (Schreyeck *et al* previously reported AlPO_4 -42 with this template. [112]) MAPO-42 has the zeolite A framework type illustrated in Figure 1.1, page 4. MAPO-5 (**AFI**) is found as an impurity, see Figure 2.19. Syntheses with divalent cobalt, and in particular zinc, cations gave highly crystalline MAPO-42, which is phase pure in the case of ZnAPO -42. TGA reveals there are *ca* 8 K222 molecules per

$wR(F) = 0.1056$. Note that the refinement was performed using a purely aluminophosphate model, because the scattering of magnesium and aluminium are so similar.

Figure 2.19: Powder X-ray diffraction patterns of MAPO-42 materials collected on the laboratory diffractometer. Materials contain divalent cations Zn^{II} (a), Co^{II} (b), Fe^{II} (c), Mn^{II} (d), Mg^{II} (e). The ZnAPO is phase pure ZnAPO-42, while the amount of MAPO-5 impurity increases (b) to (e), see text for details.



unit cell which corresponds to one molecule per supercage. Molecular modelling shows that whereas the fit of the K222 cryptand within the supercage (α -cavity) of the structure is energetically favourable, there is no uniquely favoured position. Single microcrystals of ZnAPO-42 were examined on station 9.8 at the SRS and solved³ in the same space group as reported previously ($Fm\bar{3}c$) for AlPO₄-42. Modelled scattering from disordered template molecules that fully occupy the α -cavities significantly improves the single crystal refinement residual $R(\text{obs})$ from 14.9% to 12.3%. Attempts to locate zinc cations within the cryptand in ZnAPO-42 (at 0.25, 0.25, 0.25) showed that there were none. The average bond lengths and refined scattering on the “Al” sites indicate that divalent metal substitution has occurred into those sites (the (Zn,Al)–O average bond length is 1.75(2) Å).

Syntheses in which the M/P ratios were adjusted were carried out for M = Mg and Co. The results were the same for each cation (XRD patterns for CoAPO materials are shown in Figure 2.20). As the M/P ratio increases, an impurity phase becomes apparent. Powder diffraction with synchrotron radiation shows more clearly the phases present (Figure 2.21).

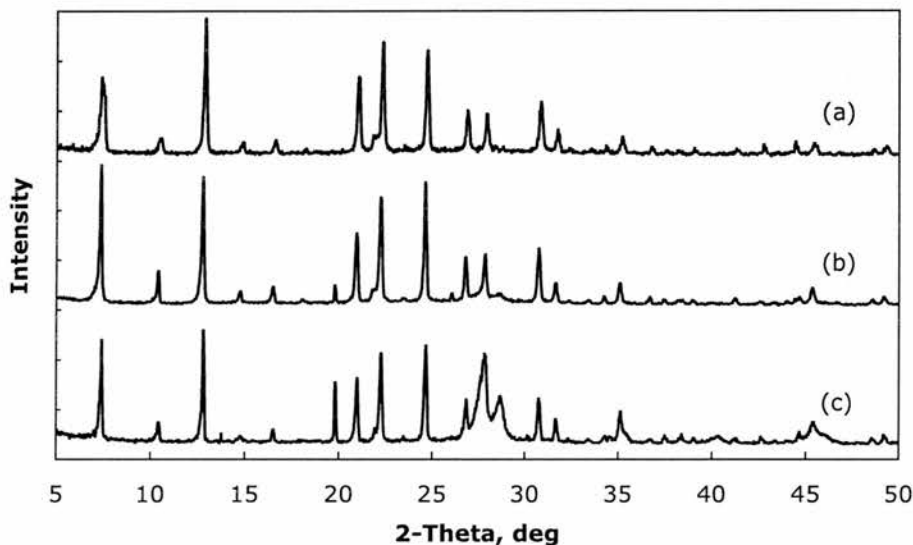
2.3.5 18-crown-6 as an additive

The results of experiments in which mixtures of 1,4,7,10,13,16-hexaoxacyclooctadecane (18-crown-6, Figure 2.12.e) and a variety of linear diamines were combined and added to metalloaluminophosphate gels is given below. Such amines are known to template layered MAPO materials. [125, 126, 127] It was conjectured that the addition of 18-crown-6 (which is known to be occluded within FAU–EMT zeolites at synthesis [128]) may yield novel three-dimensionally connected frameworks if the crown ether interacts sufficiently strongly with the amine template.

In CoAPO gels with ethylenediamine and 18-crown-6, Co^{II} containing gels crystallised as blue CoAPO-21. However, in Zn^{II} containing gels ZnAPO-41

³ZnAPO-42. $[(C_{18}N_2O_6H_{38})_{0.083}] [Zn_{0.2}Al_{0.8}PO_4]$, $M = 158.03$, cubic, $a = 23.990(8)$ Å, $V = 13806(6)$ Å³, $T = 150(2)$ K, space group $Fm\bar{3}c$ (no. 226), $Z = 96$, $\mu(0.6942 \text{ Å}) = 1.34 \text{ mm}^{-1}$, 6420 reflections measured, 1007 unique of which 312 were observed. The final $R(\text{obs})$ was 0.1233 with $wR(F) = 0.1329$.

Figure 2.20: Powder X-ray diffraction pattern of CoAPO-42 materials. Co/P in the synthesis gel is 0.05 (a), 0.10 (b), and 0.20 (c). As the ratio increase above 0.05 an impurity phase forms (*e.g.* $2\theta = 19.8^\circ$).



(AFO) was formed. Figure 2.22 shows examples of these two phases while Figure 2.23 shows the SEM of the CoAPO-21 phase confirming its purity. With *N*'-isopropyl-diethylenetriamine MAPO-34 was formed.

In the presence of 1,3-diaminopropane Mg and Co containing gels crystallise to form MAPO-21. This transforms to MAPO-25 (ATV) on heating [129] as illustrated in Figure 2.24.

Addition of 1,5-diaminopentane and 18-crown-6 to a CoAPO gel yielded the crystalline phase whose XRD is shown in Figure 2.25. From the powder diffraction profile it was not possible to identify unambiguously the framework type and so the structure remains unknown. MAPO-34 forms in the presence of 1,6-diaminohexane and 18-crown-6. The unit cell of one such crystal ($20 \times 20 \times 20 \mu\text{m}$) was obtained by microcrystal diffraction ($a = 13.80 \text{ \AA}$, $c = 14.80 \text{ \AA}$, R-centred hexagonal) confirming the determination from powder XRD data.

Preparations with 1,7-diaminoheptane or 1,8-diaminooctane (and 18-crown-6) gave similar products although the former were generally less well crystallised. Mixed phases were observed which contained both CoAPO-34

Figure 2.21: Powder X-ray diffraction pattern of microporous CoAPO collected with synchrotron radiation ($\lambda = 0.6942(1) \text{ \AA}$). The tick marks plotted below the diffractogram indicate the positions of Bragg peaks for the CoAPO-42 phase. CoAPO-5 is also present as a crystalline impurity, the most well resolved peak for this phase is at $2\theta 12.8^\circ$.

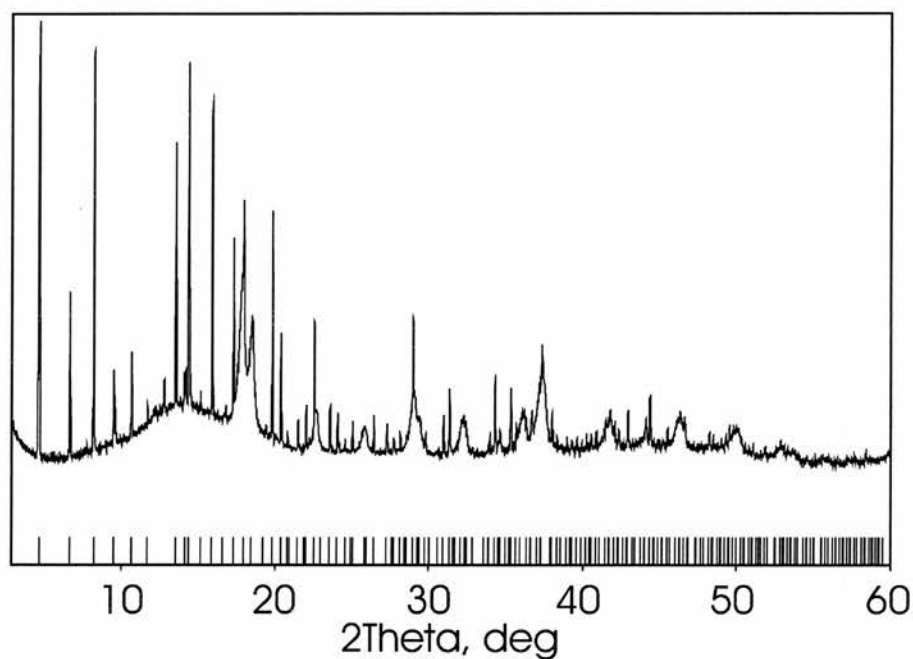


Figure 2.22: Powder X-ray diffraction patterns of CoAPO-21 (a), and ZnAPO-41 (b). An apparent impurity peak is indicated by a star in the former sample.

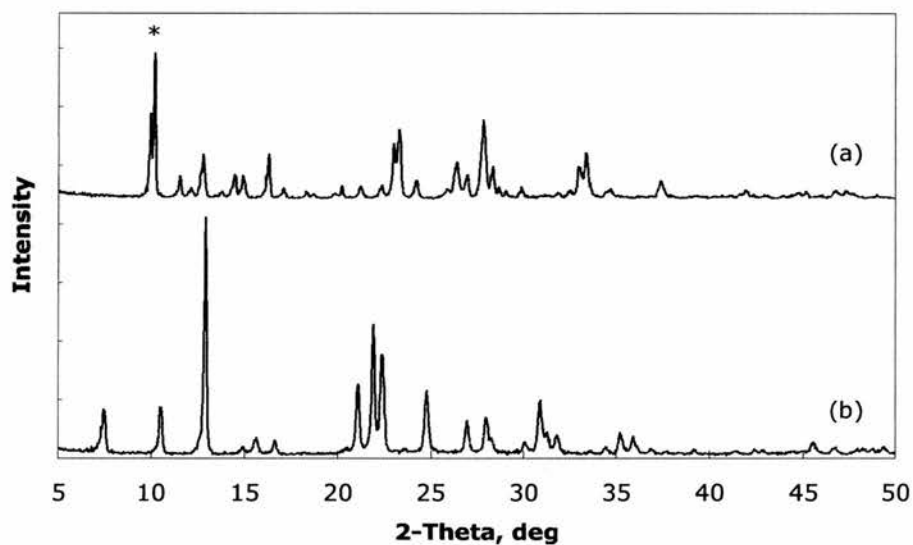


Figure 2.23: Scanning electron micrograph of CoAPO-21 plates.

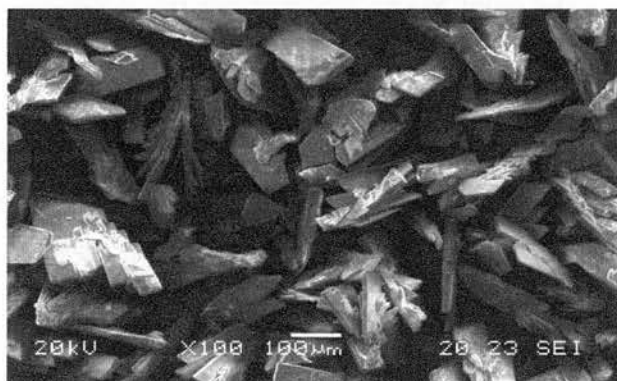


Figure 2.24: Powder X-ray diffraction patterns. MgAPO-21 (a), transforms topotactically to poorly crystalline MgAPO-25 (b), on heating.

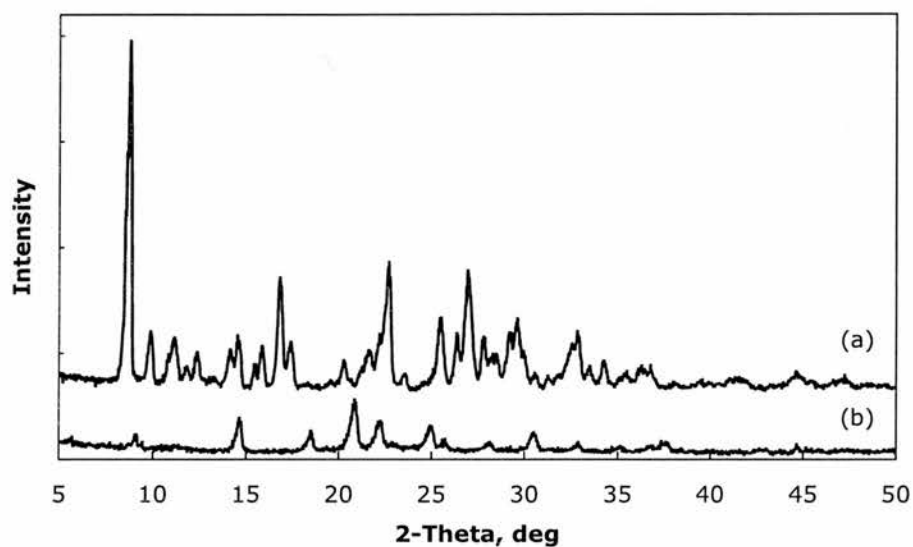
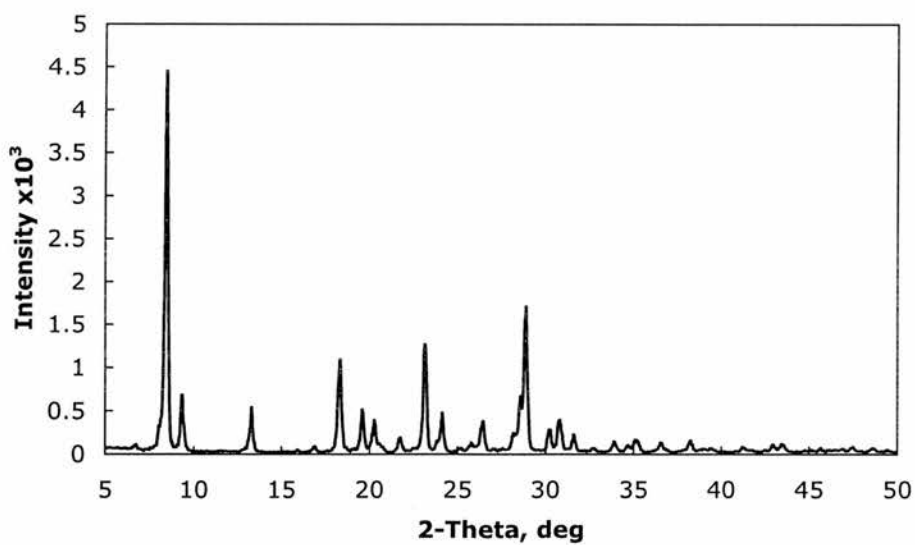


Figure 2.25: Powder X-ray diffraction pattern of an unidentified CoAPO synthesised with 1,5-diaminopentane and 18-crown-6.



and Co-UCSB-6 (**SBS**). The structure of UCSB-6 is known [99] but was determined here by single crystal X-ray diffraction.⁴ The structure of UCSB-6 was shown in Figure 2.5, page 54 and is made up of large cavities bounded by 12-rings. Figure 2.26 shows SEM images revealing the typical morphology of crystallites that were prepared.

To investigate further the effect of including 18-crown-6 in these syntheses, experiments were carried out using only the amine. Two illustrative examples will be given. With 1,5-diaminopentane a different material forms if the crown ether is not present (AlPO₄-21, as opposed to the unidentified solid). However the same phases (UCSB-6 and AlPO₄-34) crystallise from gels containing 1,8-diaminooctane whether 18-crown-6 is present or not.

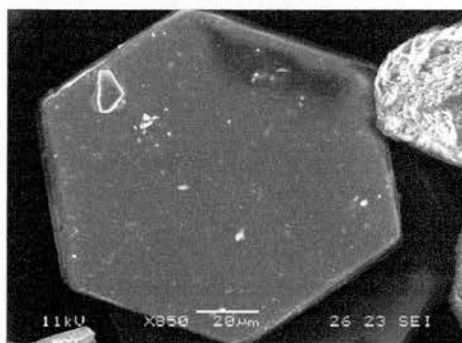
Solid state NMR spectroscopy was carried out on Zn-UCSB-6 prepared with 1,8-diaminooctane and 18-crown-6. The powder XRD confirmed that this material, containing 15% Zn, contained only one crystalline phase (Figure 2.27). ²⁷Al and ³¹P MAS NMR spectra (Figure 2.28) confirm the structure is very largely tetrahedrally-connected. Additional peaks in the ³¹P spectrum are broad and could be the result of an amorphous impurity. The ¹³C CP-MAS NMR spectrum (Figure 2.29) shows that while the 1,8-diaminooctane is present no 18-crown-6 has been occluded (an additional signal at $\delta_C \sim 70$ ppm would be expected).

2.3.6 Tmhht as a template

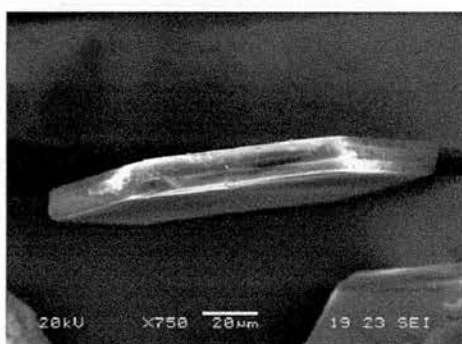
Mixtures of crystalline and amorphous solids are obtained with 1,3,5-trimethylhexahydro-1,3,5-triazine (tmhht, Figure 2.12.f). Increasing the M^{II}/P ratio from 0.1 to 0.2 in a MgAPO gel yields a more fully crystallised material; this was identified as MAPO-43 (**GIS**).

⁴Co-UCSB-6. [(Co,Al)₈P₈O₂₈], $M = 861.37$, hexagonal, $a = 17.6363(4)$ Å, $c = 27.230(1)$ Å, $V = 7334.8(4)$ Å³, $T = 293(2)$ K, space group $P6_3$ (no. 173), $Z = 8$, $\mu(\text{Mo-K}\alpha) = 0.747$ mm⁻¹, 32827 reflections measured, 7039 unique of which 1547 were observed. The final $R(\text{obs})$ was 0.2059 with $wR(F^2) = 0.3820$. Note that the refinement was performed using a purely aluminophosphate model.

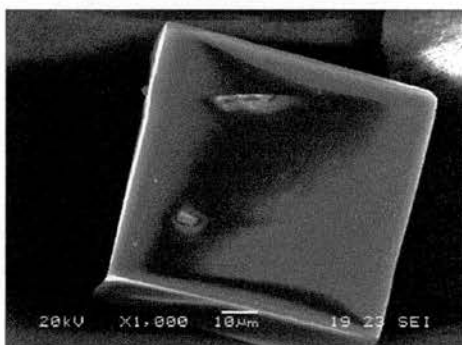
Figure 2.26: Scanning electron micrographs of crystallites synthesised with 1,8-diaminooctane and 18-crown-6. Co-UCSB-6 crystallises with a hexagonal plate morphology (a) and (b), while CoAPO-34 co-crystallises as an impurity phase (c).



(a)

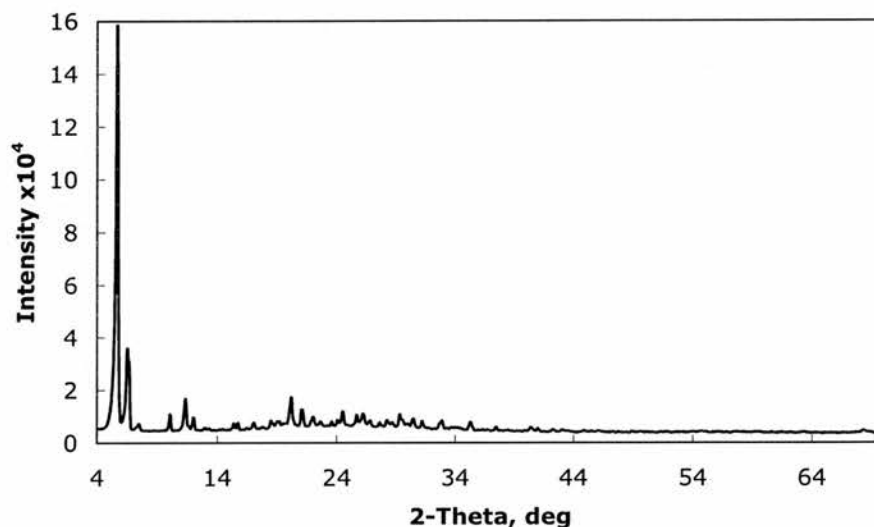


(b)



(c)

Figure 2.27: Powder X-ray diffraction pattern of Zn-UCSB-6 prepared with 1,8-diaminooctane and 18-crown-6.



2.3.7 Hhpp as a template

MgAPO-21 crystallised from gels of various inorganic compositions and water contents in the presence of 1,3,4,6,7,8-hexahydro-2*H*-pyrimido[1,2-*a*]pyrimidine (hhpp, Figure 2.12.g). An example diffraction pattern is given in Figure 2.30.

2.3.8 Hhmpp as a template

The methylated form of hhpp, 1,3,4,6,7,8-hexahydro-1-methyl-2*H*-pyrimido[1,2-*a*]pyrimidine (hbmpp, Figure 2.12.h) was added to a series of MgAPO gels in which the cation and water ratio were varied. In one case the heating time was increase from 48 to 72 hours. The results of these experiments are summarised in Table 2.5.

The products obtained were examined by powder X-ray diffraction. Crystals of sufficient size and quality for single crystal XRD were obtained from the gel given last in Table 2.5, which allowed lattice parameters to be obtained

Figure 2.28: ^{27}Al MAS NMR (a), and ^{31}P MAS NMR (b), of UCSB-6 synthesised with 1,8-diaminooctane and 18-crown-6. The principal peaks are at δ_{Al} 38.0 ppm and δ_{P} -3.8 ppm (see text for further details).

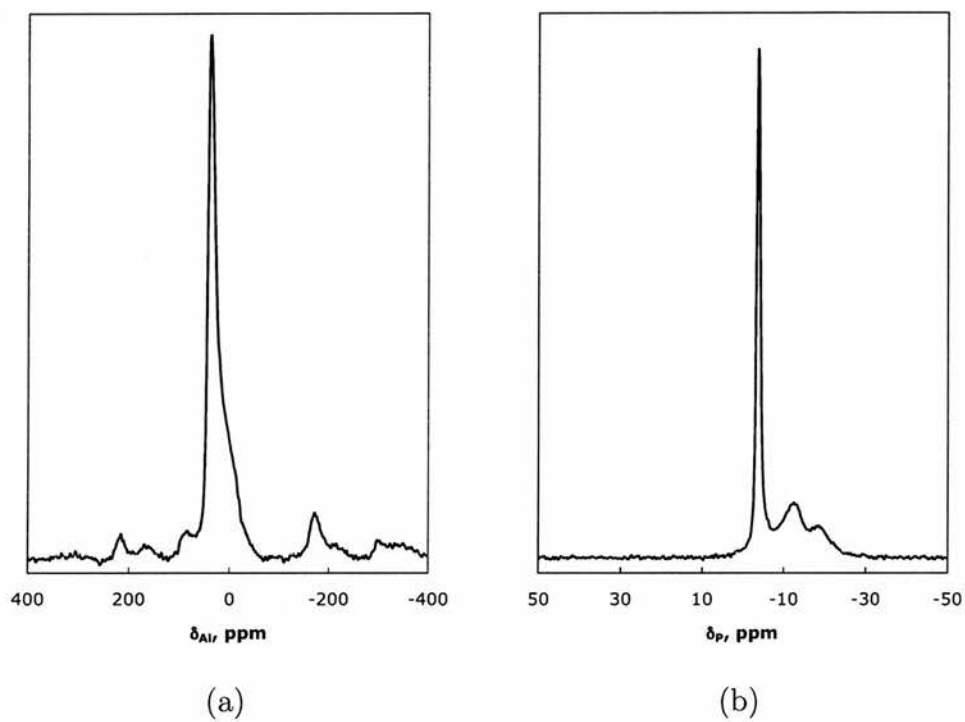


Figure 2.29: ^{13}C MAS NMR of UCSB-6 synthesised with 1,8-diaminooctane and 18-crown-6. The peaks at δ_C 40.5, 34.4, 30.9, 26.9 ppm correspond to 1,8-diaminooctane. If 18-crown-6 were occluded within cavities in the solid a signal at $\delta_C \sim 70$ ppm would be expected, however no signals (other than those shown) are observed between 200 and -40 ppm.

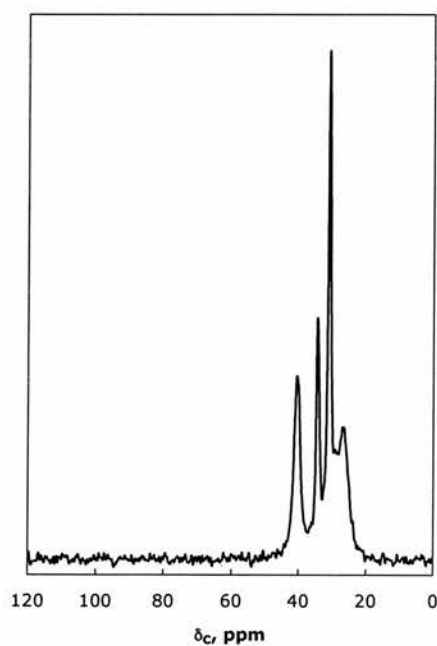
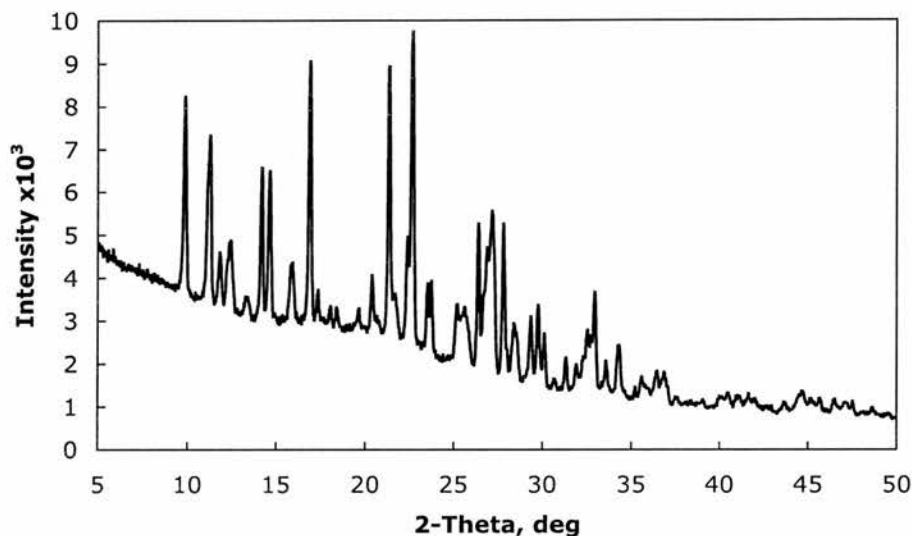


Figure 2.30: Powder X-ray diffraction pattern of MgAPO-21 synthesised with hhpp. (The sloping background is due to a faulty beam stop on the diffractometer.)



for two phases; this permitted greater confidence in the phase assignment by powder diffraction.

The products formed are again MAPO-34 and MAPO-21 (Figure 2.31). The former appears to be formed before the latter. After 48 h heating the gel containing 0.2Mg and 80H₂O had MAPO-34 as the principal phase. If this gel is heated for an additional 24 hours, MAPO-21 appears as the major phase, with some residual MAPO-34.

2.3.9 Peabcoa as a template

Use of as-received [*R*-(*R*^{*},*S*^{*})-(-)-*N*-(1-phenylethyl)-1-azabicyclo[2.2.2]octan-3-amine (the hydrochloride salt) gave a dense phase (peabcoa, Figure 2.12.i). The presence of HCl results in an initial gel *pH* of 2.5, too low for the crystallisation of aluminophosphate materials. If the free base is first obtained, the initial gel *pH* rises to 7, and the known MAPO-36 (**ATS**) framework crystallises.

Table 2.5: Summary of results of syntheses with hhmpp.

Mg : Al : H ₂ O	Heating time, h	Product (by XRD) ¹
0.1 : 0.9 : 80	48	MAPO-34 (+ MAPO-21)
0.1 : 0.9 : 400	48	MAPO-34 + MAPO-21 ²
0.2 : 0.8 : 80	48	MAPO-34 (+ MAPO-21)
0.2 : 0.8 : 80	72	MAPO-21 (+ MAPO-34)
0.2 : 0.8 : 400	48	MAPO-34 (+ MAPO-21)

¹ The minor phase is given in brackets
² *ca* 50/50 mixture

2.3.10 Troger's base as a template

Dense phases were obtained with 2,8-dimethyl-6*H*,12*H*-5,11-methanodibenzo-*[b,f]*[1,5]diazooane (Troger's base, Figure 2.12.j) in both Mg^{II} and Co^{II}-containing gels. Products were yellow in colour, possibly indicating template decomposition. Mg^{II}-containing phases are expected to be white, while those that contain tetrahedral Co^{II} are blue.

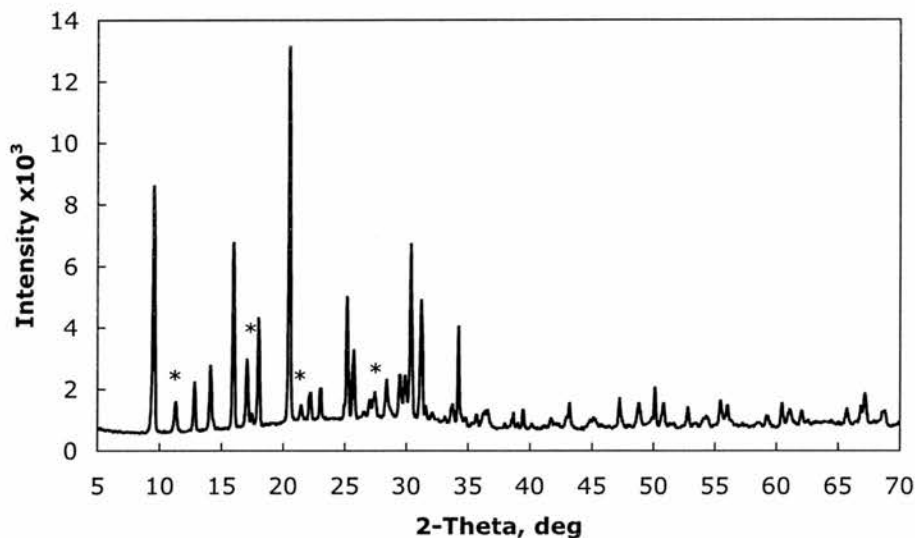
2.3.11 Spiro templates

The spiro family of quaternary ammonium salt templates 6-azoniaspiro[5.5]-undecane (asu), 8-oxa-5-azoniaspiro[4.5]decane (oasd) and benzotri(5-azonia-[4.5]dec-2-ene (btad), (Figure 2.12.k–2.12.m) will be considered together. Table 2.6 summarises the results of syntheses.

Table 2.6: Results of aluminophosphate syntheses with spiro templates.

Template	Figure	Product (by XRD)
Asu	2.12.k	MAPO-5 + dense phase
Oasd	2.12.l	dense phase
Btad	2.12.m	amorphous

Figure 2.31: Powder X-ray diffraction pattern of mixed phase MgAPO-34 and MgAPO-21 synthesised with hhmpp. MAPO-21 is indicated with starred peaks.



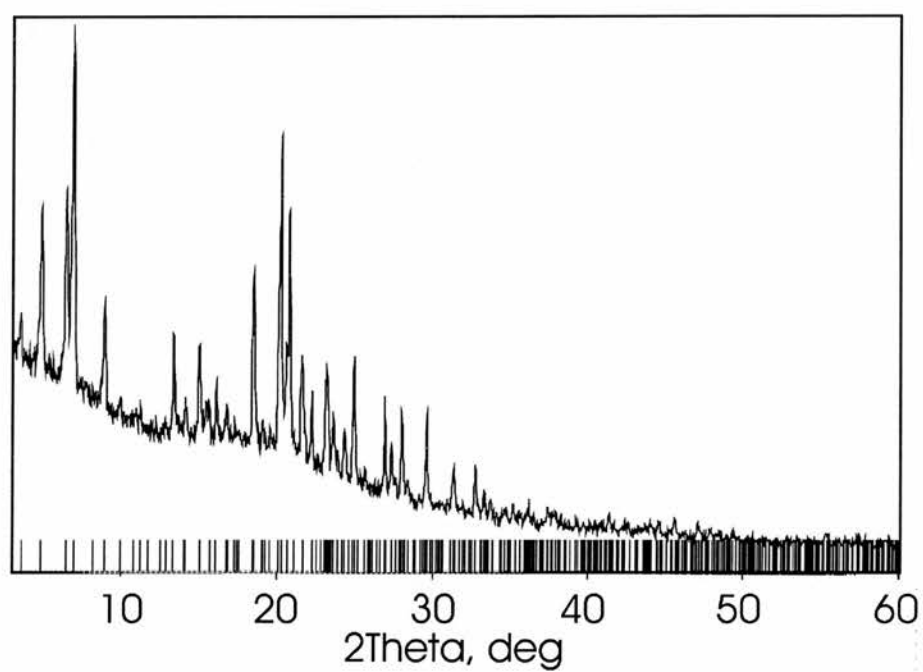
2.3.12 Pbcomb polymer as a template

Magnesiumaluminophosphate gels crystallised principally as MAPO-5 in the presence of the poly[4-(1,4-diazabicyclo[2.2.2]oct-1-ylmethyl)benzyl] template (pbcomb, Figure 2.12.n). Nevertheless, on one occasion a mixture of phases was obtained (MAPO-5 and an unknown, designated STA-4) which were separated by density with sonication. The powder diffraction pattern of the unidentified as-prepared material is given in Figure 2.32. The could be indexed in space group $P6/mmm$ with lattice parameters $a = 22.45 \text{ \AA}$ and $c = 15.19 \text{ \AA}$. On calcination under flowing oxygen the template could be removed but the framework partially collapsed. Single crystals were not obtained and subsequent attempts to synthesise this material proved unsuccessful.

2.3.13 Phosphazine base templates

Two phosphazine bases, P_1 -*t*-Bu and P_1 -*t*-Bu-tris(tetramethylene), denoted p1 (2.12.o) and p2 (2.12.p) respectively, have been examined as templates

Figure 2.32: Powder X-ray diffraction pattern of a novel MgAPO material (STA-4) prepared with pbcomb.



for microporous solids. Aluminophosphate preparations, using p1, containing Mg^{II} , Si^{IV} and Co^{II} cations all yielded solids with the MAPO-21 framework type. In contrast, the SAPO gel failed to crystallise when p2 was used as the template. Gels yielded an unidentified material when 10% Mg was included but if 20% or more was added then MgAPO-20 crystallised instead.

2.4 Discussion

The azamacrocycle tmtacn (containing tertiary nitrogen atoms) and the aza-oxacryptand K222 have been shown to be effective templates for the synthesis of open framework metalloaluminophosphates, where they are included, unbound, in cages within the structures of MAPO-18 and MAPO-42. By contrast, cyclam itself, with four secondary nitrogen atoms within the ring, remains coordinated to cobalt in the final product under similar conditions, where the macrocycle becomes an integral part of the structure. The latter kind of behaviour is similar to that observed in the cyclam-containing gallium phosphates reported previously. [111] Hydrogen-bonding between the cyclam and the aluminophosphate chain and within the chain itself are important structural features. These are distinctly different from the bonding observed between template molecules that possess tertiary amine groups and three-dimensionally connected frameworks. Presumably the ability of the secondary amine hydrogen atoms to hydrogen bond to phosphate group oxygens crucially directs the synthesis of CoAPO-cyclam-1 and the related nickel containing structure. However, in the magnesioaluminophosphate preparation cyclam directs the formation of MgAPO-18. Mg is more weakly complexed in the macrocycle than either Co or Ni and so is not expected to remain complexed. Instead cyclam remains unbound within the **AEI** cavity.

Similarly, tmtact is able to direct the formation of the phases STA-6, or a previously unknown phase STA-7, depending on the cation present in the MAPO gel. This is discussed in depth in Chapter 4.

Evidence from X-ray diffraction and sample colour indicate that in the MAPOs containing tmtacn and K222 the divalent metal cations do not remain

complexed within the macrocycle after crystallisation. For example, no X-ray scattering was observed in the centre of the K222 cryptand in ZnAPO-42 (the site refined to zero occupancy) and crystallites containing cobalt were blue before, and green after calcination, which is consistent with the oxidation of cobalt from 2+ to 3+ within the tetrahedral sites in the framework. This indicates that the cations are tetrahedrally coordinated within the framework rather than remaining complexed within the macrocyclic ligand and implies that they are more strongly bound within the framework.

In zeolite syntheses crown ethers can modify the crystallisation process so as to affect the product formed (for example, **FAU-EMT** [128]). The inclusion of 18-crown-6 into metalloaluminophosphate gels, with amines, has a subtle effect on the product formed. It is possible that the crown ether is modifying the synthesis gel by complexing metal cations during the crystallisation process. The amine templates used in this work are able to direct the formation of a large number of different framework types. However, many have presumably broken down and the fragments have then templated the AlPO_4 -21 framework. UCSB-6 may be prepared in the presence or absence of 18-crown-6 and solid state NMR spectroscopy has shown conclusively that the crown ether is not present in the material, although there is sufficient space. Preparations with 1,5-diaminopentane are different. Without 18-crown-6 AlPO_4 -21 forms, but in the presence of the ether an unidentified phase crystallises. A full structure solution of this microcrystalline material was not possible and because it was only prepared as a CoAPO NMR spectroscopy could not be used to determine whether 18-crown-6 was present in the framework. Further characterisation of this material would be highly desirable.

Secondary and tertiary amines (with the exception of Troger's base) can also act as templates for microporous solids; small pore solids MAPO-34 and MAPO-43 and large pore MAPO-36 were synthesised. However materials were also prepared that could not contain intact templates. Subtle changes in structure, for example the *N*-methylation of hhpp to form hhmpp, resulted in changes in the MAPO materials which crystallised. Although MAPO-21 could be prepared with either amine, only hhmpp could direct the crystallisation of

chabazitic MAPO-34. It is likely that these templates are breaking down however, and it is the fragments that are in fact directing MAPO-21 to form.

Spiro quaternary ammonium salts are effective templates for high-silica zeolites. [95] However, in aluminophosphate synthesis they have proved to be less effective. Dense or amorphous phases were observed with asu, oasd and btad compounds, while large pore MAPO-5 was formed with asu. MAPO-5 is known to crystallise with numerous structure directing agents [130] and can be considered a “default” framework type: it crystallises exceptionally readily. These spiro quaternary ammonium salts are therefore not promising in directing the formation of novel AlPO_4 frameworks.

The quaternary pbcomb template directed the crystallisation of a unidentified MgAPO as a minor phase with MgAPO-5. This material is at least partially stable to calcination under flowing oxygen. Preparation of material for further study proved difficult and further characterisation could not be performed.

MAPO-21 and MAPO-20 formed in the presence of phosphazine bases p1 and p2, respectively. Presumably, however, only fragments of the organic species have been occluded into the framework materials.

2.5 Conclusion

Macrocyclic and polymacrocyclic compounds containing tertiary nitrogens are excellent templates for metalloaluminophosphate materials. Tmtact, tmtacn and K222 direct the formation of STA-6 or STA-7, MAPO-18 and MAPO-42, respectively. In the final product the organocation resides in the cavities of these materials and may be removed by calcination to leave empty pores. Macrocycles containing secondary nitrogens or oxygen atoms only are less effective in directing the synthesis of materials with pores that may be emptied by calcination after synthesis. By including cations such as Mg in the synthesis gel, which is expected to be only weakly bound, 3-D frameworks are able to form. The use of cyclam resulted in an inorganic–organic hybrid material in which the macrocycle became part of the framework if more strongly bound Co

or Ni cations were included instead. The ether 18-crown-6 was not taken up by growing UCSB-6 crystallites but may influence the crystallisation process, for example, either by sequestering ions or modifying the gel pH .

The phases MAPO-5, MAPO-21 and MAPO-34 were found to crystallise with a wide variety of template molecules. These materials readily form and are not strongly influenced by organic structure directing agents. Their formation is presumably driven by kinetic factors which many template molecules are unable to overcome. Nevertheless, one polymeric quaternary ammonium salt has been shown to template a novel framework. This was observed with low reproducibility and that structure (STA-4) remains, to date, unsolved.

Chapter 3

Structural chemistry of STA-2

3.1 Introduction

Interest in the synthesis of novel aluminophosphate materials [3] has increased in the past two decades. Although structurally similar to aluminosilicate zeolites, such materials deviate in the following respects: (a) pure AlPO_4 is uncharged which precludes the possibility of ion-exchangeable extra-framework inorganic cations, and (b) aluminium species may be four, five, or six coordinate, opening up a rich structural chemistry. Nevertheless, the potential for aliovalent substitution into the aluminophosphate framework has stimulated much research into the catalytic (acid or redox) potential of these materials. [131, 132] And the possibility of incorporating functional organic molecules (such as the macrocycles considered in Chapter 2) into inorganic hosts, may generate inorganic-organic hybrid materials with novel properties. In this way materials may be created with cation exchange, non-linear optical [133] or proton conduction properties, or as “ship-in-a-bottle” catalysts. [134, 135, 136] Incorporating such functional molecules during synthesis is particularly interesting: there is then no need to calcine the solids to obtain open pores, with the consequent destruction of expensive templates, attendant safety concerns and the possibility of associated structural breakdown.

In this chapter the structural chemistry of the novel microporous solid, STA-2, is investigated. STA-2 (**St Andrews-2**) was first prepared in 1997 [98]

and is templated by either of two α,ω -bis(1-azoniabicyclo[2.2.2]octane)alkyl hydroxide templates (see below). The AlPO_4 , SAPO, MgAPO and CoAPO forms were prepared. The structure was solved from a MgAPO microcrystal and characterised with powder XRD, thermal and elemental analysis and dinitrogen adsorption. The position of the babob template was simulated and solid state NMR spectroscopy was carried out. Unexpectedly the ^{27}Al MAS NMR spectrum contained a 5-coordinate species that was not fully explained. STA-2 is of interest because the AlPO_4 form may be prepared with cationic templates even in the absence of charge balancing F^- cations. With other materials (*e.g.* DAF-1) it is not possible to prepare solids with no, or varying, metal concentrations. In order to prepare catalytic materials that were phase pure an investigation of the compositional range of STA-2 was embarked upon and the structural basis for this investigated. The variables were the template, M/P or Si/Al ratio and addition of F^- .

3.2 Experimental

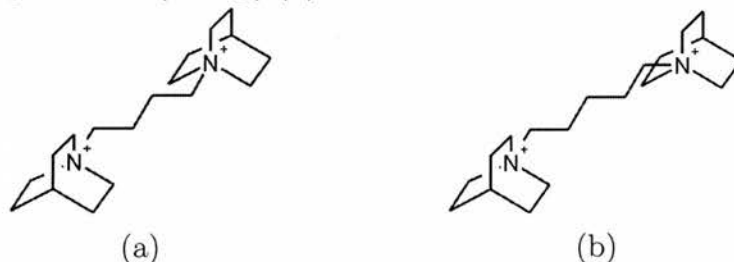
3.2.1 Synthesis

Metalloaluminophosphate materials were synthesised in a variety of compositions as described previously (page 65). The templates 1,4-bis(1-azoniabicyclo[2.2.2]octane)butyl dihydroxide (babob) and 1,5-bis(1-azoniabicyclo[2.2.2]octane)pentyl dihydroxide (babop) were employed. These are given in Figure 3.1. Both templates were synthesised *via* the Menschutkin reaction [118] from quinuclidine (Fluka, 97%) and the appropriate dibromoalkane (Aldrich, 99%) as described in the literature. [98]

3.2.2 Chemical analysis

Chemical analysis were carried out as described in Chapter 2, page 69.

Figure 3.1: STA-2 crystallises in the presence of 1,4-bis(1-azoniabicyclo[2.2.2]-octane)butyl cations (babob) (a) or, 1,5-bis(1-azoniabicyclo[2.2.2]-octane)pentyl cations (babop) (b).



3.2.3 Crystallography

Crystallography was carried out as described in Chapter 2, page 67. For structural analysis samples of as-prepared $\text{AlPO}_4(\text{F})$ -STA-2 and Mg -STA-2 were examined in capillaries on a Stoe diffractometer with $\text{Cu-K}\alpha_1$ radiation. A portion of each sample was calcined under flowing oxygen at 550°C , loaded into a quartz glass capillary and dehydrated as previously described (page 65). Powder X-ray diffraction data were collected for this sample in the same way. The powder profiles were matched using the Rietveld refinement technique in the GSAS suite of programs. [32]

3.2.4 NMR spectroscopy

To investigate short range structure in the materials MAS NMR spectroscopy was performed at the EPSRC solid state NMR Facility in Durham on a Varian UNITY*Inova* spectrometer at ambient temperature in a similar way to that previously described (page 69).

^{13}C , ^{19}F , ^{27}Al and ^{31}P NMR spectra were collected, as appropriate, for as-prepared samples of AlPO_4 and MgAPO STA-2. The following experimental parameters were used.

^{13}C DPMAS NMR spectra were collected with a Doty Scientific MAS probe with 7 mm o.d. rotors. The frequency was 75.430 MHz and an acquisition time of 30.0 ms, relaxation delay of 1.0 s, pulse angle of 90.0° and spin rate of 4.37 kHz were used. The shift reference sample was $(\text{CH}_3)_4\text{Si}$. Spectra were

obtained without the need for cross polarization and even with the relatively short 1 s recycle intensities close to quantitative were obtained.

^{27}Al DPMAS NMR spectra were collected with a Varian (Chemagnetics) APEX MAS probe from samples in 4 mm o.d. rotors at a frequency of 78.157 MHz, using an acquisition time of 10.0 ms, relaxation delay of 0.2 s, pulse angle of 22.5° and spin rate of 10.6 kHz. Spectra were referenced to 1 M $\text{Al}(\text{H}_2\text{O})_6^{3+}$ (aq).

Similarly, ^{31}P DPMAS NMR spectra were collected at a frequency of 121.420 MHz, using an acquisition time of 20.0 ms, relaxation delay of 120.0 s, pulse angle of 90.0° and spin rate of 10.6 kHz. For Mg-STA-2 a ^{31}P CP-MAS NMR spectrum was also collected (with the same parameters as before, except a relaxation delay of 1.0 s and a CP contact time of 15.0 ms were used). Spectra were referenced to 85 % H_3PO_4 (aq).

A ^{19}F DPMAS NMR spectrum was collected with a Doty Scientific XC MAS probe from a sample in a 5 mm o.d. rotor at a frequency of 282.197 MHz, using an acquisition time of 3.0 ms, relaxation delay of 10.0 s, pulse angle of 94.1° , spin rate of 14.2 kHz and referenced to CF_3Cl .

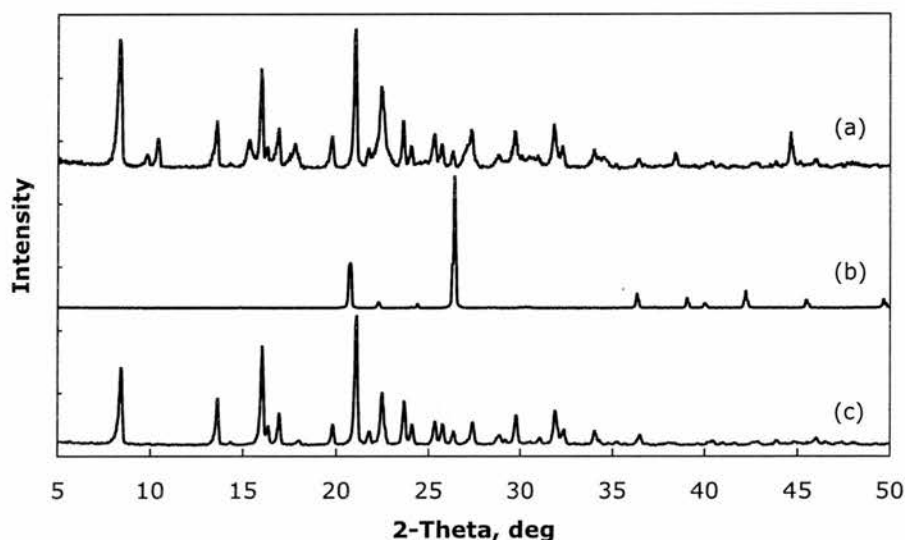
To investigate further the Al sites in STA-2, MQMAS experiments were performed using a basic two-pulse sequence. [137] The 4 mm Varian probe was used at a frequency of 78.160 MHz, using an acquisition time of 4.0 ms, relaxation delay of 0.1 s, pulse angle of 180.0° and spin rate of 15.0 kHz. The resulting spectra were sheared.

3.3 Results

3.3.1 Synthesis

Templates were successfully prepared and the ^{13}C NMR spectra found to be, for babob: δ_{C} (75.458 MHz; D_2O) 63.42 ($\text{NCH}_2\text{CH}_2\text{CH}_2\text{CH}_2\text{N}$), 55.03 ($\text{NCH}_2\text{CH}_2\text{CH}$), 23.64 ($\text{NCH}_2\text{CH}_2\text{CH}$, $\text{NCH}_2\text{CH}_2\text{CH}_2\text{CH}_2\text{N}$), 19.24 ($\text{NCH}_2\text{CH}_2\text{CH}$) and babop: δ_{C} (75.458 MHz; D_2O) 64.06 ($\text{NCH}_2\text{CH}_2\text{CH}_2\text{CH}_2\text{CH}_2\text{N}$), 54.97 ($\text{NCH}_2\text{CH}_2\text{CH}$), 23.68 ($\text{NCH}_2\text{CH}_2\text{CH}$), 23.24 ($\text{NCH}_2\text{CH}_2\text{CH}_2\text{CH}_2\text{CH}_2\text{N}$), 21.54 ($\text{NCH}_2\text{CH}_2\text{CH}_2\text{CH}_2\text{CH}_2\text{N}$), 19.36

Figure 3.2: Powder X-ray diffraction patterns of aluminophosphates crystallised with babob (R) with different amounts of fluoride included in the gel. R/P = 0.4, no fluoride (a), R/P = 0.4, F/P = 0.8 (b), and R/P = 0.8, F/P = 0.8 (c). Even in the absence of fluoride STA-2 crystallises (although a second phase is also present); if R/F = 0.5 then a second phase also forms, but if R/F = 1.0 phase pure STA-2 is obtained.



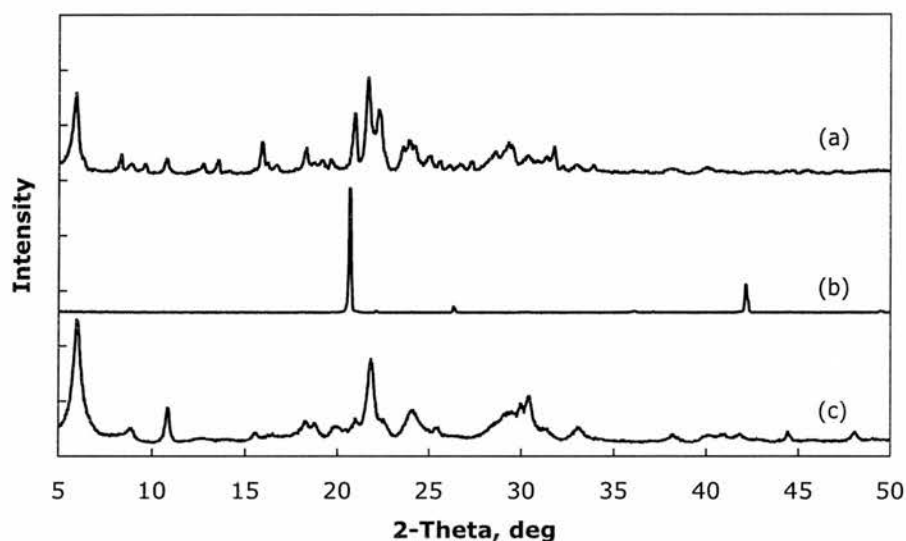
($\text{NCH}_2\text{CH}_2\text{CH}$). No signals were found that could not be accounted for; this was taken to indicate a high degree of purity.

Aluminophosphate syntheses

The powder X-ray diffraction patterns of aluminophosphate gels crystallised in 48 h at 190°C with the template babob are given in Figure 3.2. In this series the effect of fluoride on the products formed is examined. With no fluoride in the gel, STA-2 is the major phase. If enough fluoride to balance the positive charge of the template is added, a dense phase crystallises (no STA-2). However, if more template is added, STA-2 is seen as the only product. The pH of the initial gels was 7, 6 and 8, respectively.

In an analogous way, aluminophosphates were prepared with babop (Figure 3.3). The trend is broadly similar, but instead of STA-2 a previously

Figure 3.3: Powder X-ray diffraction patterns of AlPO_4s crystallised with babop (R) with different amounts of fluoride included in the gel. R/P = 0.4, no fluoride (a), R/P = 0.4, F/P = 0.8 (b), and R/P = 0.8, F/P = 0.8 (c). See text for further details.



observed [98] “layered” phase forms.

Metalloaluminophosphate syntheses

Typical MgAPO and CoAPO STA-2 phases synthesised with babop are shown in Figures 3.4 and 3.5, respectively. STA-2 may be prepared with divalent cations substituted for Al^{III} in the framework; the Co^{II} containing phase is blue, indicating this. In these examples, 15% Mg and 5% Co have replaced Al in the synthesis gel, yielding phase pure materials. Greater or lesser cation ratios promote the formation of secondary phases, however. This is illustrated in the ZnAPO prepared with babop and 5% Zn (Figure 3.6).

To investigate further the effect of varying the ratio $\text{M}^{\text{II}}/\text{P}$ in the babop-containing synthesis gel, a number of MgAPO gels were prepared and crystallised at 190°C in 48 h. The powder X-ray diffraction patterns are given in Figure 3.7. STA-2 is obtained as the major phase in all cases, however only with 15% Mg substituting for Al is it the only phase obtained. At higher Mg

Figure 3.4: Powder X-ray diffraction pattern of Mg-STA-2 (Mg/P = 0.15) crystallised with babob.

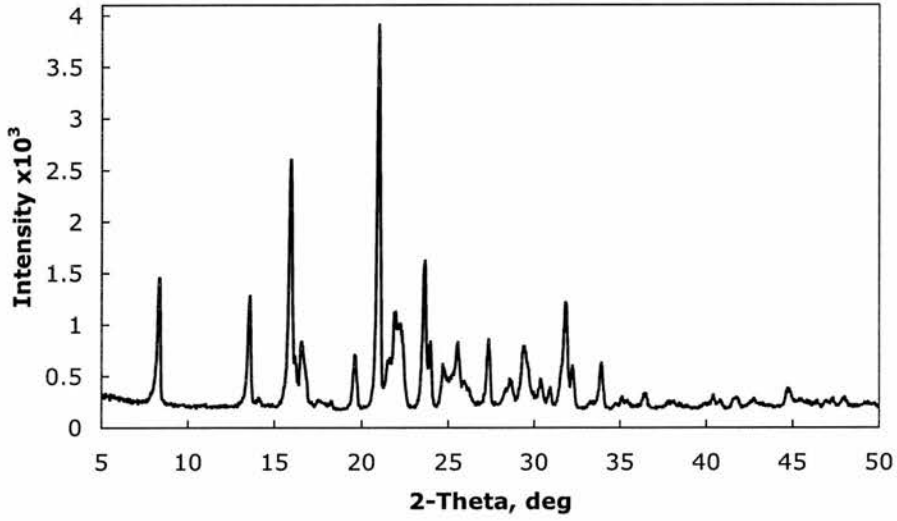


Figure 3.5: Powder X-ray diffraction pattern of Co-STA-2 (Co/P = 0.05) crystallised with babob.

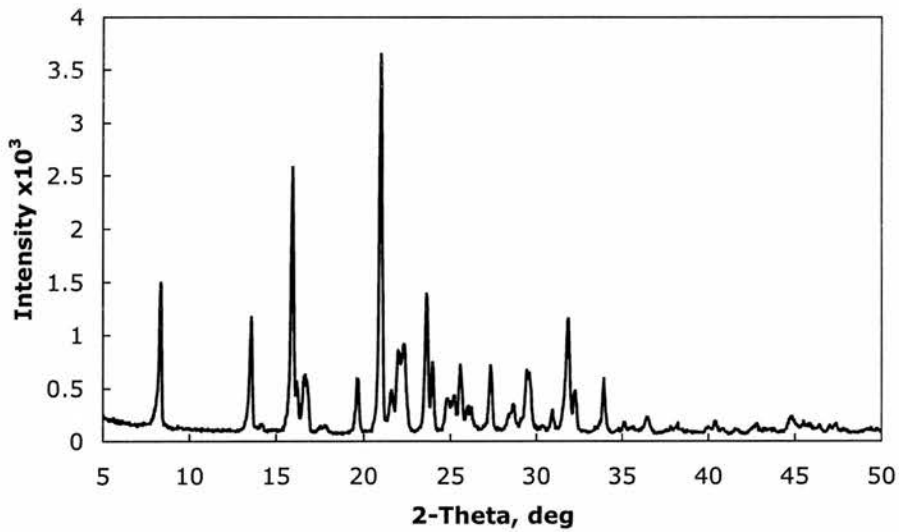
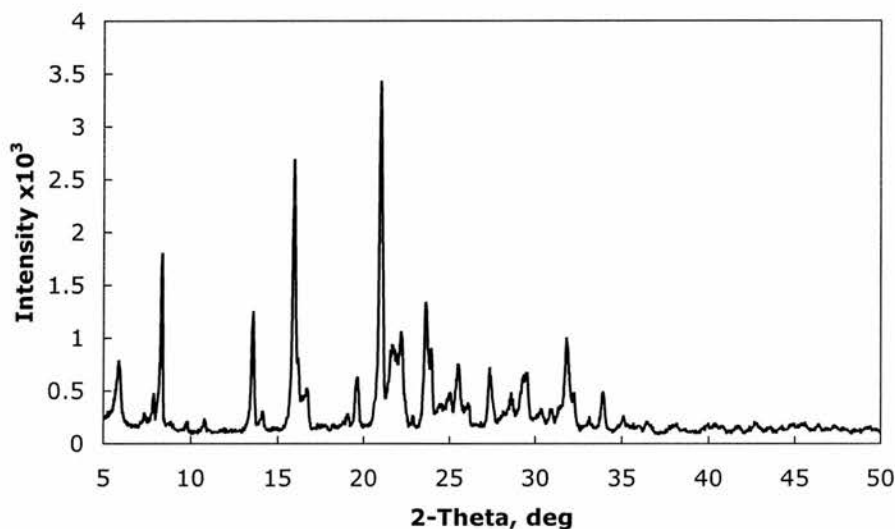


Figure 3.6: Powder X-ray diffraction patterns of ZnAPO (Zn/P = 0.05) crystallised with babop. The primary phase is Zn-STA-2, although an impurity is also present.



contents impurities are observed (with Bragg reflections at $2\theta = 7.4$ and 7.8°). At lower Mg contents the peak at $2\theta = 7.8^\circ$ is not observed, however at very low (5 %) Mg content the layered impurity is again seen.

Silicoaluminophosphate syntheses

As with the MAPO materials (synthesised with babop) secondary phases can be found in the SAPOs. This is illustrated in Figure 3.8, where SAPO-56 (**AFX**) can be seen to co-crystallise.

A layered phase is found in SAPO preparations with babop (Figure 3.9). Similar product distributions are formed with 5 % or 15 % Si in the gel, however if the heating time is reduced from the usual 168 h to 48 h then less of the layered phase is observed (as indicated by the reduction in intensity of the peak at $2\theta = 6^\circ$).

Figure 3.7: Powder X-ray diffraction patterns of MgAPOs crystallised with babob template with varying Mg/P ratios in the gel. Mg/P = 0.05 (a), Mg/P = 0.10 (b), Mg/P = 0.15 (pure STA-2) (c), Mg/P = 0.20 (d), Mg/P = 0.25 (e).

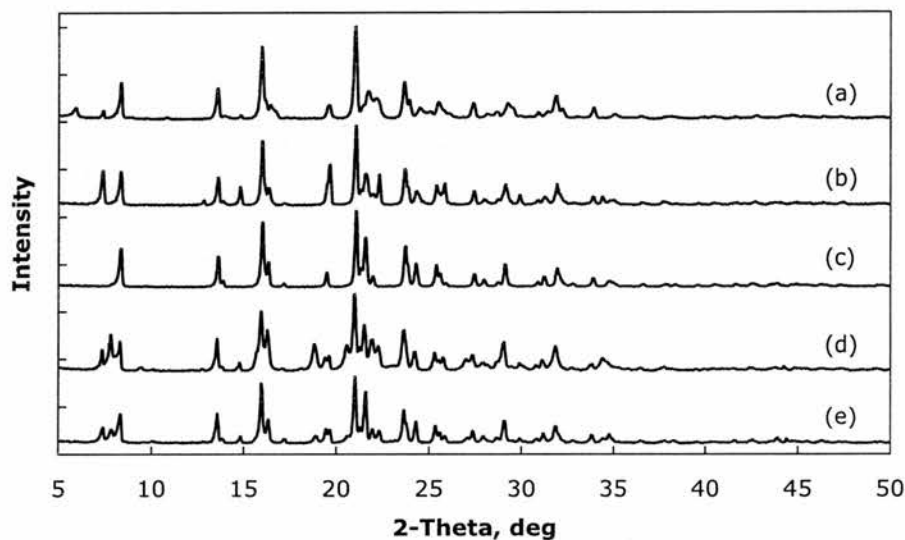


Figure 3.8: Powder X-ray diffraction pattern of Si-STA-2 (Si/Al = 0.08) crystallised with babob template. The product contains SAPO-56 as an impurity.

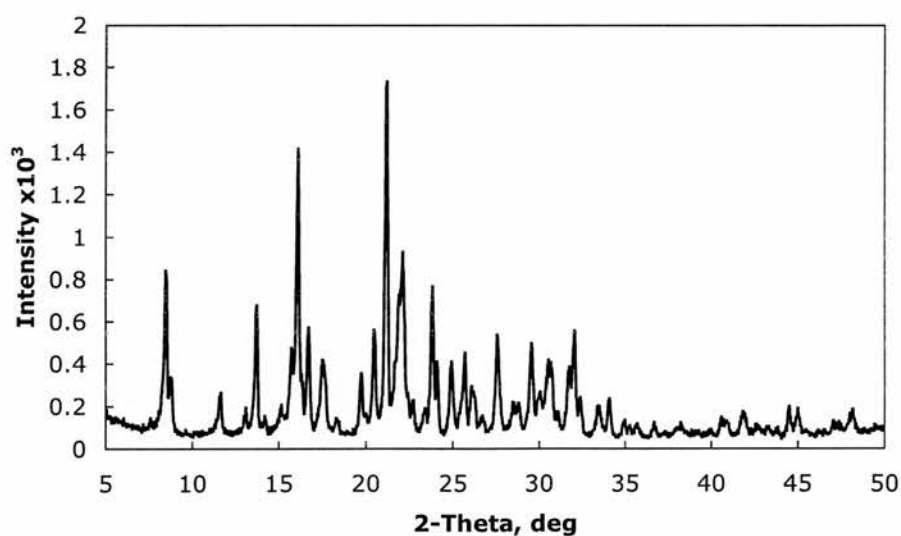
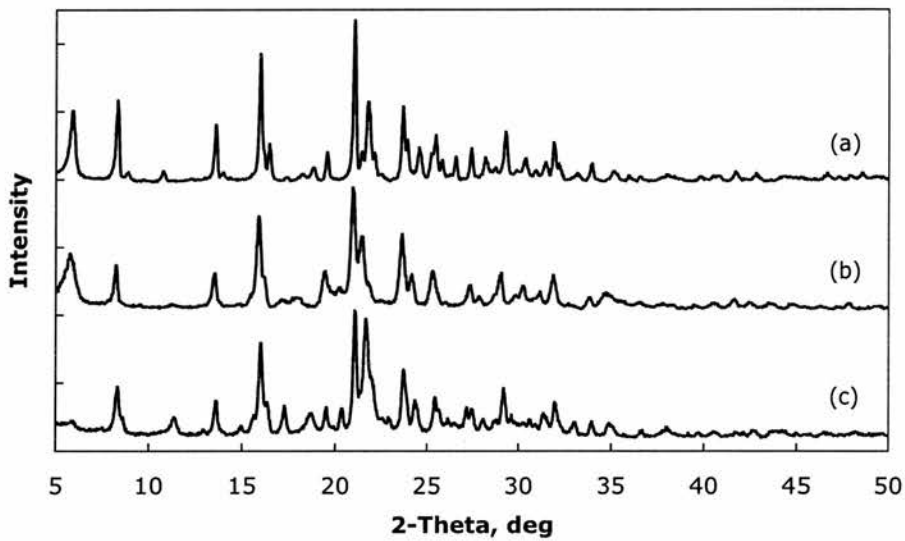


Figure 3.9: Powder X-ray diffraction patterns of SAPOs crystallised at 190 °C with babop template (R) with different amounts of Si included in the gel, and for different times. Si/Al=0.05, 168 h (a), Si/Al=0.15, 168 h (b), and Si/Al=0.15, 48 h (c).



3.3.2 NMR spectroscopy

To study the short-range structure in AlPO_4 and MgAPO samples of STA-2, materials that were phase pure by XRD were selected for study with solid state NMR spectroscopy. The AlPO_4 prepared in the presence of babob and HF, and the MgAPO prepared with 15% Mg and babob were studied.

In the $\text{AlPO}_4(\text{F})$ sample ^{27}Al and ^{31}P MAS NMR spectra show the framework is tetrahedrally connected, with δ_{Al} 35.8 ppm and δ_{P} -26.3 ppm, however there is an additional signal at δ_{Al} 12.7 ppm that corresponds to 5-coordinate Al and the ^{31}P spectra has shoulders indicating a complex signal (Figure 3.10). The signals in the ^{19}F MAS NMR spectrum at δ_{F} -117.1, -124.3 and -166.2 ppm (Figure 3.11.a) are very weak in absolute terms (even accounting for the breadth of the peaks); presumably the amount of F incorporated is low. Possible assignments for these signals are discussed below. The ^{13}C MAS NMR spectrum (Figure 3.11.b) contains signals at δ_{C} 64.2, 56.7, 24.1 and 19.8 ppm showing the template has been incorporated intact (the signals from the methylene carbons farthest from N overlap at δ_{C} 24.1 [98]).

To investigate further the additional signal seen in the ^{27}Al spectrum a multiple quantum (2-D) experiment was performed (Figure 3.12). This was able to resolve two tetrahedral sites (the two crystallographic Al sites) as well as another signal. From the literature [138] this may be assigned to 5-coordinate Al.

In the Mg-STA-2 sample the ^{27}Al spectrum is very simple and shows a single signal at δ_{Al} 33.3 ppm corresponding to tetrahedrally coordinated Al (Figure 3.13). This may be resolved into the two crystallographic sites with a MQ experiment, as before (Figure 3.14). The absence of further signals indicates that Mg is substituting only on the Al, and not on the P, sites. The ^{31}P spectrum is more complex because of the Mg substitution (Figure 3.15.a). The spectrum comprises 3 signals at δ_{P} -19.7, -26.1 and -32.2 ppm which, from the literature [139], may be assigned to $\text{P}(\text{OAl})_2(\text{OMg})_2$, $\text{P}(\text{OAl})_3(\text{OMg})$ and $\text{P}(\text{OAl})_4$, respectively. This obeys Flanigen's rules (page 34). The possibility of the template significantly affecting the measured ^{31}P spectrum is discounted by comparing the DP and CP spectra (Figure 3.15.a and 3.15.b).

Figure 3.10: ^{27}Al MAS NMR (a), and ^{31}P MAS NMR (b), spectra of $\text{AlPO}_4(\text{F})$ -STA-2.

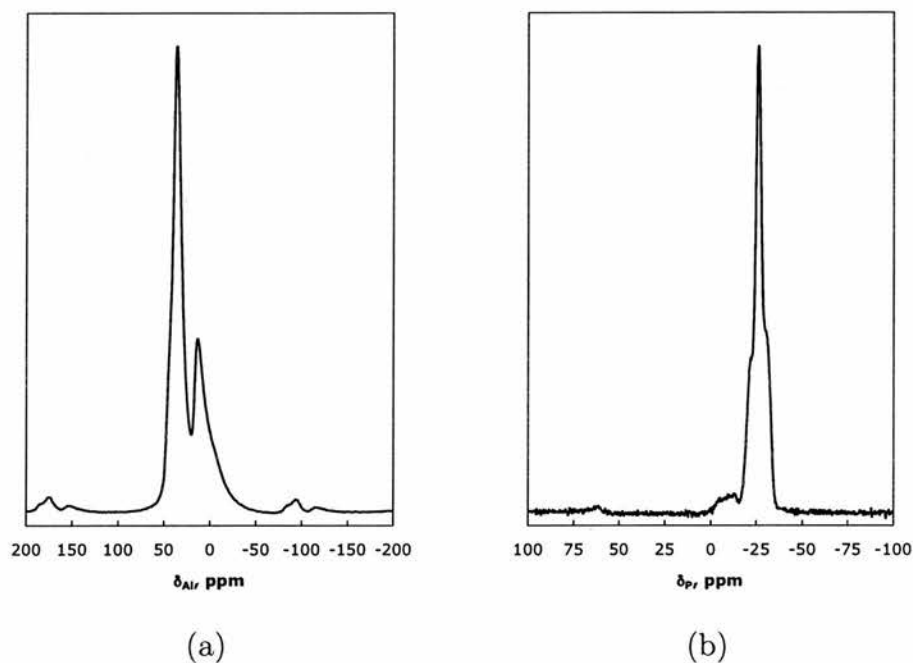


Figure 3.11: ^{19}F MAS NMR (a), and ^{13}C MAS NMR (b), spectra of $\text{AlPO}_4(\text{F})$ -STA-2.

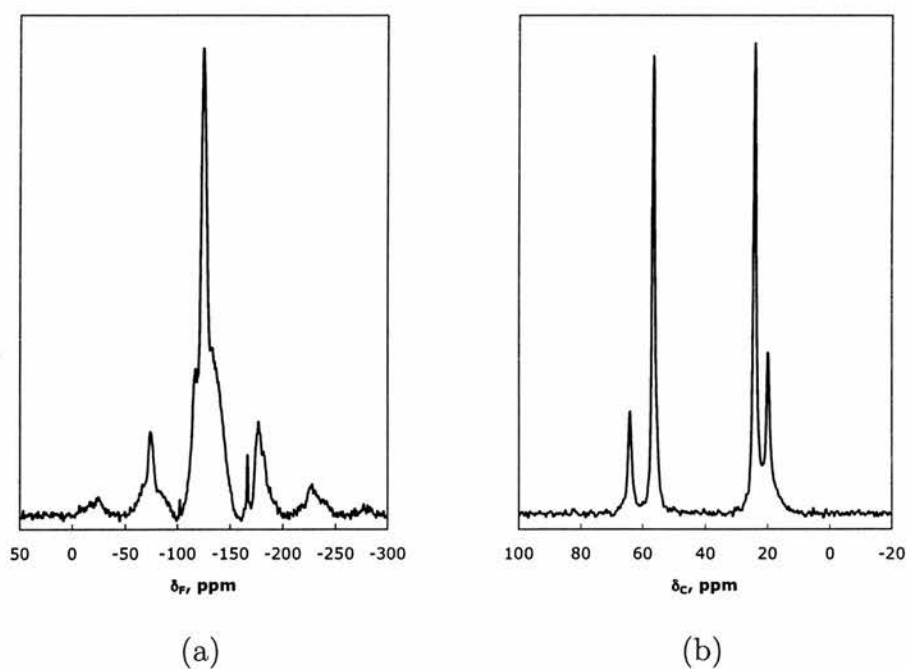


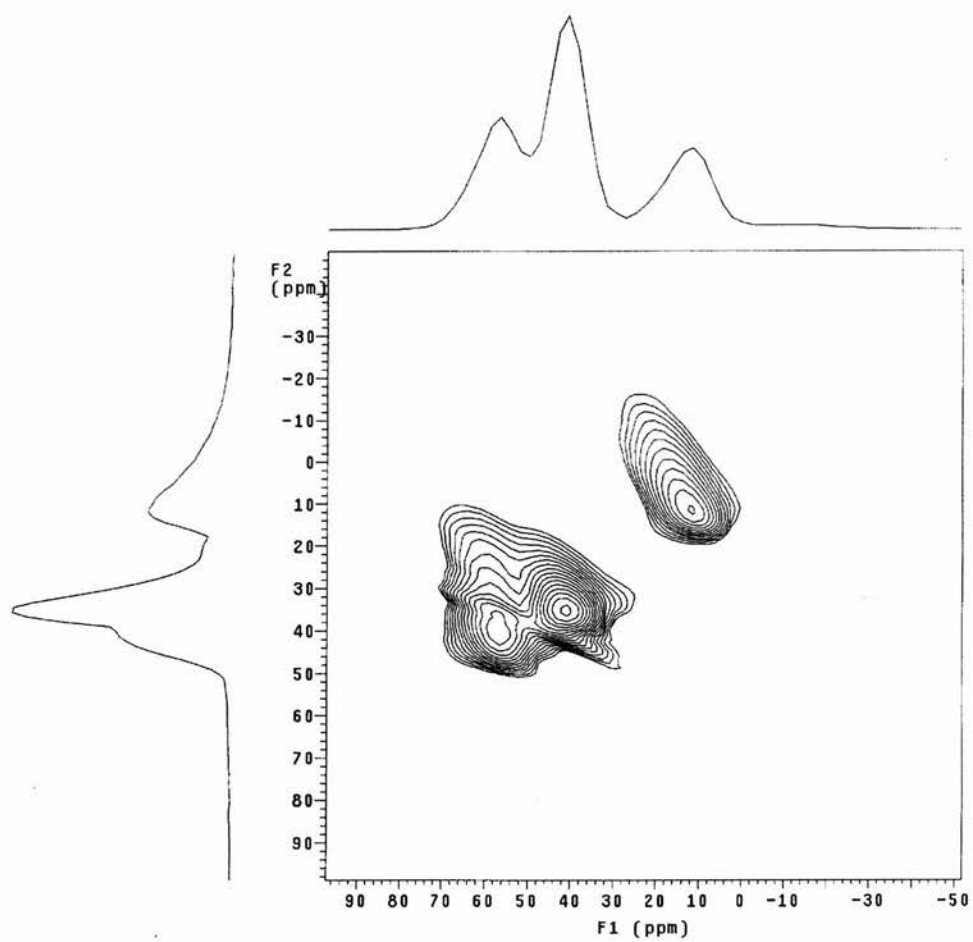
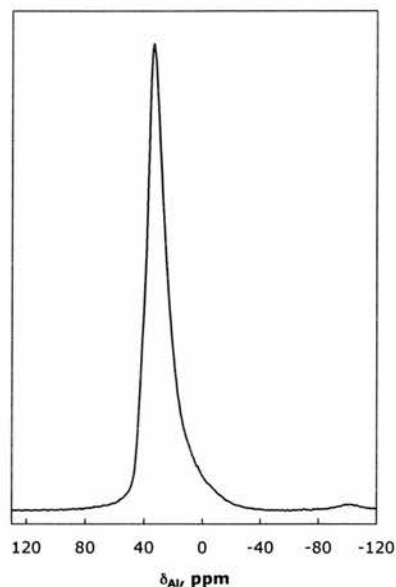
Figure 3.12: ^{27}Al MQMAS NMR spectrum of $\text{AlPO}_4(\text{F})$ -STA-2.

Figure 3.13: ^{27}Al MAS NMR of Mg-STA-2.

These are similar showing that the P species all have the same relationship to the protons in the sample. The template itself is found, as before, intact within the material by solid state ^{13}C NMR (Figure 3.16).

3.3.3 Crystallography

Rietveld refinement of powder X-ray diffraction profiles was carried out on as synthesised and calcined/dehydrated $\text{AlPO}_4(\text{F})$ -STA-2 prepared with babob (Figures 3.17 and 3.18). The published framework and (simulated) template atomic coordinates [98] for STA-2 were used in the starting model of the as-prepared sample. The framework atoms were allowed to undergo constrained refinement. The temperature factors were then carefully refined. Difference Fourier maps showed electron density unaccounted for at around 0.5 \AA from each O atom and within the 4-rings and 6-rings. Entering O atoms on these last two sites (Figure 3.21.a) and refining the fractional occupancy improved the fit (occ. = 0.13 and 0.25). OH^- and F^- have equal electron densities and so XRD is not able to distinguish the two. [140] The final cell and R -factors were

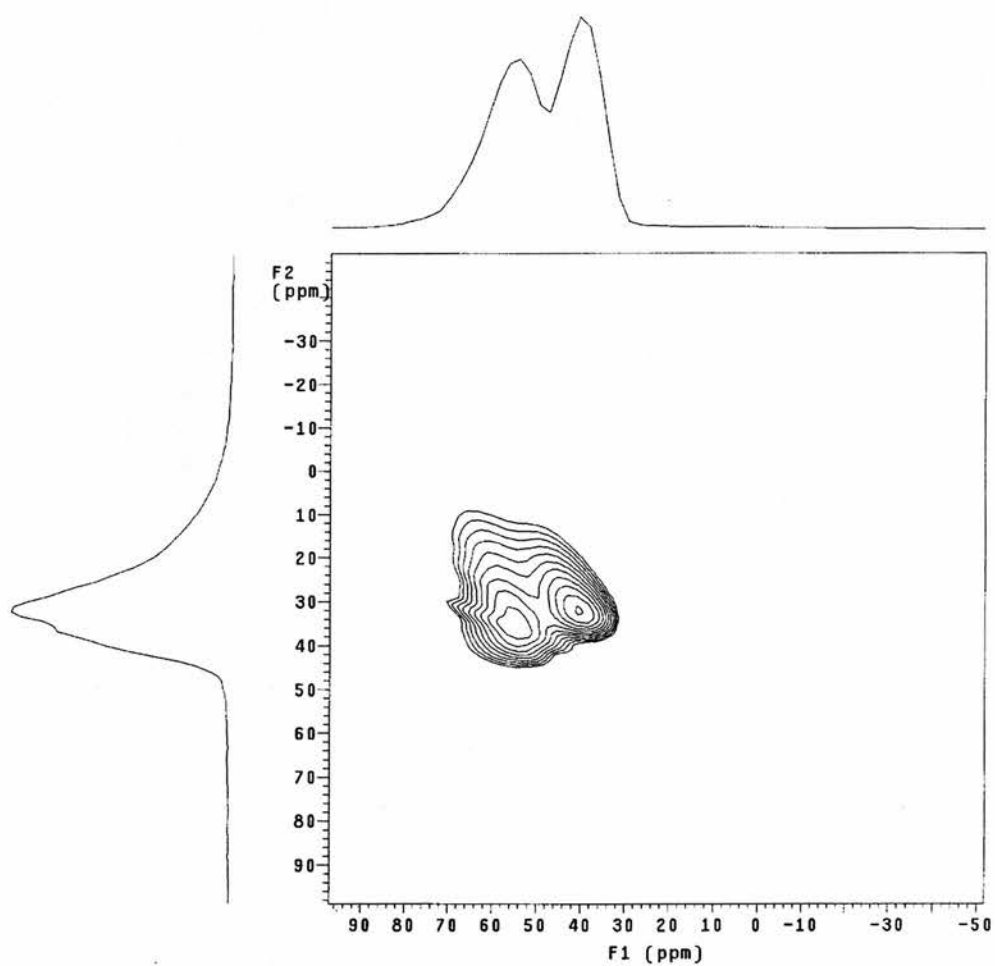
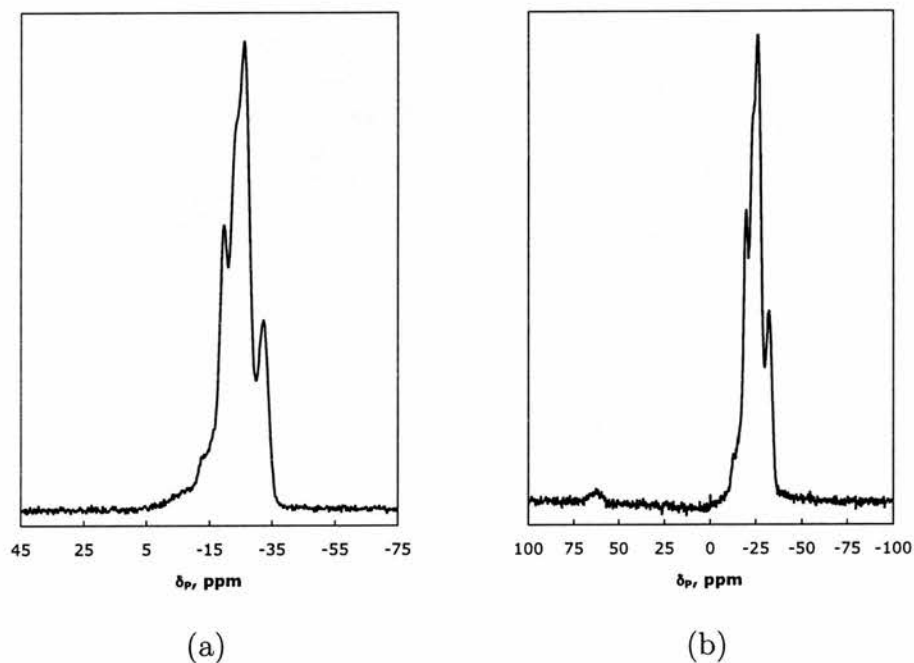
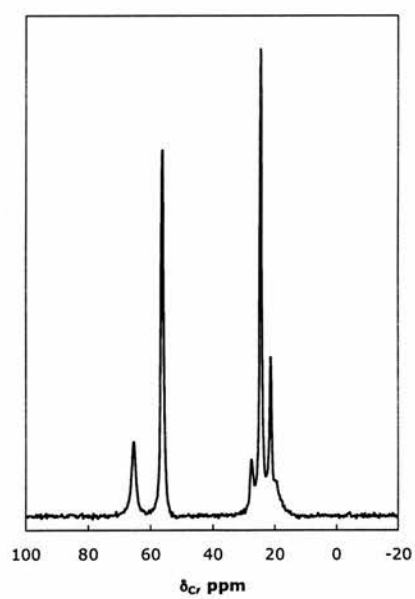
Figure 3.14: ^{27}Al MQMAS NMR spectrum of Mg-STA-2.

Figure 3.15: ^{31}P DPMAS NMR (a), and ^{31}P CPMAS NMR (b), of Mg-STA-2.Figure 3.16: ^{13}C DPMAS NMR spectrum of Mg-STA-2.

$a = 13.0245(5) \text{ \AA}$, $c = 29.598(1) \text{ \AA}$, $R_{wp} = 11.77\%$ and $R_p = 9.01\%$. In the calcined/dehydrated sample a similar approach was adopted to the refinement of the framework atoms. The final fit was $R_{wp} = 11.98\%$ and $R_p = 8.18\%$ ($a = 12.8974(4) \text{ \AA}$, $c = 30.784(1) \text{ \AA}$), see Figure 3.21.b. This equates to a 1.0% decrease in a , but a 4.0% increase in c (overall 2.0% increase in cell volume on calcination).

Similarly Rietveld refinement was carried out on as-prepared and calcined/dehydrated Mg-STA-2 prepared with Mg/P=0.15 and babop (Figures 3.19 and 3.20, respectively). The published unit cell and framework atomic coordinates [98] were used in the starting model as before. These were allowed to undergo constrained refinement. The babop template position had not been simulated and so the atomic coordinates of N, C(1), C(2), C(3), corresponding to the quinuclidine unit, were entered into the model and refined. This unit moved out in the c direction towards the ends of the cavity during refinement. Positions for carbon atoms in the methylene chain were found using difference Fourier maps at (0, 0, 0), (0, 0, 0.5) and (0, 0, 0.1), and refined. It was not possible, because of the disorder in the methylene chain, to determine more precise positions and so the carbon atoms remain linear in conformation (Figure 3.22.a). The final fit was $R_{wp} = 11.29\%$ and $R_p = 9.08\%$ with $a = 12.9819(6) \text{ \AA}$, $c = 30.931(2) \text{ \AA}$. The calcined/dehydrated Mg-STA-2 was refined in an analogous way to the aluminophosphate. The final fit was $R_{wp} = 6.71\%$ and $R_p = 4.70\%$, with $a = 12.826(1) \text{ \AA}$, $c = 30.769(3) \text{ \AA}$ (Figure 3.22.b). This equates to a 1.2% decrease in a and a 0.5% decrease in c (overall 2.9% decrease in cell volume) on calcination.

The atomic parameters and bond lengths and angles obtained during these refinements are given in Appendix B.

3.4 Discussion

STA-2 may be prepared as the aluminophosphate (even in the absence of fluoride) or as the metalloaluminophosphate, in the full range of compositions.

Figure 3.17: Rietveld refinement of X-ray powder diffraction profile of as-prepared $\text{AlPO}_4(\text{F})$ -STA-2, collected using $\text{Cu-K}\alpha_1$ X-rays at 293 K. STA-2 has space group symmetry $R\bar{3}$, with $a = 13.0245(5) \text{ \AA}$, $c = 29.598(1) \text{ \AA}$ ($R_{wp} = 11.77\%$ and $R_p = 9.01\%$). Babob template is included in positions calculated by molecular modelling, and is statistically disordered.

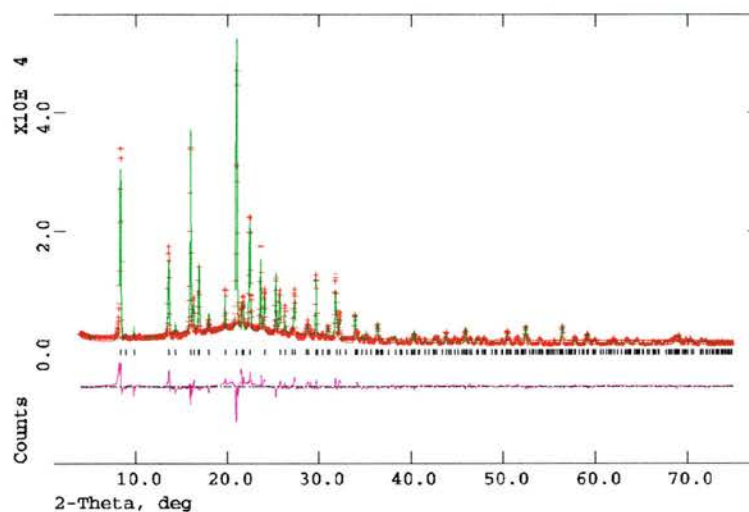


Figure 3.18: Rietveld refinement of X-ray powder diffraction profile of calcined/dehydrated $\text{AlPO}_4(\text{F})$ -STA-2, collected using $\text{Cu-K}\alpha_1$ X-rays at 293 K. STA-2 has space group symmetry $R\bar{3}$, with $a = 12.8974(4) \text{ \AA}$, $c = 30.784(1) \text{ \AA}$ ($R_{wp} = 11.98\%$ and $R_p = 8.18\%$).

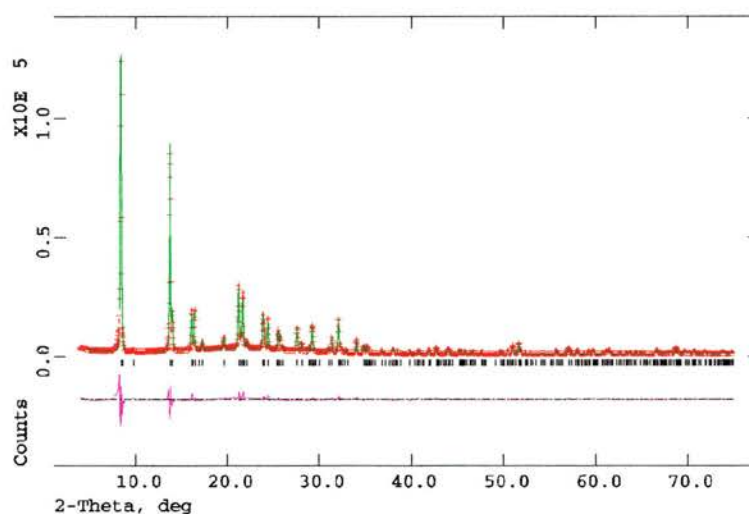


Figure 3.19: Rietveld refinement of X-ray powder diffraction profile of as-prepared Mg-STA-2, collected using Cu-K α_1 X-rays at 293 K. STA-2 has space group symmetry $R\bar{3}$, with $a = 12.9819(6)$ Å, $c = 30.931(2)$ Å ($R_{wp} = 11.29\%$ and $R_p = 9.08\%$). The likely location of the babop template was determined from difference Fourier maps.

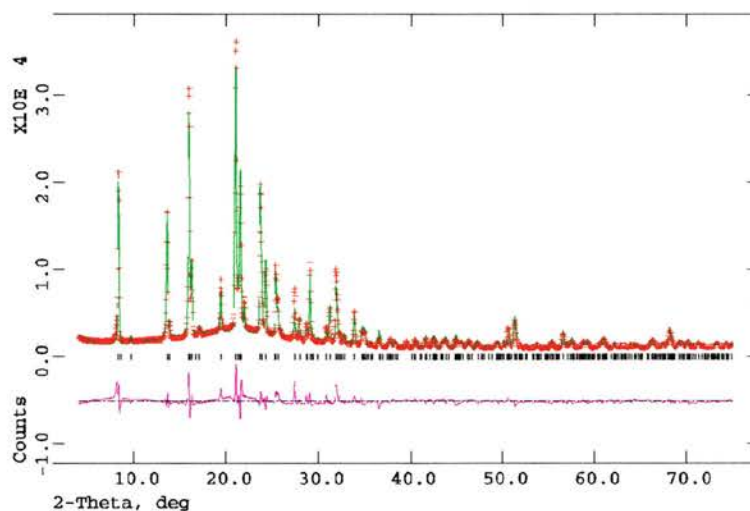


Figure 3.20: Rietveld refinement of X-ray powder diffraction profile of calcined/dehydrated Mg-STA-2, collected using Cu-K α_1 X-rays at 293 K. STA-2 has space group symmetry $R\bar{3}$, with $a = 12.826(1)$ Å, $c = 30.769(3)$ Å ($R_{wp} = 6.71\%$ and $R_p = 4.70\%$).

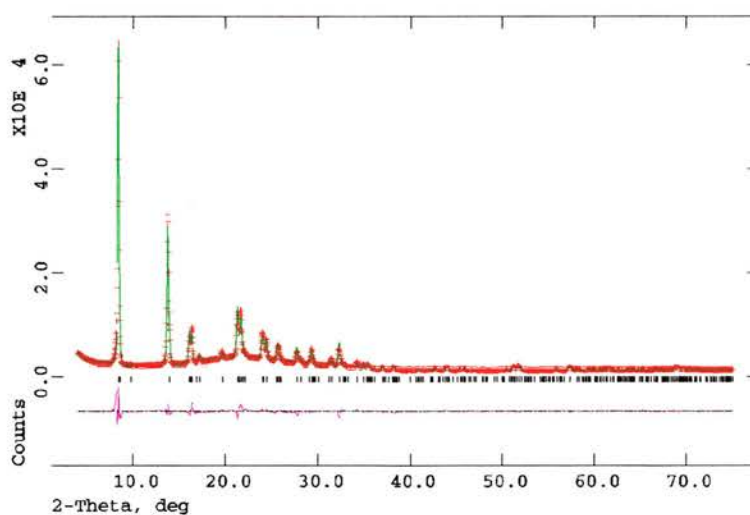


Figure 3.21: Illustrative diagrams showing the cavity (atomic coordinates from Rietveld refinements) in as-prepared (a), and calcined/dehydrated (b), $\text{AlPO}_4(\text{F})$ -STA-2.

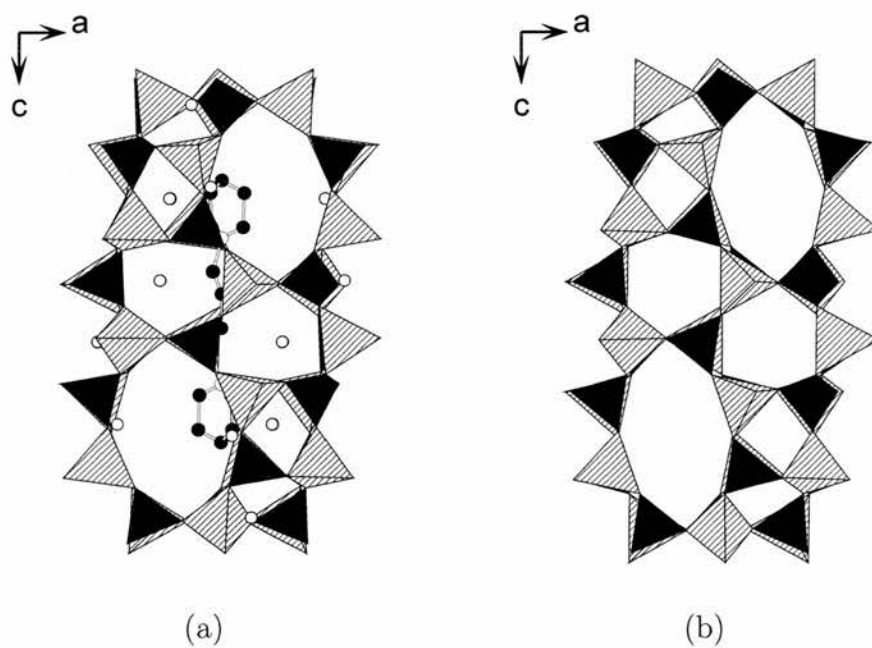
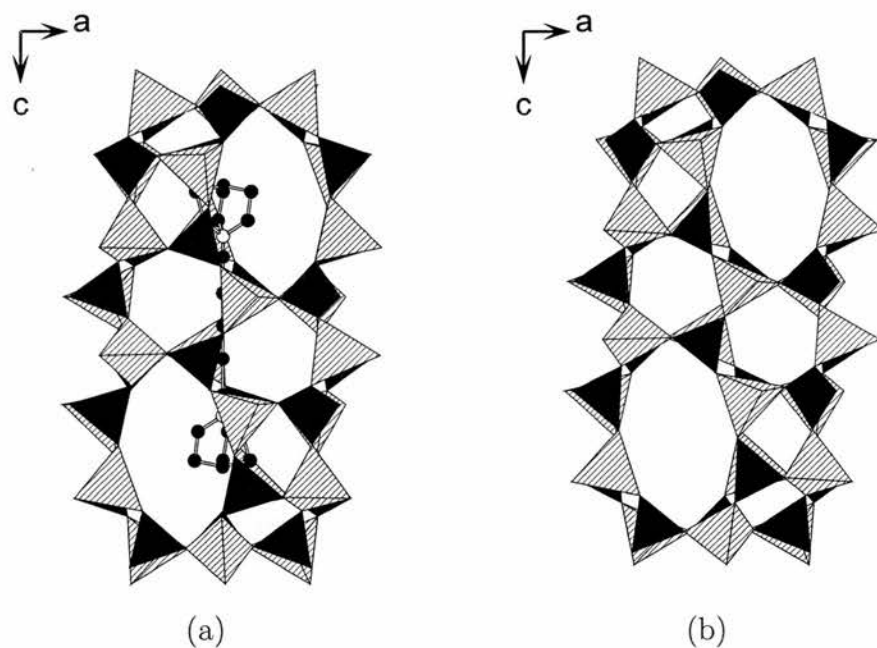


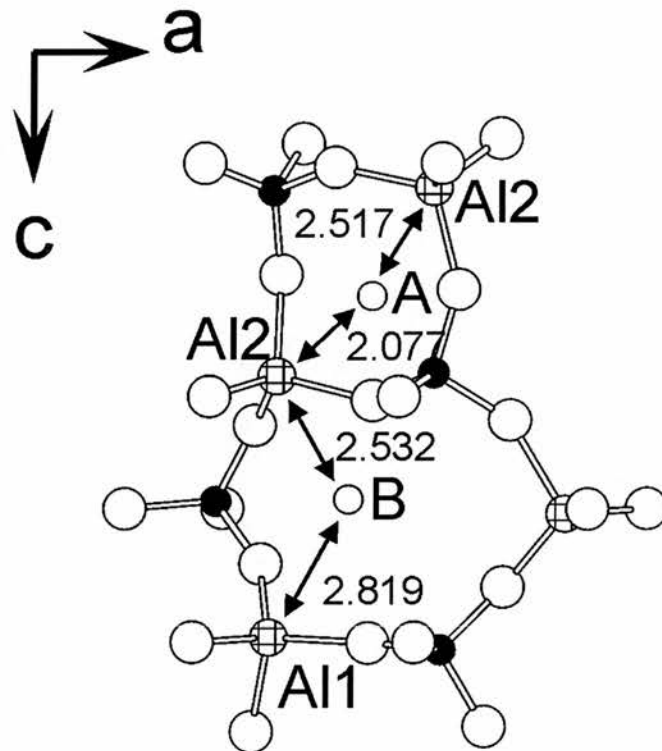
Figure 3.22: Illustrative diagrams showing the cavity (atomic coordinates from Rietveld refinements) in as-prepared (a), and calcined/dehydrated (b), Mg-STA-2.



The mechanism by which charge balance is maintained in the aluminophosphate form of STA-2 is by the incorporation of OH^- or F^- anions into the framework. However, X-ray diffraction alone cannot resolve the question of which species is present since each has the same electron density. [140] The AlPO_4 sample prepared without fluoride contains an impurity phase which also inhibits structural analysis by powder X-ray diffraction. NMR spectroscopy is able to deal more easily with additional phases, while their presence may be used to shed light on the crystallisation mechanism. In the AlPO_4 sample where fluoride is present, a 5-coordinate aluminium species is formed which can be unambiguously assigned by ^{27}Al NMR spectroscopy. [138] The multi-quantum spectrum clearly resolves the two tetrahedral Al sites within the framework also. The ^{31}P NMR spectrum indicates that phosphorus is coordinated tetrahedrally. But the shoulders present on each side of this peak may be indicative of further P environments, close to the fluoride and/or hydroxide present in the structure. X-ray diffraction and NMR spectroscopy do not indicate the presence of either crystalline or amorphous impurities in the $\text{AlPO}_4(\text{F})$ sample.

The ^{19}F NMR is complex, consisting of several broad peaks (δ_{F} -117.1 , -124.3 and -166.2 ppm) and spinning side bands, despite the very fast spinning rate (14.2 kHz). In $\text{AlPO}_4\text{-5}$, a peak at -120 ppm has been assigned variously to free F^- , fluoride balancing the template charge within the micropores, or, because of the short Al-F bond (2.19 Å), fluoride bridging two 4-ring units (see [138], and references therein). In $\text{AlPO}_4\text{-CJ2}$ peaks observed at -115 and -124 ppm were assigned by Taulelle *et al* [140] to bridged and terminal F^- respectively. In the work described here, difference Fourier maps generated during Rietveld refinement of the powder XRD data indicate two possible F^-/OH^- sites within the framework (Figure 3.23). The A site is within a 4-ring, on average 2.3 Å from each Al, which refined to an occupancy of $\frac{1}{7}$. This is in agreement with the work of Qiu *et al* (Al-F = 2.19 Å, occ. = $\frac{1}{6}$). [141] The other (B) site is within the cavity, 2.68 Å from a pair of Al atoms and 3.65 Å from a third. The occupancy refines to $\frac{1}{4}$. This would suggest the presence of F^- or OH^- bridging two Al atoms.

Figure 3.23: The two possible sites of fluoride and/or hydroxide anions, A and B, identified by difference Fourier maps of $\text{AlPO}_4(\text{F})$ -STA-2.



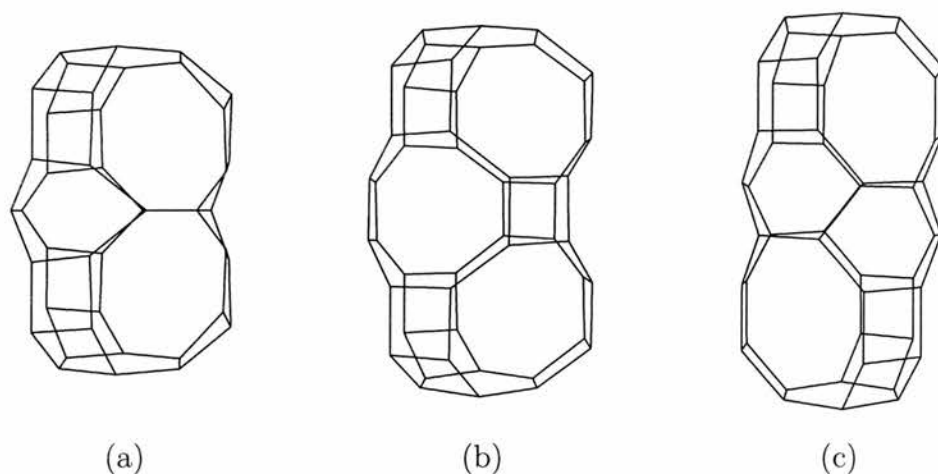
The XRD and NMR data does not permit an absolutely unambiguous determination of the species present which balance the charge on the template. It is hypothesised that much of this charge may be balanced by hydroxide species (since aluminophosphate STA-2 may be prepared without fluoride). In that case the most likely position would be the B site, closely associated with the template itself. In $\text{AlPO}_4(\text{F})$ -STA-2 it is likely, due to the low concentration of fluoride present, that the same mechanism occurs. Additionally F^- may be on the A site as well. However, this would require the 5-coordinate Al species observed be comprised of two unresolved species (and would not account for all the observed ^{19}F NMR signals). The presence of only one 5-coordinate site would support the A site as the location of F^- as this bridges Al(1) atoms whereas the B site bridges both Al(1) and Al(2).

In the Mg-STA-2 sample, Mg^{II} substituting for Al^{III} in the framework, is able to maintain charge neutrality with the template. The 5-coordinate Al species is no longer detectable by NMR indicating that Mg substitution has completely balanced the template charge (when $\text{Mg}/\text{P} = 0.15$). At higher or lower Mg/P ratios impurities phases are formed in addition to STA-2. ^{31}P NMR confirms that Mg substitutes exclusively for Al in this sample.

In each material ^{13}C MAS NMR spectroscopy showed the template moiety is occluded intact within the STA-2 framework. With babob as the template, the computer simulated minimum energy conformation within the cavity is known, [98] and including this in the structural model enabled a significant improvement in the Rietveld fit to be obtained during analysis of the powder XRD profile. Difference Fourier maps were able to help in determining the location of the babop molecule, where simulations had not been carried out.

The template may be removed from the cavities of $\text{AlPO}_4(\text{F})$ and MgAPO STA-2 without loss of structural integrity in the framework—essential if STA-2 is to be used as a catalyst. In the MgAPO this results in a decrease of 2.9% in the volume of the unit cell, in line with expectations. In the $\text{AlPO}_4(\text{F})$, however, the c axis lengthens by 4%, presumably as the 5-coordinate Al becomes tetrahedral, which results in an overall *increase* in the unit cell volume of 2.0%.

Figure 3.24: Comparison of cavities in aluminophosphates templated by α,ω -bis(1-azoniabicyclo[2.2.2]octane)alkyl cations. If the alkyl chain is propyl, butyl or pentyl structures crystallise with the AlPO_4 -17 (**ERI**) (a), AlPO_4 -56 (**AFX**) (b), and STA-2 (**SAT**) (c), frameworks, respectively. For clarity only the tetrahedral cations are represented in the diagram.



3.5 Conclusion

Most of the new framework types owe their origin to the inventive use of quaternary ammonium salts and amines as structure-directing agents, or templates. Often the cavities formed within the material follow the shape of the template; this is the case with STA-2 and the other members of the family of materials templated by α,ω -bis(1-azoniabicyclo[2.2.2]octane)alkyl cations (Figure 3.24). [98] Such bulk structural features are readily observed, but in doing so it is important not to overlook local structural details.

The preparation and characterisation of pure and metal-substituted STA-2 aluminophosphates has been investigated. STA-2 may be prepared as an AlPO_4 in the presence or absence of fluoride ions, or with varying levels of metal substitution. By combining the results of powder X-ray diffraction studies and solid state NMR spectroscopy a fuller understanding of the structure is obtained. The location of fluoride ions has been proposed from such studies in STA-2, a material not amenable to single crystal XRD studies. The mode of Mg-substitution in STA-2 has also been elucidated. STA-2 is shown to retain its structure on template removal.

Chapter 4

Structural chemistry of STA-6 and STA-7

4.1 Introduction

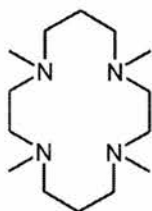
In this chapter the structural chemistry of two novel microporous solids, STA-6 and STA-7, is investigated. These were introduced in Chapter 2. Both materials are templated by 1,4,8,11-tetramethyl-1,4,8,11-tetraazacyclotetradecane, the phase which forms being dependent upon the metal cation present in the MAPO gel during crystallisation. In this chapter in-depth characterisation of the novel STA-7 phase is presented.

4.2 Experimental

4.2.1 Synthesis

Metalloaluminophosphate materials were synthesised in a variety of compositions as described previously (page 65). The template 1,4,8,11-tetramethyl-1,4,8,11-tetraazacyclotetradecane (tmtact) was employed (Figure 4.1). Tm-tact was obtained from Aldrich (97%) or prepared according to a literature method [142] by permethylating cyclam.

Figure 4.1: STA-6 and STA-7 crystallise in the presence of 1,4,8,11-tetra-methyl-1,4,8,11-tetraazacyclotetradecane (tmtact).



4.2.2 Chemical analysis

Chemical analysis were carried out as described in Chapter 2, page 69.

4.2.3 Crystallography

Crystallography was carried out as described in Chapter 2, page 67. Briefly, X-ray powder diffraction patterns of all products were collected on one of two Philips X'Pert System diffractometers for phase identification. For structural analysis samples were analysed in capillaries on Stoe STADIP diffractometers operating in transmission mode with primary monochromation and Cu-K α_1 or Fe-K α_1 X-radiation. Data obtained on the Fe-K α_1 diffractometer were collected by Dr A. D. Robertson (St Andrews). Alternatively, a similar powder diffractometer at Station 9.1 of the Synchrotron Radiation Source, CCLRC Daresbury Laboratory was used (with assistance from Dr M. Roberts) with monochromated synchrotron radiation ($\lambda = 0.99555(1)$ Å). With CoAPO materials the use of Fe-K α_1 X-rays or synchrotron radiation circumvents problems with fluorescence. Single crystal data were collected in St Andrews on either a three-circle (fixed κ) Bruker or Rigaku diffractometer each fitted with a CCD detector but equipped with Mo-K α or Cu-K α X-radiation, respectively. A Bruker diffractometer was also used (with the assistance of Dr S. Teat) at Station 9.8 of the SRS ($\lambda = 0.68840(1)$). Structures were solved by Drs P. Lightfoot or A. M. Z. Slawin, as before.

Bulk microcrystalline samples of as-prepared Mn-STA-6, Fe-STA-6 and Co-STA-7 were examined by room temperature powder diffraction at the

SRS. Similarly, samples of Ni-STA-6 and Zn-STA-7 were analysed on the Stoe diffractometer with Cu-K α_1 X-rays. The powder profiles were refined (except for Fe-STA-6) using the Rietveld method. The atomic coordinates derived from single crystal diffraction for STA-6, [103] and at room temperature for STA-7 (see below), were used as starting models. Template positions derived from modelling studies (see below) were input with large temperature factors ($U = 0.3$) and the templates permitted to exhibit statistical disorder over symmetrically equivalent positions. The fractional occupancy of the template was refined within experimentally reasonable limits. The fractional coordinates of the framework were also allowed to undergo constrained refinement.

During the course of this work Co-STA-6 was prepared with 4,11-dimethyl-1,4,8,11-tetraazabicyclo[6.6.2]hexadecane (dmtabch) by Dr T. D. Coombs (St Andrews). A sample was obtained for analysis on the Stoe diffractometer equipped with Fe-K α_1 radiation. A portion was calcined and dehydrated as before (page 65) and examined with XRD also.

4.2.4 NMR spectroscopy

To investigate short range structure in the materials MAS NMR spectroscopy was performed at the EPSRC solid state NMR Facility in Durham on a Varian UNITY*Inova* spectrometer at ambient temperature in a similar way to that previously described (page 69).

To determine whether the template is incorporated intact in STA-7 ^{13}C CPMAS NMR was carried out and the resulting spectrum compared with the one obtained previously for Mg-STA-6. [103] Data were collected (for Zn-STA-7) with a Doty Scientific MAS probe with 7 mm o.d. rotors. The frequency was 75.430 MHz and an acquisition time of 40.0 ms, relaxation delay of 1.0 s, CP contact time of 1.0 ms and spin rate of 4.23 kHz were used. The shift reference sample was $(\text{CH}_3)_4\text{Si}$.

4.2.5 Molecular modelling

Molecular modelling calculations (Monte Carlo docking and subsequent Simulated Annealing) were kindly supplied by Dr P. A. Cox of the University of Portsmouth, as before (page 70). The *pH* of synthesis (*ca* 7) favours the dicationic form of the template, and literature suggests the most stable form would be that with the two protons on alternating nitrogens in the ring system, [143, 144] so this dication was used in the modelling. In order to ensure charge neutrality in the calculation, an additional charge of 2⁻ was distributed evenly across the anionic component of the framework. The cations were assigned half their formal charge. Periodic boundary conditions were applied and the framework atoms were held fixed at their experimental positions. The energy and conformation of the template within the pore structure was determined using a Simulated Annealing method in which the template was heated for 1000 time steps of 1×10^{-15} s at 750, 600, 450, 300 and finally 200 K prior to energy minimisation. Calculations were performed using the Constant Valence Forcefield within the program Discover. [119] It was assumed that short-range interactions between the framework and the template will be dominated by the larger oxygen ions and so short range interaction terms between the cations and the template were omitted.

4.2.6 Electron microscopy

Scanning electron micrographs were collected on a Jeol JSM 5600 SEM in St Andrews. Samples of Si-STA-6, Mg-STA-6 and Co-STA-7 were sent to Prof. O. Terasaki at Tohoku University, Japan for examination by transmission electron microscopy.

4.3 Results

4.3.1 Synthesis

Tmtact was successfully prepared and the ¹³C NMR spectra found to be: δ_C (75.440 MHz; CDCl₃) 54.63 (NCH₂CH₂N), 54.46 (NCH₂CH₂CH₂N), 43.96

Table 4.1: Selected gel compositions used in this work with tmtact. The product phases obtained from X-ray diffractometry after the hydrothermal treatment of these gels is reported with inorganic chemical analysis of selected materials.

Inorganic cation ratio in synthesis gel	Principal product (by XRD)	Inorganic composition (by ICP–AES)
1.0Al : 1.0P	AlPO ₄ -21	
0.2Mg : 0.8Al : 1.0P	Mg–STA-6	Mg _{0.2} Al _{0.8} PO ₄
0.2Sc : 0.8Al : 1.0P	amorphous	
0.2Ti : 0.8Al : 1.0P	AlPO ₄ -21	
0.2Cr : 0.8Al : 1.0P	AlPO ₄ -21	
0.2Mn : 0.8Al : 1.0P	Mn–STA-6	Mn _{0.2} Al _{0.8} PO ₄
0.2Fe : 0.8Al : 1.0P	Fe–STA-6 ¹	
0.2Co : 0.8Al : 1.0P	Co–STA-7	Co _{0.2} Al _{0.8} PO ₄
0.2Ni : 0.8Al : 1.0P	AlPO ₄ -21, Ni–STA-6 ²	
0.2Cu : 0.8Al : 1.0P	AlPO ₄ -21	
0.2Zn : 0.8Al : 1.0P	Zn–STA-7	Zn _{0.2} Al _{0.8} PO ₄

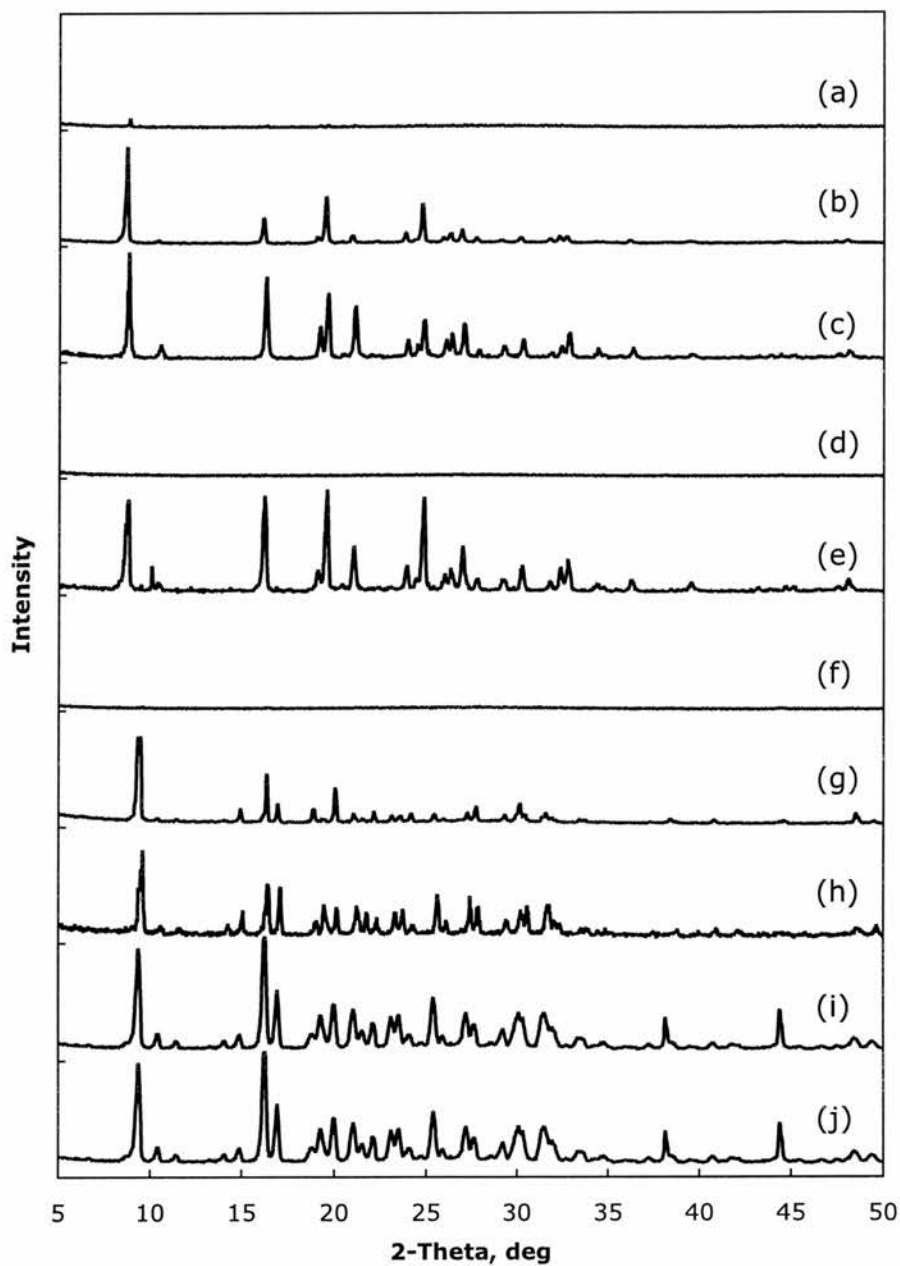
¹ A very few crystals of Fe–STA-7 also form.
² Approximately 60/40 mixture

(CH₃N), 25.03 (NCH₂CH₂CH₂N). No signals were found that could not be accounted for; this was taken to indicate a high degree of purity.

The results of selected syntheses with tmtact are given again (from Chapter 2) in Table 4.1. To investigate further the conditions of synthesis preparations were carried out at different crystallisation temperatures (Figure 4.2). Crystalline products were obtained with Mn^{II}, Fe^{II}, Co^{II} and Zn^{II} cations in the gels crystallised at 190 °C in 48 h. However, at a lower temperature (160 °C) the products obtained were all amorphous after 48 h, except for the Zn-containing preparation which yielded phase pure Zn–STA-7. Heating for longer (168 h) at 160 °C enabled crystalline products to be obtained in all cases.

The crystallisation process was studied as a function of time in a series of MgAPO, CoAPO and ZnAPO gels crystallised at 190 °C. The powder XRD

Figure 4.2: Powder X-ray diffraction patterns of solids crystallised from metalloaluminophosphates gels containing tmtact at varying temperatures. $M = \text{Mn}^{\text{II}}$, 48 h, 160 °C (a), Mn^{II} , 168 h, 160 °C (b), Mn^{II} , 48 h, 190 °C (c), Fe^{II} , 48 h, 160 °C (d), Fe^{II} , 48 h, 190 °C (e), Co^{II} , 48 h, 160 °C (f), Co^{II} , 168 h, 160 °C (g), Co^{II} , 48 h, 190 °C (h), Zn^{II} , 48 h, 160 °C (i), Zn^{II} , 48 h, 190 °C (j).



patterns of solid products (if any) obtained are shown in Figure 4.3. After 48 h all products are fully crystallised (see Figure 2.13, page 72). After 12 h and 4 h respectively, Mg–STA-6 and Zn–STA-7 are well crystallised (Figure 4.3.a and Figure 4.3.g). In the CoAPO gel Al_2O_3 is present, undissolved, after 2 h but this completely dissolves (no solid product was recovered) after 4 h. Monitoring Co–STA-7 crystallisation by XRD is difficult because a large amorphous component is always present, nevertheless Bragg peaks consistent with STA-7 are discernible after 20 h (Figure 4.3). An *in situ* powder X-ray diffraction/EXAFS spectroscopy experiment at Station 8.1 of the Daresbury SRS was performed in collaboration with Dr G. Sankar (Royal Institution) to monitor the location of Co or Zn cations during the crystallisation. However, crystallisation in the synchrotron beam proved to be unsuccessful on that occasion.

Work by Drs T. D. Coombs and V. Patinec (St Andrews) has shown that STA-6 and STA-7 may also be prepared with 4,11-dimethyl-1,4,8,11-tetraazabicyclo[6.6.2]hexadecane (dmtabch) and 1,4,7,10,13,16-hexamethyl-1,4,7,10,13,16-hexaazacyclooctadecane (hnhaco), respectively (Figure 4.4). Co–STA-6 may be prepared with the former and Co–STA-7 with the latter. If magnesium is included in gels with hnhaco MgAPO-36 forms as the major phase with Mg–STA-7 as a secondary component. [145]

4.3.2 Crystallography

The structure of STA-6 is known [103] and is elegant in its simplicity (Figure 4.5). It is constructed from chains of face-sharing double 6-rings, each one of which is rotated by 90° around the direction of the chain (the c axis) with respect to adjacent double 6-rings (Figure 4.6.a). Each of these chains links to four others *via* Al–O–P bonds perpendicular to the c axis. This results in the formation of a novel cavity (Figure 4.6.b), slightly smaller than an α -cavity, and 1-D 8-ring (4.2 \AA) pores parallel to the c axis.

In contrast to STA-6, the structure of AlPO_4 -21 is complex. The framework contains PO_4 tetrahedra and Al in tetrahedral (AlO_4) and distorted trigonal-bipyramidal (AlO_4OH) coordination. The pore system is 3-dimensional and

Figure 4.3: Powder X-ray diffraction patterns of the total solid product, from metalloaluminophosphate gels, containing tmtact after varying times (190 °C). M = Mg^{II}, 12 h (a), Co^{II}, 2 h (b), Co^{II}, 15 h (c), Co^{II}, 18 h (d), Co^{II}, 20 h (e), Co^{II}, 24 h (f), Zn^{II}, 4 h (g), Zn^{II}, 25 h (h).

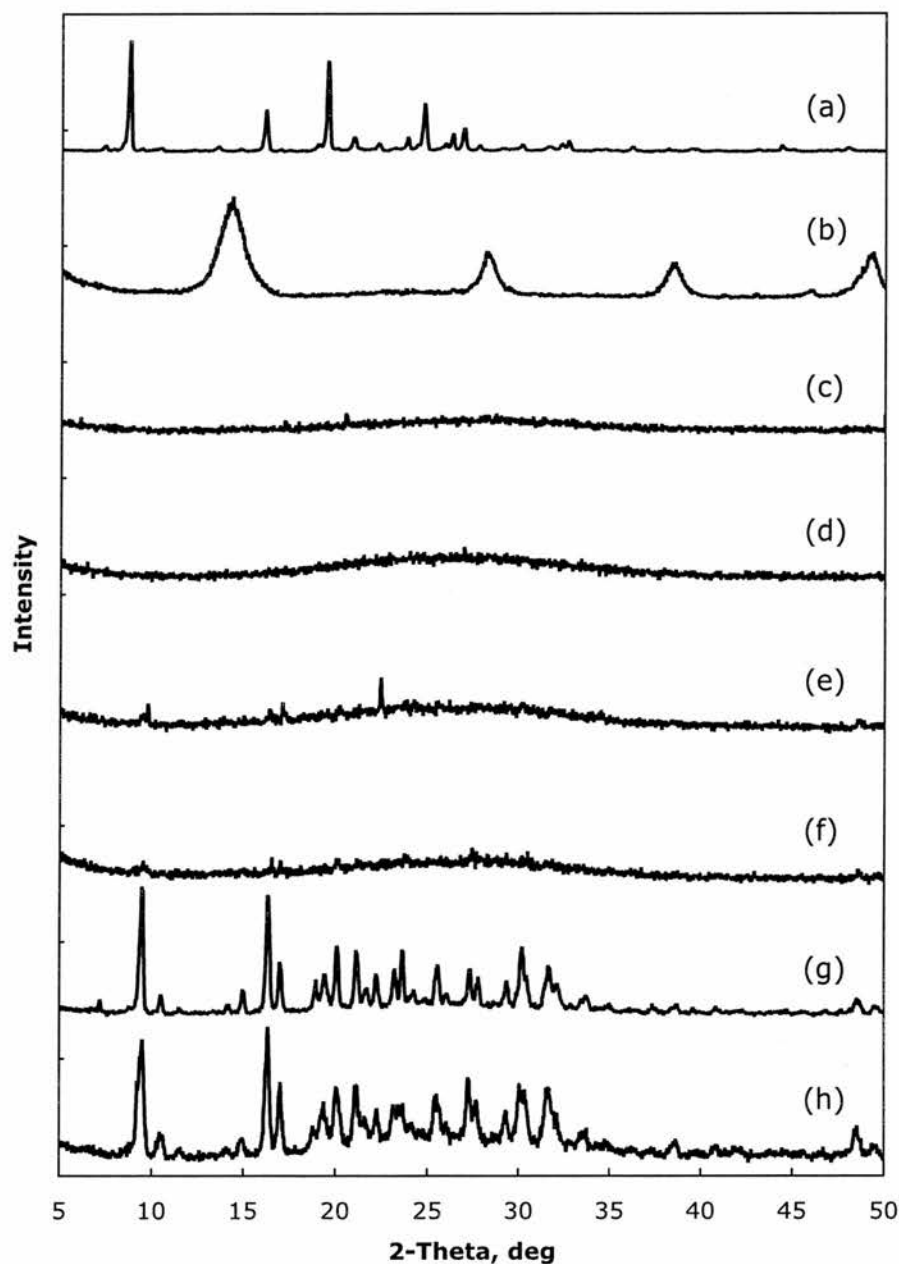
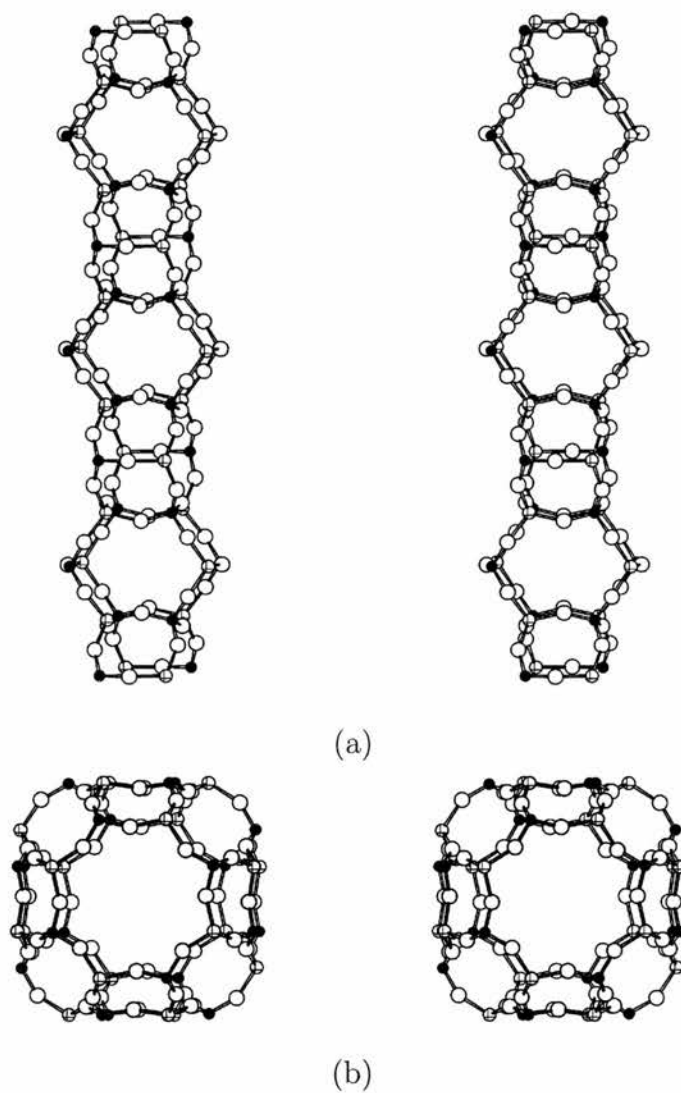


Figure 4.6: Illustrative stereoviews of the STA-6 framework, with Al as hatched spheres, P as black spheres and O as white spheres. Stereoviews showing the chains of double 6-rings that run parallel to the c axis (a), and the novel cavity (b).



defined by 8-rings (Figure 4.7.a), while the framework itself contains double-crankshaft chains (Figure 4.7.b) which are cross-linked to form a complex 2-D net in the *ab* plane of the unit cell. Within the pores dimethylammonium ions are located. A fuller structural description can be found in the paper by Smith *et al.* [146]

The structure of Co-STA-7¹ and Zn-STA-7² was solved by Dr A. M. Z. Slawin from data collected on diffractometers at St Andrews and the SRS, respectively.

In both cases the basic STA-7 framework structure was solved using the SHELXS package and refined fully anisotropically in *P4/n* using SHELXL. [147] It was not possible to identify template molecules unambiguously from the difference Fourier syntheses, because they will necessarily be disordered, as the symmetry of the template is lower than that of the framework. For tmtact templates, where modelling using the diprotonated cations had been carried out (see below), modelled positions for the carbons and nitrogens of the template were used to account for extra-framework scattering. In the space group *P4/n* the Al sites (which contain aluminium plus the divalent metal) and the P sites, are able to achieve full ordering. The difference in bond lengths between the two kinds of site is clear for all structures. For the Zn-STA-7 sample the “Al” sites have an average Al–O bond length of 1.77(2) Å and the P sites have a mean bond length of 1.515(7) Å. For the Co-STA-7 there appears to be less ordering (bond lengths of 1.67(2) Å for “Al”–O and 1.61(2) Å for P–O) which may indicate that there are domains within the crystal with different ordering arrangements.

The structure of STA-7 is fully tetrahedrally-coordinated and can best be considered as having a pore structure made up of cavities. The *c* axis projection (Figure 4.8) shows the arrangement of two distinct channel systems

¹Co-STA-7. |(C₁₄H₃₄N₄)_{2.3} (H₂O)₉| [Co_{4.8}Al_{19.2}P₂₄O₉₆], *M* = 440.17, tetragonal, *a* = 18.740(5) Å, *c* = 9.439(7) Å, *V* = 3315(3) Å³, *T* = 293(2) K, space group *P4/n* (no. 85), *Z* = 8, $\mu(\text{Cu-K}\alpha)$ = 11.75 mm⁻¹, 2642 reflections measured, 2472 unique of which 1311 were observed. The final *R*(obs) was 0.1169 with *wR*(*F*²) = 0.3134.

²Zn-STA-7. |(C₁₄H₃₄N₄)_{2.6} (H₂O)₁₀| [Zn_{4.8}Al_{19.2}P₂₄O₉₆], *M* = 429.95, tetragonal, *a* = 18.691(2) Å, *c* = 9.423(1) Å, *V* = 3292.0(6) Å³, *T* = 150(2) K, space group *P4/n* (no. 85), *Z* = 8, $\mu(0.68840)$ = 1.394 mm⁻¹, 23263 reflections measured, 4743 unique of which 3851 were observed. The final *R*(obs) was 0.0912 with *wR*(*F*²) = 0.2203.

Figure 4.7: Illustrative diagrams of the AlPO_4 -21 (**AWO**) framework showing Al and P as hatched and black tetrahedra, respectively. Al is also found in trigonal-bipyramidal coordination (white polyhedra). The framework contains 8-ring channels (a) and can be thought to be constructed from chains (b).

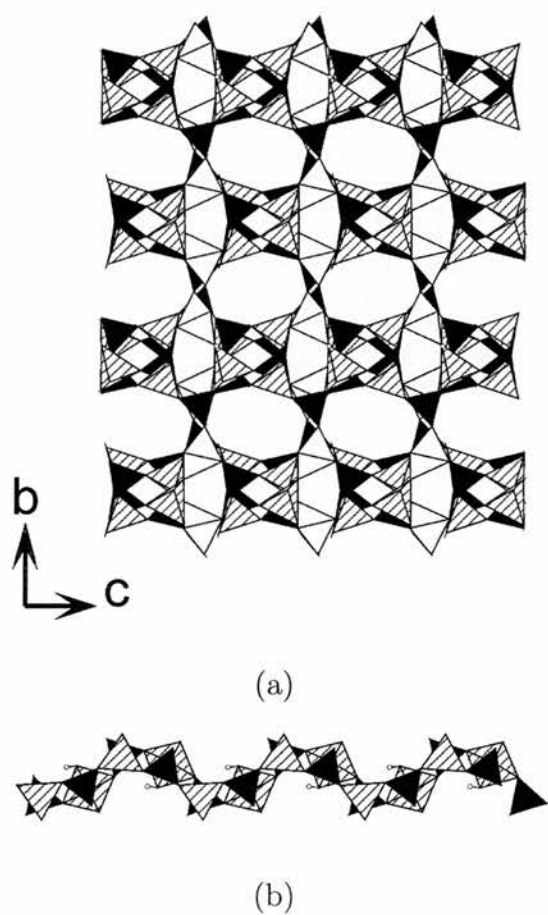
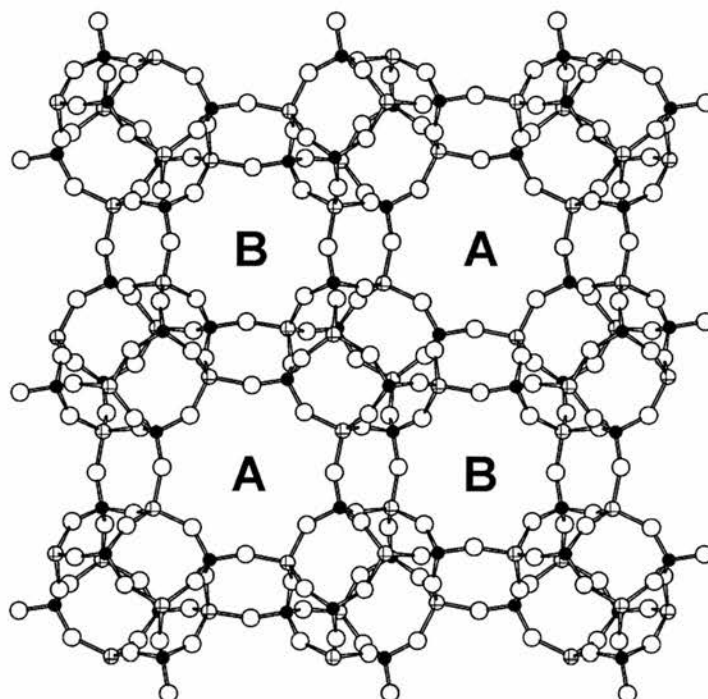


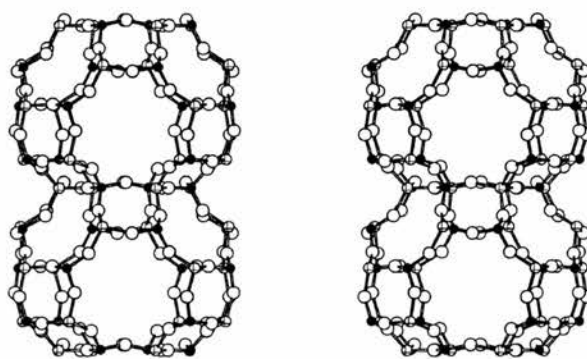
Figure 4.8: Illustrative diagram of the STA-7 framework, with Al as hatched spheres, P as black spheres and O as white spheres. Projected down the c axis the presence of two distinct pore systems, A and B, is revealed.



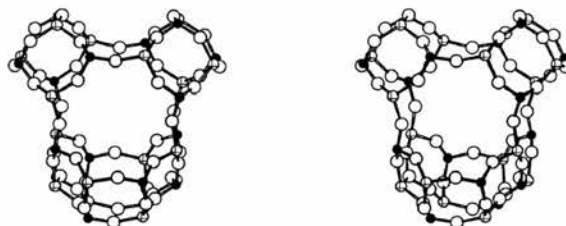
(denoted A and B), each constrained by rings containing eight tetrahedral cations and eight oxygens (8-rings). The A channels are composed of cavities, linked *via* planar 8-rings (3.9 Å in free diameter), stacked along c as shown in Figure 4.9.a. The cavities also possess four elliptical 8-ring openings to the B channel system, each opening having dimensions of 4.3×3.7 Å. The B channels (Figure 4.9.b) are connected along c *via* 8-ring windows 3.5 Å in free diameter and to the A channel system *via* the elliptical 8-rings. The framework itself may be described as being made up of chains of double 6-rings (hexagonal prisms) linked along c by single 4-rings and linked to each other by Al–O–P bonds (Figure 4.9.c).

To confirm that the single crystals of Co- and Zn-STA-7 were representative of the as-prepared bulk samples, powder diffraction profiles collected

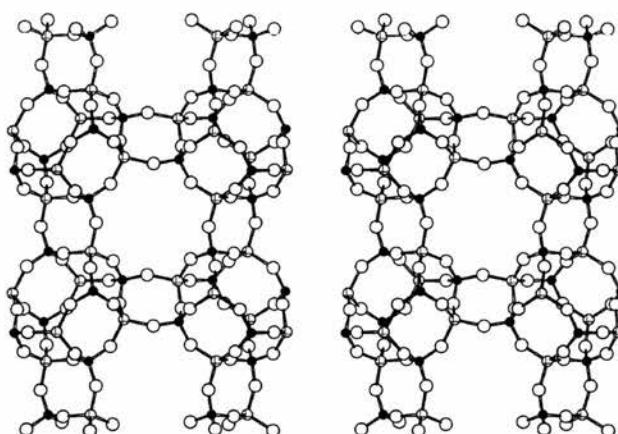
Figure 4.9: Illustrative stereoviews of the STA-7 framework, with Al as hatched spheres, P as black spheres and O as white spheres. The A channel system is made up of cavities linked along c through 8-rings (a), whereas the B system is made up of smaller interconnecting spaces, (b). The framework can be considered as sheets made up of double 6-rings linked parallel to c by 4-rings (c).



(a)

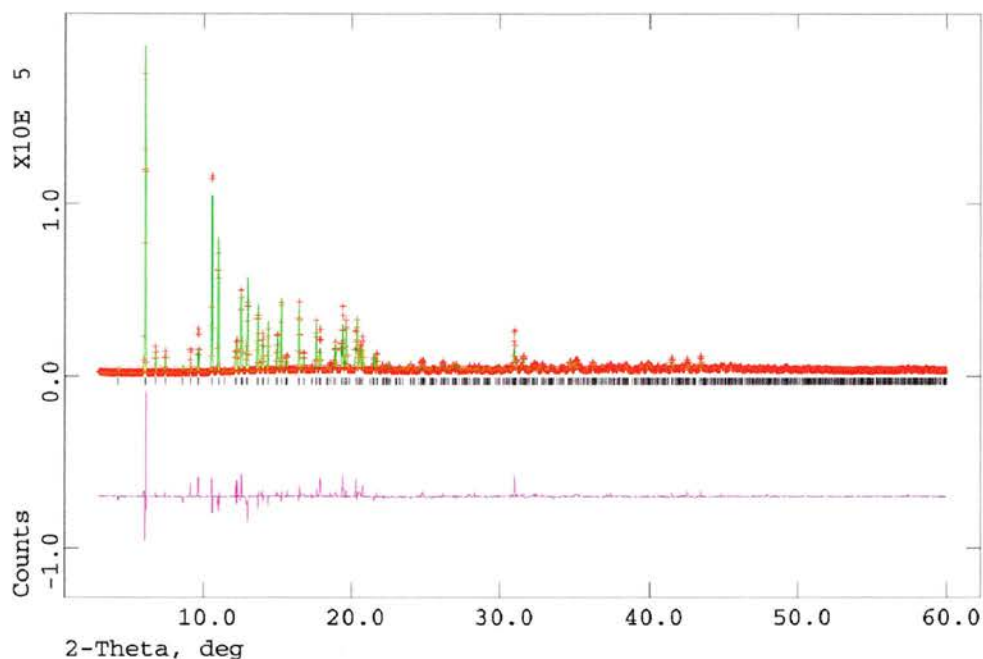


(b)



(c)

Figure 4.10: Rietveld refinement of X-ray powder diffraction profile of Co-STA-7, collected using synchrotron X-rays ($\lambda = 0.99555(1) \text{ \AA}$) at 293 K. Co-STA-7 has space group symmetry $P4/n$, with $a = 18.6401(5) \text{ \AA}$, $c = 9.3757(3) \text{ \AA}$ ($R_{wp} = 15.99\%$ and $R_p = 11.33\%$). Tmtact is included in positions calculated by molecular modelling, and statistically disordered.



in capillary mode using the SRS or Stoe diffractometers were matched using the Rietveld refinement method within the GSAS suite of programs. [32] The profile of the Zn- and Co-STA-7 samples prepared with tmtact were fitted satisfactorily using the single crystal framework structure of STA-7 at 293 K with a disordered template in the modelled position as a starting point, and allowing the framework atom positions to vary within tight constraints. A reasonable final fit (Co-STA-7, $R_{wp} = 15.99\%$, $R_p = 11.33\%$, Zn-STA-7, $R_{wp} = 16.26\%$, $R_p = 12.19\%$) indicated that no diffraction peaks extra to those from the STA-7 were present, and confirmed the bulk samples are phase pure (Figure 4.10). Unit cell parameters of $a = 18.640(2) \text{ \AA}$ and $c = 9.3755(7) \text{ \AA}$ were obtained for the Co-STA-7 and $a = 18.709(2) \text{ \AA}$ and $c = 9.428(1) \text{ \AA}$ for the Zn-STA-7.

Similarly for Mn-STA-6 the structure was refined in space group $P4/mnc$

Figure 4.11: Rietveld refinement of X-ray powder diffraction profile of Zn-STA-7, collected using Cu-K α_1 X-rays at 293 K. Zn-STA-7 has space group symmetry $P4/n$, with $a = 18.709(1)$ Å and $c = 9.428(1)$ Å ($R_{wp} = 16.26\%$ and $R_p = 12.19\%$). Tmtact is included in positions calculated by molecular modelling, and statistically disordered.

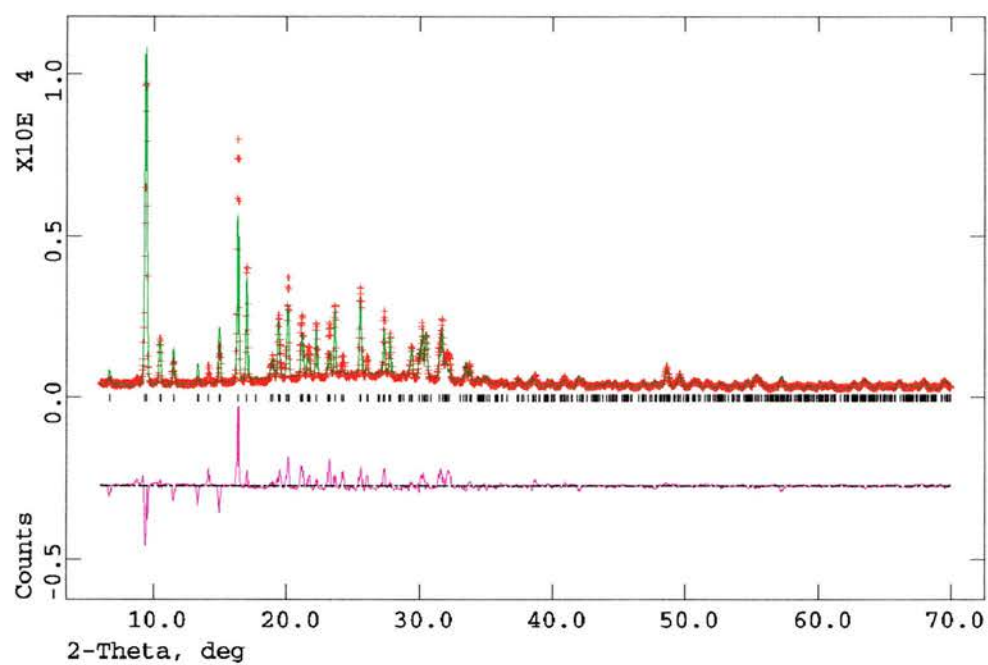
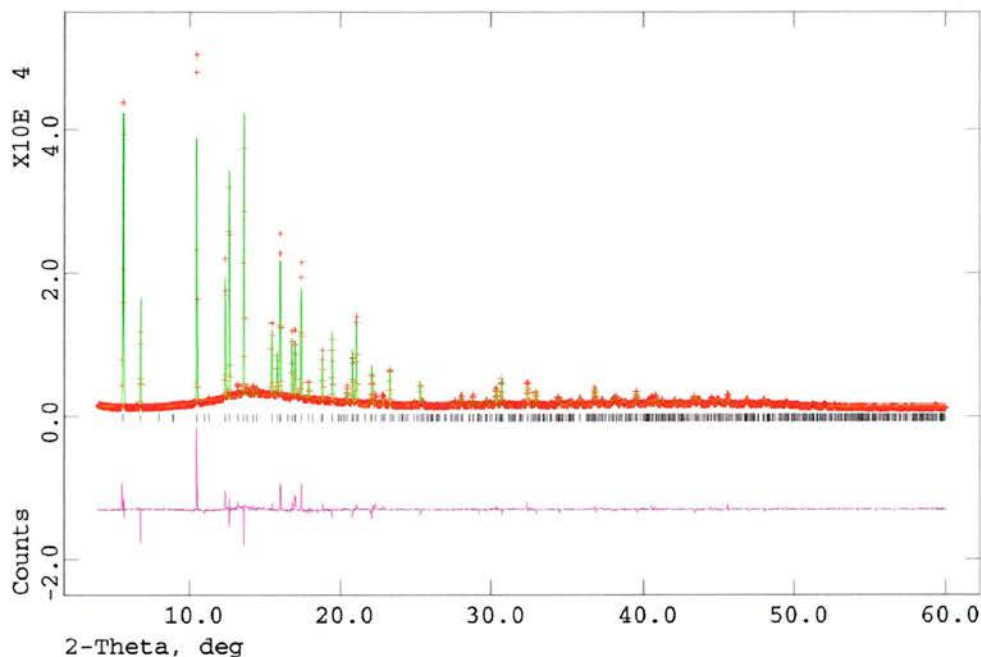


Figure 4.12: Rietveld refinement of X-ray powder diffraction profile of Mn-STA-6, collected using synchrotron X-rays ($\lambda = 0.99555(1) \text{ \AA}$) at 293 K. Mn-STA-6 has space group symmetry $P4/mnc$, with $a = 14.2727(3) \text{ \AA}$, $c = 10.3749(2) \text{ \AA}$ ($R_{wp} = 9.43\%$ and $R_p = 6.61\%$). Tm_{tact} is included in the model in positions calculated by molecular modelling, statistically disordered.



($a = 14.2727(3) \text{ \AA}$, $c = 10.3749(2) \text{ \AA}$) with final goodness of fit indices of $R_{wp} = 9.43\%$, $R_p = 6.61\%$ (Figure 4.11).

Crystals of Ni-STA-6 were obtained that were of excellent quality (by polarizing optical microscopy) but were too small for data to be collected on the laboratory diffractometer in St Andrews. Instead a sonicated fraction containing *ca* 90% Ni-STA-6 and 10% $\text{AlPO}_4\text{-21}$ was Rietveld refined (Figure 4.13). The fit ($R_{wp} = 18.30\%$ and $R_p = 13.27\%$) is poor. There are reflections present in the data that are not accounted for by the Ni-STA-6/ $\text{AlPO}_4\text{-21}$ model. Most of the difference in intensity, between the data and the model, may be accounted for by an incomplete model of the template. Because of this it was not possible to determine whether nickel is present in the macrocycle

by powder diffraction. A Ni atom positioned at the centre of the STA-6 cavity (0, 0, 0.5) refined to an occupancy of 2.67, even with $U = 0.3$. To confirm the location of the Ni EXAFS spectroscopy was performed on a sample of Ni-STA-6 at Station 7.1 of the Daresbury SRS. Plots of experimental and theoretical EXAFS are given in Figure 4.14 with fit parameters (and further experimental details) in Table 4.2. The data was refined by Miss R. García (St Andrews) with a model of the complex developed from that of a $[\text{Cu}(\text{cyclam})]^{2+}$ complex. [148] It was assumed that the principal differences would be in the M-N, rather than the M-C, distances, so the same number of shells was used for the model. The fit is sufficiently good ($R = 29.74\%$) to confirm the presence of a Ni-tmtact complex within the pores of STA-6. The Ni-N distance of *ca* 1.9 Å is indicative [149] of a tetrahedral low spin Ni^{II} complex (not a high spin octahedral complex, where Ni-N would be *ca* 2.1 Å), although a 5-coordinate complex could not be discounted absolutely. Crystals of $\text{AlPO}_4\text{-21}$ were of less high quality than those of STA-6, but their larger size meant a structure solution was obtainable in St Andrews.³ The structure was solved in monoclinic space group $P2_1/n$, $a = 8.668(2)$ Å, $b = 17.424(4)$ Å, $c = 9.135(2)$ Å, $\beta = 109.59(3)^\circ$. It was not possible, however, to show unambiguously that the Ni was present in the framework.

4.3.3 NMR spectroscopy

To determine whether STA-7 contains tmtact occluded intact, ^{13}C CP MAS NMR was performed on a sample of Zn-STA-7. The spectrum obtained previously [103] for Mg-STA-6 (Figure 4.15.a) shows signals at δ_{C} 62.8, 54.5, 43.5, 20.8 ppm that are also seen in STA-7 (δ_{C} 60.4, 54.5, 43.1, 20.9 ppm, Figure 4.15.b) and are consistent with tmtact. However, in STA-7, signals are also observed at δ_{C} 35.0, 33.0, 23.0, 11.1 ppm suggesting some tmtact has broken down and the fragments have been occluded also (presumably in the smaller B cavities).

³ $\text{AlPO}_4\text{-21}$. $[\text{Al}_{12}\text{P}_{12}\text{O}_{48}]$, $M = 596.07$, monoclinic, $a = 8.668(2)$ Å, $b = 17.424(4)$ Å, $c = 9.135(2)$ Å, $\beta = 109.59(3)^\circ$, $V = 1299.9(4)$ Å³, $T = 293(2)$ K, space group $P2_1/n$ (no. 14), $Z = 2$, $\mu(\text{Mo-K}\alpha) = 0.964$ mm⁻¹, 5102 reflections measured, 2076 unique of which 935 were observed. The final $R(\text{obs})$ was 0.1613 with $wR(F^2) = 0.3047$.

Figure 4.13: Rietveld refinement of X-ray powder diffraction profile of Ni-STA-6 (with $\text{AlPO}_4\text{-21}$ impurity), collected using $\text{Cu-K}\alpha_1$ X-rays at 293 K. Ni-STA-6 has space group symmetry $P4/mnc$, with $a = 14.333(6)$ Å, $c = 10.236(5)$ Å ($R_{wp} = 18.30\%$ and $R_p = 13.27\%$). Tmtact is included in the model in positions calculated by molecular modelling, statistically disordered.

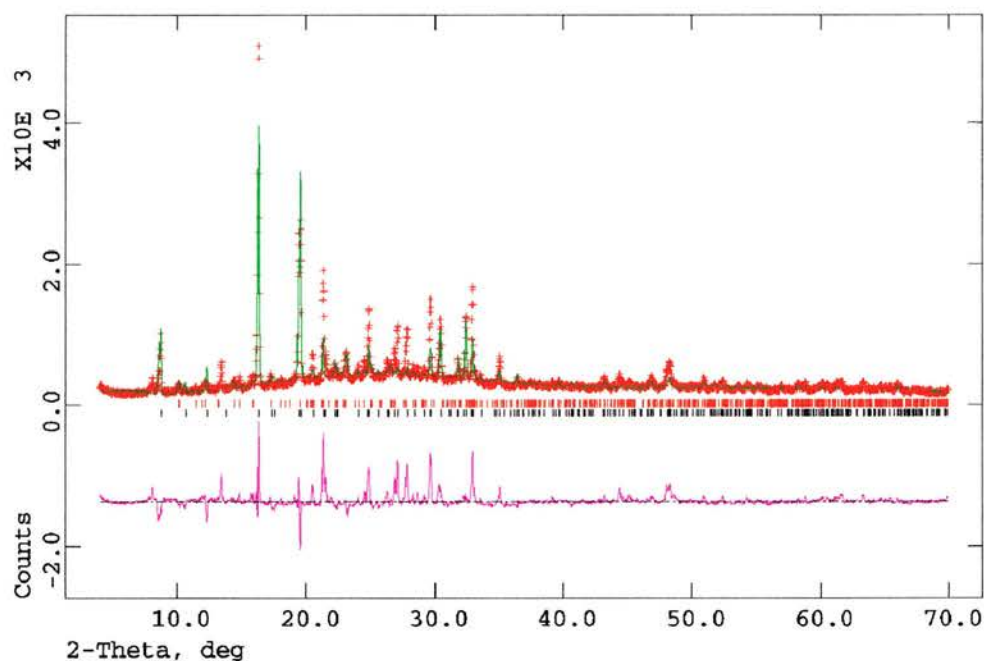


Figure 4.14: Experimental (solid line) and theoretical (dashed line) of Ni K-edge EXAFS (above) and their Fourier transforms (below) for Ni-STA-6. Data were collected and processed by Miss R. García (St Andrews) using the *EXCALIB* (raw data processing), *EXBROOK* (background subtraction) and *EXCURV98* (comparing theoretical and experimental EXAFS) programs. [150]

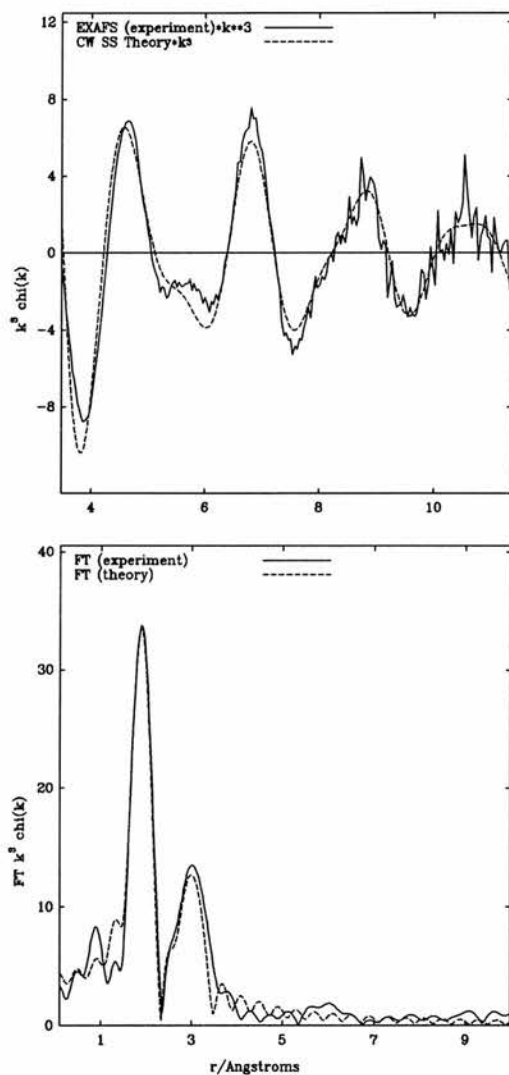


Table 4.2: Fit parameters of EXAFS data for Ni-STA-6. Data were collected at room temperature in transmission mode on Station 7.1 of the Daresbury SRS. Wavelength selection was accomplished using a double Si(111) monochromator set at 50% harmonic rejection. The Ni edge position was determined using nickel foil. The Ni-STA-6 sample was mounted as a self-supporting wafer.

Atom	Coordination Number, N	Distance, R , Å	Debye-Waller factor, σ^2 , Å ²
N	4	1.955	0.009
C	8	2.834	0.025
C	4	2.986	0.012
C	2	3.333	0.003
$R = 29.74\%$			
$FI = 0.00064$			

Figure 4.15: ¹³C MAS NMR spectra of Mg-STA-6 (a), and Zn-STA-7 (b). Tm-tact is found intact in both solids (in STA-6, for example, δ_C 62.9, 54.5, 43.5, 21.0 ppm), however further carbon-containing fragments are also present within the STA-7 pore system (see too the CHN microanalysis results below).

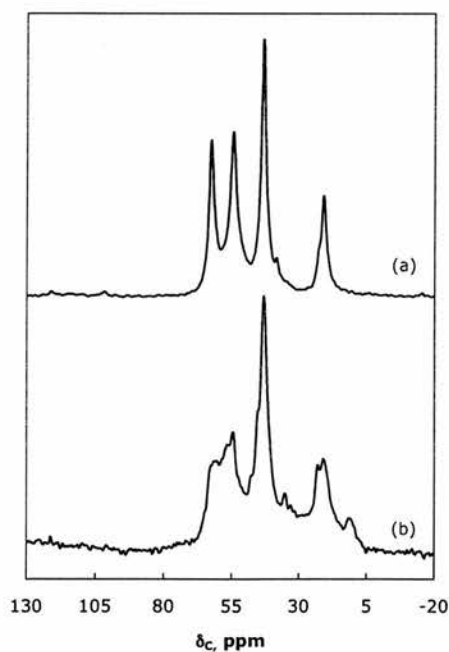


Table 4.3: Minimised non-bonded energy for tmtact in different sites within the pores of STA-6 and STA-7 (calculated by Monte Carlo docking and Simulated Annealing procedures, see text for details).

Structure	Site	Non-bonding energy, kJ mol ⁻¹
STA-6	Cavity	-50.1
STA-7	A cavity	-31.2
STA-7	B cavity	485.5

To examine the organics present in AlPO₄-21 Miss E. F. Philp (St Andrews) dissolved a sample, prepared in the presence of tmtact, in HCl, and performed conventional solution ¹³C NMR spectroscopy on the liquid obtained. This confirmed that AlPO₄-21 does not contain tmtact intact; the NMR signal observed (δ_C 37.4 ppm) is consistent with occluded dimethylammonium ions.

4.3.4 Molecular modelling

The numerical results of computations by Dr P. A. Cox to determine the non-bonding energies of the azamacrocycles within the pores of STA-6 and STA-7 frameworks are given in Table 4.3.

The tmtact molecule fits well into the STA-6 cavity (Figure 4.16), as indicated by the ready formation of STA-6 in the presence of Mg^{II}, Mn^{II} and Fe^{II}, and this is confirmed by the calculated non-bonding energy (Table 4.3). For tmtact in STA-7, the energies show that the molecule very significantly favours the larger A cavity over the intercavity regions. The computer modelled location of tmtact in STA-7 is illustrated in Figures 4.17 and 4.18. The template molecule is very strained in the smaller cavity and the high energy suggests that it is too big to be accommodated at this location.

4.3.5 Electron microscopy

Scanning electron microscopy was used to determine the morphology of crystals. Mg-STA-6 is formed in the presence of tmtact as needle-like tetragonal

Figure 4.16: Stereoview showing the modelled position of the lowest energy location of the tmtact molecular cation within the cavities of STA-6. (Determined by Monte Carlo docking followed by Simulated Annealing.)

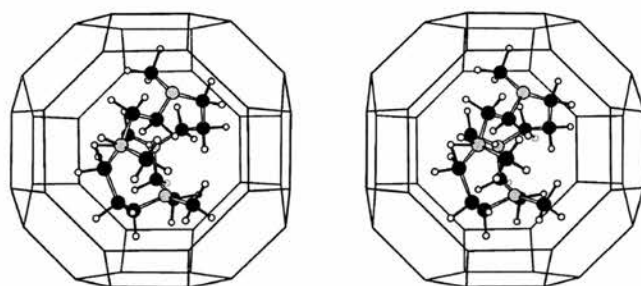


Figure 4.17: Stereoview showing the modelled position of the lowest energy location of the tmtact molecular cation within the A type cavities of STA-7. (Determined by Monte Carlo docking followed by Simulated Annealing.)

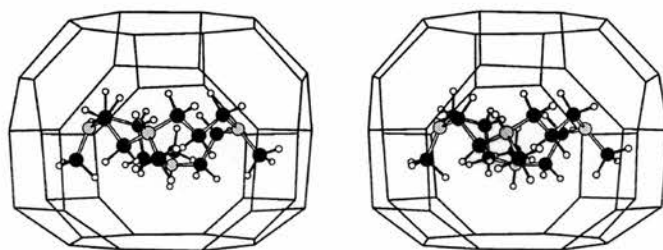
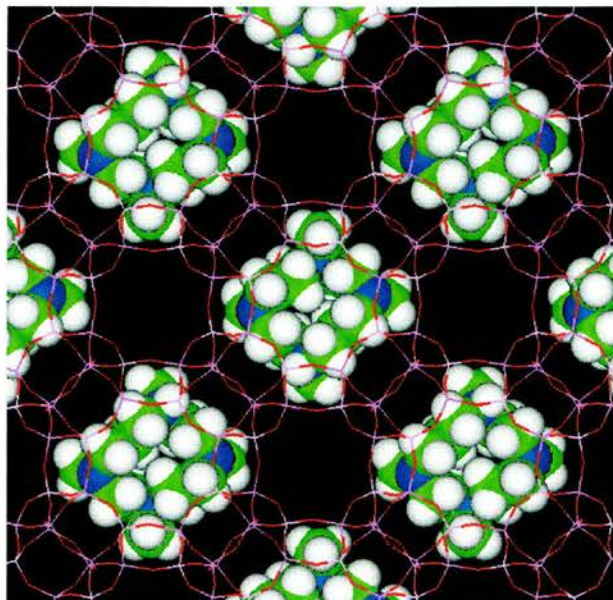


Figure 4.18: Illustrative diagram of the STA-7 structure, viewed down c , showing the location of the tmtact molecular cations.



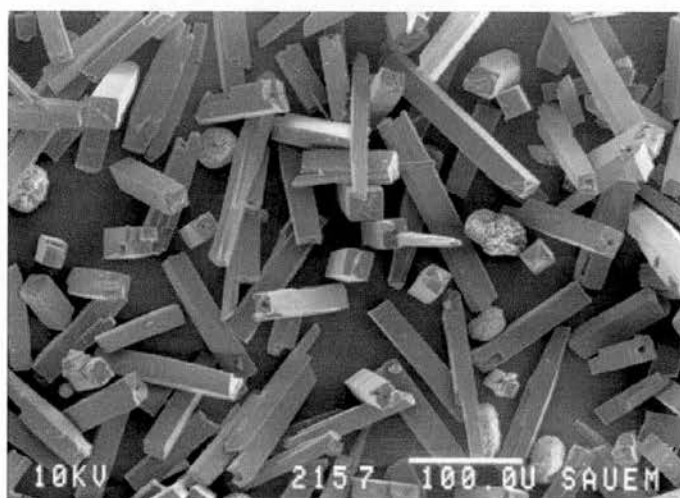
prisms (Figure 4.19.a), Mg-STA-7 (prepared in the presence of hmhaco) crystallises with pseudo-cubic morphology (Figure 4.19.b). In the presence of tmtact, Co-STA-7 crystallises as elongated tetragonal prisms $100 \times 50 \times 50 \mu\text{m}$ with the “cobalt blue” coloration typical of cobalt aluminophosphates with Co^{II} in tetrahedral coordination. Zn-STA-7 (prepared with tmtact) also crystallises as slightly elongated tetragonal prisms with dimensions $50 \times 25 \times 25 \mu\text{m}$.

To try to determine whether stacking faults or domains are present in the Co-STA-7 sample a portion was sent to Prof. O. Terasaki for analysis by transmission electron microscopy (TEM). The sample proved to be exceptionally beam sensitive and so only a single, comparatively low resolution, micrograph could be obtained (Figure 4.20). This appears to show a very well crystallised framework, with no apparent defects.

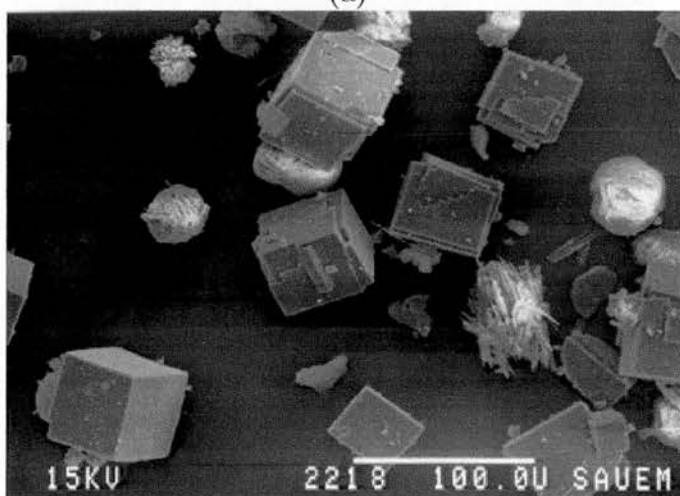
4.3.6 Chemical analysis

It is possible to arrive at a unit cell composition of the as-prepared Co- and Zn-STA-7 samples by combining the results of TGA, CHN and EDX analyses,

Figure 4.19: Scanning electron micrographs of STA-6 (a) and STA-7 (b) obtained by Mr I. Davidson (St Andrews).

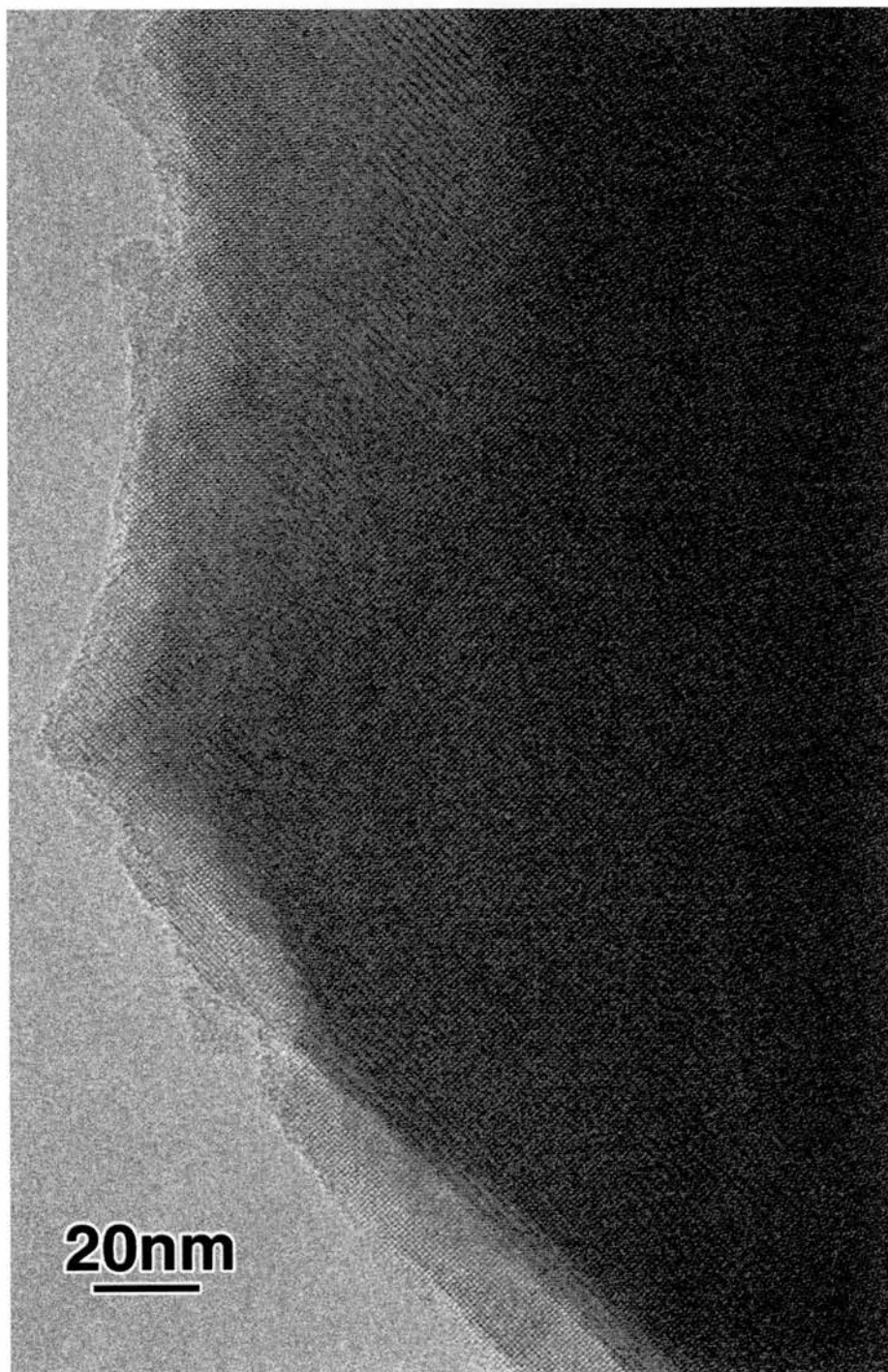


(a)



(b)

Figure 4.20: Transmission electron micrographs of Co-STA-7 obtained by Prof. O. Terasaki (Tohoku University).



and crystallography. Inorganic analysis was given in Table 4.1. TGA performed in oxygen shows endothermic weight loss below 175 °C, which can be attributed to desorption of water, and exothermic weight loss between 200 °C and 620 °C, resulting from template removal. CHN measured for Co-STA-7 is C 10.5 %, H 2.4 %, N 3.3 % (requires C 10.1 %, H 2.5 %, N 3.4 %), and for Zn-STA-7 is C 10.7 %, H 2.5 %, N 3.2 % (requires C 10.9 %, H 2.7 %, N 3.7 %). Combining this data for the Co-STA-7 sample prepared with tmtact indicates a unit cell composition of $|(C_{14}H_{34}N_4)_{2.3}(H_2O)_9|[Co_{4.8}Al_{19.2}P_{24}O_{96}]$. For the sample of Zn-STA-7 the unit cell composition is $|(C_{14}H_{34}N_4)_{2.6}(H_2O)_{10}|[Zn_{4.8}Al_{19.2}P_{24}O_{96}]$.

4.3.7 Thermal stability and porosity

Calcination of the STA-7 materials in oxygen results in complete removal of the template. Whereas magnesium and zinc-containing solids become white after calcination in oxygen, Co-STA-7 turns green, revealing that at least part of the Co^{II} is converted to Co^{III} . Adsorption of *n*-hexane results in the solid becoming blue again, indicating the cobalt is reduced to Co^{II} . To confirm that the calcined sample of Co-STA-7 retained the framework structure, the X-ray profile was examined by Rietveld refinement. [145] Using the as-prepared framework as a starting model, and refining with framework bond lengths and angles constrained to chemically reasonable values gave a good fit to the data ($a = 18.5738(12) \text{ \AA}$, $c = 9.3634(7) \text{ \AA}$, $R_{wp} = 9.2\%$, $R_p = 6.8\%$) and confirmed that the framework is retained intact.

Similarly, Co-STA-6 (prepared with dmtabch) may be calcined with retention of the framework structure (Figure 4.21). Again, this was confirmed by Rietveld refinement of the powder profile, beginning with the coordinates obtained for as-prepared STA-6 (Figure 4.22). The fit obtained is satisfactory ($a = 14.2852(9) \text{ \AA}$, $c = 10.2088(7) \text{ \AA}$, $R_{wp} = 11.39\%$, $R_p = 6.80\%$).

Nitrogen adsorption measurements on the calcined Co-STA-7 reveal a pore volume of $0.25 \text{ cm}^3 \text{ g}^{-1}$, considerably higher than that measured for calcined Mg-STA-6 ($0.13 \text{ cm}^3 \text{ g}^{-1}$) [103] and much closer to the values measured for other microporous solids containing three-dimensionally connected pores.

Figure 4.21: Powder X-ray diffraction patterns CoAPOs crystallised with 4,11-dimethyl-1,4,8,11-tetraazabicyclo[6.2.2]hexadecane template. In the as synthesised material the template is occluded within the material's pores (a), it may be removed by calcination and if carefully dehydrated *in vacuo* the framework remains intact (b).

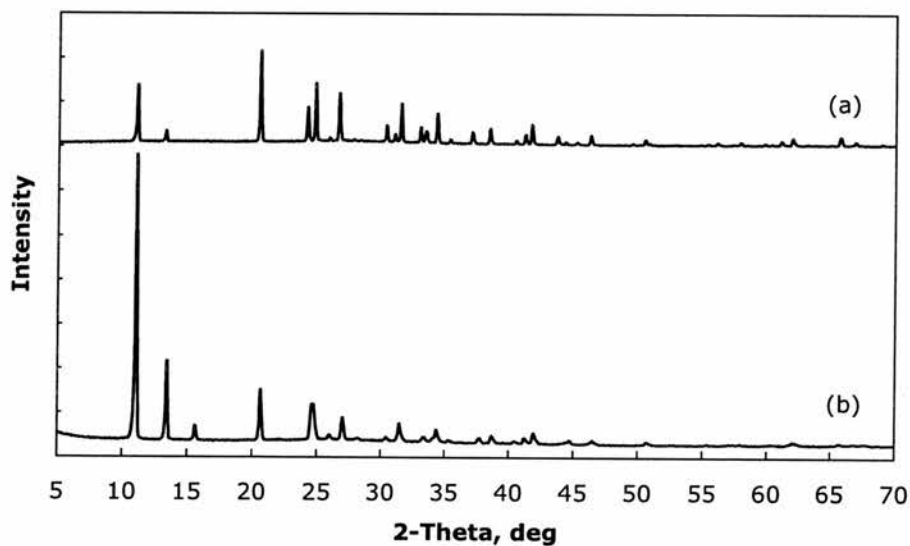
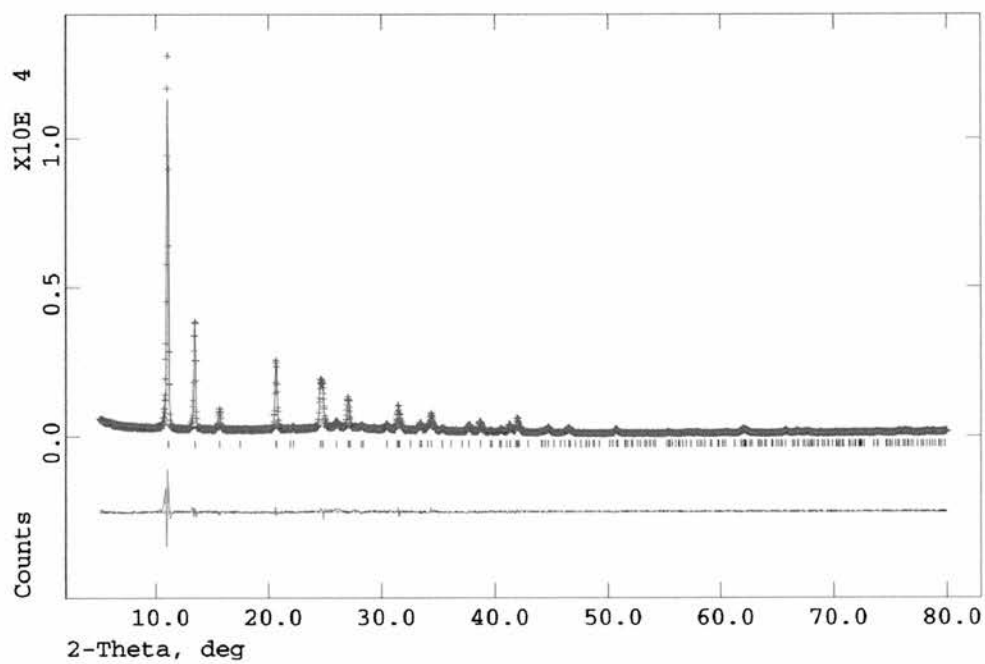


Figure 4.22: Rietveld refinement plot of a powder diffraction profile of Co-STA-6, collected using Fe- $K\alpha_1$ radiation ($P4/mnc$, $a = 14.2852(9)$, $c = 10.2088(7)$ Å, $R_{wp} = 11.39\%$ and $R_p = 6.80\%$).



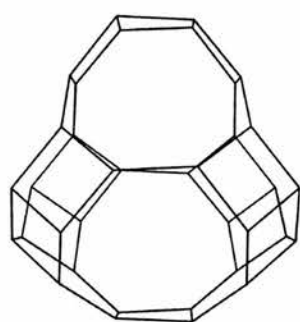
4.4 Discussion

Incorporation of divalent cations frequently results in the crystallisation of framework types different from those that form from purely aluminophosphate gel compositions (in the presence of the same organic template). For example, DAF-1 (**DFO**) [151] may only be prepared with the aluminium partially substituted by divalent cations such as magnesium and cobalt, the aluminophosphate analogue having yet to be prepared (the $\text{AlPO}_4\text{-5}$ structure crystallises instead). However, the formation of STA-6 and STA-7 is *controlled* by the divalent cations present in the gel, Mg^{II} , Si^{IV} , Mn^{II} , Fe^{II} or Ni^{II} giving STA-6, Co^{II} or Zn^{II} , STA-7. This is unique.

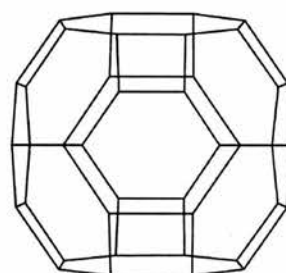
STA-7, which is prepared in the presence of cobalt or zinc (with tmtact) is a very interesting addition to the aluminophosphate family of structures, being the first zeolitic material containing two distinct and fully interconnected small pore channel systems. Although it is not possible from diffraction experiments to locate unambiguously the template molecules (which exhibit disorder and statistical occupancy), the chemical composition suggests that there are probably 2 tmtact molecules per unit cell for STA-7, plus some additional organic amine fragments and water. Molecular modelling indicates that the sites in the cavities in the A channel system are energetically highly favoured over sites in the B channel system, suggesting that the macrocycles template the formation of these cavities. There is no evidence from XRD that the cations (other than nickel) remain complexed in the macrocycle after crystallisation of STA-6 and STA-7—instead they end up in the tetrahedral sites of the aluminophosphate framework.

The A cavities of STA-7 are compared with those of STA-6 and with the aluminophosphates $\text{AlPO}_4\text{-18}$, templated by tmtacn, and $\text{AlPO}_4\text{-42}$, templated by the K222 cryptand (discussed in Chapter 2) in Figure 4.23. The use of macro[poly]cyclic templates appears to yield structures containing cavities, rather than channels. The cavities in STA-7 are 9.4 Å high with a free diameter of *ca* 10.0 Å in the *ab* plane, compared to corresponding values of 10.4 Å high and 9.0 Å in free diameter for STA-6. However, the 8-ring windows in STA-6 are 4.2 Å in diameter compared to 3.8 Å (parallel to *a*) and 3.9 Å (parallel

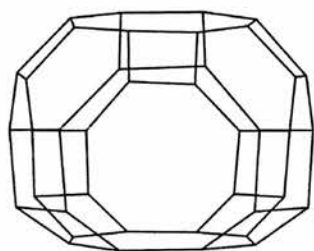
Figure 4.23: Comparison of cavities in aluminophosphates templated by azamacrocycles AlPO_4 -18 (a), AlPO_4 -42 (b), STA-6 (c), and STA-7 (d). For clarity, only the tetrahedral cations are represented in the diagram, and oxygens are omitted.



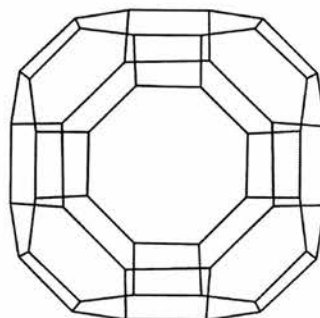
(a)



(b)

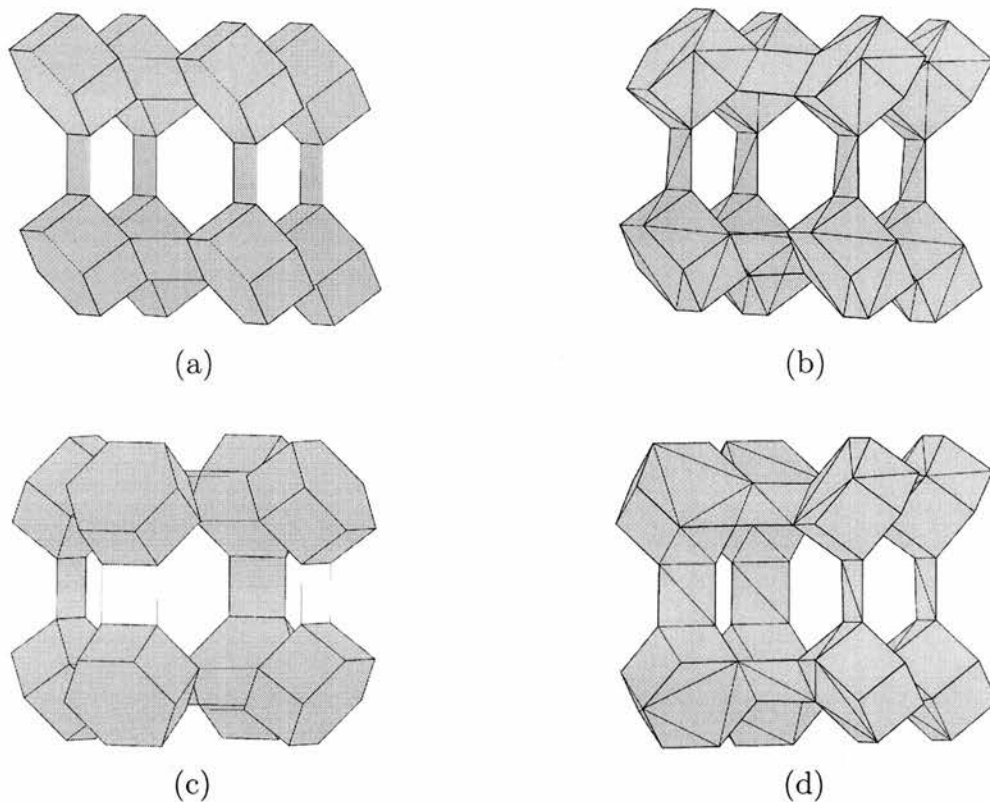


(c)



(d)

Figure 4.24: Comparison of the aluminophosphate frameworks **CHA** (a), **AEI** (b), **KFI** (c), and **SAV** (d). For clarity oxygens are omitted. See text for further details.



to *c*) in STA-7. The STA-6 topology contains $15.3 \text{ T}/1000 \text{ \AA}^3$ and STA-7 $14.4 \text{ T}/1000 \text{ \AA}^3$. Modelling results [145] indicate that whereas the *hnhaco* can be located within the STA-7 structure, its larger size results in it being unable to be located within the slightly smaller cavities of STA-6.

A systematic relationship between the **CHA**, **AEI** and **KFI** frameworks has been noted by Lillerud and Akporiaye [152] which is illustrated in Figure 4.24. Each structure is composed of a series of double 6-rings (D6Rs). In the case of **KFI** these are tilted with respect to the three orthogonal crystallographic axes and linked *via* mirror symmetry in each direction (*mmm*). Similarly in **CHA** the D6Rs are linked *via* translational symmetry (*ttt*), while in the **AEI** framework a mixture of translational and mirror symmetry exists

(ttm). Lillerud and Akporiaye predict a fourth, theoretical, framework having both translational and mirror symmetry (tmm). Through energy minimisation calculations they obtained coordinates and the unit cell $a = 18.3046 \text{ \AA}$, $c = 9.2370 \text{ \AA}$ in $P4/nmm$. This turns out to be the **SAV** framework (Figure 4.24.d). All four frameworks are of very similar lattice energies and so it should be possible to synthesise the aluminophosphate form of **KFI** with tmtact by altering the gel composition or crystallisation conditions.

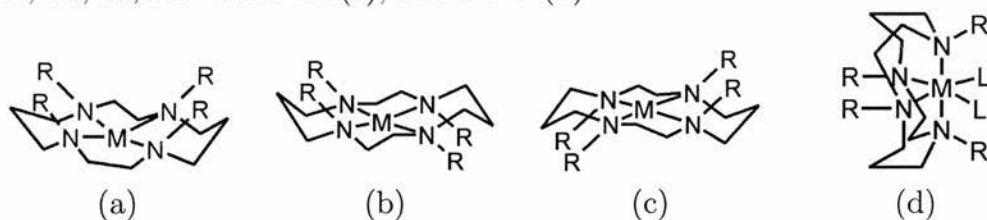
Removal of the template from STA-7 results in a 2.3% decrease in unit cell size. The colour changes upon calcination of Co-STA-7 and adsorption of *n*-hexane upon cooling are consistent with the cobalt being at least partially oxidised to Co^{III} , and remaining in the framework, followed by subsequent reduction back to Co^{II} . The pore volume of the calcined material ($0.25 \text{ cm}^3 \text{ g}^{-1}$) is comparable to that of other zeolites and aluminophosphates with three-dimensional pore systems. [145]

The question of how Co^{II} and Zn^{II} cations are able to direct the crystallisation of the STA-7 framework is intriguing. It is tempting to propose that the cation pre-organises the azamacrocycle during synthesis, and in that way subtly controls the shape of the cavity which can form around it. Yet cobalt and zinc cations are not found within the macrocycles in STA-7. Clearly if this were happening the structure directing effect would be occurring early on in the crystallisation process, during the nucleation stage.

Macrocycles may certainly adopt different conformations to accommodate cations of varying sizes. If the cation is of a similar size to the hole within the macrocycle then it will sit, planar, in the centre of the ring. But if the cation is too small, the macrocycle may reorganise itself, and wrap around the cation. Or binuclear complexes may form where two cations are complexed by the macrocycle. On the other hand, if the cation is too large, it may sit above the plane of the ring, with additional ligands (*e.g.* H_2O) complexing also. Alternatively, for very large cations, two macrocycles may form a sandwich-type complex.

There is no evidence to suggest that anything other than simple complexes

Figure 4.25: Four commonly found conformers of complexes of tetraaza macrocycles, $1R, 4S, 8R, 11S$ *trans*-I (a), $1R, 4S, 8S, 11R$ *trans*-II (b), $1R, 4R, 8S, 11S$ *trans*-III (c), and *cis*-V (d).



containing a single cation–macrocycle unit are formed during the crystallisation of STA-6 and STA-7. Tmtact could not accommodate more than one cation within its ring, and two macrocycles would not fit into the cavity of either STA-6 or STA-7. Nevertheless, tmtact is known to form a number of different *conformers*, [153, 154] four of which are illustrated in Figure 4.25.

If one such conformation were directing the structure of STA-7, in preference to STA-6, then the absence of the cobalt and zinc cations from the macrocycle must be explained. The formation constants ($\log K_f$) of divalent metal-containing complexes differ. (This is a measure of the stability of the complex.) If they are ordered by increasing Z , the following trend is found: $\text{Mg}^{\text{II}} < \text{Mn}^{\text{II}} < \text{Fe}^{\text{II}} < \text{Co}^{\text{II}} < \text{Ni}^{\text{II}} < \text{Cu}^{\text{II}} > \text{Zn}^{\text{II}}$. This is known as the Irving–Williams series [155] and is largely independent of the complexing ligand. So in the presence of divalent cations that are expected to be more weakly bound within the macrocycle (Mg^{II} , Mn^{II} , Fe^{II}) STA-6 is produced, whereas in the presence of more strongly bound Co^{II} or Zn^{II} cations (which have a similar $\log K_f$), STA-7 is prepared. The Fe^{II} cation borders cobalt and zinc, in terms of $\log K_f$ and in this case the major phase is STA-6 with only a very few crystals of STA-7 being formed. It may be conjectured that if its formation constant were a little larger then Fe–STA-7 would crystallise exclusively.

The ability of the framework to accept aliovalent substitution by particular cations is also of importance. (STA-7 was formed only as the metalloaluminophosphate.) Where this is not possible (*i.e.* in pure aluminophosphate or Cr^{II} and Cu^{II} -containing aluminophosphate gels) the AlPO_4 -21 framework

type results, and intact macrocycle is not incorporated. Yet the STA-6 aluminophosphate framework *is* stable and has been prepared during this work, albeit in the presence of the Ni-tmtact complex (although $\text{AlPO}_4\text{-21}$ also forms). And recently [156] a monoclinic form of aluminophosphate STA-6 has been prepared (co-crystallised with $\text{AlPO}_4\text{-34}$) from gels containing Cu^{II} , fluoride and cyclam. In that instance the copper remains within the macrocycle, ligated also by 2 fluorides. Presumably in these cases it is the stability of the complex which is critical to overcome the lack of aliovalent substitution to template STA-6. It is not unsurprising that nickel remains within the macrocycle, instead of migrating into the MAPO framework, as it is more stable surrounded by 4 nitrogens in square-planar geometry, than surrounded by 4 oxygens in square-planar geometry. This is due to the *N*-containing ligand being higher in the spectrochemical series than the *O*-containing one, so the ligand field splitting energy is large enough to favour square planar geometry over tetrahedral. Copper complexes may be stabilised by Jahn–Teller distortion (thus making inclusion of fluoride ions in the gel essential). A layered phase does not form (*c.f.* those seen in Chapter 2) because the fluoride ligands fill coordination sites that could be used to link the complex to an aluminophosphate layer.

Recent work [122] has also resulted in the crystallisation of distorted (orthorhombic) MAPO STA-6 frameworks which contain Ni-tmtact complexes. STA-7 has been found to form as a very minor phase if cobalt or zinc were also present in the gel. In parallel studies [123] the synthesis of Co-STA-7 was found not to be affected by the presence of Mg-STA-6 seeds, and furthermore, syntheses from gels containing mixtures of Mg^{II} and Zn^{II} give mixtures of STA-6 and STA-7. This suggests an interaction between the metal cation and the template leads to a particular phase forming. With tmtact, Ni is a strong template for the STA-6 framework, while Co and Zn are powerful templates STA-7. Yet the question of why remains.

The thermochemistry, and thus stability, of aluminophosphate frameworks has been studied by Davis *et al* [157] in calorimetric experiments. The results

of this work suggested (by extrapolation) that “all” microporous AlPO_4 frameworks are only 11–17 kJ mol^{-1} less stable than berlinite (α -quartz). However the stabilising effect of water (-11 to -30 kJ mol^{-1}) is such that microporous AlPO_4 s are energetically comparable to dense phases. This supports the conclusion that the role of the template is not to stabilise the framework but to direct the path of the crystallisation kinetically. This would seem also to be the role of cobalt, zinc and tmtact in the STA-7 syntheses. STA-7 is more open than STA-6, and so it could be conjectured that it is less energetically stable. Its crystallisation, in preference to STA-6, must be kinetically controlled. Certainly CoAPOs and ZnAPOs generally form faster than MgAPOs and SAPOs.

4.5 Conclusion

The synthesis of novel microporous framework solids, such as zeolites and aluminophosphates, continues to generate new possibilities in adsorption and catalysis.

The results on the incorporation of 1,4,8,11-tetramethyl-1,4,8,11-tetraazacyclotetradecane (tmtact) into the novel solids STA-6 and STA-7 has demonstrated that this azamacrocycle may be occluded, unbound, within aluminophosphate-based solids. This is commensurate with the work described in Chapter 2. Recent work has extended the number of macrocycles and cryptands found inside AlPO_4 pores' to include 1,4,8,11-tetraazacyclotetradecane (cyclam) [156] and 4,11-dimethyl-1,4,8,11-tetraazabicyclo[6.6.2]hexadecane (dmtabch) [158] in STA-6 and 1,4,7,10,13,16-hexamethyl-1,4,7,10,13,16-hexaazacyclooctadecane (hnhaco) [145] in STA-7, together with those on the incorporation of cyclam in AlPO_4 -34, 1,4,10,13-tetraoxa-7,16-diazacyclooctadecane (K22) into the clathrasil MU-13 [159] and the oxaza-cryptand 4,7,13,16,21,24-hexaoxa-1,10-diazabicyclo[8.8.8]hexacosane (K222), and related azacrown ethers into AlPO_4 -42 [112, 123, 160] and of porphyrins into VPI-5. [161] As yet the templating effect of metal cations has not been seen in systems other than MAPO-tmtact, but the possibility remains nonetheless.

Chapter 5

Catalytic properties of STA-2, STA-6 and STA-7

5.1 Introduction

The demand for clean technology has driven the development of new catalysts and processes in the chemical industry. Concern about the impact of liquid acids, in particular hydrofluoric and sulfuric acids, on the natural environment has made selective and active solid acid catalysts an attractive alternative. Such materials find application in numerous reactions, including isomerisation, alkylation, oligomerisation and the cracking of alkanes, alkenes and aromatics. Corma has recently reviewed the area. [131] In addition to the substantial family of aluminosilicate zeolite acids (exemplified by H-ZSM-5, HY, H-mordenite) aluminophosphate microporous solids, when controllably modified by the inclusion of tetravalent Si or divalent metal cations into the frameworks, yield solid acid catalysts too. Catalytic cracking with zeolites has had a profound impact in the last 40 years. Oil refining has been transformed by the replacement of silica–alumina catalysts by faujasite zeolites. Gasoil cracking accounts for 30% of all gasoline production [131] while also generating diesel, alkenes and *iso*-alkanes. Oxidation reactions are also significant industrially; for example, the oxidation of *p*-xylene to terephthalic acid,

and cyclohexane to adipic acid forms feedstocks for saturated polyester (terylene) and nylon 6,6 synthesis, respectively. Thomas has recently reviewed this area. [162]

In this chapter the conversion of methanol to olefins over small pore SAPO, NiSAPO, MgAPO and CoAPO materials of the STA-*n* family are investigated. Reference is made to the commercial SAPO-34 (**CHA**) catalyst and to the novel materials' acidity through an *n*-butane cracking probe reaction. The oxidation of *n*-hexane with molecular oxygen over CoAPO solids is also investigated.

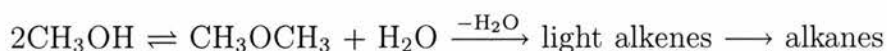
5.2 Conversion of methanol to olefins

Methanol to hydrocarbons (MTHC) technology has been the subject of much research over the last 25 years. [163] Two reactions, methanol to gasoline (MTG) and methanol to olefins (MTO) have been of particular interest. The mechanism (discussed further below) is thought to proceed *via* dimethyl ether (DME). Dimethyl ether itself has an established application as an environmentally friendly aerosol propellant (worldwide, annual production is 150 000 tonnes) and has potential as a fuel gas, replacing naphtha and diesel in small scale, widely distributed power stations such as those found in developing countries. The Haldor Topsøe process is currently being commercialised by BP for this purpose. [164] Several processes have been developed for converting methanol through to hydrocarbon products. Mobil's MTG process, which was operated commercially in New Zealand, produced 520 000 tonnes of gasoline annually. [165] This gives a route from natural gas or coal and uses a ZSM-5 (**MFI**) catalyst for the MTG step. UOP/Norsk Hydro have developed a process for MTO using a SAPO-34 catalyst that selectively produces ethene and propene, two important monomers for plastics production. Keil has recently reviewed the process technology applied to this reaction. [166]

Zamaraev and Thomas [167] demonstrated that the catalytic dehydration of all alcohols occurs over strong Brønsted acid sites, rather than Lewis ones, in zeolites. They did this by preparing a number of samples of H-ZSM-5 of

varying crystallite size, some of which were partially ion-exchanged to Na,H-ZSM-5. A correlation between catalytic activity and the concentration of bridging hydroxyl groups was observed. Moreover, the rate of dehydration declined as pyridine was adsorbed, but no reduction occurred when acetonitrile was adsorbed. Pyridine selectively adsorbs onto Brønsted acid sites, whereas acetonitrile affects only Lewis acid sites.

The principal reaction steps in the MTO reaction is summarised thus:



Methanol is dehydrated to dimethyl ether in an equilibrium limited (temperature dependent) reaction. Light alkenes are subsequently formed. Finally these react to yield alkanes and longer chain alkenes. In large pore catalysts aromatics and naphthenes would also be produced (MTG reaction). The intermediate in the initial dehydration step is a protonated surface methoxyl group that undergoes nucleophilic attack by methanol. The last step occurs *via* a classical carbenium ion mechanism with concurrent H-transfer. It is the second step, in which the first C–C bond forms, which has been the subject of much research work (see the review by Stöcker [163] for further details). Four classes of intermediate have been proposed: carbenes, radicals, carbonium ions and oxonium ions (in fresh catalysts). However, an induction period is observed with many catalysts suggesting that a different mechanism dominates in partially coked materials. This has been called the “carbon pool” mechanism, [168, 169] and is thought to involve adsorbed intermediates reacting with methanol or DME to form alkenes. These intermediates may be carbenium, oxonium, cyclopentyl or benzenium ions or polymethylbenzenes. [170]

Heavy side products, “coke”, are often responsible for deactivating microporous solid catalysts, either because they poison active sites or simply because they block the materials’ pores. Coke though is not necessarily inert with respect to reactants or intermediates and can affect activity and selectivity. But it does not always have a negative impact on the catalysed reaction as it can increase shape selectivity. An illustrative example of this is in Mobil’s disproportionation of toluene process (*c.f.* Figure 1.14.c, page 45). Very high

selectivity for *p*-xylene occurs when an **MFI** zeolite is coked at high temperature [171] forming polyaromatics on the outer surface of the crystallites. The selectivity increases because reaction on the outer (unselective) surface acid sites is blocked and the sieving properties of the zeolite are improved. [172] Coke deposition has been studied by others in variable space velocity experiments [173] and in reactors such as the oscillating microbalance reactor. [174]

In the MTO reaction zeolites deactivate very quickly due to coking. SAPO-34 deactivates more slowly than chabazite, both of which have the **CHA** framework topology, because the former has fewer acid sites. Liang *et al* found no loss in catalytic performance with a sample of SAPO-34 after regenerating it 55 times. [175] The nature of the acid sites in SAPO-34 has been studied by Smith *et al* with neutron diffraction which revealed two different bridging OH groups of approximately equal occupancy. [176] The acid site strength was determined from the shift in O–H frequency following CO adsorption at 77 K. Methylbenzenes, methylnaphthalenes and, after longer times on stream, pyrene have been found in SAPO-34 catalysts during MTO conversion. [177] Chen *et al* have studied the effect of crystallite size on deactivation and selectivity with SAPO-34. Their results showed that a lower alkene yield was obtained in 0.25 μm crystallites (presumably due to kinetic control) and 2.5 μm crystallites (due to diffusion limitations). Optimum alkene yields were obtained with crystallites of 0.4–0.5 μm . Coking rates increased as the crystallite size increased, but stabilised at a lower level for the largest crystallites. Transition state selectivity (in favour of ethene) appeared to be induced by coking.

Selectivity towards ethene can also be enhanced by the incorporation of Ni into the SAPO-34 framework. Inui has reported selectivities of 86% at 425° C without apparent deactivation after 11 h with NiSAPO-34. [178] Kevan *et al* also observed enhanced ethene production with NiSAPOs with framework types **AEI**, **CHA**, **ERI** and **LEV**. [179] Inui has developed a complex synthesis procedure (which is largely designed to obtain very homogeneous gels) to obtain NiSAPO materials with framework Ni. [178] The incorporation of Ni reduces the strength of the acid sites in these catalysts which in turn

affects selectivity and lifetime. Kevan [179] found that there was a particular level of Ni (0.03 mol dm^{-3} in the gel) required for optimum catalytic results; excess Ni did not go into the framework. They, and Thomas *et al.*, [180] also identified SAPO-18 as being a catalyst that will retain both its activity and selectivity longer than SAPO-34.

The strategy applied during the work described here was limited by access to the various reactors used. It was therefore not destined to be exhaustive, but instead aimed to explore the acid catalytic properties of selected materials and obtain data that could be used in an initial assessment of their potential. Materials of the STA-*n* family were investigated with various cations substituted into the framework (see below). Materials containing trace amounts of Ni were also examined to assess the effect on selectivity (as discussed above). To try to correlate these results with acidity preliminary work, although far from comprehensive, was also carried out (see Section 5.3).

5.2.1 Experimental

Materials with the STA-2, STA-6 and STA-7 frameworks were synthesised as described previously. [109, 145] Si-STA-7 was prepared by a method developed by Miss R. García. [181] SAPO-34 was synthesised by literature methods. [182] NiSAPOs were made by adding Ni to SAPO gels as nickel(II) acetate. Chemical analysis of selected materials was undertaken with EDX analysis.

Methanol to olefins experiments employing 2–3.7 g (3 or 5 cm^3) of catalyst were carried out in the Atmospheric Gas Reactor-1 (AGR-1) at BP's Sunbury research centre. This reactor comprised a vertically mounted tubular furnace equipped with a quartz glass tube (i.d. 8 mm) surrounded by glass wool, into which the pre-calcined catalyst pellets (-40 +100 mesh¹) were loaded. The catalyst was supported on a porous frit in the reactor tube and the remaining space was filled with quartz granules (Fluka). All samples were activated by heating at $5 \text{ }^\circ\text{C min}^{-1}$ to $130 \text{ }^\circ\text{C}$, isothermal for 2 h then $5 \text{ }^\circ\text{C min}^{-1}$ to $425 \text{ }^\circ\text{C}$,

¹This fraction will not block the frit and cause a pressure drop over the catalyst bed, nor will it allow the reactant stream pass easily around the catalyst leading to "maldistribution".

isothermal overnight, under flowing nitrogen. Nitrogen (controlled by a needle valve) was also used as the carrier gas and methanol (Aldrich) delivered into the top of the reactor *via* a calibrated syringe pump at either 1.0 or 1.7 cm³ h⁻¹ (weight hourly space velocity, WHSV = *ca* 0.5 h⁻¹), depending on catalyst volume, so that gas hourly space velocity (GHSV) remained constant. The product stream was passed through an ice-cooled trap into which liquids condensed before the gaseous products were sampled with a gas syringe (flushed once). Analysis of both liquid and gaseous products was performed offline on a Unicam 610 Series gas chromatograph equipped with a packed column and thermal conductivity detector (TCD). The TCD allowed detection of nitrogen which was used as an internal standard. A heating program of 80–120 °C at 10 °C min⁻¹, 120–200 °C at 20 °C min⁻¹, then isothermal for 10 min was sufficient for resolution of all observed signals. Products were identified by GC–MS (BP, Sunbury) and by injecting standard samples into the GC. Response factors were obtained from the literature. [183]

Reactions were performed in St Andrews with a system which consisted a Cambridge Reactor Design (CRD) model 5000 plug flow reactor² coupled to a CE Instruments 8000^{TOP} gas chromatograph (Figure 5.1). Catalyst samples were loaded into a quartz glass tube (i.d. 9.5 mm) mounted vertically in a water cooled tubular furnace. A Eurotherm temperature controller and a system of cascading thermocouples (including a master K-type thermocouple mounted within the catalyst bed) kept the catalyst within $\pm 0.25^\circ$ of the set-point temperature. This was facilitated by the water cooled jacket which surrounded the furnace. Four lines, regulated by Brooks mass flow controllers, were available for gases. Liquid reagents were delivered *via* a calibrated Razel Scientific Instruments syringe pump. All materials entering the reactor were passed through an air heated system of stainless steel baffles (the “enclosure”). Thus they reached the catalyst with minimum pulsing and were hot and well mixed. The gas stream could be manually directed to vent before reaching the

²A number of safety features are built into the reactor system. These enable automatic shutdown if over heating (>900 °C), over pressure (>40 psi), loss of cooling water/heating air, or current leakage (>30 mA) occurs. Failure of the power supply stops the furnace and syringe pump operating; moreover it will also close the mass flow controlled gas lines. Once tripped the safety system must be manually reset before the reactor will operate again.

Figure 5.1: CRD plug flow reactor system. The vertical tubular furnace can be seen in the centre of the picture, the mass flow valves to the rear and the Brooks and Eurotherm controller below. To the left is the syringe pump and the CE Instruments GC and Fisons integrator are sited to the right.



reaction tube. The product stream (at ambient temperature) was connected to the GC for online analysis *via* an air-actuated Valco six-way gas sampling valve (GSV). A septum assembly allowed sampling by gas syringe for offline analysis. The reaction temperature and gas flow rates could be set manually (with the Eurotherm and Brooks controllers) or with proprietary software³ for the IBM-compatible PC. During the experiment the reaction temperature and gas flow rates were set and monitored by the computer. Online analysis of the gas stream was triggered by the reactor.

Before each experiment catalyst samples were pelleted, crushed and sieved.

³Two programs control and monitor the reactor system. *CRD5000 Setup*, [184] generates a file ("gen-exp.dat") which contains details of the pre-treatment and experiment to be run (flow rates, temperatures *etc.*). Up to 100 runs, of equal length, each ending in an analysis of the product gas stream, may be setup. *CRD5000 Run*, [185] sends instructions to the mass flow and temperature controllers, at the appropriate time according to that specified in the setup file. This program also monitors data coming back from the reactor, in real time, and plots graphs of absolute temperature, variation from the set point temperature, gas flow rates and pressure with respect to time. The gas flow rates and temperatures are ultimately controlled by the Brooks and Eurotherm controllers, not the computer.

A fraction of $-40 +100$ mesh particles was loaded into the reactor tube, supported on a porous frit, and mounted in the furnace. The reactor system was prepared for use.⁴ As-prepared catalyst (220 mg) was calcined *in situ* under He/O₂ each flowing at $25 \text{ cm}^3 \text{ min}^{-1}$. During calcination the gas stream exiting the reactor was vented rather than being allowed to pass through the GSV. After calcination the reactor was automatically purged for 30 min under $25 \text{ cm}^3 \text{ min}^{-1}$ He.

Isothermal MTO experiments were carried out as before. Methanol (Cannon) was delivered *via* a calibrated syringe pump at $0.236 \text{ cm}^3 \text{ h}^{-1}$,⁵ $\text{WHSV} = 0.9 \text{ h}^{-1}$. Helium was used as the carrier gas ($50 \text{ cm}^3 \text{ min}^{-1}$). The furnace temperature was set to $425 \text{ }^\circ\text{C}$ (achieved as fast as possible) and analysis made every *ca* 20 min for 6 h. Gas chromatography was performed with a Chrompack PLOT (CP PoraPLOT U) $25 \text{ m} \times 0.53 \text{ mm}$ i.d. fused silica capillary column, with He carrier gas ($5 \text{ cm}^3 \text{ min}^{-1}$), using the heating program: 2 min isothermal at $40 \text{ }^\circ\text{C}$, $40\text{--}150 \text{ }^\circ\text{C}$ at $20 \text{ }^\circ\text{C min}^{-1}$, then 5 min isothermal at $150 \text{ }^\circ\text{C}$. Response factors were obtained from the literature. [183] Once the reaction was complete the reactor was automatically purged with He ($25 \text{ cm}^3 \text{ min}^{-1}$) for 10 h at $100 \text{ }^\circ\text{C}$.

Problems with the CRD reactor meant that a sample of Si-STA-7 was sent to Dr A. Beale at the Royal Institution for testing (using a similar system), and those results are given below. Initial calcination and subsequent catalyst regeneration was carried out by heating under N₂ at $535 \text{ }^\circ\text{C}$ for 1 h and subsequently in air for 1 h. Catalysis was performed with 195 mg (as-prepared weight) of $20 \mu\text{m}$ catalyst particles at $400 \text{ }^\circ\text{C}$, $450 \text{ }^\circ\text{C}$ and $500 \text{ }^\circ\text{C}$ (twice), regenerating the catalyst between each run. Methanol and N₂ flow rates of $3.0 \text{ cm}^3 \text{ h}^{-1}$ and $60 \text{ cm}^3 \text{ min}^{-1}$ were used, respectively (methanol $\text{WHSV} = 11.9 \text{ h}^{-1}$). Analysis

⁴Power and water were turned on and the safety circuit reset. The laboratory high-pressure air line regulator was adjusted to 60 psi and the enclosure heater set manually to $70 \text{ }^\circ\text{C}$. Helium and oxygen regulators were adjusted to 35 psi. The mass flow controllers were tested to confirm steady operation. If this was not achieved within a few minutes the valve was opened 100% for a short time before the flow was reduced. The GSV heater was set to $70 \text{ }^\circ\text{C}$. The GC injector and detector were set to $200 \text{ }^\circ\text{C}$ and the FID lit with H₂ and air pressures of 11.5 psi and 13 psi respectively.

⁵The liquid flow rate was set initially at $0.45 \text{ cm}^3 \text{ min}^{-1}$ for 2 min so that 0.9 cm^3 of MeOH completely filled the line between the syringe and the reactor.

Table 5.1: Gel and catalyst composition data for materials used in the MTO reaction.

Material	Framework type code	Cation ratio in synthesis gel	Inorganic composition (EDX)
SAPO-34	CHA	0.6Si : 1.0Al : 1.0P	$\text{Si}_{0.5}\text{AlP}_{0.5}\text{O}_4$
NiSAPO-34	CHA	0.1Ni : 0.6Si : 1.0Al : 1.0P	$\text{Ni}_{0.01}\text{Si}_{0.4}\text{AlP}_{0.6}\text{O}_4$
SAPO-56	AFX	0.6Si : 1.0Al : 1.0P	
Si-STA-2	SAT	0.1Si : 0.9Al : 1.0P	
NiSi-STA-2	SAT	0.02Ni : 0.2Si : 1.0Al : 0.8P	
Si-STA-6	SAS	0.2Si : 1.0Al : 0.8P	$\text{Si}_{0.12}\text{AlP}_{0.88}\text{O}_4$
NiSi-STA-6	SAS	0.02Ni : 0.2Si : 1.0Al : 0.8P	$\text{Ni}_{0.01}\text{Si}_{0.25}\text{AlP}_{0.75}\text{O}_4$
Mg-STA-6	SAS	0.08Mg : 0.92Al : 1.0P	
Si-STA-7	SAV	0.25Si : 0.75Al : 1.0P	
Co-STA-7	SAV	0.2Co : 0.8Al : 1.0P	$\text{Co}_{0.12}\text{Al}_{0.88}\text{PO}_4$

was carried out with gas chromatography after 10 mins during the runs at 400 °C and 450 °C and after 5 and 40 mins during the run at 500 °C.

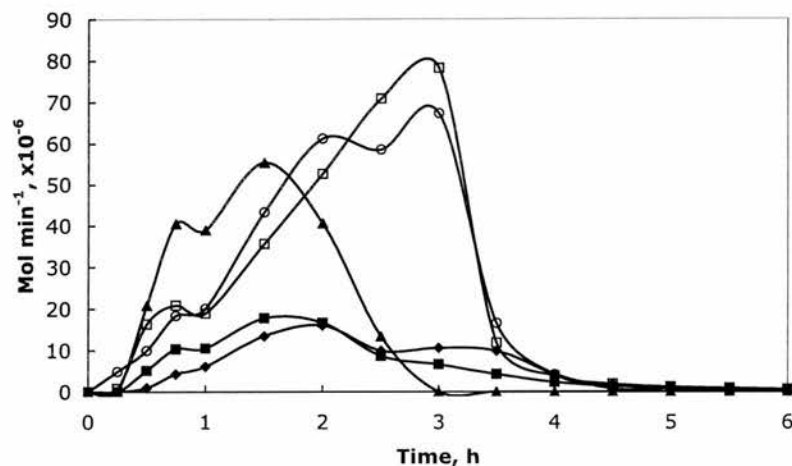
Spent catalysts were examined by powder X-ray diffraction and TGA to determine crystallinity and coking level in an analogous way to that described in previously chapters.

5.2.2 Results

Catalyst samples were successfully prepared with compositions given in Table 5.1. Powder XRD showed the **ATO**, **AFX**, **CHA**, **SAT** and **SAV** materials to be phase pure and crystalline; the **SAS** material showed minor impurity peaks that could be attributed to SAPO-43 (**GIS**). All materials were calcined and were shown by XRD to retain their structures.

The MTO reaction was carried out isothermally at 425 °C in reactors at Sunbury and St Andrews. Initial experiments were performed at Sunbury: SAPO-34, Si-STA-6 and Co-STA-7 were studied with 3 cm³ catalyst beds; reactions with SAPO-34 and Si-STA-6 were repeated, along with NiSAPO-34 and NiSi-STA-6, with 5 cm³ beds. The results of these experiments are plotted in Figures 5.2–5.8. The composition of the product streams at peak

Figure 5.2: Plot of product stream composition (mol min^{-1}) vs time (h) with a SAPO-34 catalyst bed volume of 3 cm^3 . Key: ■ ethane, □ ethene, ○ propene, ◆ C_4s and ▲ DME.



conversion is tabulated in Table 5.2. Cumulative hydrocarbon production after 5 h is illustrated in Figure 5.9. Subsequently, SAPO-34, SAPO-56, Si-STA-2, NiSi-STA-2, Si-STA-6 and Mg-STA-6 were studied with small (*ca* 0.3 cm^3) catalyst beds at St Andrews. Plots of hydrocarbon yield *versus* time are given in Figures 5.10–5.15. The composition of the product streams after *ca* 20 mins reaction is given in Table 5.3. The results of MTO experiments carried out at the Royal Institution at increasing temperatures (with a supplied sample of Si-STA-7) are given in Table 5.4.

All materials (except Co-STA-7) retained their structures after the reaction (by powder XRD). Powder patterns for Si-STA-7 before reaction and after the MTO runs are shown in Figure 5.16. The structure remains highly crystalline after four regenerations. Coke deposited on the catalysts during the reaction was measured by TGA and found to be in the range 2.1–9.1 wt%. Co-STA-7 coked least and SAPO-34 the most. Ni containing materials contained less coke than the SAPO analogues, commensurate with their lower overall conversions.

Figure 5.3: Plot of product stream composition (mol min^{-1}) vs time (h) with a SAPO-34 catalyst bed volume of 5 cm^3 . Key: ■ ethane, □ ethene, ○ propene, ◆ C_4s and ▲ DME.

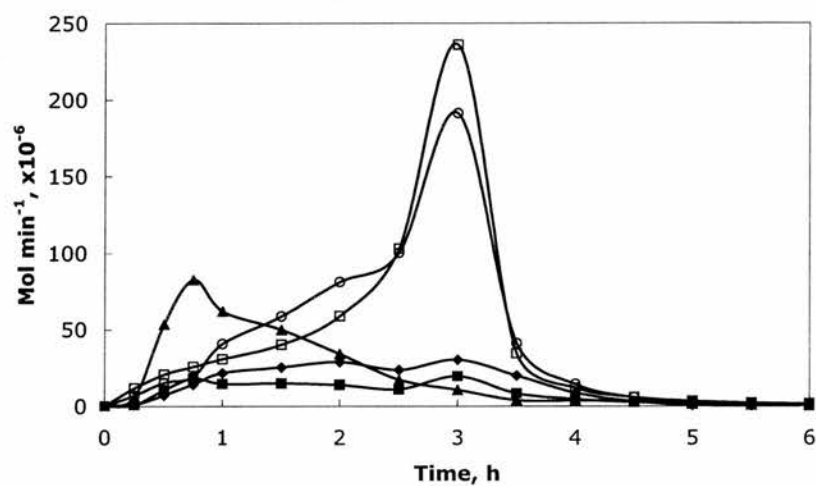


Figure 5.4: Plot of product stream composition (mol min^{-1}) vs time (h) with a NiSAPO-34 catalyst bed volume of 5 cm^3 . Key: ■ ethane, □ ethene, ○ propene, ◆ C_4s and ▲ DME.

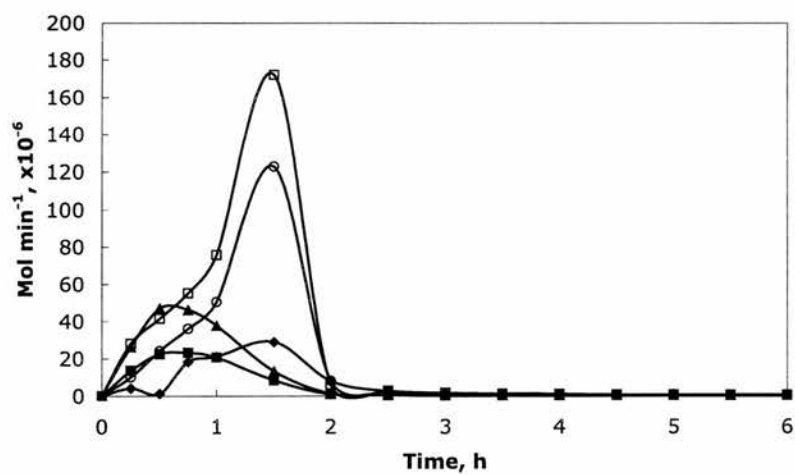


Figure 5.5: Plot of product stream composition (mol min^{-1}) vs time (h) with a Si-STA-6 catalyst bed volume of 3 cm^3 . Key: ■ ethane, □ ethene, ○ propene, ◆ C_4s and ▲ DME.

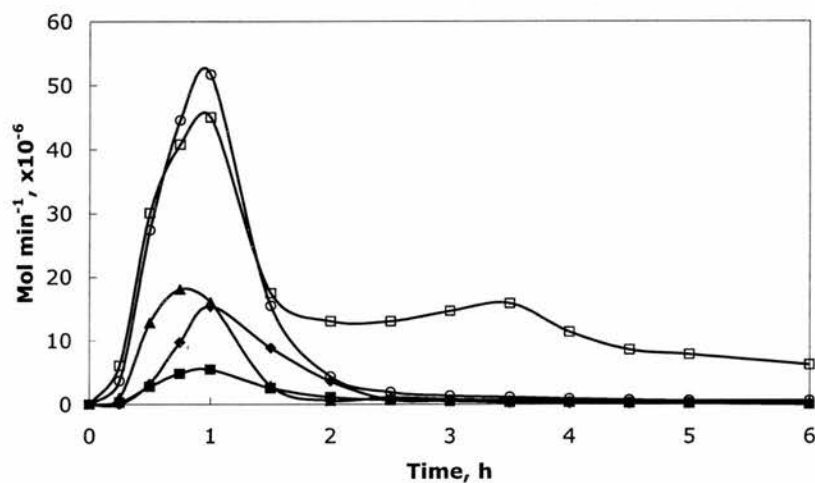


Figure 5.6: Plot of product stream composition (mol min^{-1}) vs time (h) with a Si-STA-6 catalyst bed volume of 5 cm^3 . Key: ■ ethane, □ ethene, ○ propene, ◆ C_4s and ▲ DME.

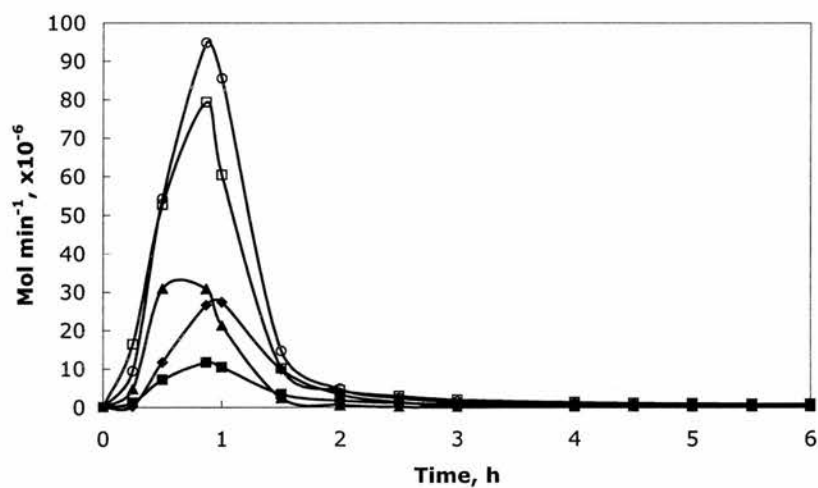


Figure 5.7: Plot of product stream composition (mol min^{-1}) vs time (h) with a NiSi-STA-6 catalyst bed volume of 5 cm^3 . Key: ■ ethane, □ ethene, ○ propene, ◆ C_4s and ▲ DME.

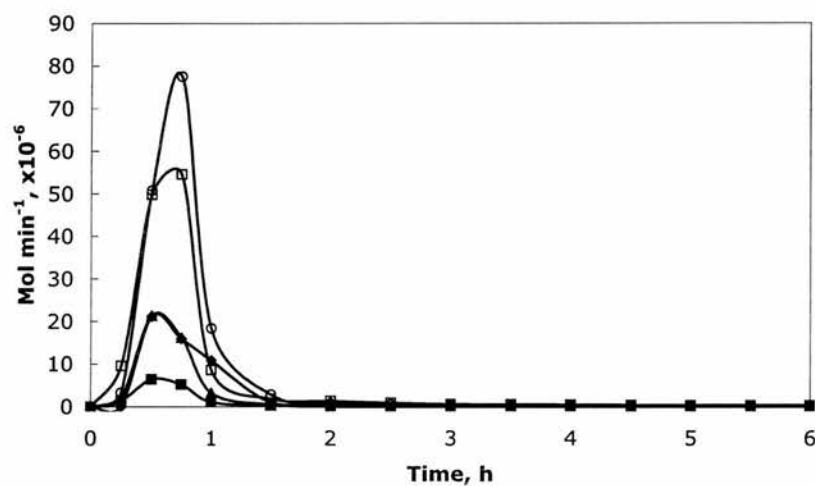


Figure 5.8: Plot of product stream composition (mol min^{-1}) vs time (h) with a Co-STA-7 catalyst bed volume of 3 cm^3 . Key: ■ ethane, □ ethene, ○ propene, ◆ C_4s and ▲ DME.

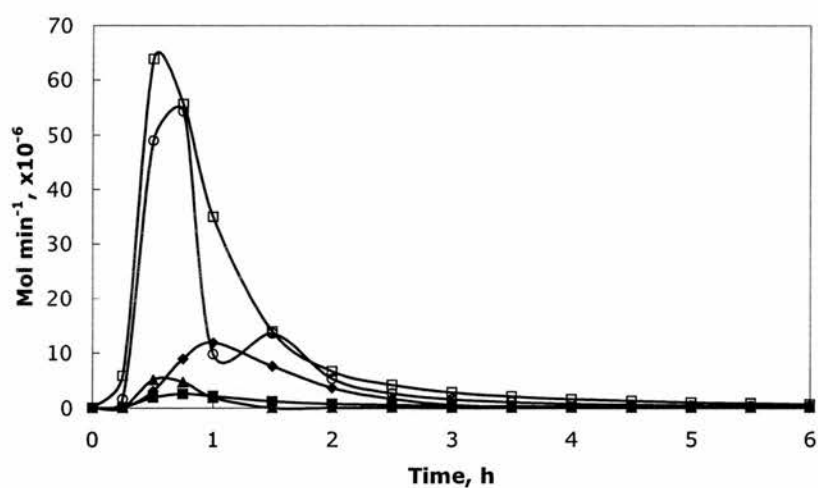


Table 5.2: MTO conversion data for SAPO-34, NiSAPO-34, Si-STA-6, NiSi-STA-6 and Co-STA-7.

Material	Bed vol- ume, cm ³	Time on stream, ² min	Distribution of products, ¹ mol %						C ₂ H ₄ / C ₃ H ₆	
			DME	C ₂ H ₆	C ₂ H ₄	C ₃ H ₆	C ₄	C ₄	C ₃ H ₆	C ₃ H ₆
SAPO-34	3	180	0.0	4.1	48.1	41.4	6.5	1.2		
SAPO-34	5	180	2.2	4.0	48.4	39.2	6.2	1.2		
NiSAPO-34	5	90	3.9	2.4	49.8	35.5	8.4	1.4		
Si-STA-6	3	60	12.0	4.1	33.7	38.7	11.5	0.9		
Si-STA-6	5	52	12.7	4.8	32.6	39.0	11.0	0.8		
NiSi-STA-6	5	45	9.6	3.1	32.2	45.8	9.4	0.7		
Co-STA-7	3	30	4.2	1.5	51.9	39.9	2.5	1.3		

¹ Trace amounts of CH₄ were detected but were too low for integration.

² Time at which ethene production peaked.

Figure 5.9: Plot of cumulative hydrocarbon and DME production (mol) after 5 h on stream at 425 °C, SAPO-34 (a), Si-STA-6 (b), and Co-STA-7 (c) with catalyst bed volumes of 3 cm³ and SAPO-34 (d), NiSAPO-34 (e), Si-STA-6 (f), and NiSi-STA-6 (g), with catalyst bed volumes of 5 cm³.

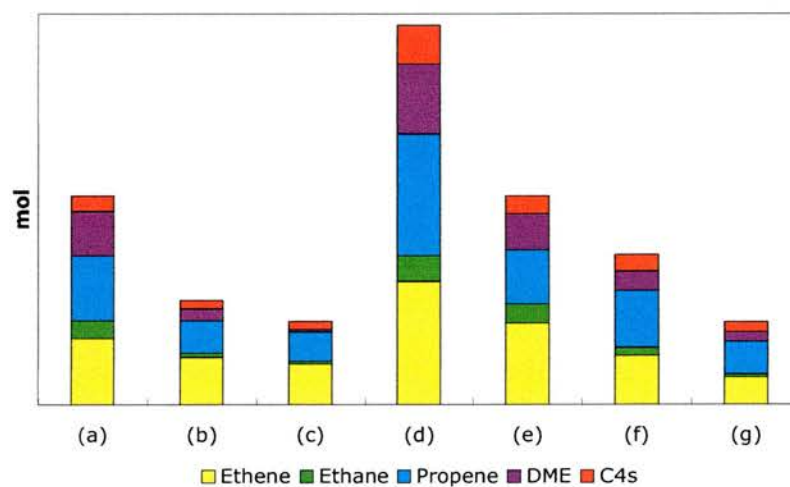


Figure 5.10: Plot of product stream composition (wt %) vs time (h) with a SAPO-34. Key: ■ ethane, + methane, □ ethene, ○ propene, ◆ C₄s, × C₅s and ▲ DME.

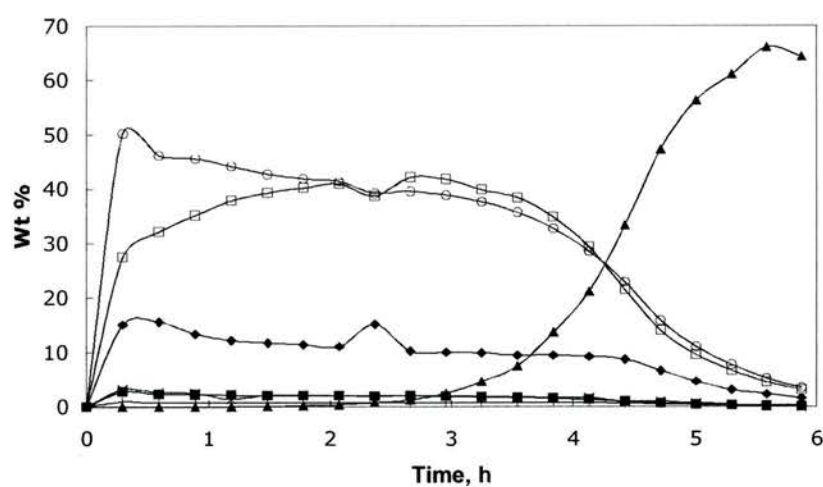


Figure 5.11: Plot of product stream composition (wt %) *vs* time (h) with a SAPO-56. Key: ■ ethane, + methane, □ ethene, ○ propene, ◆ C₄s, × C₅s and ▲ DME.

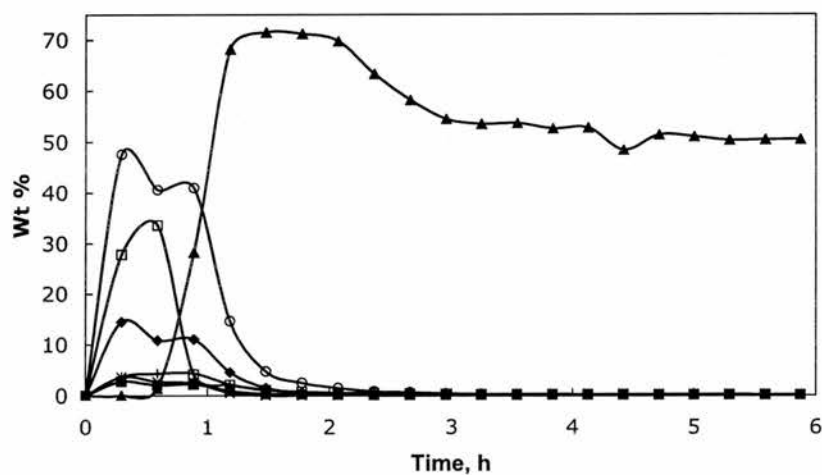


Figure 5.12: Plot of product stream composition (wt %) *vs* time (h) with a Si-STA-2. Key: ■ ethane, + methane, □ ethene, ○ propene, ◆ C₄s, × C₅s and ▲ DME.

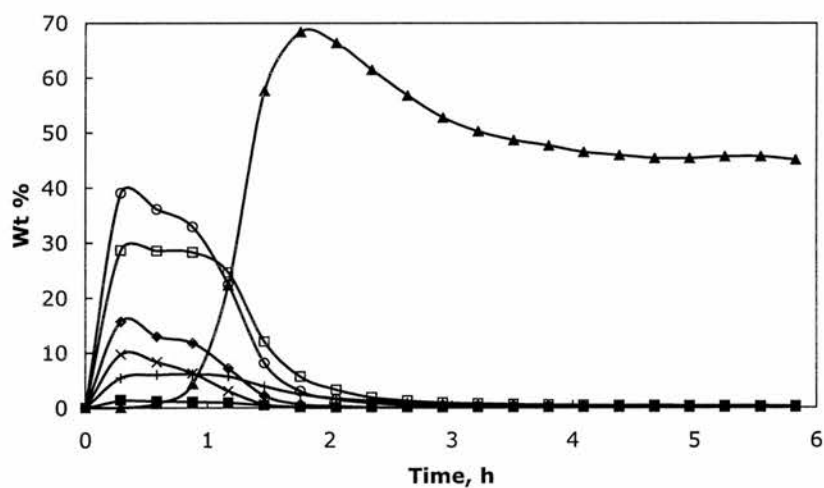


Figure 5.13: Plot of product stream composition (wt %) vs time (h) with a NiSi-STA-2. Key: ■ ethane, + methane, □ ethene, ○ propene, ◆ C₄s, × C₅s and ▲ DME.

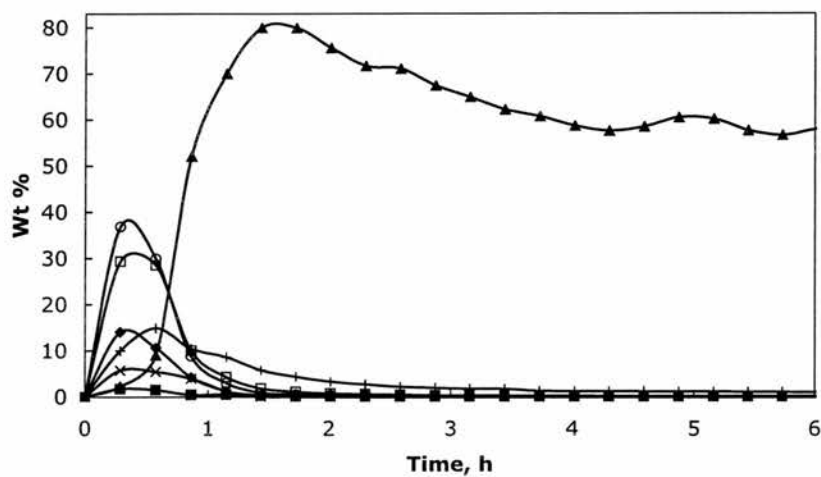


Figure 5.14: Plot of product stream composition (wt %) vs time (h) with a Si-STA-6. Key: ■ ethane, + methane, □ ethene, ○ propene, ◆ C₄s, × C₅s and ▲ DME.

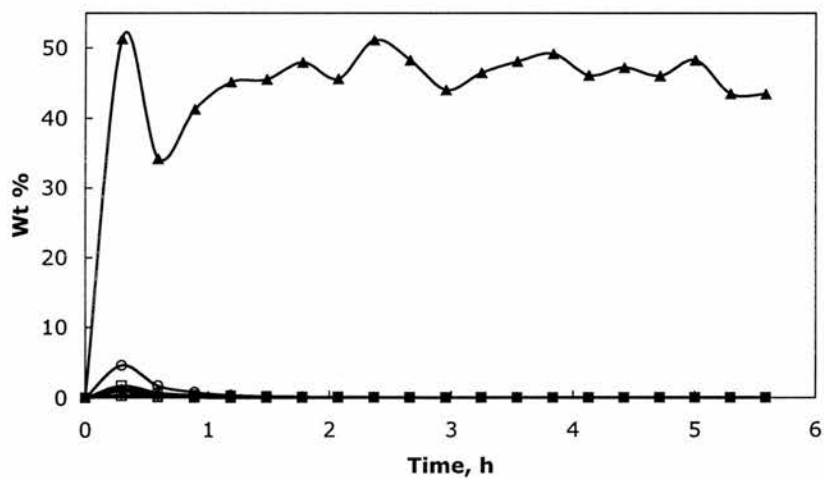


Figure 5.15: Plot of product stream composition (wt %) *vs* time (h) with a Mg-STA-6. Key: ■ ethane, + methane, □ ethene, ○ propene, ◆ C₄s, × C₅s and ▲ DME.

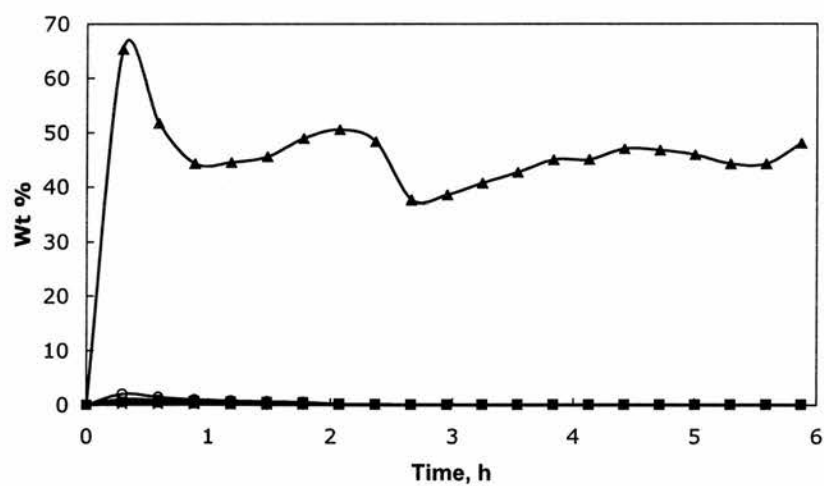


Table 5.3: MTO conversion data for SAPO-34, SAPO-56, Si-STA-2, NiSi-STA-2, Si-STA-6 and Mg-STA-6 after *ca* 20 min on stream.

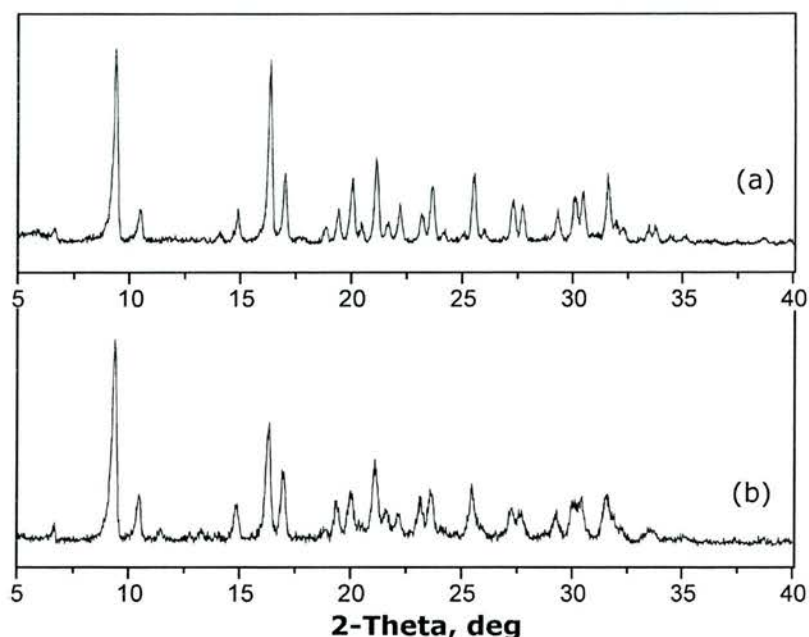
Material	Conversion, wt%	Distribution of products, ¹ wt %									
		DME	CH ₄	C ₂ H ₆	C ₂ H ₄	C ₃ H ₆	C ₄	C ₅	C ₂ H ₄ / C ₃ H ₆		
SAPO-34	100	0	1.0	2.8	27.5	50.3	15.1	3.3	0.5		
SAPO-56	100	0	3.7	2.7	27.8	47.6	14.5	3.6	0.6		
Si-STA-2	100	0	5.4	1.4	28.6	39.1	15.7	9.7	0.7		
NiSi-STA-2	100	2.2	10.0	1.7	29.3	36.9	14.1	5.8	0.8		
Si-STA-6 ²	60.5	51.3	0.4	0.3	1.7	4.6	1.3	0.9	0.4		
Mg-STA-6	70.4	65.3	0.5	0.6	1.1	2.0	0.6	0.2	0.6		

¹ Water excluded in calculation.² Si-STA-6 was calcined *ex situ*, but activated within the reactor.

Table 5.4: MTO conversion data for Si-STA-7 provided by Dr A. Beale (Royal Institution). Catalysis was performed with a single sample at 400 °C, 450 °C and 500 °C (twice). Between each run the catalyst was regenerated in flowing oxygen.

Temp, °C	Time on stream, min	Conver- sion, wt%	Distribution of products, wt%									
			DME	CH ₄	C ₂ H ₄	C ₃ H ₆	C ₄ H ₈	C ₅ H ₁₀	C ₂ H ₄ / C ₃ H ₆			
400	10	35.8	97.5	0.4	0.9	1.2	0	0	0	0.8		
450	10	95.5	58.6	5.2	13.6	18.9	2.9	0.8	0.7			
500	5	92.5	15.8	6.7	31.4	33.7	6.4	3.0	0.9			
500	40	54.3	97.0	1.8	0.7	0.5	0	0	1.3			
500	5	94.4	5.9	6.4	34.3	43.6	8.1	1.0	0.8			
500	40	67.6	96.4	2.1	0.8	0.6	0.1	0	1.3			

Figure 5.16: Powder X-ray diffraction patterns of Si-STA-7, as-prepared (a) and after MTO reaction, 4 cycles (b).



5.2.3 Discussion

The methanol to olefins reaction was carried out over a selection of materials of varying catalyst volumes. These will be discussed together. SAPO-34, the catalyst used commercially, performed best in terms of lifetime, with good activity and excellent selectivity to ethene and propene. After *ca* 20 min 28 wt% ethene is present in the product stream, this increased to 40 wt% after 2 h (at the expense of propene). 10–15 wt% C₄ hydrocarbons are also produced. In the Sunbury experiments an induction period was observed while DME, but no hydrocarbons, are produced. This is consistent with the mechanism proposed by Haw *et al* [186, 187] who envisage the active site in SAPO-34 to include a methylbenzene molecule. They suggested this forms during a kinetic induction period but cannot then pass through the material's small pores. Methylbenzene acts as a “scaffold” on which C–C bonds are formed or broken

(as opposed to going *via* higher-energy intermediates or transition states). To a lesser extent an induction period is also found with the STA-*n* materials.

Si-STA-2 and SAPO-56 have similar activities and selectivities. This is perhaps unsurprising, given the similarity in the shape and size of the cavity in these materials (see Figure 3.24, page 121). The catalyst lifetimes are much reduced when compared with SAPO-34.

Si-STA-6 also has a lower overall activity and shorter lifetime than SAPO-34. The small catalyst bed samples (SAPO and MgAPO) are particularly poor (in the product stream hydrocarbons constitute only 9.3 wt% and 5.5 wt%, respectively). Anomalously the ethene level remains high in the 3 cm³ bed run (but not the others). The reasons behind these observations will not be speculated upon further.

The structure of Co-STA-7 collapses quickly (presumably due to hydrolysis of Co-O bonds) and so the total activity is very low. The methanol WHSV used for the Si-STA-7 experiment is at least an order of magnitude higher than the others so direct comparison is unfair. Interestingly the ethene/propene ratio of both **SAV** materials reaches 1.3, comparable with that found in SAPO-34, but significantly greater than the other catalysts tested.

The inclusion of small amounts of Ni in the catalysts (SAPO-34, STA-2 and STA-6) reduced catalyst lifetime, but promotes the formation of C₁-C₂ products. Levels of Ni are very low and not expected to be in tetrahedral coordination within the framework (the samples are not blue). In NiSi-STA-2, for example, the methane production doubles to 10% at the expense of propene, and in particularly C₅ hydrocarbons, compared to Si-STA-2. The ethene/propene ratio increase for **CHA** and **SAT** materials but not **SAS**.

5.2.4 Conclusion

Materials with the **SAT** and **SAV** framework types possess 3-D pore systems and are promising catalysts for the conversion of methanol to olefins. The **SAS** framework contains 1-D channels and it is presumably for this reason that its activity is less good. Si-STA-7 **SAV** is particularly selective towards ethene (*c.f.* commercial SAPO-34). Catalyst lifetimes are lower, but reaction

conditions have not yet been optimised.

Including Ni in the materials would seem to offer the improved ethene/propene ratios reported in the literature. [178] Ni is expected to be extra-framework by the methods of synthesis employed in the present work; if it were to be incorporated into the framework further benefits *may* be conferred. The SAV framework possessed two interconnecting channel systems parallel to the *c* axis, so the inclusion of extra-framework Ni (if such a material could be prepared) may be less harmful to the overall activity and may further improve selectivity towards ethene.

5.3 *n*-Butane cracking

The active sites in acid catalysts were described in Chapter 1. Both experimental and theoretical studies of the origin of Brønsted acidity in zeolites have been carried out. [188, 189, 190] A proton is attached to an oxygen neighbouring an Al and Si atom which results in a “bridging hydroxyl group”. The first description of the structure of such groups in zeolites was provided by Uytterhoeven *et al* [191] who proposed a structure based on a Si–OH group, strongly influenced by the neighbouring Al (as described previously). This model was supported by data that showed the number of bridging hydroxyl groups was equal in number to the Al atoms in the framework. The Si–OH vibration frequency was also observed to decrease with respect to a terminal silanol because of the interaction with the Al. The model was altered later so that the oxygen was chemically bonded to both Si and Al atoms. [192]

The increased acidity of the bridging hydroxyl proton relative to one in a terminal silanol group can be explained [193] with reference to Gutmann’s rules:

- (i) the length of the nearest bonds to the site where donor–acceptor interaction occurs increases with increasing strength of the interaction;
- (ii) the bond length increases as its ionicity increases;

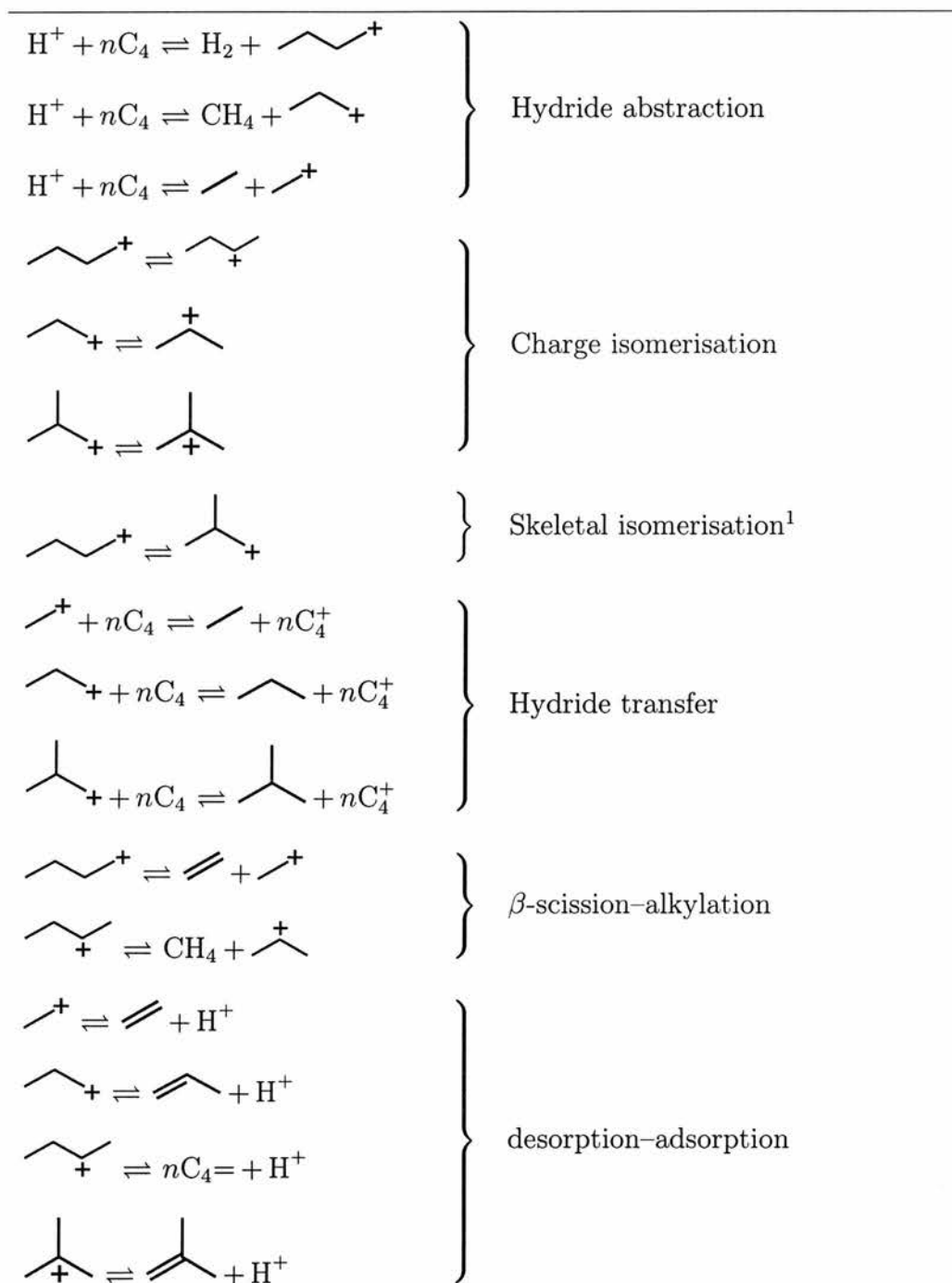
- (iii) the lengths of the bonds generated in a coordination site increase as the coordination number increases.

In the bridging hydroxyl group the coordination of the oxygen will increase the length of the OH bond with respect to the terminal silanol making the proton more acidic. The increase in the electronegativity in the neighbourhood of the OH will induce transfer of electron density from H to O (the more electronegative atom), also increasing the length of the OH bond.

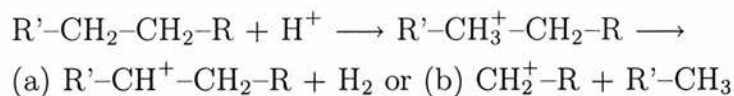
The key questions in designing solid acid catalysts are: (i) what type of acid site is required (Brønsted or Lewis)? (ii) what acid strength is required to activate the reactant molecules? and (iii) how can the number of the required acid sites be maximised?

A number of methods are commonly applied to characterise surface acidity, including: (i) titration methods, (ii) adsorption and temperature programmed desorption (TPD) of bases, (iii) infra-red spectroscopy, and (iv) probe reactions. The titration methods involve a series of indicators with different pK_{as} . This method has problems, not least the fact that the equilibrium is rarely achieved due to diffusion constraints brought about by the limited pore space. In the TPD method an excess of ammonia, pyridine, *n*-butylamine or quinoline are typically adsorbed onto the solid, the amount that is chemically adsorbed correlating to the number of acid sites. Their strength is determined by calorimetry to yield the heat of adsorption at different base loadings. However, the base may decompose and will adsorb on both Brønsted and Lewis acid sites. Infra-red spectroscopy can overcome this latter difficulty. Pyridinium ions (pyridine protonated by a Brønsted site) produce bands (*ca* 1540 cm^{-1} and 1640 cm^{-1}) different from those coordinated to Lewis acid sites (*ca* 1450 cm^{-1} and 1620 cm^{-1}). [131] Qualitative data are obtained by measuring the intensity of these bands normalised with extinction coefficients given in the literature. [194, 195] This allows the number of Brønsted and Lewis acid sites capable of retaining pyridine at a given temperature to be calculated. Alternatively probe reactions, such as butane cracking, may be used. This will be considered in detail now.

Cracking reactions involve Brønsted acid sites. The mechanism is complex

Table 5.5: Principal intermediate species formed during *n*-butane cracking reactions over zeolites (see text for further details).¹ Not thermodynamically favoured at typical reaction temperatures. [196]

(see Table 5.5) and so will only be briefly outlined here, but the primary process is thought to involve the protonation of the alkane at the Brønsted acid site to form a carbonium ion (a penta-coordinated carbon). This then decomposes to a carbenium ion (carbocation) and (a) H_2 , or (b) an alkane, thus:



The carbenium ions subsequently re-protonate the zeolite and desorb as alkenes. This reaction pathway is important when operating at high temperatures and low reactant pressures, particularly when there are no alkenes in the feed. Evidence comes from two directions, (a) the products formed (especially H_2 , CH_4 and alkenes) agree with mechanistic expectations [197] and, (b) rapid H/D exchange in alkanes occurs without cracking, implying that the formation of carbenium ions is not rate limiting. [198]

Secondary reactions such as hydride transfer, alkylation, isomerisation and β -scission, may occur if the lifetime of the carbenium ions are significant (see Table 5.5). This is the case if strong acid sites are present because the carbenium ions will be more strongly adsorbed and so have a greater probability of collision with other molecules from the gas phase before desorption. Hydride and alkyl shifts are facile in carbocations which results in complex product distributions.

Hydride transfer and cyclisation reactions form aromatic compounds and coke. (Although, for aromatic compounds to appear in the product stream the zeolite pores must be of adequate size.) Such reactions should not be considered true cracking steps. The coke is a polymeric product with a complex and often ill-defined molecular formula that, in the case of alkane cracking, is formed *via* the alkenes produced during the cracking process.

In the following section the acidity of four materials is examined by this method. Materials with the **CHA** and **SAT** frameworks performed best in the MTO reaction and so these were selected for further characterisation. For comparison materials with the **ATO** and **AFX** frameworks were also examined.

Further to this, the acidity of these and other materials are assessed by the temperature programmed desorption of *n*-butylamine.

5.3.1 Experimental

SAPO-34, SAPO-56 and Mg–STA-2 were made as described previously, Si–STA-3 (ATO) was prepared according to the literature. [110]

Cracking reactions were carried out with *n*-butane (BOC, 99.7%) at $2\text{ cm}^3\text{ min}^{-1}$, $\text{GHSV} = 6.7\text{ h}^{-1}$ in the CRD reactor described above. Helium was used as the carrier gas ($28\text{ cm}^3\text{ min}^{-1}$). Catalysts of $-40 +100$ mesh were calcined *in situ* as before. During the run the temperature was raised from $350\text{--}550\text{ }^\circ\text{C}$ in 25 ° steps. The furnace heating rate was $10\text{ }^\circ\text{C min}^{-1}$. At each temperature analysis was performed after 30 min and 60 min to check reproducibility and the results averaged. Analysis was performed by GC (FID detector) with a Chrompack PLOT ($\text{Al}_2\text{O}_3/\text{KCl}$) $25\text{ m} \times 0.53\text{ mm}$ i.d. fused silica capillary column, with He carrier gas ($5\text{ cm}^3\text{ min}^{-1}$), using a heating program 2 min isothermal at $40\text{ }^\circ\text{C}$, $40\text{--}60\text{ }^\circ\text{C}$ at $10\text{ }^\circ\text{C min}^{-1}$, 4 min isothermal at $60\text{ }^\circ\text{C}$, $60\text{--}110\text{ }^\circ\text{C}$ at $20\text{ }^\circ\text{C min}^{-1}$, then 5 min isothermal at $110\text{ }^\circ\text{C}$. Eluting peaks were identified from work done previously in this laboratory. [199] Once the reaction was complete the reactor was automatically purged with He ($25\text{ cm}^3\text{ min}^{-1}$) for 10 h at $100\text{ }^\circ\text{C}$.

SAPO-34, SAPO-56, Si–STA-2, Si–STA-3 and Si–STA-6 were activated in a tube furnace at $300\text{ }^\circ\text{C}$ for 5 h under dry flowing nitrogen. Base was then adsorbed onto the solid for 1 h at $100\text{ }^\circ\text{C}$ by allowing the gas flow to bubble first through neat *n*-butylamine before entering the furnace. The physisorbed amine was partially removed by heating the samples under flowing nitrogen for a further 1 h. TGA was performed on portions of *ca* 12 mg, under flowing nitrogen ($110\text{ cm}^2\text{ min}^{-1}$).

5.3.2 Results

The ability of four materials, SAPO-34, SAPO-56, Mg–STA-2 and Si–STA-3, to crack *n*-butane was studied. The former three are small pore, while the

latter is a large pore material. SAPO-34 and SAPO-56 were prepared from gels described in Section 5.2.2 while Mg-STA-2 and Si-STA-3 were crystallised from gels of composition 0.15Mg:0.85Al:1.0P and 0.2Si:1.0Al:0.8P, respectively. Overall conversions are given as Arrhenius plots (Figure 5.17); the product selectivities are given in Tables 5.6–5.9. A “blank” run over quartz granules (of the same size as the catalyst pellets) resulted in a conversion of less than 1 wt% at 550 °C.

Hydrocarbon production at *ca* 20 wt% conversion is illustrated in Figure 5.18.

Figure 5.17: Arrhenius plots of rates of *n*-butane cracking for SAPO-34 (○), SAPO-56 (△), Mg-STA-2 (◇) and Si-STA-3 (□). GHSV = 6.7 h⁻¹.

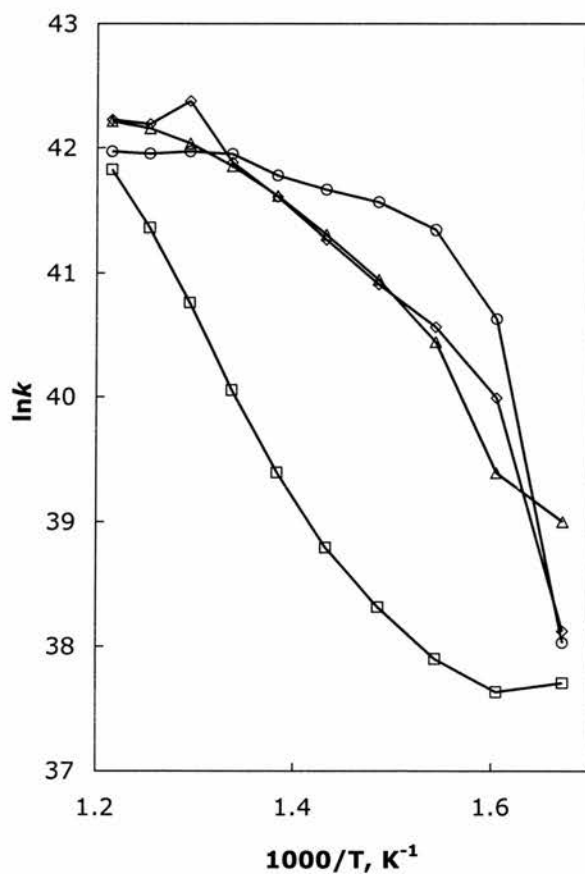


Table 5.6: Conversion and product distribution data for *n*-butane cracking by SAPO-34.

Temp, °C	Conver- sion, wt%	Distribution of products, wt%													
		CH ₄	C ₂ H ₆	C ₂ H ₄	C ₃ H ₈	C ₃ H ₆	<i>i</i> -C ₄ H ₁₀	<i>E</i> -C ₄ H ₈	C ₄ H ₈	<i>i</i> -C ₄ H ₈	<i>Z</i> -C ₄ H ₈	C ₄₊	C ₃ H ₈ / C ₃ H ₆		
325	0.8	0	0	6.9	71.8	4.1	0	4.3	0	0	2.8	10.2	17.5		
350	10.6	0.5	0.5	1.7	83.1	2.6	0	1.4	0.6	0.6	1.0	8.1	32.0		
375	21.6	0.6	0.6	1.9	84.9	3.1	0	1.2	0.6	0.7	0.8	5.6	27.2		
400	26.9	1.0	1.1	2.7	83.7	3.9	0	1.2	0.6	0.8	0.8	4.1	21.6		
425	29.8	1.6	2.0	4.0	80.3	5.0	0.3	1.3	0.7	1.0	0.9	3.0	16.2		
450	33.3	2.7	3.1	5.8	75.4	6.4	0.3	1.3	0.8	1.1	1.0	2.0	11.8		
475	39.6	4.5	4.9	7.4	69.4	7.5	0.6	1.3	0.9	1.3	1.0	1.2	9.2		
500	40.4	7.6	7.5	9.7	59.8	9.2	0.6	1.4	1.0	1.5	1.0	0.8	6.5		
525	39.7	13.0	11.3	12.2	46.2	11.0	0.6	1.4	1.1	1.6	1.1	0.5	4.2		
550	40.4	18.7	14.8	14.0	32.4	13.6	0.7	1.5	1.2	1.8	1.1	0.3	2.4		

Table 5.7: Conversion and product distribution data for *n*-butane cracking by SAPO-56.

Temp, °C	Conver- sion, wt%	Distribution of products, wt%												
		CH ₄	C ₂ H ₆	C ₂ H ₄	C ₃ H ₈	C ₃ H ₆	<i>i</i> -C ₄ H ₁₀	<i>E</i> -C ₄ H ₈	C ₄ H ₈	<i>i</i> -C ₄ H ₈	Z-C ₄ H ₈	C ₄₊	C ₃ H ₈ / C ₃ H ₆	
325	2.1	0	0.7	3.1	70.4	2.4	0	1.4	0	2.9	1.0	18.1	29.3	
350	3.1	0	0.8	2.9	68.9	2.5	0	1.9	0	2.9	1.4	18.7	27.8	
375	8.8	0.7	0.8	2.6	63.4	2.6	11.6	1.3	0.6	2.2	0.9	13.2	24.0	
400	14.5	1.1	1.2	3.5	67.3	3.4	9.1	1.2	0.6	2.2	0.9	9.3	19.8	
425	20.8	1.8	1.9	4.7	69.0	4.2	7.4	1.2	0.7	2.1	0.9	6.1	16.3	
450	28.3	2.8	3.0	5.9	68.8	5.2	5.7	1.2	0.7	2.0	0.9	3.9	13.4	
475	35.9	4.5	4.6	7.1	66.6	6.2	4.2	1.1	0.7	1.9	0.8	2.1	10.7	
500	43.1	7.5	7.2	8.4	60.9	7.4	2.9	1.1	0.8	1.8	0.8	1.3	8.2	
525	48.6	12.3	11.0	9.8	51.3	8.6	1.8	1.0	0.8	1.7	0.8	0.9	5.9	
550	51.5	19.6	16.2	11.0	37.1	9.8	1.2	1.0	0.8	1.6	0.8	1.0	3.8	

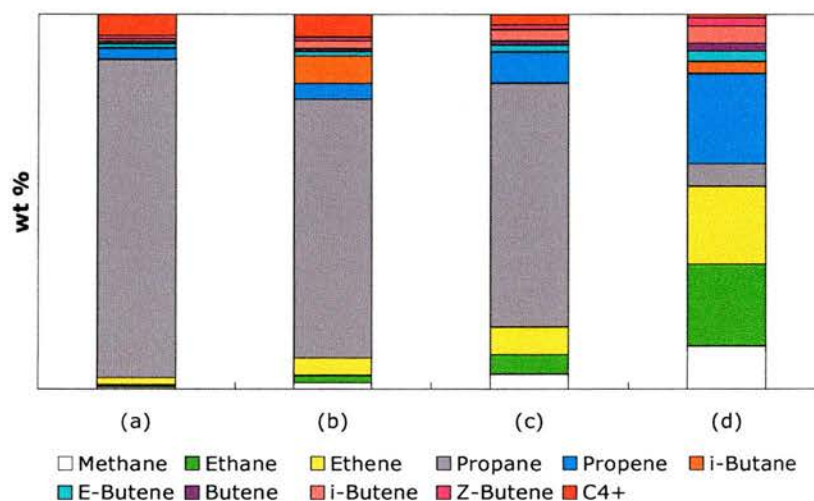
Table 5.8: Conversion and product distribution data for *n*-butane cracking by Mg-STA-2.

Temp, °C	Conver- sion, wt%	Distribution of products, wt%													
		CH ₄	C ₂ H ₆	C ₂ H ₄	C ₃ H ₈	C ₃ H ₆	<i>i</i> -C ₄ H ₁₀	<i>E</i> -C ₄ H ₈	C ₄ H ₈	<i>i</i> -C ₄ H ₈	<i>Z</i> -C ₄ H ₈	C ₄₊	C ₃ H ₈ / C ₃ H ₆		
325	0.9	0	0	5.2	76.5	5.0	0	0	0	5.4	0	7.9	15.3		
350	5.6	1.3	1.5	3.7	70.9	4.8	0	2.0	1.0	3.4	1.5	10.0	14.8		
375	9.9	1.7	2.1	4.7	71.5	5.8	0	1.9	0.9	3.2	1.4	6.6	12.3		
400	14.0	2.7	3.4	6.2	68.6	7.2	0	1.9	1.0	3.2	1.4	4.3	9.6		
425	20.0	4.0	5.2	7.4	65.2	8.3	0	1.8	1.0	3.0	1.4	2.7	7.8		
450	28.1	5.8	7.4	8.4	59.6	9.3	1.0	1.7	1.0	2.8	1.2	1.8	6.4		
475	37.0	8.3	10.4	9.7	52.8	10.5	0.9	1.5	1.0	2.5	1.2	1.2	5.1		
500	60.7	11.5	14.1	11.3	43.9	11.7	0.7	1.4	1.0	2.3	1.1	0.8	3.7		
525	50.4	15.5	18.0	13.2	32.9	13.3	0.7	1.4	1.1	2.3	1.1	0.6	2.5		
550	52.1	19.3	21.3	15.2	21.8	15.1	0.6	1.4	1.1	2.2	1.1	0.7	1.4		

Table 5.9: Conversion and product distribution data for *n*-butane cracking by Si-STA-3.

Temp, °C	Conver- sion, wt%	Distribution of products, wt%													C ₃ H ₈ / C ₃ H ₆	
		CH ₄	C ₂ H ₆	C ₂ H ₄	C ₃ H ₈	C ₃ H ₆	<i>i</i> -C ₄ H ₁₀	<i>E</i> -C ₄ H ₈	C ₄ H ₈	<i>i</i> -C ₄ H ₈	<i>Z</i> -C ₄ H ₈	C ₄₊	C ₃ H ₈	C ₃ H ₆		
325	0.6	0	0	31.2	14.1	19.8	0	8.5	0	8.9	6.2	11.3	0.7	0.7		
350	0.5	0	0	13.0	14.5	21.9	0	11.2	0	19.4	8.1	11.9	0.7	0.7		
375	0.7	0	5.7	10.7	11.6	21.1	0	10.0	2.8	20.9	8.1	9.1	0.5	0.5		
400	1.0	4.5	9.3	12.5	9.2	20.3	0	8.5	5.0	17.8	6.8	6.1	0.5	0.5		
425	1.7	7.0	14.3	15.7	8.2	20.9	0	7.1	3.9	13.9	5.5	3.6	0.4	0.4		
450	3.1	9.1	18.1	18.3	7.3	22.1	0	5.4	3.3	10.3	4.2	1.8	0.3	0.3		
475	5.9	10.5	20.6	19.9	6.9	23.5	0	4.2	2.7	7.6	3.2	0.8	0.3	0.3		
500	12.1	10.9	21.0	20.0	6.3	23.5	4.0	3.2	2.2	5.7	2.5	0.7	0.3	0.3		
525	21.9	11.6	21.8	20.8	6.0	24.1	3.2	2.7	2.1	4.6	2.3	0.8	0.2	0.2		
550	35.0	12.7	22.7	22.1	5.5	24.2	2.3	2.3	1.9	3.8	1.7	0.8	0.2	0.2		

Figure 5.18: Plot of hydrocarbon production (wt%) at *ca* 20% conversion, SAPO-34 (a), SAPO-56 (b), Mg–STA-2 (c), and Si–STA-3 (d).



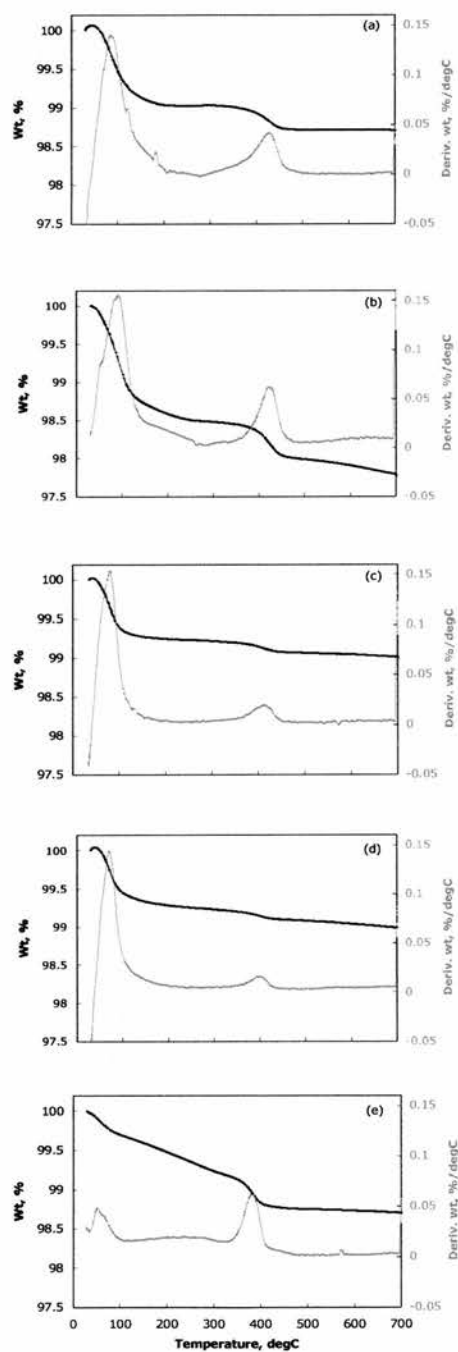
The temperature maximum during the weight loss while *n*-butylamine desorbs was found to be as follows for each material: SAPO-34 = 429.9 °C, SAPO-56 = 423.9 °C, Si–STA-6 = 413.2 °C, Si–STA-2 = 404.3 °C and Si–STA-3 = 383.7 °C (see Figure 5.19).

5.3.3 Discussion

The rate of catalytic hydrocarbon (*n*-butane) cracking, and the observed product distribution, correlates to acid site strength. [200] The distribution also depends on reaction temperature, contact time and conversion. But, as was introduced above, the primary mechanism yields hydrogen, methane, propene and butenes. If secondary reactions take place (H-transfer, β -scission, isomerisation, alkylation) to yield alkanes such as propane, this is indicative of strong acid sites. *n*-Butane is a useful probe molecule (with the materials of interest here) because it is small enough to fit within 8-ring pores, but also large enough for the product distribution to indicate the cracking mechanism.

The Arrhenius plots (Figure 5.17) show clearly, since they deviate from linearity, that deactivation has occurred during the reactions. SAPO-34 has

Figure 5.19: TGA plots for the desorption of *n*-butylamine from SAPO-34, 429.9 °C (a), SAPO-56, 423.9 °C (b), Si-STA-6, 413.2 °C (c), Si-STA-2, 404.3 °C (d) and Si-STA-3, 383.7 °C (e).



deactivated most and Si-STA-3 least. The maximum conversion for SAPO-34 is 40 wt%, for Si-STA-3 it is 35 wt%, for SAPO-56 it is 52 wt% and for Mg-STA-2 it is 61 wt%. Conversions of less than 10 wt% are generally required for coking to become insignificant. [151]

SAPO-56 and Mg-STA-2 are of intermediate acidity, between SAPO-34 and Si-STA-3, which show the highest and lowest rates, respectively. The amount of propane generated relative to propene in these reactions is indicative of the mechanism. The maximum propane/propene ratios for SAPO-34, SAPO-56, Mg-STA-2 and Si-STA-3 are 32.0, 29.3, 15.3 and 0.7, respectively. In Si-STA-3 the level of propane production is low and not affected significantly by temperature (1.9 wt% at 550 °C). This suggests the primary mechanism is dominating and that the material possesses few strong acid sites. In contrast, with SAPO-34 the rate of propane production is high, but increases more slowly between 375 °C and 475 °C, after which it falls sharply. At 475 °C 27.5 wt% propane is produced. The secondary mechanism becomes less important as the reaction progresses (presumably the strong acid sites are poisoned before the weaker ones), nevertheless SAPO-34 contains many strong acid sites. With SAPO-56 and Mg-STA-2 *ca* 26 wt% propane is produced at 500 °C, the maximum for both solids. But while the secondary mechanism dominates throughout with SAPO-56 a sharp change occurs at 500 °C for Mg-STA-2. Both these solids contain some strong acid sites. On the basis of these results the materials can be written in order of acidity, thus: SAPO-34 > SAPO-56 > Mg-STA-2 > Si-STA-3.

The temperature at which *n*-butylamine desorbs from a solid acid can be related quantitatively to acid site strength (presuming diffusion is not severely limited and the probe molecule does not react). On the basis of the results obtained the materials can be written in order of acidity, thus: SAPO-34 > SAPO-56 > Si-STA-6 > Si-STA-2 > Si-STA-3. This is in agreement with the cracking reactions.

5.3.4 Conclusion

The rate of *n*-butane cracking, coupled with the product distribution, can be used as a probe reaction to determine acid site strength in small pore silicoaluminophosphates and related materials. So too can the temperature at which *n*-butylamine desorbs. SAPO-34 was found to be the strongest acid of those tested, and Si-STA-3 the weakest. SAPO-56, Si-STA-6, Si-STA-2 and Mg-STA-2 are of intermediate acidity (and are comparable to Si-STA-7 [181]). The activity and lifetimes observed in the MTO reaction may be correlated to this result (SAPO-34 being most active for the longest time, while the STA-2 and STA-7 materials were less active), although the mechanistic considerations discussed above suggest the situation is more complex.

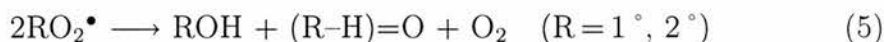
5.4 Oxidation catalysis

Liquid phase oxidation reactions have historically employed soluble metal salts or complexes and molecular oxygen (O_2), hydrogen peroxide (H_2O_2) or alkyl hydroperoxides (RO_2H) as the oxidant. Heterogeneous oxidation catalysts have, however, been developed for certain reactions. In the 1970s a Ti^{IV}/SiO_2 was commercialised by Shell for the production of propylene oxide, while in the 1980s Enichem developed the titanium silicate TS-1 (**MFI**) for a variety of reactions, including epoxidation. [201] The oxidation of alkanes is a promising area for developing heterogeneous catalysts based on metalloaluminophosphate materials. A selection of the materials discussed in the previous chapters have been examined in this reaction. Firstly some possible mechanisms for oxidation reactions, and challenges in liquid phase catalysis will be discussed.

Metals such as Ti, V, Mn, Fe, Co, Mo and W may be incorporated into the framework structure of zeolites and aluminophosphates to create catalytic sites for oxidation reactions. These typically follow one of three mechanisms: (i) free radical chain autoxidation, (ii) catalytic oxygen transfer, or (iii) oxidation of coordinated substrates, followed by reoxidation of the reduced metal ion.

One electron oxidants such as Mn^{III} , Fe^{III} and Co^{III} catalyse free radical chain autoxidation processes [202] by promoting the decomposition of alkyl

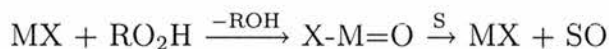
hydroperoxides to alkoxy and alkyl peroxy radicals. Thus:



Oxygen transfer reactions occur with H_2O_2 or RO_2H and may be divided into two classes, depending on the intermediate formed. The peroxometal pathway:



typically involves early transition metals with d^0 electron configurations such as Ti^{IV} , V^{V} , Mo^{VI} and W^{VI} . The metal acts as a Lewis acid and the reaction does not involve a change in the metal ion's oxidation state. Molecular oxygen is not a suitable oxidant and so H_2O_2 or *tert*-butyl hydroperoxide (TBHP) must be used. In contrast, the oxometal (Mars–van Krevelen) mechanism involves a two electron redox reaction at the metal centre:



and is usually accomplished by late or first row transition metals such as V^{V} , Cr^{VI} , Mn^{V} , Ru^{VI} , Ru^{VIII} and Os^{VIII} . Molecular oxygen may be used as the oxidant. Vanadium, for example, can follow either mechanism, depending on the substrate: alkene epoxidation and heteroatom oxidation usually proceed *via* the peroxometal pathway, while benzylic and allylic oxidation proceed *via* the oxometal pathway. Metals which catalyse oxidation reactions *via* either pathway are also capable of one electron transfer processes, which lead to competition from free radical processes. In the liquid phase it can be difficult to distinguish between the oxometal mechanism and competing homolytic pathways.

The stability of heterogeneous catalysts is of particular interest as robustness is clearly required for commercial viability. Thermal stability is certainly an issue with aluminophosphate based catalysts, but so too is *leaching*. The metal cations (Mn, Co *etc.*) which form the active sites within aluminophosphate-based catalysts may be leached out of the framework during liquid phase reactions. Solvolysis of M–O bonds occurs owing to the strong complexation and solvolytic properties of oxidants such as H₂O₂ and RO₂H and/or products (H₂O, ROH, RCO₂H *etc.*). In the reaction considered in this work it is the carboxylic acids which are most likely to leach metal cations. Leached cations can sometimes be more active (homogeneous) catalysts and so this possibility should be investigated. To observe the effect (if any) of leaching the catalyst should be filtered *at the reaction temperature* and a portion of the filtrate allowed to react further. If no further reaction is observed the catalyst would appear to be truly heterogeneous. Filtering at reaction temperature, as opposed to cooling first, precludes the readsorption of the leached metal cations onto the solid, or changes in the oxidation state of the metal cations in solution. Recycling the catalyst without loss of activity does not show rigorously that the reaction is proceeding heterogeneously as very small (0.1 %) amounts of leached cations may be responsible for the observed activity.

The most widely studied class of framework substituted cobalt catalysts are the CoAPO microporous solids, where it is widely accepted Co substitutes for Al. [203] The redox properties depend strongly on the framework type. EXAFS studies of CoAPO-5, CoAPO-18, CoAPO-36 and CoAPO-44 have shown that the fraction of cobalt present in the calcined materials as Co^{III} is 0.20, 0.45, 1.00 and 0.80, respectively. [204] Co^{II} is stabilised in CoAPO-5 and CoAPO-36 by an oxygen vacancy in the Co coordination sphere which leads to Lewis acidity. The reason why Co^{II} is oxidised to Co^{III} in some materials and stabilised by oxygen vacancies in others is unclear, however it will certainly have an affect on the observed activity in a particular reaction. Leaching can also be a problem with CoAPO catalysts. Belkhir *et al* found that in the aerobic oxidation of cyclohexane to adipic acid the acetic acid solvent leached Co^{II} from the framework, which was catalysing the observed reaction

homogeneously. [205] In similar work Vanoppen *et al* found that by using a strong non-polar solvent (cyclohexane) Co was not leached, however conversion had to be limited to 10% to prevent excessive adipic acid formation, which would itself leach Co. [206]

The reaction considered here is the oxidation of *n*-hexane, with Co-substituted aluminophosphate catalysts; further consideration will not be given to other reactions, see the reviews by Sheldon [201, 207] for further examples. Selective oxidation of hydrocarbons on the terminal carbon is of industrial interest as a route to feedstocks such as linear alcohols or adipic acid. But obtaining selectivity at this site is a challenging task. In biological systems enzymes such as heme iron cytochromes P-450 [208] and non-heme iron methane monooxygenase [209] catalyse the selective insertion of one oxygen atom derived from a reductive activation of dioxygen into a substrate. Under homogeneous conditions without steric constraints, regioselectivity in such autoxidation reactions is governed by the relative C–H bond-dissociation energies, which decrease from primary to secondary to tertiary carbon atoms (435 kJ mol⁻¹, 396 kJ mol⁻¹ and 381 kJ mol⁻¹, respectively). [210] (A fuller description of homogeneous alkane oxidation catalysis may be found in the book by Parshall and Ittel. [202])

Alkanes may be oxidised unselectively by air in the presence of metal aluminophosphate catalysts. More usefully Thomas *et al* have recently shown that selectivity can be obtained with the appropriate catalyst: MAPO-18 (M = Mn, Co), in the case of the terminal methyl group oxidation of *n*-pentane, *n*-hexane, *n*-octane [211] and *n*-dodecane [212] and MAPO-5 (M = Fe, Mn, Co) in the oxidation of cyclohexane. [213] MnAPO-18 and CoAPO-18 were found to be superior to all but one previously reported inorganic catalyst for these reactions, having a regioselectivity of 65.5% and 61.3%, respectively, for the terminal methyl group in *n*-hexane after 24 h (see Table 5.10, for further details). No C₃ products were observed (or C₄ in the case of *n*-octane). However, in the case of *n*-pentane C₂ and C₃ ketones are the principal products after 24 h. To confirm heterogeneous catalysis the hot-filtering method described above was employed and no further reaction was seen. Similarly, equimolar

Table 5.10: Results of *n*-alkane oxidation reactions by MAPOs. [211]

Catalyst	Pore diameter	Substrate	Metal	C ₁ selectivity, mol %	Conversion, mol %
MAPO-18	3.8 Å × 3.8 Å	<i>n</i> -pentane	Mn	39	8.2
			Co	33	8.8
		<i>n</i> -hexane	Mn	66	8.7
			Co	61	7.2
		<i>n</i> -octane	Mn	62	6.8
			Co	60	7.2
MAPO-11	3.9 Å × 6.3 Å	<i>n</i> -hexane	Co	19	3.6
MAPO-36	6.5 Å × 7.5 Å	<i>n</i> -pentane	Mn	0	5.9
			Co	5	5.5
		<i>n</i> -hexane	Mn	0	5.4
			Co	23	5.2
		<i>n</i> -octane	Mn	7	5.9
			Co	12	5.8
MAPO-5	7.3 Å × 7.3 Å	<i>n</i> -hexane	Co	9	2.4

Reactions were carried out in a 150 cm³ PEEK-lined autoclave containing 50 g of substrate, 1.5 MPa air and 0.5 g catalyst.

mixtures of *n*-hexane and cyclohexane were reacted over CoAPO-18, with no oxidation of the cyclohexane being observed. This was taken to indicate the oxidation takes place *within* the catalyst's pores.

A free radical chain autoxidation mechanism was proposed by Thomas *et al*, [211] which was supported by three experiments. Firstly it was shown that an observed induction period in the yield *versus* time plots could be reduced by the use of a free-radical initiator such as *tert*-butyl hydroperoxide. Secondly, the addition of a radical scavenger, 1% hydroquinone, was seen to greatly hinder the reaction, and thirdly, cyclohexyl peroxide radicals were directly observed during the oxidation of cyclohexane. Thomas *et al* argue that the selectivity observed in the oxidation reactions with MAPO-18 materials derives from the favoured geometry the substrate encounters at the active site.

In the free radical chain autoxidation mechanism the alkane does not interact with the active catalytic site, instead the metal cation catalyses the

decomposition of the intermediate alkyl hydroperoxide, (3) and (3') in the Scheme given above. The terminal selectivity would have to be imposed by constraints on the geometry of the bimolecular reaction between the oxyradical and the alkane, rather than the approach of the alkane to the active site as Thomas *et al* propose. Labinger [214] has argued that the former appears plausible because it suggests that selectivity is imposed not by the geometry of a single alkane within a cage (which is relatively spacious) but by the probability of an oxyradical reacting with an alkane molecule within, or emerging from, a channel in which it is strongly constrained to move in a fully extended conformation. Additionally, this model would imply that (a) the rate of termination, (5) and (5'), is substantially less than the rate of propagation (2) in a small pore microporous solid because of a disfavoured cyclic transition state, and that (b) the effect on diffusion and molecular encounter statistics resulting from the constraints of the small pore system would mean that the relative probability of two low concentration molecules (RO_2^\bullet) meeting would be much less than in an unconstrained system. This would make the reactions (5) and (5') less probable compared with the reaction of the low concentration oxyradical and the high concentration alkane (2). If one or both of these proposals is valid it would explain the observed simultaneous increase in activity and selectivity (normally these vary inversely with respect to one another).

5.4.1 Experimental

$\text{Co}_{0.1}\text{Al}_{0.9}\text{PO}_4$ -18, [215] $\text{Co}_{0.1}\text{Al}_{0.9}\text{PO}_4$ -34, [182] $\text{Co}_{0.08}\text{Al}_{0.92}\text{PO}_4$ -42, [112] $\text{Co}_{0.05}\text{Al}_{0.9}\text{PO}_4$ -STA-2, $\text{Co}_{0.1}\text{Al}_{0.9}\text{PO}_4$ -STA-2 and $\text{Co}_{0.1}\text{Al}_{0.9}\text{PO}_4$ -STA-7 were synthesised by modification of literature methods. Materials were calcined to removed the template molecule which oxidises framework M^{II} to M^{III} (see Figure 5.20).

To investigate the CoAPO microporous solids' ability to catalyse the oxidation of *n*-hexane, reactions were carried out in a Parr Instruments stirred-autoclave micro reactor (Figure 5.21).⁶ The autoclave was charged with the solid catalyst and liquid internal standard (1,2-dichlorobenzene, Aldrich, 99 %)

⁶The system includes a Parr 4592 stainless steel reactor (50 cm³ capacity, unlined)

Figure 5.20: As-prepared CoAPO material containing tetrahedral Co^{II} (blue), and Co^{III} after calcination (green).



and *n*-hexane (Aldrich, 99+ %) substrate. The liquid charge was not allowed exceed two-thirds autoclave capacity. Gas (5% v/v O_2 in N_2 , BOC, β standard) was admitted from a cylinder to a pressure of 1.5–2.0 MPa. The magnetic stirrer rate was set to *ca* 400 rpm and the heater to 100–140 °C. To prevent damage to the liner a low heating rate (2 °C min^{-1}) was used. Experiments were carried out in 12–48 h.

Although liquid samples may be withdrawn from the reactor *via* the sampling tube whenever the reactor is pressurised, this is inappropriate in a reaction that includes a gaseous reactant. Instead a sample was taken after the reactor had been cooled and opened. This was filtered before being analysed by gas chromatography with a CE Instruments GC 8000^{TOP} equipped with a flame ionisation detector (FID) and a Fisons DP700 data processor (integrator). An SGE BP-21 (FFAP) 30 m \times 0.32 mm i.d. fused silica capillary column was employed, with He carrier gas (2 $\text{cm}^3 \text{min}^{-1}$). This column equipped with a Parr 4842 controller unit (incorporating a Watlow model 989 temperature controller) and a Parr A1120HC water-cooled magnetic stirrer drive. A PTFE (Teflon) cup was used to line the inside of the vessel. The reactor head is fitted with a pressure gauge, safety rupture disk, J-type thermocouple, magnetic stirrer drive and valves for liquid sampling *via* a dip-tube, gas inlet and release. All fittings ($\frac{1}{4}$ " male NPT) were adapted to $\frac{1}{8}$ " Swagelok. Leak-tight operation was ensured with a black FFKM (Kalrez) O-ring seal (brown FKM (Viton) O-rings are also available). Prior to use the reactor was thoroughly tested for leaks and the stirring rate calibrated with a tachometer. Electrical safety was ensured with an appropriate circuit incorporated into the control unit which was reset before each experiment (after the thermocouple had been connected and the power switched on). A one-way valve inserted into the gas inlet line, and an externally vented trap attached to the busting disk port, ensured that the reactor contents would not enter either the gas cylinder or laboratory air should the autoclave become over pressurised.

Figure 5.21: Parr Instruments micro reactor system (see text for further details).



enabled separation of all the products of reaction, including carboxylic acids, using the heating program 30–150 °C at 20 °C min⁻¹, followed by 5 min isothermal. Products were identified by GC–MS (CATS Service, St Andrews) and the injection of standard reference samples into the GC.

Further experiments were performed using a locally constructed glass-and-PTFE reaction vessel. [216] The reactor consisted of a *ca* 240 cm³ thick walled glass vessel, sealed with a PTFE valve, through which 5% v/v O₂ in N₂ (as before) could be admitted. The reactor was heated in an oil bath and agitation was achieved from below with a PTFE-enclosed magnetic stirrer. The glass vessel was certified to withstand 1 MPa pressure. For this reason oxidant pressure was limited to 0.5 MPa and the temperature to 80 °C. Products were analysed by GC as described previously.

Samples of Co–STA-2 and Co–STA-7 were sent to Dr R. Raja at the University of Cambridge for testing under similar reaction conditions to those used in the original work of Thomas *et al.* [211] Air was used as the oxidant (3 MPa) and reactions were performed on *n*-octane as well as *n*-hexane (10 g) with 0.15 g of catalyst at 100 °C.

5.4.2 Results

The results of selected experiments carried out in the stainless steel and glass reactors are given in Tables 5.11 and 5.12, respectively. Reactions carried out in the stainless steel reactor, in the absence of a catalyst, but within a PTFE-liner, were found to yield small amounts of C₂ and C₃ oxidised products after 24 h at 100 °C. In a single reaction carried out without a catalyst, or the liner, no reaction was observed. Selected reactions were repeated and the same qualitative results obtained. The use of calcined catalyst which had had *n*-hexane adsorbed into it after calcination did not appear to affect the activity either.

Similar results were found by Dr R. Raja with Co–STA-2 and Co–STA-7: these were not found to convert significant levels of *n*-alkane to C₁ oxidised products (see Tables 5.13 and 5.14).

Table 5.11: Oxidation of *n*-hexane. Reactions were performed in the Parr stainless steel reactor (see text for further details). Oxidation products are recorded qualitatively (with a “×” if observed and a “–” if not) after analysis by gas chromatography.

Catalyst (wt, g)	Volume of hexane, cm ³	O ₂ /N ₂ , MPa	Temp., °C	Time, h	Products		
					C ₁	C ₂	C ₃
CoAPO-18 (0.1)	15	1.5	100	12	–	–	–
CoAPO-18 (0.1)	15	1.5	100	24	–	–	–
CoAPO-18 (0.1)	15	1.5	100	48	–	×	×
CoAPO-18 (0.1)	15	1.5	120	24	×	×	×
CoAPO-18 (0.1)	10	2.0	120	24	–	×	×
CoAPO-18 (0.1)	10 ¹	2.0	120	24	–	–	–
CoAPO-18 (0.1)	15	1.5	140	24	×	×	×
CoAPO-34 (0.1)	15	1.5	100	24	–	–	–
CoAPO-34 (0.1)	15 ²	1.5	100	24	–	×	×
CoAPO-34 (0.2)	15	1.5	100	48	–	–	–
CoAPO-34 (0.2)	15	1.5	140	24	×	×	×
CoAPO-34 (0.1)	5	1.5	140	24	×	×	×
CoAPO-42 (0.1)	15	1.5	100	24	–	×	×
CoAPO-42 (0.1)	15	1.5	120	24	–	×	×
CoAPO-42 (0.1)	15	1.5	140	24	–	×	×

¹ 5 cm³ dichloromethane also present.
² 0.1 g acetic acid also present.

Table 5.12: Oxidation of *n*-hexane. Reactions were performed in the glass reactor (see text for further details). As before, oxidation products are recorded qualitatively (with a “×” if observed and a “–” if not) after analysis by gas chromatography.

Catalyst (wt, g)	Volume of hexane, cm ³	O ₂ /N ₂ , MPa	Temp., °C	Time, h	Products		
					C ₁	C ₂	C ₃
CoAPO-34 (0.25)	15	0.5	80	48	–	–	–
CoAPO-34 (0.25)	15 ¹	0.5	80	48	–	–	–
CoAPO-34 (0.5)	10	0.5	80	24	–	–	–

¹ 0.02 g di-*t*-butyl peroxide also present.

Table 5.13: Oxidation of *n*-hexane. Reactions were performed by Dr R. Raja at the University of Cambridge (see text for further details).

Catalyst	Time, h	Conversion, mol %	Distribution of products, mol %										
			A ₁	B ₁	C ₁	D	E	F ₂	G ₂	H ₃	I ₃	Others	
Co _{0.05} -STA-2	8	3.5	-	4.1	4.6	-	-	-	21.4	12.6	43.7	8.3	5.2
	24	11.4	-	-	11.6	-	-	-	6.3	35.4	9.1	30.7	7.3
Co _{0.10} -STA-2	8	5.8	2.5	4.6	3.6	-	1.3	19.4	6.2	44.5	11.2	6.5	
	24	13.5	-	-	9.4	-	3.9	7.5	23.4	15.5	32.9	7.6	
Co _{0.20} -STA-7	8	12.1	-	-	-	-	-	19.2	6.5	39.5	22.3	12.2	
	24	19.6	-	-	-	-	-	11.2	31.6	16.8	28.5	11.6	

n-hexane = 10 g, catalyst = 0.15 g, oxidant (air) = 3.0 MPa, temp = 100 °C.
 Products: A₁ = 1-hexanol, B₁ = 1-hexanal, C₁ = hexanoic acid, D = adipic acid, E = 1,6-hexanediol + 1,6-hexanedial, F₂ = 2-hexanol, G₂ = 2-hexanone, H₃ = 3-hexanol, I₃ = 3-hexanone, others = fragmentation products.
 Scheme: alkane → -ol → -one → acid.

Table 5.14: Oxidation of *n*-octane. Reactions were performed by Dr R. Raja at the University of Cambridge (see text for further details).

Catalyst	Time, h	Conver- sion, mol %	Distribution of products, mol %										
			A ₁ '	B ₁ '	C ₁ '	D'	E'	F ₂ '	G ₂ '	H ₃ '	I ₃ '	Others	
Co _{0.05} -STA-2	8	2.1	-	6.2	1.9	-	-	-	6.4	61.3	3.7	16.5	4.2
	24	9.3	-	-	7.5	-	-	-	3.9	66.2	-	17.9	4.4
Co _{0.10} -STA-2	8	4.7	2.9	5.0	2.5	-	2.6	8.3	57.5	6.6	10.0	4.7	
	24	15.2	-	-	10.2	-	7.2	5.2	50.8	4.1	16.3	6.2	
Co _{0.20} -STA-7	8	19.7	-	-	-	-	-	6.3	15.9	27.4	41.0	9.3	
	24	25.0	-	-	-	-	-	5.1	19.3	20.5	42.5	12.7	

n-octane = 10 g, catalyst = 0.15 g, oxidant (air) = 3.0 MPa, temp = 100 °C.
Products: A₁' = 1-octanol, B₁' = 1-octanal, C₁' = octanoic acid, D' = diacids, E' = 1,8-octanediol, F₂' = 2-octanol, G₂' = 2-octanone, H₃' = 3-octanol, I₃' = 3-octanone, others = fragmentation products.
Scheme: alkane → -ol → -one → acid.

5.4.3 Discussion

In all the reactions carried out in St Andrews either no oxidation products, or only very low yields of such products, were observed. The conversion of *n*-hexane was approximately 2% at best, although the conversion in terms of oxygen is much greater. Production of C₁ (terminally) oxidised products was, in all cases, at least an order of magnitude less than that of each C₂ or C₃ oxidised compound. The low overall yields mean reliable quantitative data was not obtained.

Activity was observed in the “blank” reactions (*i.e.* those performed without a catalyst). Since these tests were not carried out with a fresh liner, some leached Co was presumably carried over from the previous reaction. This homogeneous Co is assumed to be responsible for the majority of the observed products in all these reactions. This is supported by the fact that most *n*-hexane was unselectively oxidised, *i.e.* not terminally oxidised. The rate of heterogeneous reaction will be slower, limited by diffusion, and so very little terminal oxidation is observed because of the competing, homogeneous, reaction. Increasing the oxygen/*n*-hexane ratio, or adding promoters such as acetic acid or di-*t*-butyl peroxide were not sufficient to increase the heterogeneously catalysed reaction rate.

The use of a glass reactor was expected to eliminate cross-contamination by leached Co, while its larger volume enabled more advantageous oxygen/*n*-hexane ratios to be employed (so that *n*-hexane conversion could be increased). However, the reaction is very slow at temperatures lower than 100 °C and no conversion was obtained.

In view of the poor results obtained with CoAPO-18, CoAPO-34 and CoAPO-42 materials, Co-STA-2 and Co-STA-7 were not studied in St Andrews. The results obtained by Dr R. Raja show that these catalysts oxidise *n*-hexane and *n*-octane unselectively, giving mainly C₂ and C₃ functionalised products. No C₁ products are observed with Co-STA-7. The higher cobalt loaded STA-2 materials produce more di-oxidised products. The overall conversions are relatively high, reflecting the increase in oxidant. These results are somewhat surprising given the materials' pore sizes (see Table 5.15) and

Table 5.15: Summary of results of *n*-hexane and *n*-octane oxidation reactions by MAPOs.

Catalyst	Pore diameter	Substrate	C ₁ selectivity, mol %	Conversion, mol %
CoAPO-18 ¹	3.8 Å × 3.8 Å	<i>n</i> -hexane	61	7.2
		<i>n</i> -octane	60	7.2
CoAPO-36 ¹	6.5 Å × 7.5 Å	<i>n</i> -hexane	0	5.4
		<i>n</i> -octane	12	5.8
CoAPO-5 ¹	7.3 Å × 7.3 Å	<i>n</i> -hexane	9	2.4
Co-STA-2 ²	5.5 Å × 3.0 Å	<i>n</i> -hexane	10.5	12.5
		<i>n</i> -octane	8.9	12.3
Co-STA-7 ²	3.8 Å × 3.8 Å + 3.9 Å × 3.9 Å	<i>n</i> -hexane	0	19.6
		<i>n</i> -octane	0	25.0

¹ Reactions were carried out by Thomas *et al* with 50 g of substrate, 1.5 MPa air and 0.5 g catalyst. [211]

² Reactions were carried out in the present work with 10 g of substrate, 3.0 MPa air and 0.15 g catalyst.

suggest that the reaction may be proceeding homogeneously, although further work is required to confirm this.

5.4.4 Conclusion

The reaction conditions necessary for selective terminal oxidation are experimentally difficult to obtain. The novel materials Co-STA-2 and Co-STA-7 do not produce significant amounts of terminally oxidised products. This suggests the AlPO₄-18 framework is special, given its ability to yield C₁ oxidised products, and that this is an exception, rather than a general case, in small pore materials.

Epilogue

The synthesis of microporous solids with novel framework topologies is challenging, but essential if catalysts are to be prepared that are both active and selective in industrially important reactions. To this end the materials crystallised with 1,4,8,11-tetramethyl-1,4,8,11-tetraazacyclotetradecane, and other macrocycles, have been studied. The use of macrocycles and other amines to template microporous solids shows potential for further discoveries. Two materials have been crystallised during this work (a MgAPO with poly[4-(1,4-diazabicyclo[2.2.2]oct-1-ylmethyl)benzyl] and a CoAPO with 1,5-diaminopentane/18-crown-6) with structures that could not be identified on the basis of their powder XRD patterns. These materials, in particular, require further investigation so that their structures may be solved and their physicochemical properties determined.

The local structural details of $\text{AlPO}_4(\text{F})$ -STA-2 and Mg-STA-2 have been studied. This work could be extended to encompass the pure aluminophosphate and silicoaluminophosphate analogues. The mode by which charge balance is maintained in the former is of particular interest. With MQMAS NMR spectroscopy it should be possible to show this (although impurities make the system complex). Similarly NMR spectroscopy would reveal the environments of silicon in Si-STA-2. The location of cations (Si, Mg) at increasingly high substitution levels must also be investigated since the number and location of such cations influences catalytic properties.

STA-7 possesses a novel framework type (designated **SAV** by the International Zeolite Association) which has been characterised during this project. Its ability, and that of selected STA-2 and STA-6 samples, have been examined for the conversion of methanol to olefins and other reactions. But there

is scope for studying further acidic materials of the STA- n family (substituted with different cations and at different levels) in these reactions. The acid site strength, as well as the framework structure, is of critical importance. The former can be adjusted in these materials by judicious use of framework cation substitution at synthesis, the latter has been considered above.

Appendix A

Single crystal XRD data

In this Appendix atomic coordinates and temperature factors for the key materials studied in this work are presented. The framework structures were solved by single crystal XRD diffraction by either Dr P. Lightfoot or Dr A. M. Z. Slawin (St Andrews). Template positions were derived from molecular modelling studies performed by Dr P. A. Cox (Portsmouth). Selected bond lengths and angles are given here for the structures solved during this work. Coordinates for other materials (STA-2, STA-6 and CoAPO-cyclam-1) are included for reference as they have been used as starting models in Rietveld refinements of powder XRD data.

Table A.1: Atomic coordinates and thermal parameters for STA-2 (**SAT**) templated by babob, from single crystal XRD data and molecular modelling refined in space group $R\bar{3}$, with lattice parameters $a = 12.726(2)$ Å, $c = 30.939(6)$ Å. [98]

Atom	x	y	z	U_{iso}	Occ.
Al(1)	0.7533	0.7572	0.2954	0.0165	1.00
Al(2)	0.5762	0.9023	0.2165	0.0217	1.00
P(1)	0.5778	0.9043	0.1144	0.0194	1.00
P(2)	0.7568	1.0013	0.2914	0.0137	1.00
O(1)	0.6138	0.9393	0.1617	0.0348	1.00
O(2)	0.5341	0.7532	0.2251	0.0350	1.00
O(3)	0.7928	0.9072	0.2939	0.0386	1.00
O(4)	0.4612	0.9280	0.2310	0.0356	1.00
O(5)	0.7014	0.9959	0.2472	0.0337	1.00
O(6)	0.8644	1.1224	0.2968	0.0348	1.00
O(7)	0.6689	0.9831	0.3267	0.0461	1.00
O(8)	0.6563	0.0092	0.0856	0.0342	1.00
N(1)	0.0000	0.0000	0.1025	0.0688	1.00
C(1)	0.0000	0.0000	0.1842	0.0983	1.00
C(2)	-0.0415	0.0827	0.1662	0.1350	1.00
C(3)	-0.0415	0.0787	0.1177	0.1410	1.00
C(4)	-0.0312	0.0351	0.0556	0.2156	1.00
C(5)	0.0000	0.0000	0.0241	0.1887	1.00
H(1)	0.0000	0.0000	0.2147	0.0000	1.00
H(2)	0.0103	0.1631	0.1757	0.0000	1.00
H(3)	-0.1222	0.0567	0.1762	0.0000	1.00
H(4)	0.0090	0.1580	0.1069	0.0000	1.00
H(5)	-0.1226	0.0498	0.0498	0.0000	1.00
H(6)	0.0075	0.1208	0.0540	0.0000	1.00
H(7)	-0.1164	0.0017	0.0540	0.0000	1.00
H(8)	0.0851	0.0322	0.0249	0.0000	1.00
H(9)	-0.0211	0.0263	-0.0015	0.0000	1.00

Table A.2: Atomic coordinates and thermal parameters for Mg-STA-6 (SAS) templated with tmtact, from single crystal XRD data and molecular modelling refined in space group $P4/mnc$, with lattice parameters $a = 14.322(2) \text{ \AA}$, $c = 10.424(1) \text{ \AA}$. [103]

Atom	x	y	z	U_{iso}	Occ.
Al(1)	0.2689(1)	0.1091(1)	0	0.0210(5)	1.00
Al(2)	0.3907(1)	-0.10928(1)	-0.25	0.0314(6)	1.00
P(1)	0.61008(8)	-0.11008(8)	-0.25	0.0305(5)	1.00
P(2)	0.2666(1)	-0.1137(1)	0	0.0241(5)	1.00
O(1)	0.2414(4)	-0.0114(3)	0	0.038(1)	1.00
O(2)	0.3209(3)	-0.1397(3)	-0.1174(4)	0.049(1)	1.00
O(3)	0.5093(3)	-0.1278(3)	-0.2135(5)	0.050(1)	1.00
O(4)	0.1750(4)	-0.1661(4)	0	0.043(1)	1.00
O(5)	0.6683(3)	-0.1381(3)	-0.1386(5)	0.064(2)	1.00
N(1)	0.5595	0.6718	0.0547	0.3	0.09
N(2)	0.5368	0.3621	0	0.3	0.09
N(3)	0.4221	0.5146	0.2956	0.3	0.09
N(4)	0.4938	0.5105	0.7902	0.3	0.09
C(1)	0.4937	0.7371	1	0.3	0.09
C(2)	0.6187	0.3376	0.0918	0.3	0.09
C(3)	0.4966	0.4748	0.3812	0.3	0.09
C(4)	0.4092	0.5505	0.7258	0.3	0.09
C(5)	0.4451	0.32	0.0477	0.3	0.09
C(6)	0.4066	0.348	0.1815	0.3	0.09
C(7)	0.3685	0.4473	0.2101	0.3	0.09
C(8)	0.4508	0.605	0.2332	0.3	0.09
C(9)	0.5145	0.5906	0.1159	0.3	0.09
C(10)	0.646	0.6501	0.9782	0.3	0.09
C(11)	0.648	0.5692	0.8802	0.3	0.09
C(12)	0.581	0.5662	0.7643	0.3	0.09
C(13)	0.5025	0.4061	0.7672	0.3	0.09
C(14)	0.5593	0.3481	0.8665	0.3	0.09

Table A.3: Atomic coordinates and thermal parameters for Co-STA-7 (SAV) templated by tmtact, from single crystal XRD data and molecular modelling refined in space group $P4/n$, with lattice parameters $a = 18.740(5)$ Å, $c = 9.439(7)$ Å.

Atom	x	y	z	U_{iso}	Occ.
Al(1)	0.0661(2)	0.5513(2)	0.3350(3)	0.107(3)	0.70
Al(2)	-0.0453(1)	0.6642(1)	-0.1571(3)	0.053(2)	0.70
Al(3)	0.0660(2)	0.8344(2)	0.0833(3)	0.057(2)	0.70
Co(1)	0.0661(2)	0.5513(2)	0.3350(3)	0.018(1)	0.30
Co(2)	-0.0453(1)	0.6642(1)	-0.1571(3)	0.043(2)	0.30
Co(3)	0.0660(2)	0.8344(2)	0.0833(3)	0.057(2)	0.30
P(1)	0.0675(2)	0.6661(2)	0.0924(3)	0.0467(7)	1.00
P(2)	-0.0490(2)	0.8337(2)	-0.1596(3)	0.0452(7)	1.00
P(3)	-0.0554(2)	0.4349(2)	0.3361(3)	0.0451(8)	1.00
O(1)	0.0602(5)	0.6278(4)	0.2396(8)	0.064(2)	1.00
O(2)	0.0803(5)	0.5745(5)	0.5058(9)	0.071(3)	1.00
O(3)	0.1370(5)	0.5002(5)	0.2824(9)	0.069(3)	1.00
O(4)	-0.0129(5)	0.5051(5)	0.3198(9)	0.073(3)	1.00
O(5)	-0.0008(5)	0.6544(5)	0.006(1)	0.080(3)	1.00
O(6)	0.0097(5)	0.6306(5)	-0.2909(9)	0.074(3)	1.00
O(7)	-0.1265(5)	0.6214(4)	-0.156(1)	0.072(3)	1.00
O(8)	-0.0639(5)	0.7524(4)	-0.1914(9)	0.067(3)	1.00
O(9)	-0.0127(5)	0.8440(6)	-0.011(1)	0.086(3)	1.00
O(10)	0.1365(5)	0.8668(4)	-0.010(1)	0.068(3)	1.00
O(11)	0.0599(5)	0.8766(4)	0.2431(9)	0.067(3)	1.00
O(12)	0.0800(5)	0.7470(5)	0.126(1)	0.075(3)	1.00
N(1)	0.3948	0.2638	0.6431	0.05	0.13
N(2)	0.0717	0.2598	0.6719	0.05	0.13
N(3)	0.2803	0.4072	0.6005	0.05	0.13
N(4)	0.2251	0.1373	0.6606	0.05	0.13
C(1)	0.4601	0.2412	0.5655	0.05	0.13
C(2)	0.0052	0.2818	0.5974	0.05	0.13
C(3)	0.2906	0.3986	0.7556	0.05	0.13
C(4)	0.227	0.0861	0.5396	0.05	0.13
C(5)	0.1258	0.3187	0.6827	0.05	0.13
C(6)	0.1551	0.3497	0.542	0.05	0.13
C(7)	0.204	0.4157	0.5565	0.05	0.13
C(8)	0.3248	0.3598	0.5071	0.05	0.13
C(9)	0.3329	0.28	0.547	0.05	0.13
C(10)	0.3766	0.2174	0.767	0.05	0.13

continued on next page

Table A.3: *Continued*

Atom	x	y	z	U_{iso}	Occ.
C(11)	0.3562	0.1382	0.7411	0.05	0.13
C(12)	0.2777	0.1183	0.7735	0.05	0.13
C(13)	0.1512	0.1486	0.7171	0.05	0.13
C(14)	0.1005	0.1904	0.6164	0.05	0.13

Table A.4: Selected bond distances for Co-STA-7 (**SAV**) templated with tmtact.

Atom-Atom	Distance, Å
Al(1)-O(1)	1.697(8)
Al(1)-O(2)	1.691(9)
Al(1)-O(3)	1.710(9)
Al(1)-O(4)	1.72(1)
Al(2)-O(5)	1.76(1)
Al(2)-O(6)	1.75(1)
Al(2)-O(7)	1.721(9)
Al(2)-O(8)	1.721(8)
Al(3)-O(9)	1.74(1)
Al(3)-O(10)	1.698(9)
Al(3)-O(11)	1.707(8)
Al(3)-O(12)	1.705(9)
P(1)-O(1)	1.570(8)
P(1)-O(5)	1.54(1)
P(1)-O(10)	1.560(9)
P(1)-O(12)	1.565(9)
P(2)-O(3)	1.580(9)
P(2)-O(7)	1.548(9)
P(2)-O(8)	1.578(8)
P(2)-O(9)	1.57(1)
P(3)-O(2)	1.573(8)
P(3)-O(4)	1.55(1)
P(3)-O(6)	1.56(1)
P(3)-O(11)	1.550(8)

Table A.5: Selected bond angles for Co-STA-7 (**SAV**) templated with tm-tact.

Atom – Atom – Atom	Angle, °
O(2) – Al(1) – O(1)	107.4(4)
O(2) – Al(1) – O(3)	107.4(5)
O(1) – Al(1) – O(3)	111.7(4)
O(2) – Al(1) – O(4)	110.1(4)
O(1) – Al(1) – O(4)	108.9(4)
O(3) – Al(1) – O(4)	111.2(5)
O(8) – Al(2) – O(7)	105.6(4)
O(8) – Al(2) – O(6)	109.3(5)
O(7) – Al(2) – O(6)	111.1(5)
O(8) – Al(2) – O(5)	111.1(5)
O(7) – Al(2) – O(5)	111.3(5)
O(6) – Al(2) – O(5)	108.4(5)
O(10) – Al(3) – O(12)	110.1(5)
O(10) – Al(3) – O(11)	110.0(5)
O(12) – Al(3) – O(11)	104.4(4)
O(10) – Al(3) – O(9)	111.0(5)
O(12) – Al(3) – O(9)	110.6(5)
O(11) – Al(3) – O(9)	110.5(5)
O(5) – P(1) – O(10)	110.0(5)
O(5) – P(1) – O(12)	111.7(5)
O(10) – P(1) – O(12)	109.1(5)
O(5) – P(1) – O(1)	109.4(5)
O(10) – P(1) – O(1)	110.5(5)
O(12) – P(1) – O(1)	106.2(5)
O(7) – P(2) – O(9)	107.3(5)
O(7) – P(2) – O(8)	108.3(5)
O(9) – P(2) – O(8)	111.5(5)
O(7) – P(2) – O(3)	111.3(5)
O(9) – P(2) – O(3)	111.0(5)
O(8) – P(2) – O(3)	107.4(5)
O(4) – P(3) – O(11)	108.3(5)
O(4) – P(3) – O(6)	111.0(5)
O(11) – P(3) – O(6)	110.3(5)
O(4) – P(3) – O(2)	110.0(5)
O(11) – P(3) – O(2)	107.5(5)
O(6) – P(3) – O(2)	109.5(5)
P(1) – O(1) – Al(1)	148.2(6)

continued on next page

Table A.5: *Continued*

Atom - Atom - Atom	Angle, °
P(3) - O(2) - Al(1)	146.1(6)
P(2) - O(3) - Al(1)	144.1(6)
P(3) - O(4) - Al(1)	149.7(6)
P(1) - O(5) - Al(2)	147.7(7)
P(3) - O(6) - Al(2)	143.8(6)
P(2) - O(7) - Al(2)	146.5(6)
P(2) - O(8) - Al(2)	148.9(6)
P(2) - O(9) - Al(3)	144.7(7)
P(1) - O(10) - Al(3)	144.9(6)
P(3) - O(11) - Al(3)	151.3(6)
P(1) - O(12) - Al(3)	149.3(7)

Table A.6: Atomic coordinates and thermal parameters for Zn–STA-7 (SAV) templated by tmtact, from single crystal XRD data and molecular modelling refined in space group $P4/n$, with lattice parameters $a = 18.691(2)$ Å, $c = 9.423(1)$ Å.

Atom	x	y	z	U_{iso}	Occ.
Al(1)	0.06521(4)	0.66548(3)	0.08049(7)	0.0223(2)	0.80
Al(2)	-0.04419(4)	0.83607(3)	-0.15605(7)	0.0221(2)	0.80
Al(3)	-0.05065(4)	0.43423(4)	0.33459(7)	0.0262(2)	0.80
Zn(1)	0.06403(6)	0.66497(6)	0.0805(1)	0.0283(3)	0.20
Zn(2)	-0.04401(5)	0.83608(5)	-0.1562(1)	0.0168(2)	0.20
Zn(3)	-0.05024(5)	0.43416(6)	0.3352(1)	0.0208(2)	0.20
P(1)	0.06489(3)	0.55720(2)	0.33558(5)	0.0254(1)	1.00
P(2)	-0.05034(2)	0.66641(2)	-0.16022(5)	0.0263(1)	1.00
P(3)	0.06733(3)	0.83418(2)	0.09549(5)	0.0262(1)	1.00
O(1)	0.0593(1)	0.62405(8)	0.2451(2)	0.0505(5)	1.00
O(2)	0.0749(1)	0.5809(1)	0.4891(2)	0.0495(5)	1.00
O(3)	0.1288(1)	0.51258(9)	0.2938(2)	0.0484(5)	1.00
O(4)	-0.00461(9)	0.51641(9)	0.3214(2)	0.0479(5)	1.00
O(5)	-0.01476(9)	0.6564(1)	-0.0164(2)	0.0476(5)	1.00
O(6)	-0.00287(9)	0.63711(9)	-0.2784(2)	0.0460(5)	1.00
O(7)	-0.12185(9)	0.6292(1)	-0.1574(2)	0.0538(5)	1.00
O(8)	-0.0626(1)	0.74461(8)	-0.1912(2)	0.0544(5)	1.00
O(9)	-0.0001(1)	0.8459(1)	0.0114(2)	0.0527(5)	1.00
O(10)	0.1326(1)	0.8620(1)	0.0170(2)	0.0493(5)	1.00
O(11)	0.0606(1)	0.86991(9)	0.2391(2)	0.0506(5)	1.00
O(12)	0.0802(1)	0.75543(8)	0.1223(2)	0.0540(5)	1.00
N(1)	0.3948	0.2638	0.6431	0.05	0.13
N(2)	0.0717	0.2598	0.6719	0.05	0.13
N(3)	0.2803	0.4072	0.6005	0.05	0.13
N(4)	0.2251	0.1373	0.6606	0.05	0.13
C(1)	0.4601	0.2412	0.5655	0.05	0.13
C(2)	0.0052	0.2818	0.5974	0.05	0.13
C(3)	0.2906	0.3986	0.7556	0.05	0.13
C(4)	0.227	0.0861	0.5396	0.05	0.13
C(5)	0.1258	0.3187	0.6827	0.05	0.13
C(6)	0.1551	0.3497	0.542	0.05	0.13
C(7)	0.204	0.4157	0.5565	0.05	0.13
C(8)	0.3248	0.3598	0.5071	0.05	0.13
C(9)	0.3329	0.28	0.547	0.05	0.13
C(10)	0.3766	0.2174	0.767	0.05	0.13

continued on next page

Table A.6: *Continued*

Atom	x	y	z	U_{iso}	Occ.
C(11)	0.3562	0.1382	0.7411	0.05	0.13
C(12)	0.2777	0.1183	0.7735	0.05	0.13
C(13)	0.1512	0.1486	0.7171	0.05	0.13
C(14)	0.1005	0.1904	0.6164	0.05	0.13

Table A.7: Selected bond distances for Zn-STA-7 (**SAV**) templated with tmtact.

Atom-Atom	Distance, Å
Al(1)-O(12)	1.749(2)
Al(1)-O(10)	1.753(2)
Al(1)-O(5)	1.760(2)
Al(1)-O(1)	1.737(2)
Al(2)-O(7)	1.772(2)
Al(2)-O(8)	1.775(2)
Al(2)-O(9)	1.790(2)
Al(2)-O(3)	1.800(2)
Al(3)-O(2)	1.745(2)
Al(3)-O(4)	1.765(2)
Al(3)-O(6)	1.749(2)
Al(3)-O(11)	1.739(2)
P(1)-O(3)	1.509(2)
P(1)-O(4)	1.512(2)
P(1)-O(1)	1.516(2)
P(1)-O(2)	1.525(2)
P(2)-O(5)	1.521(2)
P(2)-O(6)	1.525(2)
P(2)-O(7)	1.507(2)
P(2)-O(8)	1.508(2)
P(3)-O(9)	1.504(2)
P(3)-O(10)	1.518(2)
P(3)-O(11)	1.514(2)
P(3)-O(12)	1.513(2)

Table A.8: Selected bond angles for Zn-STA-7 (**SAV**) templated with tm-tact.

Atom – Atom – Atom	Angle, °
O(1) – Al(1) – O(12)	103.75(9)
O(1) – Al(1) – O(10)	111.20(9)
O(12) – Al(1) – O(10)	109.3(1)
O(1) – Al(1) – O(5)	111.47(9)
O(12) – Al(1) – O(5)	110.2(1)
O(10) – Al(1) – O(5)	110.72(9)
O(7) – Al(2) – O(8)	104.63(9)
O(7) – Al(2) – O(9)	111.9(1)
O(8) – Al(2) – O(9)	110.7(1)
O(7) – Al(2) – O(3)	111.16(9)
O(8) – Al(2) – O(3)	109.4(1)
O(9) – Al(2) – O(3)	109.04(9)
O(11) – Al(3) – O(2)	106.22(9)
O(11) – Al(3) – O(6)	111.94(9)
O(2) – Al(3) – O(6)	108.26(9)
O(11) – Al(3) – O(4)	109.4(1)
O(2) – Al(3) – O(4)	109.58(9)
O(6) – Al(3) – O(4)	111.30(9)
O(3) – P(1) – O(4)	112.2(1)
O(3) – P(1) – O(1)	111.3(1)
O(4) – P(1) – O(1)	107.8(1)
O(3) – P(1) – O(2)	108.1(1)
O(4) – P(1) – O(2)	109.7(1)
O(1) – P(1) – O(2)	107.6(1)
O(7) – P(2) – O(8)	108.5(1)
O(7) – P(2) – O(5)	108.4(1)
O(8) – P(2) – O(5)	111(1)
O(7) – P(2) – O(6)	111.3(1)
O(8) – P(2) – O(6)	107.2(1)
O(5) – P(2) – O(6)	110.6(1)
O(9) – P(3) – O(12)	111.3(1)
O(9) – P(3) – O(11)	109.7(1)
O(12) – P(3) – O(11)	107.0(1)
O(9) – P(3) – O(10)	111.5(1)
O(12) – P(3) – O(10)	106.7(1)
O(11) – P(3) – O(10)	110.5(1)
P(1) – O(1) – Al(1)	149.9(1)

continued on next page

Table A.8: *Continued*

Atom - Atom - Atom	Angle, °
P(1) - O(2) - Al(3)	145.5(1)
P(1) - O(3) - Al(2)	143.4(1)
P(1) - O(4) - Al(3)	148.4(1)
P(2) - O(5) - Al(1)	145.3(1)
P(2) - O(6) - Al(3)	145.8(1)
P(2) - O(7) - Al(2)	143.9(1)
P(2) - O(8) - Al(2)	150.2(1)
P(3) - O(9) - Al(2)	146.7(1)
P(3) - O(10) - Al(1)	143.4(1)
P(3) - O(11) - Al(3)	146.6(1)
P(3) - O(12) - Al(1)	150.7(1)

Table A.9: Atomic coordinates and thermal parameters for CoAPO–cyclam-1, from single crystal XRD data refined in space group $P2_1/c$, with lattice parameters $a = 14.9780(8) \text{ \AA}$, $b = 14.7200(8) \text{ \AA}$, $c = 8.4792(5) \text{ \AA}$, $\beta = 98.323(1)^\circ$. [123]

Atom	x	y	z	U_{iso}	Occ.
Al(1)	0.75679(5)	0.77786(5)	0.40482(9)	0.0187(2)	1.00
Co(1)	0.5	0.5	0	0.0257(2)	1.00
Co(2)	1	0.5	0.5	0.0245(2)	1.00
P(1)	0.66294(4)	0.63284(4)	0.17797(8)	0.0208(2)	1.00
P(2)	0.82969(5)	0.62180(5)	0.62820(8)	0.0226(2)	1.00
O(1)	0.5652(1)	0.6127(1)	0.1232(2)	0.0294(5)	1.00
O(2)	0.7113(1)	0.6482(1)	0.0301(2)	0.0331(5)	1.00
O(3)	0.7115(1)	0.5553(1)	0.2747(2)	0.0280(4)	1.00
O(4)	0.6735(1)	0.7214(1)	0.2784(2)	0.0273(4)	1.00
O(5)	0.8319(1)	0.7021(1)	0.5128(2)	0.0272(4)	1.00
O(6)	0.9120(1)	0.5656(1)	0.6327(2)	0.0383(5)	1.00
O(7)	0.8217(1)	0.6569(1)	0.7944(2)	0.0349(5)	1.00
O(8)	0.7419(1)	0.5675(1)	0.5719(2)	0.0420(5)	1.00
N(1)	0.5907(2)	0.4068(2)	0.1259(3)	0.0369(6)	1.00
N(2)	1.0999(2)	0.5136(2)	0.7018(3)	0.0409(7)	1.00
N(3)	0.4250(2)	0.4829(2)	0.1891(3)	0.0387(6)	1.00
N(4)	1.0456(2)	0.6279(2)	0.4324(3)	0.0455(7)	1.00
C(1)	0.5389(2)	0.3650(2)	0.2419(4)	0.056(1)	1.00
C(2)	0.4861(2)	0.4372(2)	0.3150(4)	0.055(1)	1.00
C(3)	0.3851(2)	0.5683(2)	0.2387(4)	0.053(1)	1.00
C(4)	0.3248(2)	0.6130(3)	0.1021(5)	0.063(1)	1.00
C(5)	0.3709(2)	0.6589(2)	-0.0240(5)	0.055(1)	1.00
C(6)	1.1235(2)	0.6112(2)	0.7035(5)	0.061(1)	1.00
C(7)	1.1316(3)	0.6430(2)	0.5374(5)	0.064(1)	1.00
C(8)	1.0480(3)	0.6363(2)	0.2602(4)	0.063(1)	1.00
C(9)	0.9579(3)	0.6156(3)	0.1611(4)	0.066(1)	1.00
C(10)	0.9283(2)	0.5181(2)	0.1505(4)	0.055(1)	1.00
H(1)	0.638(2)	0.446(2)	0.180(3)	0.06(1)	1.00
H(2)	0.377(1)	0.440(2)	0.155(4)	0.07(1)	1.00
H(3)	0.726(2)	0.559(3)	0.457(1)	0.07(1)	1.00
H(4)	1.154(1)	0.481(2)	0.682(4)	0.045(9)	1.00
H(5)	1.001(2)	0.673(6)	0.454(4)	0.07(1)	1.00
H(6)	0.5797(2)	0.3348(2)	0.3248(4)	0.067	1.00
H(7)	0.4978(2)	0.3199(2)	0.1890(4)	0.067	1.00
H(8)	0.4517(2)	0.4096(2)	0.3908(4)	0.066	1.00

continued on next page

Table A.9: *Continued*

Atom	x	y	z	U_{iso}	Occ.
H(9)	0.5273(2)	0.4811(2)	0.3714(4)	0.066	1.00
H(10)	0.4331(2)	0.6099(2)	0.2797(4)	0.063	1.00
H(11)	0.3502(2)	0.5555(2)	0.3240(4)	0.063	1.00
H(12)	0.2881(2)	0.6580(3)	0.1463(5)	0.076	1.00
H(13)	0.2842(2)	0.5672(3)	0.0502(5)	0.076	1.00
H(14)	0.3275(2)	0.6969(2)	-0.0898(5)	0.065	1.00
H(15)	0.4186(2)	0.6979(2)	0.0275(5)	0.065	1.00
H(16)	1.1802(2)	0.6209(2)	0.7726(5)	0.073	1.00
H(17)	1.0772(2)	0.6460(2)	0.7453(5)	0.073	1.00
H(18)	1.1467(3)	0.7071(2)	0.5393(5)	0.077	1.00
H(19)	1.1795(3)	0.6099(2)	0.4971(5)	0.077	1.00
H(20)	1.0931(3)	0.5949(2)	0.2301(4)	0.075	1.00
H(21)	1.0660(3)	0.6976(2)	0.2370(4)	0.075	1.00
H(22)	0.9120(3)	0.6504(3)	0.2040(4)	0.08	1.00
H(23)	0.9599(3)	0.6374(3)	0.0537(4)	0.08	1.00
H(24)	0.8786(2)	0.5114(2)	0.0643(4)	0.066	1.00
H(25)	0.9778(2)	0.4806(2)	0.1259(4)	0.066	1.00

Table A.10: Atomic coordinates and thermal parameters for MgAPO-18 (**AEI**) templated with cyclam, from single crystal XRD data and molecular modelling refined in space group $Cmc2_1$, with lattice parameters $a = 13.790(3)$ Å, $b = 12.891(3)$ Å, $c = 18.922(4)$ Å.

Atom	x	y	z	U_{iso}	Occ.
Al(1)	0.1078(8)	0.963(1)	0.0558(6)	0.040(3)	1.00
Al(2)	0.222(1)	1.103(1)	0.3389(7)	0.057(4)	1.00
Al(3)	0.1179(9)	0.779(1)	0.3281(6)	0.043(4)	1.00
P(1)	0.2312(6)	0.9068(7)	0.4422(5)	0.025(2)	1.00
P(2)	0.1107(6)	1.2302(7)	0.4528(4)	0.021(2)	1.00
P(3)	0.1228(7)	0.9634(8)	0.2228(5)	0.036(3)	1.00
O(1)	0.140(2)	1.174(3)	0.385(2)	0.08(1)	1.00
O(2)	0.149(2)	0.833(2)	0.401(1)	0.037(6)	1.00
O(3)	0.266(1)	1.005(2)	0.394(2)	0.050(6)	1.00
O(4)	0	1.247(3)	0.434(2)	0.05(1)	1.00
O(5)	0	0.990(3)	0.042(2)	0.034(9)	1.00
O(6)	0.327(2)	0.837(2)	0.461(1)	0.034(6)	1.00
O(7)	0	0.738(2)	0.325(1)	0.019(7)	1.00
O(8)	0.326(3)	1.167(3)	0.317(2)	0.09(1)	1.00
O(9)	0.171(2)	1.055(2)	0.269(1)	0.025(6)	1.00
O(10)	0.151(2)	0.961(2)	0.140(2)	0.062(6)	1.00
O(11)	0.146(2)	1.169(2)	0.526(1)	0.035(7)	1.00
O(12)	0.132(2)	0.860(2)	0.263(1)	0.051(8)	1.00
O(13)	0.202(2)	0.951(2)	0.520(1)	0.041(7)	1.00
O(14)	0	1.005(4)	0.225(3)	0.07(1)	1.00
O(15)	0	0.41(1)	0.01(1)	0.45(8)	1.00
C(1)	0	0.373(9)	0.154(7)	0.08(4)	1.00
C(2)	0	0.30(1)	0.088(8)	0.10(5)	1.00
N(1)	0	0.49(1)	0.188(9)	0.14(6)	1.00
N(2)	0	0.269(5)	0.032(3)	0.02(2)	1.00

Table A.11: Selected bond distances for MgAPO-18 (**AEI**) templated with cyclam.

Atom-Atom	Distance, Å
Al(1)-O(10)	1.71(4)
Al(1)-O(11)	1.87(3)
Al(1)-O(13)	1.84(3)
Al(1)-O(5)	1.55(2)
Al(2)-O(1)	1.70(4)
Al(2)-O(3)	1.74(3)
Al(2)-O(8)	1.71(4)
Al(2)-O(9)	1.62(2)
Al(3)-O(12)	1.63(3)
Al(3)-O(2)	1.59(3)
Al(3)-O(7)	1.71(2)
Al(3)-O(8)	1.65(4)
P(1)-O(13)	1.62(3)
P(1)-O(2)	1.68(3)
P(1)-O(3)	1.64(3)
P(1)-O(6)	1.64(2)
P(2)-O(1)	1.53(3)
P(2)-O(11)	1.66(2)
P(2)-O(4)	1.58(1)
P(2)-O(6)	1.63(3)
P(3)-O(10)	1.61(4)
P(3)-O(12)	1.54(3)
P(3)-O(14)	1.78(2)
P(3)-O(9)	1.61(2)

Table A.12: Selected bond angles for MgAPO-18 (**AEI**) templated with cyclam.

Atom – Atom – Atom	Angle, °
O(10) – Al(1) – Al(1)	110.4(9)
O(10) – Al(1) – O(11)	100(1)
O(10) – Al(1) – O(13)	96(1)
O(11) – Al(1) – Al(1)	106.5(8)
O(13) – Al(1) – Al(1)	134.8(8)
O(13) – Al(1) – O(11)	104(1)
O(5) – Al(1) – Al(1)	17(1)
O(5) – Al(1) – O(10)	120(2)
O(5) – Al(1) – O(11)	115(2)
O(5) – Al(1) – O(13)	118(2)
O(1) – Al(2) – O(3)	109(2)
O(1) – Al(2) – O(8)	115(2)
O(3) – Al(2) – O(8)	101(2)
O(9) – Al(2) – O(1)	109(2)
O(9) – Al(2) – O(3)	112(1)
O(9) – Al(2) – O(8)	111(2)
O(12) – Al(3) – O(7)	107(1)
O(12) – Al(3) – O(8)	114(2)
O(2) – Al(3) – O(12)	110(2)
O(2) – Al(3) – O(7)	114(1)
O(2) – Al(3) – O(8)	111(2)
O(8) – Al(3) – O(7)	100(2)
O(13) – P(1) – O(2)	117(1)
O(13) – P(1) – O(3)	108(2)
O(13) – P(1) – O(6)	101(1)
O(3) – P(1) – O(2)	112(1)
O(6) – P(1) – O(2)	110(1)
O(6) – P(1) – O(3)	108(1)
O(1) – P(2) – O(11)	113(2)
O(1) – P(2) – O(4)	97(2)
O(1) – P(2) – O(6)	110(2)
O(4) – P(2) – O(11)	123(2)
O(4) – P(2) – O(6)	114(2)
O(6) – P(2) – O(11)	100(1)
O(10) – P(3) – O(14)	105(2)
O(12) – P(3) – O(10)	116(1)
O(12) – P(3) – O(14)	109(2)

continued on next page

Table A.12: *Continued*

Atom - Atom - Atom	Angle, °
O(12) - P(3) - O(9)	110(1)
O(9) - P(3) - O(10)	116(1)
O(9) - P(3) - O(14)	99(2)
P(2) - O(1) - Al(2)	149(2)
Al(3) - O(2) - P(1)	146(2)
P(1) - O(3) - Al(2)	142(1)
P(2) - O(4) - P(2)	149(2)
Al(1) - O(5) - Al(1)	147(3)
P(2) - O(6) - P(1)	150(2)
Al(3) - O(7) - Al(3)	143(2)
Al(3) - O(8) - Al(2)	142(2)
Al(2) - O(9) - P(3)	154(2)
P(3) - O(10) - Al(1)	146(2)
P(2) - O(11) - Al(1)	127(1)
P(3) - O(12) - Al(3)	157(2)
P(1) - O(13) - Al(1)	136(2)
P(3) - O(14) - P(3)	145(3)

Table A.13: Atomic coordinates and thermal parameters for MgAPO-18 (**AEI**) templated with tmtacn, from single crystal XRD data and molecular modelling refined in space group $C2/c$, with lattice parameters $a = 13.795(3) \text{ \AA}$, $b = 12.830(3) \text{ \AA}$, $c = 18.815(5) \text{ \AA}$, $\beta = 89.959(7)^\circ$.

Atom	x	y	z	U_{iso}	Occ.
Al(1)	0.8895(2)	0.9596(2)	0.1655(1)	0.0165(6)	1.00
Al(2)	0.8828(2)	0.2254(2)	0.9385(1)	0.0179(6)	1.00
Al(3)	0.2267(2)	0.0961(2)	0.0495(1)	0.0181(6)	1.00
P(1)	0.7722(2)	0.0963(2)	0.0554(1)	0.0171(5)	1.00
P(2)	0.1113(1)	0.2324(2)	0.9382(1)	0.0177(5)	1.00
P(3)	0.1187(1)	0.9643(2)	0.1667(1)	0.0173(5)	1.00
O(1)	0.1803(5)	0.0474(6)	0.1306(4)	0.037(2)	1.00
O(2)	0.1405(5)	0.1760(6)	0.0061(4)	0.034(2)	1.00
O(3)	0.0053(4)	0.2615(5)	0.9422(4)	0.036(2)	1.00
O(4)	0.8466(5)	0.1647(6)	0.0178(4)	0.036(2)	1.00
O(5)	0.8168(5)	0.0538(5)	0.1236(3)	0.034(2)	1.00
O(6)	0.0124(5)	0.9949(6)	0.1582(4)	0.034(2)	1.00
O(7)	0.1377(5)	0.8583(5)	0.1335(4)	0.033(2)	1.00
O(8)	0.3319(5)	0.1678(5)	0.0702(4)	0.037(2)	1.00
O(9)	0.8529(5)	0.9590(6)	0.2551(3)	0.037(2)	1.00
O(10)	0.8163(5)	0.3399(5)	0.9242(4)	0.038(2)	1.00
O(11)	0.1300(5)	0.1636(5)	0.8733(4)	0.036(2)	1.00
O(12)	0.2600(5)	-0.0091(5)	0.9929(4)	0.034(2)	1.00
N(1)	0.4871	0.9778	0.3703	0.19	0.35
N(2)	0.6485	0.8244	0.2436	0.19	0.35
N(3)	0.3755	0.8121	0.2228	0.19	0.35
C(1)	0.5055	0.9672	0.4491	0.19	0.35
C(2)	0.294	0.7434	0.2477	0.19	0.35
C(3)	0.5795	0.9698	0.3269	0.19	0.35
C(4)	0.6241	0.8582	0.319	0.19	0.35
C(5)	0.4061	0.907	0.3455	0.19	0.35
C(6)	0.3788	0.9136	0.2642	0.19	0.35
C(7)	0.5634	0.8148	0.1922	0.19	0.35
C(8)	0.4707	0.753	0.2171	0.19	0.35
C(9)	0.7117	0.7295	0.2439	0.19	0.35

Table A.14: Selected bond distances for MgAPO-18 (**AEI**) templated with tmtacn.

Atom-Atom	Distance, Å
Al(1)-O(5)	1.758(7)
Al(1)-O(6)	1.759(7)
Al(1)-O(9)	1.760(6)
Al(1)-O(11)	1.763(7)
Al(2)-O(3)	1.754(7)
Al(2)-O(4)	1.756(7)
Al(2)-O(7)	1.751(7)
Al(2)-O(10)	1.752(7)
Al(3)-O(1)	1.769(7)
Al(3)-O(2)	1.771(7)
Al(3)-O(8)	1.762(7)
Al(3)-O(12)	1.779(7)
P(1)-O(4)	1.524(7)
P(1)-O(5)	1.524(6)
P(1)-O(10)	1.519(6)
P(1)-O(12)	1.508(7)
P(2)-O(2)	1.522(7)
P(2)-O(3)	1.511(6)
P(2)-O(8)	1.510(7)
P(2)-O(11)	1.527(7)
P(3)-O(1)	1.523(7)
P(3)-O(6)	1.528(7)
P(3)-O(7)	1.519(7)
P(3)-O(9)	1.523(6)

Table A.15: Selected bond angles for MgAPO-18 (**AEI**) templated with tmtacn.

Atom – Atom – Atom	Angle, °
O(5) – Al(1) – O(6)	109.8(4)
O(5) – Al(1) – O(9)	105.6(3)
O(5) – Al(1) – O(11)	110.1(4)
O(6) – Al(1) – O(9)	110.6(3)
O(6) – Al(1) – O(11)	110.2(4)
O(9) – Al(1) – O(11)	110.5(4)
O(3) – Al(2) – O(4)	110.9(4)
O(3) – Al(2) – O(7)	110.4(4)
O(3) – Al(2) – O(10)	106.8(4)
O(4) – Al(2) – O(7)	109.8(4)
O(4) – Al(2) – O(10)	110.7(4)
O(7) – Al(2) – O(10)	108.1(4)
O(1) – Al(3) – O(2)	111.1(4)
O(1) – Al(3) – O(8)	106.9(4)
O(1) – Al(3) – O(12)	110.0(3)
O(2) – Al(3) – O(8)	110.7(3)
O(2) – Al(3) – O(12)	109.6(4)
O(8) – Al(3) – O(12)	108.4(4)
O(4) – P(1) – O(5)	108.9(4)
O(4) – P(1) – O(10)	110.4(4)
O(4) – P(1) – O(12)	110.3(4)
O(5) – P(1) – O(10)	107.7(4)
O(5) – P(1) – O(12)	111.2(4)
O(10) – P(1) – O(12)	108.3(4)
O(2) – P(2) – O(3)	109.4(4)
O(2) – P(2) – O(8)	110.6(4)
O(2) – P(2) – O(11)	110.6(4)
O(3) – P(2) – O(8)	107.3(4)
O(3) – P(2) – O(11)	110.2(4)
O(8) – P(2) – O(11)	108.6(4)
O(1) – P(3) – O(6)	108.0(4)
O(1) – P(3) – O(7)	110.3(4)
O(1) – P(3) – O(9)	108.6(4)
O(6) – P(3) – O(7)	110.6(4)
O(6) – P(3) – O(9)	111.1(4)
O(7) – P(3) – O(9)	108.3(4)
P(3) – O(1) – Al(3)	146.5(5)

continued on next page

Table A.15: *Continued*

Atom – Atom – Atom	Angle, °
P(2) – O(2) – Al(3)	147.2(5)
P(2) – O(3) – Al(2)	149.9(5)
P(1) – O(4) – Al(2)	147.2(5)
P(1) – O(5) – Al(1)	148.7(4)
P(3) – O(6) – Al(1)	148.3(5)
P(3) – O(7) – Al(2)	147.1(5)
P(2) – O(8) – Al(3)	147.9(5)
P(3) – O(9) – Al(1)	148.3(5)
P(1) – O(10) – Al(2)	146.4(5)
P(2) – O(11) – Al(1)	145.4(5)
P(1) – O(12) – Al(3)	147.9(5)

Table A.16: Atomic coordinates and thermal parameters for ZnAPO-42 (LTA) templated with K222, from single crystal XRD data and molecular modelling refined in space group $Fm\bar{3}c$, with lattice parameters $a = 23.990(8)$ Å.

Atom	x	y	z	U_{iso}	Occ.
Al(1)	0	0.1839(6)	0.0899(7)	0.027(4)	0.80
Zn(1)	0	0.1839(6)	0.0899(7)	0.027(4)	0.20
P(1)	0	0.0942(8)	0.1867(7)	0.028(4)	1.00
O(1)	0	0.1086(9)	0.245(2)	0.046(8)	1.00
O(2)	0	0.148(2)	0.151(1)	0.04(1)	1.00
O(3)	0.049(1)	0.0597(9)	0.1738(6)	0.047(7)	1.00
N(1)	0.1505	0.2667	0.2603	0.1267	0.083
N(2)	0.3435	0.2354	0.2068	0.1267	0.083
O(4)	0.3585	0.3041	0.3095	0.1267	0.083
O(5)	0.1467	0.3134	0.1363	0.1267	0.083
O(6)	0.2732	0.3122	0.135	0.1267	0.083
O(7)	0.2015	0.1583	0.2904	0.1267	0.083
O(8)	0.2425	0.3355	0.3076	0.1267	0.083
O(9)	0.3044	0.1136	0.231	0.1267	0.083
C(1)	0.1503	0.25	0.1503	0.1267	0.083
C(2)	0.3283	0.3283	0.1717	0.1267	0.083
C(3)	0.3636	0.2878	0.1779	0.1267	0.083
C(4)	0.1353	0.2333	0.3118	0.1267	0.083
C(5)	0.1471	0.3288	0.2689	0.1267	0.083
C(6)	0.1855	0.3542	0.3139	0.1267	0.083
C(7)	0.1822	0.1952	0.3339	0.1267	0.083
C(8)	0.238	0.1144	0.3087	0.1267	0.083
C(9)	0.2835	0.3677	0.3376	0.1267	0.083
C(10)	0.25	0.0821	0.25	0.1267	0.083
C(11)	0.3322	0.331	0.3565	0.1267	0.083
C(12)	0.2879	0.1459	0.183	0.1267	0.083
C(13)	0.3618	0.244	0.312	0.1267	0.083
C(14)	0.3336	0.1881	0.1664	0.1267	0.083
C(15)	0.3802	0.2194	0.2555	0.1267	0.083
C(16)	0.1191	0.247	0.2095	0.1267	0.083
C(17)	0.1827	0.3291	0.0906	0.1267	0.083
C(18)	0.2371	0.3547	0.1123	0.1267	0.083

Table A.17: Selected bond distances for ZnAPO-42 (**LTA**) templated with K222.

Atom-Atom	Distance, Å
Al(1)-O(1)	1.77(5)
Al(1)-O(2)	1.72(5)
Al(1)-O(3)	1.75(3)
P(1)-O(1)	1.43(5)
P(1)-O(2)	1.53(5)
P(1)-O(3)	1.47(3)

Table A.18: Selected bond angles for ZnAPO-42 (**LTA**) templated with K222.

Atom - Atom - Atom	Angle, °
O(1) - Al(1) - O(2)	105(1)
O(1) - Al(1) - O(3)	105.9(8)
O(2) - Al(1) - O(3)	114.3(8)
O(3) - Al(1) - O(3)	109(1)
O(1) - P(1) - O(2)	109(1)
O(1) - P(1) - O(3)	109(1)
O(2) - P(1) - O(3)	110(1)
O(3) - P(1) - O(3)	106(1)

Table A.19: Atomic coordinates and thermal parameters for Co-UCSB-6 (**SBS**) templated with 1,8-diaminooctane, from single crystal XRD data refined in space group $P6_3$, with lattice parameters $a = 17.6363(4)$ Å, $c = 27.230(1)$ Å.

Atom	x	y	z	U_{iso}	Occ.
Al(1)	1.482(1)	0.325(1)	0.9071(6)	0.006(4)	1.00
Al(2)	1.332(1)	0.489(1)	0.5828(6)	0.011(5)	1.00
Al(3)	1.090(1)	0.361(1)	0.4997(8)	0.026(5)	1.00
Al(4)	0.846(1)	0.333(1)	0.3816(7)	0.021(5)	1.00
Al(5)	1.157(1)	0.490(1)	0.7021(7)	0.023(6)	1.00
Al(6)	0.933(1)	0.250(1)	0.8476(7)	0.021(5)	1.00
Al(7)	0.757(1)	0.062(1)	0.4348(7)	0.025(5)	1.00
Al(8)	1.266(1)	0.359(1)	0.7863(7)	0.028(5)	1.00
P(1)	0.843(1)	0.325(1)	0.9074(6)	0.021(4)	1.00
P(2)	1.157(1)	0.491(1)	0.5842(6)	0.020(5)	1.00
P(3)	1.271(1)	0.365(1)	0.4930(8)	0.047(6)	1.00
P(4)	1.334(1)	0.490(1)	0.7003(6)	0.029(5)	1.00
P(5)	0.850(1)	0.512(1)	0.3812(7)	0.033(5)	1.00
P(6)	1.314(1)	0.245(1)	0.8467(7)	0.030(5)	1.00
P(7)	0.935(1)	0.237(1)	0.4360(6)	0.023(5)	1.00
P(8)	1.096(1)	0.362(1)	0.7907(7)	0.045(6)	1.00
O(1)	1.080(2)	0.397(2)	0.729(1)	0.04(1)	1.00
O(2)	1.098(3)	0.398(3)	0.544(2)	0.07(2)	1.00
O(3)	0.898(2)	0.307(2)	0.859(1)	0.013(8)	1.00
O(4)	1.423(5)	0.578(5)	0.719(3)	0.15(3)	1.00
O(5)	1.302(2)	0.293(3)	0.799(2)	0.04(1)	1.00
O(6)	0.993(2)	0.273(2)	0.489(1)	0.03(1)	1.00
O(7)	0.989(4)	0.287(4)	0.796(2)	0.10(2)	1.00
O(8)	0.890(2)	0.331(2)	0.960(1)	0.011(8)	1.00
O(9)	1.416(2)	0.314(2)	0.860(1)	0.006(7)	1.00
O(10)	1.15(1)	0.387(9)	0.476(5)	0.53(9)	1.00
O(11)	1.251(2)	0.509(2)	0.710(1)	0.021(9)	1.00
O(12)	1.268(3)	0.533(3)	0.566(2)	0.06(2)	1.00
O(13)	1.450(2)	0.336(2)	0.9615(9)	0.001(7)	1.00
O(14)	0.870(2)	0.437(2)	0.392(1)	0.012(9)	1.00
O(15)	0.752(3)	0.276(3)	0.903(2)	0.07(2)	1.00
O(16)	1.139(3)	0.570(2)	0.565(1)	0.03(1)	1.00
O(17)	0.865(2)	0.131(2)	0.446(1)	0.026(9)	1.00
O(18)	1.159(2)	0.328(2)	0.785(1)	0.025(8)	1.00
O(19)	1.272(3)	0.266(3)	0.488(2)	0.06(1)	1.00

continued on next page

Table A.19: *Continued*

Atom	x	y	z	U_{iso}	Occ.
O(20)	0.902(5)	0.337(4)	0.416(3)	0.18(3)	1.00
O(21)	1.306(3)	0.154(3)	0.832(1)	0.06(1)	1.00
O(22)	0.876(4)	0.341(4)	0.332(2)	0.14(3)	1.00
O(23)	1.003(4)	0.223(3)	0.391(2)	0.10(2)	1.00
O(24)	0.998(2)	0.246(2)	0.8923(9)	0.005(7)	1.00
O(25)	0.871(3)	0.436(4)	0.901(2)	0.09(2)	1.00
O(26)	0.721(3)	0.247(3)	0.379(2)	0.06(1)	1.00
O(27)	1.332(3)	0.465(3)	0.633(2)	0.10(2)	1.00
O(28)	1.302(3)	0.399(3)	0.547(2)	0.10(2)	1.00
O(29)	1.138(2)	0.468(2)	0.643(3)	0.08(1)	1.00
O(30)	1.314(2)	0.400(2)	0.729(1)	0.03(1)	1.00

Table A.20: Selected bond distances for Co–UCSB-6 (**SBS**) templated with 1,8-diaminooctane.

Atom–Atom	Distance, Å
Al(1)–O(13)	1.64(3)
Al(1)–O(15)	1.84(5)
Al(1)–O(15)	1.84(5)
Al(1)–O(25)	1.76(6)
Al(1)–O(25)	1.76(5)
Al(1)–O(9)	1.68(3)
Al(2)–O(12)	1.72(5)
Al(2)–O(16)	1.66(4)
Al(2)–O(16)	1.66(4)
Al(2)–O(27)	1.42(6)
Al(2)–O(28)	1.70(5)
Al(3)–O(10)	1.1(1)
Al(3)–O(13)	1.75(3)
Al(3)–O(13)	1.75(3)
Al(3)–O(2)	1.33(5)
Al(3)–O(6)	1.66(4)
Al(4)–O(14)	1.70(3)
Al(4)–O(20)	1.35(8)
Al(4)–O(22)	1.45(7)
Al(4)–O(26)	1.94(4)
Al(5)–O(1)	1.68(4)
Al(5)–O(11)	1.54(4)

continued on next page

Table A.20: *Continued*

Atom-Atom	Distance, Å
Al(5)-O(29)	1.65(7)
Al(5)-O(4)	1.62(7)
Al(5)-O(4)	1.62(7)
Al(6)-O(21)	1.70(5)
Al(6)-O(21)	1.70(4)
Al(6)-O(24)	1.69(3)
Al(6)-O(3)	1.48(3)
Al(6)-O(7)	1.65(7)
Al(7)-O(17)	1.69(4)
Al(7)-O(19)	1.68(4)
Al(7)-O(19)	1.68(4)
Al(7)-O(24)	1.58(3)
Al(7)-O(24)	1.58(3)
Al(8)-O(18)	1.68(3)
Al(8)-O(22)	2.06(7)
Al(8)-O(22)	2.06(6)
Al(8)-O(30)	1.74(4)
Al(8)-O(5)	1.62(4)
P(1)-O(15)	1.40(5)
P(1)-O(25)	1.77(6)
P(1)-O(3)	1.75(3)
P(1)-O(8)	1.64(4)
P(2)-O(12)	1.78(5)
P(2)-O(16)	1.67(4)
P(2)-O(2)	1.82(5)
P(2)-O(29)	1.64(7)
P(3)-O(10)	2.4(1)
P(3)-O(19)	1.76(4)
P(3)-O(28)	1.58(6)
P(3)-O(8)	1.51(3)
P(3)-O(8)	1.51(3)
P(4)-O(11)	1.67(4)
P(4)-O(27)	1.89(6)
P(4)-O(30)	1.64(4)
P(4)-O(4)	1.65(7)
P(5)-O(14)	1.55(3)
P(5)-O(26)	1.50(4)
P(5)-O(26)	1.50(4)

continued on next page

Table A.20: *Continued*

Atom-Atom	Distance, Å
P(6)-O(21)	1.58(4)
P(6)-O(23)	1.88(6)
P(6)-O(23)	1.88(6)
P(6)-O(5)	1.63(4)
P(6)-O(9)	1.62(3)
P(7)-O(17)	1.67(4)
P(7)-O(20)	2.18(7)
P(7)-O(23)	1.81(6)
P(7)-O(6)	1.69(4)
P(8)-O(1)	1.85(4)
P(8)-O(18)	1.52(3)
P(8)-O(7)	1.69(6)

Table A.21: Selected bond angles for Co-UCSB-6 (**SBS**) templated with 1,8-diaminooctane.

Atom - Atom - Atom	Angle, °
O(13) - Al(1) - O(15)	116(2)
O(13) - Al(1) - O(25)	95(2)
O(15) - Al(1) - O(25)	114(2)
O(9) - Al(1) - O(13)	116(2)
O(9) - Al(1) - O(15)	112(2)
O(9) - Al(1) - O(25)	101(2)
O(12) - Al(2) - O(28)	107(3)
O(16) - Al(2) - O(12)	100(2)
O(16) - Al(2) - O(28)	109(2)
O(27) - Al(2) - O(12)	119(2)
O(27) - Al(2) - O(16)	112(2)
O(27) - Al(2) - O(28)	109(3)
O(10) - Al(3) - O(13)	61(7)
O(10) - Al(3) - O(6)	126(8)
O(13) - Al(3) - O(6)	114(2)
O(2) - Al(3) - O(10)	118(8)
O(2) - Al(3) - O(13)	100(2)
O(2) - Al(3) - O(6)	116(3)
O(14) - Al(4) - O(26)	115(2)
O(20) - Al(4) - O(14)	92(3)
O(20) - Al(4) - O(22)	115(4)

continued on next page

Table A.21: *Continued*

Atom - Atom - Atom	Angle, °
O(20) - Al(4) - O(26)	126(4)
O(22) - Al(4) - O(14)	100(3)
O(22) - Al(4) - O(26)	105(3)
O(1) - Al(5) - O(29)	104(2)
O(11) - Al(5) - O(1)	114(2)
O(11) - Al(5) - O(29)	105(2)
O(11) - Al(5) - O(4)	107(3)
O(4) - Al(5) - O(1)	114(3)
O(4) - Al(5) - O(29)	113(3)
O(21) - Al(6) - O(24)	116(2)
O(21) - Al(6) - O(7)	105(3)
O(3) - Al(6) - O(21)	105(2)
O(3) - Al(6) - O(24)	114(2)
O(3) - Al(6) - O(7)	106(3)
O(7) - Al(6) - O(24)	111(2)
O(17) - Al(7) - O(19)	97(2)
O(24) - Al(7) - O(17)	107(2)
O(24) - Al(7) - O(19)	108(2)
O(18) - Al(8) - O(22)	114(2)
O(30) - Al(8) - O(18)	111(2)
O(30) - Al(8) - O(22)	102(2)
O(5) - Al(8) - O(18)	123(2)
O(5) - Al(8) - O(22)	103(3)
O(5) - Al(8) - O(30)	102(2)
Al(5) - O(1) - P(8)	122(2)
Al(3) - O(10) - P(3)	123(9)
Al(5) - O(11) - P(4)	152(2)
Al(2) - O(12) - P(2)	124(3)
Al(1) - O(13) - Al(3)	136(2)
P(5) - O(14) - Al(4)	149(2)
P(1) - O(15) - Al(1)	132(3)
Al(2) - O(16) - P(2)	140(3)
Al(7) - O(17) - P(7)	136(2)
P(8) - O(18) - Al(8)	143(2)
Al(7) - O(19) - P(3)	119(2)
Al(3) - O(2) - P(2)	149(4)
Al(4) - O(20) - P(7)	128(4)
P(6) - O(21) - Al(6)	149(3)

continued on next page

Table A.21: *Continued*

Atom – Atom – Atom	Angle, °
Al(4) – O(22) – Al(8)	135(4)
P(7) – O(23) – P(6)	120(3)
Al(7) – O(24) – Al(6)	141(2)
P(1) – O(25) – Al(1)	149(3)
P(5) – O(26) – Al(4)	139(3)
Al(2) – O(27) – P(4)	150(3)
P(3) – O(28) – Al(2)	141(4)
P(2) – O(29) – Al(5)	154(3)
Al(6) – O(3) – P(1)	138(2)
P(4) – O(30) – Al(8)	131(3)
Al(5) – O(4) – P(4)	146(5)
Al(8) – O(5) – P(6)	138(3)
P(7) – O(6) – Al(3)	131(2)
Al(6) – O(7) – P(8)	126(4)
P(3) – O(8) – P(1)	137(2)
Al(1) – O(9) – P(6)	135(2)
O(15) – P(1) – O(25)	106(3)
O(15) – P(1) – O(3)	113(3)
O(15) – P(1) – O(8)	120(3)
O(25) – P(1) – O(3)	105(2)
O(8) – P(1) – O(25)	100(2)
O(8) – P(1) – O(3)	112(2)
O(16) – P(2) – O(12)	101(2)
O(16) – P(2) – O(2)	108(2)
O(2) – P(2) – O(12)	103(2)
O(29) – P(2) – O(12)	115(2)
O(29) – P(2) – O(16)	114(2)
O(29) – P(2) – O(2)	115(2)
O(19) – P(3) – O(10)	127(4)
O(28) – P(3) – O(10)	107(4)
O(28) – P(3) – O(19)	106(3)
O(8) – P(3) – O(10)	92(4)
O(8) – P(3) – O(19)	118(2)
O(8) – P(3) – O(28)	105(3)
O(11) – P(4) – O(27)	107(2)
O(11) – P(4) – O(4)	107(3)
O(27) – P(4) – O(4)	114(3)
O(30) – P(4) – O(11)	109(2)

continued on next page

Table A.21: *Continued*

Atom - Atom - Atom	Angle, °
O(30) - P(4) - O(27)	106(2)
O(30) - P(4) - O(4)	114(3)
O(26) - P(5) - O(14)	108(2)
O(21) - P(6) - O(23)	107(2)
O(21) - P(6) - O(5)	110(2)
O(21) - P(6) - O(9)	109(2)
O(5) - P(6) - O(23)	109(2)
O(5) - P(6) - O(9)	100(2)
O(9) - P(6) - O(23)	121(2)
O(17) - P(7) - O(20)	127(2)
O(17) - P(7) - O(23)	97(2)
O(20) - P(7) - O(23)	114(3)
O(6) - P(7) - O(17)	105(2)
O(6) - P(7) - O(20)	105(2)
O(6) - P(7) - O(23)	108(2)
O(18) - P(8) - O(1)	108(2)
O(18) - P(8) - O(7)	117(3)
O(7) - P(8) - O(1)	92(3)

Table A.22: Atomic coordinates and thermal parameters for $\text{AlPO}_4\text{-21}$ (**AWO**) templated with tmtact fragments, from single crystal XRD data refined in space group $P2_1/n$, with lattice parameters $a = 8.668(2) \text{ \AA}$, $b = 17.424(4) \text{ \AA}$, $c = 9.135(2) \text{ \AA}$, $\beta = 109.59(3)^\circ$.

Atom	x	y	z	U_{iso}	Occ.
Al(1)	0.9351(6)	0.2042(3)	0.7027(7)	0.022(2)	1.00
Al(2)	1.4907(7)	0.1690(3)	0.8118(7)	0.029(2)	1.00
Al(3)	1.6366(7)	-0.1107(3)	0.6627(8)	0.027(2)	1.00
P(1)	1.7969(6)	-0.2114(3)	0.4739(7)	0.026(1)	1.00
P(2)	1.2491(6)	0.1635(3)	0.9946(6)	0.025(1)	1.00
P(3)	1.6610(6)	0.0696(3)	0.6339(6)	0.025(1)	1.00
O(1)	1.085(1)	0.1529(6)	0.872(1)	0.023(3)	1.00
O(2)	1.716(1)	-0.0106(6)	0.660(1)	0.024(3)	1.00
O(3)	0.771(1)	0.2531(6)	0.540(2)	0.029(3)	1.00
O(4)	1.550(1)	0.0885(6)	0.731(2)	0.026(3)	1.00
O(5)	1.773(1)	-0.1414(6)	0.562(2)	0.030(3)	1.00
O(6)	1.559(1)	0.0842(6)	0.461(2)	0.024(3)	1.00
O(7)	1.380(1)	0.1388(6)	0.932(2)	0.025(3)	1.00
O(8)	1.637(1)	-0.2260(6)	0.338(1)	0.023(3)	1.00
O(9)	1.065(1)	0.1938(6)	0.589(2)	0.028(3)	1.00
O(10)	0.960(1)	0.2901(6)	0.825(2)	0.031(3)	1.00
O(11)	0.810(1)	0.1214(6)	0.679(2)	0.032(3)	1.00
O(12)	1.835(1)	-0.2826(6)	0.576(2)	0.030(3)	1.00
O(13)	1.265(2)	0.1084(7)	1.131(2)	0.040(4)	1.00
N(1)	2.069(3)	-0.010(1)	0.781(3)	0.077(7)	1.00
C(1)	2.138(3)	-0.064(1)	0.909(4)	0.088(9)	1.00
C(2)	2.154(4)	-0.014(2)	0.663(5)	0.14(1)	1.00

Table A.23: Selected bond distances for AlPO_4 -21 (**AWO**) templated with tmtact fragments.

Atom-Atom	Distance, Å
Al(1)-O(1)	1.88(1)
Al(1)-O(3)	1.88(1)
Al(1)-O(9)	1.79(1)
Al(1)-O(10)	1.84(1)
Al(1)-O(11)	1.77(1)
Al(2)-O(4)	1.74(1)
Al(2)-O(7)	1.76(1)
Al(2)-O(8)	1.75(1)
Al(2)-O(12)	1.73(1)
Al(3)-O(2)	1.88(1)
Al(3)-O(5)	1.81(1)
Al(3)-O(6)	1.75(1)
Al(3)-O(10)	1.94(1)
Al(3)-O(13)	1.79(2)
P(1)-O(5)	1.51(1)
P(1)-O(8)	1.54(1)
P(1)-O(9)	1.52(1)
P(1)-O(12)	1.52(1)
P(2)-O(1)	1.50(1)
P(2)-O(3)	1.51(1)
P(2)-O(7)	1.50(1)
P(2)-O(13)	1.55(1)
P(3)-O(2)	1.47(1)
P(3)-O(4)	1.55(1)
P(3)-O(6)	1.55(1)
P(3)-O(11)	1.52(1)
N(1)-C(1)	1.47(3)
N(1)-C(2)	1.49(4)

Table A.24: Selected bond angles for AlPO₄-21 (**AWO**) templated with tmtact fragments.

Atom – Atom – Atom	Angle, °
O(10) – Al(1) – O(1)	88.7(6)
O(10) – Al(1) – O(3)	90.8(6)
O(11) – Al(1) – O(1)	86.5(5)
O(11) – Al(1) – O(10)	132.9(6)
O(11) – Al(1) – O(3)	90.2(6)
O(11) – Al(1) – O(9)	109.0(6)
O(3) – Al(1) – O(1)	175.0(6)
O(9) – Al(1) – O(1)	92.1(5)
O(9) – Al(1) – O(10)	118.0(6)
O(9) – Al(1) – O(3)	92.5(6)
O(12) – Al(2) – O(4)	108.8(6)
O(12) – Al(2) – O(7)	109.0(7)
O(12) – Al(2) – O(8)	112.6(6)
O(4) – Al(2) – O(7)	108.7(6)
O(4) – Al(2) – O(8)	108.9(6)
O(8) – Al(2) – O(7)	108.7(6)
O(13) – Al(3) – O(10)	91.3(6)
O(13) – Al(3) – O(2)	86.9(6)
O(13) – Al(3) – O(5)	112.2(6)
O(2) – Al(3) – O(10)	174.3(6)
O(5) – Al(3) – O(10)	97.8(6)
O(5) – Al(3) – O(2)	87.9(6)
O(6) – Al(3) – O(10)	86.0(5)
O(6) – Al(3) – O(13)	133.7(7)
O(6) – Al(3) – O(2)	91.4(5)
O(6) – Al(3) – O(5)	114.0(6)
O(12) – P(1) – O(8)	108.2(6)
O(5) – P(1) – O(12)	111.8(8)
O(5) – P(1) – O(8)	108.5(6)
O(9) – P(1) – O(12)	111.0(7)
O(9) – P(1) – O(5)	107.5(6)
O(9) – P(1) – O(8)	109.8(7)
O(1) – P(2) – O(13)	109.3(7)
O(1) – P(2) – O(3)	109.0(6)
O(3) – P(2) – O(13)	114.0(8)
O(7) – P(2) – O(1)	109.3(7)
O(7) – P(2) – O(13)	105.1(7)

continued on next page

Table A.24: *Continued*

Atom - Atom - Atom	Angle, °
O(7) - P(2) - O(3)	110.0(7)
O(11) - P(3) - O(4)	110.9(7)
O(11) - P(3) - O(6)	108.8(7)
O(2) - P(3) - O(11)	108.8(7)
O(2) - P(3) - O(4)	109.8(7)
O(2) - P(3) - O(6)	111.3(7)
O(6) - P(3) - O(4)	107.2(7)
P(2) - O(1) - Al(1)	141.1(7)
P(3) - O(2) - Al(3)	141.8(7)
P(2) - O(3) - Al(1)	130.3(7)
P(3) - O(4) - Al(2)	137.9(7)
P(1) - O(5) - Al(3)	137.6(7)
P(3) - O(6) - Al(3)	143.0(8)
P(2) - O(7) - Al(2)	142.6(8)
P(1) - O(8) - Al(2)	134.4(7)
P(1) - O(9) - Al(1)	158.6(8)
Al(1) - O(10) - Al(3)	142.8(7)
P(3) - O(11) - Al(1)	161.4(8)
P(1) - O(12) - Al(2)	136.7(8)
P(2) - O(13) - Al(3)	135.9(8)

Appendix B

Rietveld refinement data

In this Appendix atomic coordinates and temperature factors obtained during Rietveld profile refinement of powder XRD data are presented. Selected bond lengths and angles are also given. Initial models were developed from single crystal XRD and molecular modelling (see Appendix A). For further details of the refinement procedure see Chapters 2–4.

Table B.1: Atomic coordinates and thermal parameters for NiAPO–cyclam-1 from Rietveld profile refinement of powder XRD data in space group $P2_1/c$, with lattice parameters $a = 14.862(2) \text{ \AA}$, $b = 14.627(2) \text{ \AA}$, $c = 8.4692(7) \text{ \AA}$, $\beta = 98.134(6)^\circ$.

Atom	x	y	z	U_{iso}	Occ.
Al(1)	0.75679	0.77786	0.40482	0.0187	1.00
Ni(1)	0.5	0.5	0	0.0257	1.00
Ni(2)	1	0.5	0.5	0.0245	1.00
P(1)	0.66294	0.63284	0.17797	0.0208	1.00
P(2)	0.82969	0.6218	0.6282	0.0226	1.00
O(1)	0.56522	0.61272	0.1232	0.0294	1.00
O(2)	0.71128	0.64824	0.0301	0.0331	1.00
O(3)	0.71151	0.55526	0.2747	0.0280	1.00
O(4)	0.67345	0.72135	0.2784	0.0273	1.00
O(5)	0.83194	0.70208	0.5128	0.0272	1.00
O(6)	0.91204	0.56558	0.6327	0.0383	1.00
O(7)	0.8217	0.65688	0.7944	0.0349	1.00
O(8)	0.74191	0.56745	0.5719	0.0420	1.00
N(1)	0.5907	0.4068	0.1259	0.0369	1.00
N(2)	1.0999	0.5136	0.7018	0.0409	1.00
N(3)	1.0456	0.6279	0.4324	0.0455	1.00
N(4)	0.425	0.4829	0.1891	0.0387	1.00
C(1)	0.3851	0.5683	0.2387	0.0525	1.00
C(2)	0.3248	0.613	0.1021	0.0629	1.00
C(3)	0.3709	0.6589	-0.024	0.0546	1.00
C(4)	1.1235	0.6112	0.7035	0.0612	1.00
C(5)	1.1316	0.643	0.5374	0.0640	1.00
C(6)	1.048	0.6363	0.2602	0.0627	1.00
C(7)	0.9579	0.6156	0.1611	0.0664	1.00
C(8)	0.9283	0.5181	0.1505	0.0548	1.00
C(9)	0.5389	0.365	0.2419	0.0555	1.00
C(10)	0.4861	0.4372	0.315	0.0554	1.00

Table B.2: Selected bond distances for NiAPO-cyclam-1.

Atom-Atom	Distance, Å
Al(1)-O(2)	1.7190(1)
Al(1)-O(4)	1.7287(1)
Al(1)-O(5)	1.7388(1)
Al(1)-O(7)	1.7239(1)
Ni(1)-N(1)	2.0990(2)
Ni(1)-N(4)	2.0917(2)
Ni(2)-N(2)	2.1088(2)
Ni(2)-N(3)	2.0969(2)
Ni(2)-O(6)	2.0756(1)
P(1)-O(1)	1.4901(2)
P(1)-O(2)	1.5459(1)
P(1)-O(3)	1.5207(1)
P(1)-O(4)	1.5448(1)
P(2)-O(5)	1.5312(1)
P(2)-O(6)	1.4705(1)
P(2)-O(7)	1.5186(1)
P(2)-O(8)	1.5444(3)
N(1)-C(3)	1.4606(1)
N(1)-C(9)	1.4648(1)
N(3)-C(5)	1.4668(1)
N(3)-C(5)	1.4690(1)
N(4)-C(1)	1.4694(1)
N(4)-C(10)	1.4610(1)
C(1)-C(2)	1.5085(1)
C(2)-C(3)	1.5059(1)
C(4)-C(5)	1.5026(1)
C(5)-C(7)	1.5070(1)
C(7)-C(8)	1.4914(2)
C(9)-C(10)	1.5006(1)

Table B.3: Selected bond angles for NiAPO-cyclam-1.

Atom – Atom – Atom	Angle, °
O(2) – Al(1) – O(4)	111.899(6)
O(2) – Al(1) – O(5)	110.843(6)
O(2) – Al(1) – O(7)	106.612(8)
O(4) – Al(1) – O(5)	111.811(8)
O(4) – Al(1) – O(7)	109.615(6)
O(5) – Al(1) – O(7)	105.736(7)
N(1) – Ni(1) – N(1)	179.98
N(1) – Ni(1) – N(4)	84.657(6)
N(1) – Ni(1) – N(4)	95.343(6)
N(1) – Ni(1) – O(1)	92.247(8)
N(1) – Ni(1) – O(1)	87.753(8)
N(4) – Ni(1) – N(4)	179.972
N(4) – Ni(1) – O(1)	88.403(5)
N(4) – Ni(1) – O(1)	91.597(5)
O(1) – Ni(1) – O(1)	180
O(6) – Ni(2) – O(6)	180
O(6) – Ni(2) – N(2)	86.716(7)
O(6) – Ni(2) – N(2)	93.284(7)
O(6) – Ni(2) – N(3)	89.321(7)
O(6) – Ni(2) – N(3)	90.679(7)
N(2) – Ni(2) – N(2)	180
N(2) – Ni(2) – N(3)	85.379(3)
N(2) – Ni(2) – N(3)	94.621(3)
N(2) – Ni(2) – N(3)	85.379(3)
N(3) – Ni(2) – N(3)	180
O(1) – P(1) – O(2)	108.710(6)
O(1) – P(1) – O(3)	112.815(5)
O(1) – P(1) – O(4)	110.799(3)
O(2) – P(1) – O(3)	107.792(5)
O(2) – P(1) – O(4)	107.550(5)
O(3) – P(1) – O(4)	108.994(7)
O(5) – P(2) – O(6)	110.620(6)
O(5) – P(2) – O(7)	110.130(7)
O(5) – P(2) – O(8)	106.947(6)
O(6) – P(2) – O(7)	109.809(5)
O(6) – P(2) – O(8)	112.564(8)
O(7) – P(2) – O(8)	106.660(5)
N(4) – C(1) – C(2)	111.667(5)

continued on next page

Table B.3: *Continued*

Atom - Atom - Atom	Angle, °
N(2) - C(4) - C(5)	110.009(3)
N(3) - C(5) - C(4)	110.036(6)
N(3) - C(5) - C(7)	113.056(6)
N(2) - C(8) - C(7)	111.873(3)
N(1) - C(9) - C(10)	109.759(7)
C(1) - C(2) - C(3)	117.167(6)
C(5) - C(7) - C(8)	117.189(1)

Table B.4: Atomic coordinates and thermal parameters for as-prepared $\text{AlPO}_4(\text{F})\text{-STA-2}$ (**SAT**) templated by babob from Rietveld profile refinement of powder XRD data in space group $R\bar{3}$, with lattice parameters $a = 13.0245(5) \text{ \AA}$, $c = 29.598(1) \text{ \AA}$.

Atom	x	y	z	U_{iso}	Occ.
Al(1)	0.760699	0.766644	0.297995	0.031	1.00
Al(2)	0.562358	0.900921	0.220187	0.031	1.00
P(1)	0.567967	0.90147	0.115111	0.0021	1.00
P(2)	0.755414	1.005021	0.291026	0.0173	1.00
O(1)	0.592561	0.937397	0.162482	0.0218	1.00
O(2)	0.517469	0.756962	0.231758	0.0226	1.00
O(3)	0.793671	0.910777	0.295321	0.0256	1.00
O(4)	0.434272	0.913702	0.234021	0.054	1.00
O(5)	0.691162	0.998422	0.248004	0.0175	1.00
O(6)	0.860051	1.119388	0.295026	0.0075	1.00
O(7)	0.663177	0.97857	0.326775	0.0204	1.00
O(8)	0.636027	0.013396	0.088218	0.02	1.00
N(1)	0	0	0.1025	0.069	1.00
C(1)	0	0	0.1842	0.098	1.00
C(2)	-0.0415	0.0827	0.1662	0.135	1.00
C(3)	-0.0415	0.0787	0.1177	0.141	1.00
C(4)	-0.0312	0.0351	0.0556	0.216	1.00
C(5)	0	0	0.0241	0.189	1.00
O(4-ring)	0.1857	0.3739	0.1585	0.025	0.14
O(6-ring)	0.2219	0.4449	0.0432	0.025	0.25

Table B.5: Selected bond distances for as-prepared $\text{AlPO}_4(\text{F})\text{-STA-2}$ (**SAT**) templated with babob.

Atom-Atom	Distance, Å
Al(1)-O(3)	1.70547(7)
Al(1)-O(6)	1.75784(7)
Al(1)-O(7)	1.66389(5)
Al(1)-O(8)	1.82160(6)
Al(2)-O(1)	1.76368(8)
Al(2)-O(2)	1.69661(7)
Al(2)-O(4)	1.80448(7)
Al(2)-O(5)	1.72467(6)
P(1)-O(1)	1.46200(6)
P(1)-O(2)	1.65788(6)
P(1)-O(4)	1.32899(5)
P(1)-O(8)	1.50074(5)
P(2)-O(3)	1.54363(6)
P(2)-O(5)	1.50239(5)
P(2)-O(6)	1.43532(6)
P(2)-O(7)	1.50585(5)
C(1)-C(2)	1.52263(6)
C(2)-C(3)	1.43642(7)
C(3)-C(4)	1.94805(8)
C(4)-C(3)	1.94805(8)
C(4)-C(4)	1.29604(5)
C(4)-C(5)	1.19546(4)
C(5)-C(4)	1.19546(4)
C(5)-C(5)	1.42660(7)
N(1)-C(3)	1.44889(5)
N(1)-C(4)	1.57695(6)

Table B.6: Selected bond angles for as-prepared $\text{AlPO}_4(\text{F})\text{-STA-2}$ (**SAT**) templated with babob.

Atom - Atom - Atom	Angle, °
O(3) - Al(1) - O(6)	116.783
O(3) - Al(1) - O(7)	114.983(1)
O(3) - Al(1) - O(8)	100.248(1)
O(6) - Al(1) - O(7)	110.101
O(6) - Al(1) - O(8)	105.671(1)

continued on next page

Table B.6: *Continued*

Atom – Atom – Atom	Angle, °
O(7) – Al(1) – O(8)	107.743(3)
O(1) – Al(2) – O(2)	113.601
O(1) – Al(2) – O(4)	106.670(1)
O(1) – Al(2) – O(5)	105.076(2)
O(2) – Al(2) – O(4)	103.446
O(2) – Al(2) – O(5)	112.843(1)
O(4) – Al(2) – O(5)	115.311(1)
O(1) – P(1) – O(2)	112.388
O(1) – P(1) – O(4)	120.881(1)
O(1) – P(1) – O(8)	105.620(3)
O(2) – P(1) – O(4)	99.205(1)
O(2) – P(1) – O(8)	104.896(1)
O(4) – P(1) – O(8)	112.851(2)
O(3) – P(2) – O(5)	114.604(1)
O(3) – P(2) – O(6)	107.574
O(3) – P(2) – O(7)	107.338(1)
O(5) – P(2) – O(6)	109.997
O(5) – P(2) – O(7)	102.979(3)
O(6) – P(2) – O(7)	114.481(1)
Al(2) – O(1) – P(1)	149.182(2)
Al(2) – O(2) – P(1)	133.987(1)
Al(1) – O(3) – P(2)	151.089
Al(2) – O(4) – P(1)	144.544(2)
Al(2) – O(5) – P(2)	139.081(1)
Al(1) – O(6) – P(2)	165.898
Al(1) – O(7) – P(2)	154.611(1)
Al(1) – O(8) – P(1)	149.769
C(3) – N(1) – C(3)	110.817(1)
C(3) – N(1) – C(4)	80.030(3)
C(3) – N(1) – C(4)	123.515
C(3) – N(1) – C(4)	116.163(1)
C(4) – N(1) – C(4)	48.527(2)
C(2) – C(1) – C(2)	108.443(1)
C(1) – C(2) – C(3)	108.516(1)

Table B.7: Atomic coordinates and thermal parameters for calcined $\text{AlPO}_4(\text{F})\text{-STA-2}$ (**SAT**) templated by babob from Rietveld profile refinement of powder XRD data in space group $R\bar{3}$, with lattice parameters $a = 12.8974(4) \text{ \AA}$, $c = 30.784(1) \text{ \AA}$.

Atom	x	y	z	U_{iso}	Occ.
Al(1)	0.752988	0.759672	0.294374	0.016	1.00
Al(2)	0.575968	0.908527	0.215948	0.022	1.00
P(1)	0.575252	0.906246	0.117162	0.019	1.00
P(2)	0.759114	1.006389	0.290882	0.014	1.00
O(1)	0.621061	0.953713	0.162026	0.035	1.00
O(2)	0.538116	0.759567	0.224575	0.035	1.00
O(3)	0.789541	0.906605	0.294083	0.039	1.00
O(4)	0.456287	0.926806	0.227698	0.036	1.00
O(5)	0.701961	1.002428	0.246606	0.034	1.00
O(6)	0.868778	1.123358	0.295658	0.035	1.00
O(7)	0.670018	0.985707	0.326777	0.046	1.00
O(8)	0.651687	-0.00319	0.086391	0.034	1.00

Table B.8: Selected bond distances for calcined $\text{AlPO}_4(\text{F})\text{-STA-2}$ (**SAT**) templated with babob.

Atom-Atom	Distance, \AA
Al(1)-O(3)	1.70885(6)
Al(1)-O(6)	1.69468(6)
Al(1)-O(7)	1.77690(5)
Al(1)-O(8)	1.83106(5)
Al(2)-O(1)	1.75909(6)
Al(2)-O(2)	1.74985(6)
Al(2)-O(4)	1.71259(5)
Al(2)-O(5)	1.74070(5)
P(1)-O(1)	1.50653(5)
P(1)-O(2)	1.52592(5)
P(1)-O(4)	1.49516(5)
P(1)-O(8)	1.44291(4)
P(2)-O(3)	1.52480(5)
P(2)-O(5)	1.53821(5)
P(2)-O(6)	1.47113(5)
P(2)-O(7)	1.51859(4)

Table B.9: Selected bond angles for calcined $\text{AlPO}_4(\text{F})$ -STA-2 (**SAT**) templated with babob.

Atom – Atom – Atom	Angle, °
O(3) – Al(1) – O(6)	111.569
O(3) – Al(1) – O(7)	112.183(1)
O(3) – Al(1) – O(8)	112.064(1)
O(6) – Al(1) – O(7)	107.376(1)
O(6) – Al(1) – O(8)	108.355
O(7) – Al(1) – O(8)	104.945(3)
O(1) – Al(2) – O(2)	111.807
O(1) – Al(2) – O(4)	108.974
O(1) – Al(2) – O(5)	104.013(2)
O(2) – Al(2) – O(4)	110.072
O(2) – Al(2) – O(5)	109.421(1)
O(4) – Al(2) – O(5)	112.446(1)
O(1) – P(1) – O(2)	115.15
O(1) – P(1) – O(4)	111.938
O(1) – P(1) – O(8)	107.608(2)
O(2) – P(1) – O(4)	109.574
O(2) – P(1) – O(8)	109.413(1)
O(4) – P(1) – O(8)	102.340(1)
O(3) – P(2) – O(5)	110.519(1)
O(3) – P(2) – O(6)	109.746
O(3) – P(2) – O(7)	107.229(1)
O(5) – P(2) – O(6)	108.764
O(5) – P(2) – O(7)	109.328(3)
O(6) – P(2) – O(7)	111.253(1)
Al(2) – O(1) – P(1)	137.133(2)
Al(2) – O(2) – P(1)	145.608
Al(1) – O(3) – P(2)	153.075
Al(2) – O(4) – P(1)	150.086(1)
Al(2) – O(5) – P(2)	140.236(1)
Al(1) – O(6) – P(2)	168.885
Al(1) – O(7) – P(2)	153.295(1)
Al(1) – O(8) – P(1)	146.594(1)

Table B.10: Atomic coordinates and thermal parameters for as-prepared Mg-STA-2 (**SAT**) templated by babop from Rietveld profile refinement of powder XRD data in space group $R\bar{3}$, with lattice parameters $a = 12.9819(6)$ Å, $c = 30.931(2)$ Å.

Atom	x	y	z	U_{iso}	Occ.
Al(1)	0.7511	0.7556	0.29842	0.0057	0.85
Al(2)	0.5724	0.8993	0.21398	0.0057	0.85
Mg(1)	0.7511	0.7556	0.29842	0.0057	0.15
Mg(2)	0.5724	0.8993	0.21398	0.0057	0.15
P(1)	0.583071	0.907487	0.113321	0.0057	1.00
P(2)	0.76007	1.001554	0.288362	0.0057	1.00
O(1)	0.622498	0.947207	0.159661	0.0057	1.00
O(2)	0.537491	0.757642	0.228403	0.0057	1.00
O(3)	0.794681	0.906659	0.294194	0.0057	1.00
O(4)	0.46641	0.931289	0.229876	0.0057	1.00
O(5)	0.709944	0.99872	0.246779	0.0057	1.00
O(6)	0.867251	1.124033	0.296483	0.0057	1.00
O(7)	0.663117	0.985099	0.322769	0.0057	1.00
O(8)	0.669727	-0.009478	0.079392	0.0057	1.00
N(1)	0	0	0.120001	0.0057	1.00
C(1)	0	0	0.187765	0.0057	1.00
C(2)	0.001951	0.101666	0.180087	0.0057	1.00
C(3)	-0.019272	0.089387	0.141265	0.0057	1.00
C(4)	0	0	0	0.0057	1.00
C(5)	0	0	0.043965	0.0057	1.00
C(6)	0	0	0.092509	0.0057	1.00

Table B.11: Selected bond distances for as-prepared Mg–STA-2 (**SAT**) templated with babop.

Atom–Atom	Distance, Å
Al,Mg(1)–O(3)	1.75(1)
Al,Mg(1)–O(6)	1.71(1)
Al,Mg(1)–O(7)	1.73(1)
Al,Mg(1)–O(8)	1.87(1)
Al,Mg(2)–O(1)	1.80(1)
Al,Mg(2)–O(2)	1.72(1)
Al,Mg(2)–O(4)	1.70(1)
Al,Mg(2)–O(5)	1.89(1)
P(1)–O(1)	1.52265(7)
P(1)–O(2)	1.61022(7)
P(1)–O(4)	1.55466(7)
P(1)–O(8)	1.52193(5)
P(2)–O(3)	1.51841(7)
P(2)–O(5)	1.43361(6)
P(2)–O(6)	1.52148(7)
P(2)–O(7)	1.57911(6)
N(1)–C(1)	2.0960(1)
N(1)–C(3)	1.46017(6)
C(1)–C(2)	1.32874(6)
C(1)–C(3)	1.94119(7)
C(2)–C(3)	1.22449(6)
C(3)–C(6)	1.99344(7)
C(4)–C(5)	1.35990(7)
C(5)–C(6)	1.50153(8)

Table B.12: Selected bond angles for as-prepared Mg–STA-2 (**SAT**) templated with babop.

Atom – Atom – Atom	Angle, °
O(3) – Al,Mg(1) – O(6)	108.2(7)
O(3) – Al,Mg(1) – O(7)	116.6(6)
O(3) – Al,Mg(1) – O(8)	117.7(6)
O(6) – Al,Mg(1) – O(7)	108.5(6)
O(6) – Al,Mg(1) – O(8)	102.9(6)
O(7) – Al,Mg(1) – O(8)	101.8(6)
O(1) – Al,Mg(2) – O(2)	118.0(6)

continued on next page

Table B.12: *Continued*

Atom – Atom – Atom	Angle, °
O(1) – Al,Mg(2) – O(4)	112.6(6)
O(1) – Al,Mg(2) – O(5)	102.1(5)
O(2) – Al,Mg(2) – O(4)	112.0(6)
O(2) – Al,Mg(2) – O(5)	104.2(6)
O(4) – Al,Mg(2) – O(5)	106.4(6)
O(1) – P(1) – O(2)	112.694
O(1) – P(1) – O(4)	108.642
O(1) – P(1) – O(8)	113.891(3)
O(2) – P(1) – O(4)	108.628
O(2) – P(1) – O(8)	114.385(2)
O(4) – P(1) – O(8)	97.231(1)
O(3) – P(2) – O(5)	113.605(1)
O(3) – P(2) – O(6)	109.954
O(3) – P(2) – O(7)	110.448(1)
O(5) – P(2) – O(6)	109.946
O(5) – P(2) – O(7)	106.280(4)
O(6) – P(2) – O(7)	106.301(2)
Al,Mg(2) – O(1) – P(1)	139.5(4)
Al,Mg(2) – O(2) – P(1)	142.6(4)
Al,Mg(1) – O(3) – P(2)	148.8(4)
Al,Mg(2) – O(4) – P(1)	146.1(4)
Al,Mg(2) – O(5) – P(2)	139.5(3)
Al,Mg(1) – O(6) – P(2)	166.5(4)
Al,Mg(1) – O(7) – P(2)	147.6(4)
Al,Mg(1) – O(8) – P(1)	135.0(4)
C(3) – N(1) – C(3)	101.283(2)
C(3) – N(1) – C(6)	116.772(2)
C(2) – C(1) – C(2)	116.877
C(1) – C(2) – C(3)	98.898(1)
N(1) – C(3) – C(2)	115.365(2)
C(5) – C(4) – C(5)	180
C(4) – C(5) – C(6)	180
N(1) – C(6) – C(5)	180

Table B.13: Atomic coordinates and thermal parameters for calcined Mg-STA-2 (**SAT**) templated by babop from Rietveld profile refinement of powder XRD data in space group $R\bar{3}$, with lattice parameters $a = 12.826(1)$ Å, $c = 30.769(3)$ Å.

Atom	x	y	z	U_{iso}	Occ.
Al(1)	0.751623	0.75478	0.293268	0.0165	0.85
Al(2)	0.563036	0.901565	0.21624	0.0226	0.85
Mg(1)	0.751623	0.75478	0.293268	0.0165	0.15
Mg(2)	0.563039	0.901559	0.216244	0.0226	0.15
P(1)	0.574602	0.910809	0.119061	0.0194	1.00
P(2)	0.757715	0.999321	0.290442	0.0137	1.00
O(1)	0.613041	0.940254	0.161215	0.0348	1.00
O(2)	0.523514	0.748032	0.224923	0.0349	1.00
O(3)	0.794716	0.906952	0.29428	0.0386	1.00
O(4)	0.43942	0.912639	0.230425	0.0356	1.00
O(5)	0.692323	0.993871	0.248457	0.0337	1.00
O(6)	0.856364	1.123952	0.296592	0.0348	1.00
O(7)	0.661835	0.981495	0.325225	0.0461	1.00
O(8)	0.623376	-0.042044	0.074935	0.0341	1.00

Table B.14: Selected bond distances for calcined Mg-STA-2 (**SAT**) templated with babop.

Atom-Atom	Distance, Å
Al,Mg(1)-O(3)	1.7427(1)
Al,Mg(1)-O(6)	1.7600(1)
Al,Mg(1)-O(7)	1.7700(1)
Al,Mg(1)-O(8)	1.7975(1)
Al,Mg(2)-O(1)	1.7905(2)
Al,Mg(2)-O(2)	1.791(1)
Al,Mg(2)-O(4)	1.7175(1)
Al,Mg(2)-O(5)	1.7807(1)
P(1)-O(1)	1.3718(1)
P(1)-O(2)	1.5155(1)
P(1)-O(4)	1.4558(1)
P(1)-O(8)	1.4907(1)
P(2)-O(3)	1.4849(1)
P(2)-O(5)	1.5227(1)
P(2)-O(6)	1.4729(1)
P(2)-O(7)	1.5585(1)

Table B.15: Selected bond angles for calcined Mg-STA-2 (**SAT**) templated with babop.

Atom - Atom - Atom	Angle, °
O(3) - Al,Mg(1) - O(6)	112.077
O(3) - Al,Mg(1) - O(7)	109.207(2)
O(3) - Al,Mg(1) - O(8)	112.738(1)
O(6) - Al,Mg(1) - O(7)	102.370(2)
O(6) - Al,Mg(1) - O(8)	123.244(1)
O(7) - Al,Mg(1) - O(8)	93.988(7)
O(1) - Al,Mg(2) - O(2)	108.12
O(1) - Al,Mg(2) - O(4)	115.782(1)
O(1) - Al,Mg(2) - O(5)	104.874(6)
O(2) - Al,Mg(2) - O(4)	106.710(1)
O(2) - Al,Mg(2) - O(5)	107.788(2)
O(4) - Al,Mg(2) - O(5)	113.256(3)
O(1) - P(1) - O(2)	119.782
O(1) - P(1) - O(4)	113.667(2)
O(1) - P(1) - O(8)	136.830(5)

continued on next page

Table B.15: *Continued*

Atom –	Atom	– Atom	Angle, °
O(2) –	P(1)	– O(4)	93.354(1)
O(2) –	P(1)	– O(8)	97.790(4)
O(4) –	P(1)	– O(8)	81.949(4)
O(3) –	P(2)	– O(5)	114.789(1)
O(3) –	P(2)	– O(6)	114.322
O(3) –	P(2)	– O(7)	111.831(2)
O(5) –	P(2)	– O(6)	108.263
O(5) –	P(2)	– O(7)	101.523(7)
O(6) –	P(2)	– O(7)	104.930(2)
Al,Mg(2) –	O(1)	– P(1)	142.012(5)
Al,Mg(2) –	O(2)	– P(1)	136.545(1)
Al,Mg(1) –	O(3)	– P(2)	147.48
Al,Mg(2) –	O(4)	– P(1)	144.744(4)
Al,Mg(2) –	O(5)	– P(2)	144.220(1)
Al,Mg(1) –	O(6)	– P(2)	157.765(1)
Al,Mg(1) –	O(7)	– P(2)	149.957(2)
Al,Mg(1) –	O(8)	– P(1)	141.556(2)

Table B.16: Atomic coordinates and thermal parameters for Co–STA-7 (SAV) templated by tmtact from Rietveld profile refinement of powder XRD data in space group $P4/n$, with lattice parameters $a = 18.6401(5)$ Å, $c = 9.3757(3)$ Å.

Atom	x	y	z	U_{iso}	Occ.
Al(1)	0.061192	0.663125	0.088136	0.0258	0.80
Al(2)	-0.048459	0.830592	-0.163922	0.027	0.80
Al(3)	-0.046256	0.437012	0.335679	0.0252	0.80
Co(1)	0.061192	0.663125	0.088136	0.0258	0.20
Co(2)	-0.048459	0.830592	-0.163922	0.027	0.20
Co(3)	-0.046256	0.437012	0.335679	0.0252	0.20
P(1)	0.05751	0.556777	0.328992	0.0268	1.00
P(2)	-0.056766	0.659348	-0.152109	0.0268	1.00
P(3)	0.071024	0.833717	0.086049	0.0272	1.00
O(1)	0.043777	0.623536	0.250792	0.0479	1.00
O(2)	0.05382	0.583913	0.471879	0.0473	1.00
O(3)	0.137223	0.528171	0.294375	0.0465	1.00
O(4)	-0.012439	0.523218	0.306147	0.0477	1.00
O(5)	-0.022275	0.641689	-0.005623	0.0452	1.00
O(6)	-0.017696	0.630771	-0.263575	0.0461	1.00
O(7)	-0.128096	0.628528	-0.178959	0.0499	1.00
O(8)	-0.076131	0.735743	-0.171462	0.0524	1.00
O(9)	0.012231	0.847435	-0.002963	0.0492	1.00
O(10)	0.146187	0.852409	0.010893	0.0458	1.00
O(11)	0.098055	0.87007	0.24734	0.0524	1.00
O(12)	0.084137	0.744004	0.129866	0.0503	1.00
N(1)	0.3948	0.2638	0.6431	0.2	0.28
N(2)	0.0717	0.2598	0.6719	0.2	0.28
N(3)	0.2803	0.4072	0.6005	0.2	0.28
N(4)	0.2251	0.1373	0.6606	0.2	0.28
C(1)	0.4601	0.2412	0.5655	0.2	0.28
C(2)	0.0052	0.2818	0.5974	0.2	0.28
C(3)	0.2906	0.3986	0.7556	0.2	0.28
C(4)	0.227	0.0861	0.5396	0.2	0.28
C(5)	0.1258	0.3187	0.6827	0.2	0.28
C(6)	0.1551	0.3497	0.542	0.2	0.28
C(7)	0.204	0.4157	0.5565	0.2	0.28
C(8)	0.3248	0.3598	0.5071	0.2	0.28
C(9)	0.3329	0.28	0.547	0.2	0.28
C(10)	0.3766	0.2174	0.767	0.2	0.28

continued on next page

Table B.16: *Continued*

Atom	x	y	z	U_{iso}	Occ.
C(11)	0.3562	0.1382	0.7411	0.2	0.28
C(12)	0.2777	0.1183	0.7735	0.2	0.28
C(13)	0.1512	0.1486	0.7171	0.2	0.28
C(14)	0.1005	0.1904	0.6164	0.2	0.28
O	0.25	0.75	0.3428	0.4	0.64
O	0.1764	0.74449	0.4623	0.2	0.79
O	0.0924	0.7466	0.4881	0.2	0.09
O	0.25	0.75	0.215215	0.1202	0.08

Table B.17: Selected bond distances for Co-STA-7 (**SAV**) templated with tmtact.

Atom-Atom	Distance, Å
Al(1)-O(1)	1.72500(5)
Al(1)-O(5)	1.83112(4)
Al(1)-O(10)	1.88557(4)
Al(1)-O(12)	1.61519(4)
Al(2)-O(3)	1.97387(4)
Al(2)-O(7)	1.68535(5)
Al(2)-O(8)	1.84306(5)
Al(2)-O(9)	1.91200(4)
Al(3)-O(2)	1.85134(6)
Al(3)-O(4)	1.74817(5)
Al(3)-O(6)	1.86398(4)
Al(3)-O(11)	1.88305(4)
P(1)-O(1)	1.46683(3)
P(1)-O(2)	1.43363(4)
P(1)-O(3)	1.61165(4)
P(1)-O(4)	1.46192(4)
P(2)-O(5)	1.55176(4)
P(2)-O(6)	1.38069(3)
P(2)-O(7)	1.47011(4)
P(2)-O(8)	1.48021(4)
P(3)-O(9)	1.40102(3)
P(3)-O(10)	1.60650(4)
P(3)-O(11)	1.73201(5)
P(3)-O(12)	1.73924(4)

Table B.18: Selected bond angles for Co-STA-7 (**SAV**) templated with tmtact.

Atom – Atom – Atom	Angle, °
O(1) – Al(1) – O(5)	99.856(2)
O(1) – Al(1) – O(12)	103.590(2)
O(5) – Al(1) – O(10)	116.922(2)
O(10) – Al(1) – O(12)	92.832(1)
O(3) – Al(2) – O(7)	116.752(1)
O(3) – Al(2) – O(8)	118.055(1)
O(7) – Al(2) – O(8)	100.793
O(8) – Al(2) – O(9)	110.694
O(2) – Al(3) – O(4)	112.054
O(2) – Al(3) – O(6)	105.032(1)
O(2) – Al(3) – O(11)	107.005(1)
O(4) – Al(3) – O(6)	109.573
O(1) – P(1) – O(2)	99.171(2)
O(1) – P(1) – O(3)	109.933(1)
O(2) – P(1) – O(3)	110.435
O(2) – P(1) – O(4)	104.187
O(5) – P(2) – O(6)	111.688(2)
O(5) – P(2) – O(7)	116.319
O(5) – P(2) – O(8)	114.431
O(6) – P(2) – O(8)	114.017(1)
O(9) – P(3) – O(10)	112.416(2)
O(9) – P(3) – O(12)	115.221
O(10) – P(3) – O(12)	100.928
O(11) – P(3) – O(12)	97.415(1)
Al(1) – O(1) – P(1)	140.531
Al(3) – O(2) – P(1)	147.143(1)
Al(2) – O(3) – P(1)	130.122
Al(3) – O(4) – P(1)	133.765
Al(1) – O(5) – P(2)	136.939
Al(3) – O(6) – P(2)	150.852
Al(2) – O(7) – P(2)	138.157
Al(2) – O(8) – P(2)	148.201
Al(2) – O(9) – P(3)	154.555
Al(1) – O(10) – P(3)	123.178(1)
Al(3) – O(11) – P(3)	127.380(1)
Al(1) – O(12) – P(3)	143.418(1)

Table B.19: Atomic coordinates and thermal parameters for Zn–STA-7 (SAV) templated by tmtact from Rietveld profile refinement of powder XRD data in space group $P4/n$, with lattice parameters $a = 18.709(1)$ Å and $c = 9.428(1)$ Å.

Atom	x	y	z	U_{iso}	Occ.
Al(1)	0.06412	0.66568	0.0809	0.025	0.80
Al(2)	-0.04423	0.83599	-0.1578	0.025	0.80
Al(3)	-0.0507	0.43481	0.3358	0.025	0.80
Zn(1)	0.06412	0.66568	0.0809	0.025	0.20
Zn(2)	-0.04423	0.83599	-0.1578	0.025	0.20
Zn(3)	-0.0507	0.43481	0.3358	0.025	0.20
P(1)	0.064413	0.55768	0.3363	0.025	1.00
P(2)	-0.05021	0.66685	-0.1622	0.025	1.00
P(3)	0.06624	0.8342	0.0942	0.025	1.00
O(1)	0.0574	0.6243	0.2463	0.025	1.00
O(2)	0.0754	0.5807	0.4878	0.025	1.00
O(3)	0.1273	0.5128	0.2903	0.025	1.00
O(4)	-0.005	0.5162	0.3239	0.025	1.00
O(5)	-0.0151	0.6567	-0.0189	0.025	1.00
O(6)	-0.0026	0.6359	-0.2775	0.025	1.00
O(7)	-0.1221	0.6292	-0.1598	0.025	1.00
O(8)	-0.0624	0.7442	-0.1932	0.025	1.00
O(9)	-0.0021	0.8449	0.0127	0.025	1.00
O(10)	0.1297	0.863	0.0146	0.025	1.00
O(11)	0.0599	0.8703	0.2363	0.025	1.00
O(12)	0.0795	0.7556	0.1207	0.025	1.00
N(1)	0.4156	0.2761	0.6787	0.04	0.25
N(2)	0.0795	0.2305	0.6832	0.04	0.25
N(3)	0.2605	0.3903	0.5089	0.04	0.25
N(4)	0.2241	0.0795	0.6545	0.04	0.25
C(1)	0.4652	0.2611	0.5592	0.04	0.25
C(2)	0.0496	0.2345	0.5373	0.04	0.25
C(3)	0.263	0.4625	0.5744	0.04	0.25
C(4)	0.2484	0.02837	0.5444	0.04	0.25
C(5)	0.1092	0.2993	0.7392	0.04	0.25
C(6)	0.1847	0.3237	0.6972	0.04	0.25
C(7)	0.1943	0.349	0.5426	0.04	0.25
C(8)	0.3289	0.3489	0.5139	0.04	0.25
C(9)	0.3671	0.3394	0.6591	0.04	0.25
C(10)	0.3812	0.2112	0.7406	0.04	0.25

continued on next page

Table B.19: *Continued*

Atom	x	y	z	U_{iso}	Occ.
C(11)	0.3289	0.1699	0.6455	0.04	0.25
C(12)	0.2851	0.1146	0.7298	0.04	0.25
C(13)	0.1675	0.1294	0.6013	0.04	0.25
C(14)	0.1215	0.1642	0.7191	0.04	0.25
O(13)	0.25	0.25	0.134476	0.025	0.63
O(14)	0.25	0.25	0.396761	0.025	1.83
O(15)	0.25	0.25	0.021742	0.025	1.00

Table B.20: Selected bond distances for Zn–STA-7 (**SAV**) templated with tmtact.

Atom–Atom	Distance, Å
Al,Zn(1)–O(1)	1.7454(1)
Al,Zn(1)–O(5)	1.7637(1)
Al,Zn(1)–O(10)	1.7673(1)
Al,Zn(1)–O(12)	1.7477(1)
Al,Zn(2)–O(3)	1.7806(1)
Al,Zn(2)–O(7)	1.7728(1)
Al,Zn(2)–O(8)	1.7823(1)
Al,Zn(2)–O(9)	1.7979(1)
Al,Zn(3)–O(2)	1.7502(2)
Al,Zn(3)–O(4)	1.7501(1)
Al,Zn(3)–O(6)	1.7456(1)
Al,Zn(3)–O(11)	1.7534(1)
P(1)–O(1)	1.51355(9)
P(1)–O(2)	1.5058(1)
P(1)–O(3)	1.5092(1)
P(1)–O(4)	1.5175(1)
P(2)–O(5)	1.5141(1)
P(2)–O(6)	1.51997(9)
P(2)–O(7)	1.5186(1)
P(2)–O(8)	1.4940(1)
P(3)–O(9)	1.50514(9)
P(3)–O(10)	1.50445(9)
P(3)–O(11)	1.5049(1)
P(3)–O(12)	1.5122(1)

Table B.21: Selected bond angles for Zn-STA-7 (SAV) templated with tmtact.

Atom – Atom – Atom	Angle, °
O(1) – Al,Zn(1) – O(5)	111.945(4)
O(1) – Al,Zn(1) – O(10)	109.978(4)
O(1) – Al,Zn(1) – O(12)	104.309(4)
O(5) – Al,Zn(1) – O(10)	109.906(5)
O(5) – Al,Zn(1) – O(12)	110.159(1)
O(10) – Al,Zn(1) – O(12)	110.428(1)
O(3) – Al,Zn(2) – O(7)	111.060(1)
O(3) – Al,Zn(2) – O(8)	110.775(3)
O(3) – Al,Zn(2) – O(9)	109.182(6)
O(7) – Al,Zn(2) – O(8)	104.666
O(7) – Al,Zn(2) – O(9)	111.204(2)
O(8) – Al,Zn(2) – O(9)	109.899
O(2) – Al,Zn(3) – O(4)	109.525(1)
O(2) – Al,Zn(3) – O(6)	108.925(2)
O(2) – Al,Zn(3) – O(11)	107.158(5)
O(4) – Al,Zn(3) – O(6)	111.113(1)
O(4) – Al,Zn(3) – O(11)	109.176(1)
O(6) – Al,Zn(3) – O(11)	110.855(3)
O(1) – P(1) – O(2)	107.933(5)
O(1) – P(1) – O(3)	111.394(3)
O(1) – P(1) – O(4)	107.688(1)
O(2) – P(1) – O(3)	108.979(2)
O(2) – P(1) – O(4)	109.645(1)
O(3) – P(1) – O(4)	111.135(1)
O(5) – P(2) – O(6)	109.628(6)
O(5) – P(2) – O(7)	108.231(2)
O(5) – P(2) – O(8)	111.239
O(6) – P(2) – O(7)	110.674(1)
O(6) – P(2) – O(8)	108.583(3)
O(7) – P(2) – O(8)	108.486
O(9) – P(3) – O(10)	111.610(5)
O(9) – P(3) – O(11)	109.128(4)
O(9) – P(3) – O(12)	110.675
O(10) – P(3) – O(11)	110.207(4)
O(10) – P(3) – O(12)	107.533(1)
O(11) – P(3) – O(12)	107.602(4)
P(1) – O(1) – Al,Zn(1)	149.299(1)

continued on next page

Table B.21: *Continued*

Atom	-	Atom	-	Atom	Angle, °
P(1)	-	O(2)	-	Al,Zn(3)	144.852(4)
P(1)	-	O(3)	-	Al,Zn(2)	146.693(1)
P(1)	-	O(4)	-	Al,Zn(3)	149.122
P(2)	-	O(5)	-	Al,Zn(1)	145.959(1)
P(2)	-	O(6)	-	Al,Zn(3)	148.076(1)
P(2)	-	O(7)	-	Al,Zn(2)	143.898
P(2)	-	O(8)	-	Al,Zn(2)	150.197(2)
P(3)	-	O(9)	-	Al,Zn(2)	144.733(1)
P(3)	-	O(10)	-	Al,Zn(1)	146.214(1)
P(3)	-	O(11)	-	Al,Zn(3)	148.221
P(3)	-	O(12)	-	Al,Zn(1)	150.900(2)

Table B.22: Atomic coordinates and thermal parameters for Mn-STA-6 (**SAS**) templated by tmtact from Rietveld profile refinement of powder XRD data in space group $P4/mnc$, with lattice parameters $a = 14.2727(3)$ Å, $c = 10.3749(2)$ Å.

Atom	x	y	z	U_{iso}	Occ.
Al(1)	0.2695	0.1074	0	0.021	1.00
Al(2)	0.3865	-0.1135	-0.25	0.0314	1.00
P(1)	0.605	-0.1050	-0.25	0.0305	1.00
P(2)	0.2652	-0.1161	0	0.0241	1.00
O(1)	0.2508	-0.0115	0	0.038	1.00
O(2)	0.3203	-0.1351	-0.118	0.0491	1.00
O(3)	0.5057	-0.1255	-0.2099	0.0495	1.00
O(4)	0.1781	-0.1687	0	0.0427	1.00
O(5)	0.6631	-0.1415	-0.148	0.064	1.00
N(1)	0.5595	0.6718	0.0547	0.09	0.16
N(2)	0.5368	0.3621	0	0.09	0.16
N(3)	0.4221	0.5146	0.2956	0.09	0.16
N(4)	0.4938	0.5105	0.7902	0.09	0.16
C(1)	0.4937	0.7371	1	0.09	0.16
C(2)	0.6187	0.3376	0.0918	0.09	0.16
C(3)	0.4966	0.4748	0.3812	0.09	0.16
C(4)	0.4092	0.5505	0.7258	0.09	0.16
C(5)	0.4451	0.32	0.0477	0.09	0.16
C(6)	0.4066	0.348	0.1815	0.09	0.16
C(7)	0.3685	0.4473	0.2101	0.09	0.16
C(8)	0.4508	0.605	0.2332	0.09	0.16
C(9)	0.5145	0.5906	0.1159	0.09	0.16
C(10)	0.646	0.6501	0.9782	0.09	0.16
C(11)	0.648	0.5692	0.8802	0.09	0.16
C(12)	0.581	0.5662	0.7643	0.09	0.16
C(13)	0.5025	0.4061	0.7672	0.09	0.16
C(14)	0.5593	0.3481	0.8665	0.09	0.16

Table B.23: Selected bond distances for Mn-STA-6 (**SAS**) templated with tmtact.

Atom-Atom	Distance, Å
Al(1)-O(1)	1.71784(3)
Al(1)-O(5)	1.87108(3)
Al(2)-O(2)	1.69463(3)
Al(2)-O(3)	1.75975(3)
P(1)-O(3)	1.50608(3)
P(1)-O(5)	1.44576(2)
P(2)-O(1)	1.50775(3)
P(2)-O(2)	1.47765(2)
P(2)-O(4)	1.45251(3)

Table B.24: Selected bond angles for Mn-STA-6 (**SAS**) templated with tmtact.

Atom - Atom - Atom	Angle, °
O(1) - Al,Mn(1) - O(4)	116.065
O(1) - Al(1) - O(5)	109.669
O(4) - Al(1) - O(5)	105.764
O(5) - Al(1) - O(5)	109.701(2)
O(2) - Al(2) - O(2)	116.979(1)
O(2) - Al(2) - O(3)	109.232(1)
O(2) - Al(2) - O(3)	108.258
O(3) - Al(2) - O(3)	104.121
O(3) - P(1) - O(3)	116.224
O(3) - P(1) - O(5)	105.471(1)
O(3) - P(1) - O(5)	115.512
O(5) - P(1) - O(5)	97.379(2)
O(1) - P(2) - O(2)	104.746
O(1) - P(2) - O(4)	113.31
O(2) - P(2) - O(2)	111.389(2)
O(2) - P(2) - O(4)	111.167
Al(1) - O(1) - P(2)	163.233
Al(2) - O(2) - P(2)	158.849
Al(2) - O(3) - P(1)	145.688(1)
Al(1) - O(4) - P(2)	156.143
Al(1) - O(5) - P(1)	143.389(1)

Table B.25: Atomic coordinates and thermal parameters for Ni-STA-6 (SAS) templated by tmtact from Rietveld profile refinement of powder XRD data in space group $P4/mnc$, with lattice parameters $a = 14.333(6)$ Å, $c = 10.236(5)$ Å.

Atom	x	y	z	U_{iso}	Occ.
Al(1)	0.275732	0.110917	0	0.025	1.00
Al(2)	0.391213	0.891213	0.75	0.025	1.00
P(1)	0.608526	0.891474	0.75	0.025	1.00
P(2)	0.274241	0.883559	0	0.025	1.00
O(1)	0.229829	0.989988	0	0.025	1.00
O(2)	0.33382	0.892687	0.878355	0.025	1.00
O(3)	0.508714	0.881496	0.806328	0.025	1.00
O(4)	0.311569	0.791432	0	0.025	1.00
O(5)	0.654248	0.887571	0.868024	0.025	1.00
N(1)	0.5595	0.6718	0.0547	0.3	0.09
N(2)	0.5368	0.3621	0	0.3	0.09
N(3)	0.4221	0.5146	0.2956	0.3	0.09
N(4)	0.4938	0.5105	0.7902	0.3	0.09
C(1)	0.4937	0.7371	1	0.3	0.09
C(2)	0.6187	0.3376	0.0918	0.3	0.09
C(3)	0.4966	0.4748	0.3812	0.3	0.09
C(4)	0.4092	0.5505	0.7258	0.3	0.09
C(5)	0.4451	0.32	0.0477	0.3	0.09
C(6)	0.4066	0.348	0.1815	0.3	0.09
C(7)	0.3685	0.4473	0.2101	0.3	0.09
C(8)	0.4508	0.605	0.2332	0.3	0.09
C(9)	0.5145	0.5906	0.1159	0.3	0.09
C(10)	0.646	0.6501	0.9782	0.3	0.09
C(11)	0.648	0.5692	0.8802	0.3	0.09
C(12)	0.581	0.5662	0.7643	0.3	0.09
C(13)	0.5025	0.4061	0.7672	0.3	0.09
C(14)	0.5593	0.3481	0.8665	0.3	0.09
Ni(1)	0	0	0.5	0.3	2.67

Table B.26: Selected bond distances for Ni-STA-6 (**SAS**) templated with tmtact.

Atom-Atom	Distance, Å
Al(1)-O(1)	1.8540(7)
Al(1)-O(5)	1.6830(6)
Al(2)-O(2)	1.5502(6)
Al(2)-O(3)	1.7856(6)
P(1)-O(3)	1.5490(5)
P(1)-O(5)	1.3755(6)
P(2)-O(1)	1.6529(7)
P(2)-O(2)	1.5155(6)
P(2)-O(4)	1.4247(6)
Ni(1)-N(2)	2.0457(8)
Ni(1)-N(4)	2.155(1)

Table B.27: Selected bond angles for Ni-STA-6 (**SAS**) templated with tmtact.

Atom - Atom - Atom	Angle, °
O(1) - Al(1) - O(5)	102.924(6)
O(5) - Al(1) - O(5)	106.77(4)
O(2) - Al(2) - O(3)	103.17(3)
O(2) - Al(2) - O(3)	102.67(1)
O(3) - Al(2) - O(3)	104.561(6)
O(3) - P(1) - O(3)	108.003(8)
O(3) - P(1) - O(5)	96.28(3)
O(3) - P(1) - O(5)	108.69(1)
O(1) - P(2) - O(2)	97.893(4)
O(2) - P(2) - O(2)	110.49(4)
O(2) - P(2) - O(4)	82.439(3)
Al(1) - O(1) - P(2)	136.563
Al(2) - O(2) - P(2)	173.789(3)
Al(2) - O(3) - P(1)	138.05(2)
Al(1) - O(5) - P(1)	171.310(3)
N(2) - Ni(1) - N(2)	90.000

Table B.28: Atomic coordinates and thermal parameters for Co-STA-6 (**SAS**) templated by dmtabch from Rietveld profile refinement of powder XRD data in space group $P4/mnc$, with lattice parameters $a = 14.2852(9)$, $c = 10.2088(7)$ Å.

Atom	x	y	z	U_{iso}	Occ.
Al(1)	0.2689	0.1091	0	0.021	1.00
Al(2)	0.3907	0.8907	0.75	0.031	1.00
P(1)	0.6101	0.8899	0.75	0.031	1.00
P(2)	0.2666	0.8863	0	0.024	1.00
O(1)	0.2414	0.9886	0	0.038	1.00
O(2)	0.3209	0.8603	0.8826	0.049	1.00
O(3)	0.5093	0.8722	0.7865	0.049	1.00
O(4)	0.175	0.8339	0	0.043	1.00
O(5)	0.6683	0.8619	0.8614	0.064	1.00

Table B.29: Selected bond distances for Co-STA-6 (**SAS**) templated with dmtabch.

Atom-Atom	Distance, Å
Al,Co(1)-O(1)	1.7656(1)
Al,Co(1)-O(4)	1.7444(1)
Al,Co(1)-O(5)	1.72582(9)
Al,Co(2)-O(2)	1.73645(9)
Al,Co(2)-O(3)	1.7547(1)
P(1)-O(3)	1.50872(9)
P(1)-O(5)	1.46443(7)
P(2)-O(1)	1.5051(1)
P(2)-O(2)	1.47515(8)
P(2)-O(4)	1.5075(1)

Table B.30: Selected bond angles for Co-STA-6 (SAS) templated with dmtabch.

Atom – Atom – Atom	Angle, °
O(1) – Al,Co(1) – O(4)	109.806
O(1) – Al,Co(1) – O(5)	110.468(1)
O(4) – Al,Co(1) – O(5)	107.943(1)
O(5) – Al,Co(1) – O(5)	110.142(5)
O(2) – Al,Co(2) – O(2)	108.694(5)
O(2) – Al,Co(2) – O(3)	110.561(3)
O(2) – Al,Co(2) – O(3)	108.695(1)
O(2) – Al,Co(2) – O(3)	110.561(3)
O(3) – Al,Co(2) – O(3)	109.629
O(3) – P(1) – O(3)	112.39
O(3) – P(1) – O(5)	107.715(3)
O(3) – P(1) – O(5)	110.937(1)
O(3) – P(1) – O(5)	107.715(3)
O(5) – P(1) – O(5)	107.035(5)
O(1) – P(2) – O(2)	111.731(1)
O(1) – P(2) – O(4)	105.933
O(2) – P(2) – O(2)	108.675(5)
O(2) – P(2) – O(4)	109.354(1)
Al,Co(1) – O(1) – P(2)	153.306
Al,Co(2) – O(2) – P(2)	150.733(2)
Al,Co(2) – O(3) – P(1)	147.546(2)
Al,Co(1) – O(4) – P(2)	152.434
Al,Co(1) – O(5) – P(1)	150.025(2)

Appendix C

Publications

P. A. Wright, M. J. Maple, A. M. Z. Slawin, V. Patinec, R. A. Aitken, S. Welsh, and P. A. Cox, *J. Chem. Soc., Dalton Trans.*, 2000, p. 1243.

M. J. Maple, E. F. Philp, A. M. Z. Slawin, P. Lightfoot, P. A. Cox, and P. A. Wright, *J. Mater. Chem.*, 2001, **11**, 98.

R. García, M. J. Maple, T. D. Coombs, A. M. Z. Slawin, A. Beale, G. Sankar, P. A. Cox and P. A. Wright, *in preparation*.

References

- [1] J. Rouquérol, D. Avnir, C. W. Fairbridge, D. H. Everett, J. H. Haynes, N. Pericone, J. D. F. Ramsay, K. S. W. Sing, and K. K. Unger, *Pure Appl. Chem.*, 1994, **66**, 1739.
- [2] A. F. Cronstedt, *Kongl. Svenska Vetenskaps Akademiens Handlingar.*, 1756, **17**, 20.
- [3] S. T. Wilson, B. M. Lok, C. A. Messina, T. R. Cannan, and E. M. Flanigen, *J. Am. Chem. Soc.*, 1982, **104**, 1146.
- [4] L. B. McCusker, F. Liebau, and G. Engelhardt, *Pure Appl. Chem.*, 2001, **73**, 381.
- [5] J. V. Smith, *Mineral. Soc. Am. Spec. Pap.*, 1963, **1**, 281.
- [6] J. V. Smith, *Chem. Rev.*, 1988, **88**, 149.
- [7] C. Baerlocher, W. M. Meier, and D. H. Olson, *Atlas of Zeolite Framework Types*, Elsevier, Amsterdam, 5th ed., 2001.
- [8] H. de Sainte Claire-Deville, *C. R. Hebd. Seances Acad. Sci.*, 1862, **54**, 324.
- [9] R. M. Barrer, *J. Chem. Soc.*, 1948, p. 127.
- [10] E. M. Flanigen, R. L. Patton, and S. T. Wilson, *Stud. Surf. Sci. Catal.*, 1988, **37**, 13.
- [11] R. M. Barrer, *Zeolites and Clay Minerals as Sorbents and Molecular Sieves*, Academic, London, 1978.
- [12] A. Damour, *Ann. Mines*, 1840, **17**, 191.
- [13] H. Eichhorn, *Poggendorf Ann. Phys. Chem.*, 1858, **105**, 126.
- [14] G. Friedel, *Bull. Soc. Franc. Mineral. Cristallogr.*, 1896, **19**, 94.
- [15] F. Grandjean, *C. R. Hebd. Seances Acad. Sci.*, 1909, **149**, 866.

- [16] O. Weigel and E. Steinhoff, *Z. Kristallog.*, 1925, **61**, 125.
- [17] W. H. Taylor, *Z. Kristallog.*, 1930, **74**, 1.
- [18] J. W. McBain, *The Sorption of Gases and Vapours by Solids*, Rutledge, London, 1930.
- [19] R. M. Barrer, *Discuss. Faraday Soc.*, 1949, **7**, 135.
- [20] D. W. Breck, W. G. Eversole, R. M. Milton, T. B. Reed, and T. L. Thomas, *J. Am. Chem. Soc.*, 1956, **78**, 5963.
- [21] T. B. Reed and D. W. Breck, *J. Am. Chem. Soc.*, 1956, **78**, 5972.
- [22] R. M. Barrer and P. J. Denny, *J. Chem. Soc.*, 1961, p. 971.
- [23] R. J. Cernik, W. Clegg, C. R. A. Catlow, G. Bushnell-Wye, J. V. Flaherty, G. N. Greaves, M. Hamichi, I. Burrows, D. J. Taylor, and S. J. Teat, *J. Synchrotron Radiat.*, 1997, **4**, 279.
- [24] W. J. Moore, *Physical Chemistry*, Longman, London, 5th ed., 1972.
- [25] M. M. Wolfson, *An Introduction to X-ray Crystallography*, CUP, Cambridge, 2nd ed., 1997.
- [26] A. M. Z. Slawin, *Chem. Br.*, 1998, **10**, 31.
- [27] W. Clegg, *Crystal Structure Determination*, OUP, Oxford, 1998.
- [28] ed. C. Giacovazzo, *Fundamentals of Crystallography*, OUP, Oxford, 1992.
- [29] J. M. Robertson and I. Woodward, *J. Chem. Soc.*, 1937, p. 219.
- [30] I. L. Karle, H. Hauptman, J. Karle, and A. B. Wing, *Acta Crystallogr.*, 1958, **11**, 257.
- [31] H. M. Rietveld, *Acta Crystallogr.*, 1967, **22**, 151.
- [32] A. C. Larson and R. B. von Dreele General Structure Analysis System (GSAS), Technical Report LAUR 86-748, Los Alamos National Laboratory, 1994.
- [33] ed. R. A. Young, *The Rietveld Method*, OUP, Oxford, 1993.
- [34] ed. A. K. Cheetham and P. Day, *Solid State Chemistry: Techniques*, Clarendon, Oxford, 1987.
- [35] E. O. Stejskal and J. D. Memory, *High Resolution NMR in the Solid State: Fundamentals of CP/MAS*, OUP, New York, 1994.

- [36] P. Zeeman, *Nature (London)*, 1897, **55**, 347.
- [37] K. T. Mueller, B. Q. Sun, G. Chingas, J. W. Zwanziger, T. Terao, and A. Pines, *J. Magn. Reson.*, 1990, **86**, 270.
- [38] L. Frydman and J. S. Harwood, *J. Am. Chem. Soc.*, 1995, **117**, 5367.
- [39] L. Pauling, *J. Am. Chem. Soc.*, 1929, **51**, 1010.
- [40] A. S. Wills and I. D. Brown, *Valist for Windows*, v. 1.5, 1998.
- [41] W. Loewentstein, *Am. Mineral.*, 1954, **39**, 92.
- [42] R. G. Bell, R. A. Jackson, and C. R. A. Catlow, *Zeolites*, 1992, **12**, 870.
- [43] C. R. A. Catlow, A. R. George, and C. M. Freeman, *J. Chem. Soc., Chem. Commun.*, 1996, p. 1311.
- [44] J. A. Tossell, *Am. Mineral.*, 1993, **78**, 911.
- [45] J. Klinowski, J. M. Thomas, C. A. Fyfe, and J. S. Hartman, *J. Phys. Chem.*, 1981, **85**, 2590.
- [46] J. F. Stebbins, P. Zhao, S. K. Lee, and X. Cheng, *Am. Mineral.*, 1999, **84**, 1680.
- [47] W. Depmeier, *Acta Crystallogr., Sect. C: Cryst. Struct. Commun.*, 1984, **40**, 226.
- [48] A. Huang and S.-J. Hwu, *Chem. Mater.*, 2001, **13**, 1794.
- [49] E. Dempsey, G. H. Köhl, and D. H. Olson, *J. Phys. Chem.*, 1969, **73**, 387.
- [50] M. Sato, K. Maeda, and K. Hirasawa, *Chem. Lett.*, 1994, p. 1543.
- [51] K.-P. Schröder and J. Sauer, *J. Phys. Chem.*, 1993, **97**, 6579.
- [52] M. Goepper and J. L. Guth, *Zeolites*, 1991, **11**, 477.
- [53] D. W. Lewis, G. Sankar, J. K. Wyles, J. M. Thomas, C. R. A. Catlow, and D. J. Willcock, *Angew. Chem., Int. Ed. Engl.*, 1997, **36**, 2675.
- [54] D. E. Akporiaye, I. M. Dahl, A. Karlsson, and R. Wendelbo, *Angew. Chem., Int. Ed. Engl.*, 1998, **37**, 609.
- [55] Q. Gao, B. M. Weckhuysen, and R. A. Schoonheydt, *Microporous Mesoporous Mater.*, 1999, **27**, 75.

- [56] D. W. Breck, *Zeolite Molecular Sieves*, Wiley, New York, 1974.
- [57] C. Baelocher and W. M. Meier, *Helv. Chim. Acta*, 1969, **52**, 1853.
- [58] E. M. Flanigen, J. M. Bennett, R. W. Grose, J. P. Cohen, R. L. Patton, R. M. Kirchner, and J. V. Smith, *Nature (London)*, 1978, **271**, 512.
- [59] A. Moini, K. D. Schmitt, E. W. Valyocsik, and R. F. Polomski, *Zeolites*, 1994, **10**, 522.
- [60] M. E. Davis and R. F. Lobo, *Chem. Mater.*, 1992, **4**, 756.
- [61] J. Ciric US Pat. 3,950,496, 1976.
- [62] A. P. Stevens, A. M. Gorman, C. M. Freeman, and P. A. Cox, *J. Chem. Soc., Faraday Trans.*, 1996, p. 2065.
- [63] R. Szostak, *Molecular Sieves: Principles of Synthesis and Identification*, Van Nostrand Reinhold, New York, 1989.
- [64] R. J. Francis and D. O'Hare, *J. Chem. Soc., Dalton Trans.*, 1998, p. 3133.
- [65] S. P. Zhdanov, *Adv. Chem. Ser.*, 1971, **101**, 20.
- [66] G. T. Kerr, *J. Phys. Chem.*, 1966, **70**, 1047.
- [67] F. Testa, R. Szostak, R. Chiappetta, R. Aiello, A. Fonseca, and J. B. Nagy, *Zeolites*, 1997, **18**, 106.
- [68] S. Oliver, A. Kuperman, and G. A. Ozin, *Angew. Chem., Int. Ed. Engl.*, 1998, **37**, 46.
- [69] L. A. Villaescusa, P. S. Wheatley, I. Bull, P. Lightfoot, and R. E. Morris, *J. Am. Chem. Soc.*, 2001, **123**, 8797.
- [70] C. S. Cundy and P. A. Cox, *Chem. Rev.*, 2003, **103**, 663.
- [71] M. E. Davis, *Nature (London)*, 2002, **417**, 813.
- [72] J. J. Berzelius, *Edinburgh New Philos. J.*, 1836, **21**, 223.
- [73] J. M. Thomas, *Angew. Chem., Int. Ed. Engl.*, 1994, **33**, 913.
- [74] J. M. Thomas, R. G. Bell, and P. A. Wright, *Bull. Soc. Chim. Fr.*, 1994, **131**, 463.
- [75] B. C. Gates, *Catalytic Chemistry*, Wiley, New York, 1992.

- [76] S. M. Csicsery, *Zeolites*, 1984, **4**, 202.
- [77] G. C. Bond, *Heterogeneous Catalysis: Principles and Applications*, Clarendon, Oxford, 2nd ed., 1987.
- [78] J. M. Thomas and W. J. Thomas, *Principals and Practice of Heterogeneous Catalysis*, VCH, Weinheim, 1997.
- [79] R. E. Morris and P. A. Wright, *Chem. Ind. (London)*, 1998, p. 256.
- [80] W. T. A. Harrison, T. E. Gier, G. D. Stucky, R. W. Broach, and R. A. Bedard, *Chem. Mater.*, 1996, **8**, 145.
- [81] J. Shailaja, J. Sivaguru, S. Uppili, A. Joy, and V. Ramamurthy, *Micro-porous Mesoporous Mater.*, 2001, **48**, 319.
- [82] A. K. Cheetham, G. Férey, and T. Loiseau, *Angew. Chem., Int. Ed. Engl.*, 1999, **38**, 3268.
- [83] K. Maeda, Y. Kiyozumi, and F. Mizukami, *Angew. Chem., Int. Ed. Engl.*, 1994, **33**, 2335.
- [84] O. M. Yaghi, H. Li, C. Davis, D. Richardson, and T. L. Groy, *Acc. Chem. Res.*, 1998, **31**, 474.
- [85] G. Férey, *Chem. Mater.*, 2001, **13**, 3084.
- [86] C. T. Kresge, M. E. Leonowicz, W. J. Roth, J. C. Vaturi, and J. S. Beck, *Nature (London)*, 1992, **359**, 710.
- [87] P. B. Moore and J. Shen, *Nature (London)*, 1983, **306**, 356.
- [88] M. E. Davis, C. Saldarriaga, C. Montes, J. Garces, and C. Crowder, *Nature (London)*, 1988, **331**, 698.
- [89] R. M. Dessau, J. L. Schlenker, and J. B. Higgins, *Zeolites*, 1990, **10**, 522.
- [90] K. J. Balkus Jr, A. G. Gabrielov, and N. Sandler, *Mater. Res. Symp. Proc.*, 1995, **368**, 369.
- [91] R. F. Lobo, M. T. C. C. Freyhardt, S. Khodabandeh, P. Wagner, C.-Y. Chen, K. J. Balkus Jr, S. I. Zones, and M. E. Davis, *J. Am. Chem. Soc.*, 1997, **119**, 8474.
- [92] T. Wessels, C. Baerlocher, L. B. McCusker, and E. J. Croyghton, *J. Am. Chem. Soc.*, 1999, **121**, 6242.

- [93] P. Wagner, O. Terasaki, S. Ritsch, J. G. Nery, S. I. Zones, M. E. Davis, and K. J. Hiraga, *J. Phys. Chem. B*, 1999, **103**, 8245.
- [94] M. G. Wu, M. W. Deem, S. A. Elomari, R. C. Medrud, S. I. Zones, T. Maesen, C. Kibby, C.-Y. Chen, and I. Y. Chan, *J. Phys. Chem. B*, 2002, **106**, 264.
- [95] L. A. Villaescusa, P. A. Barrett, and M. A. Cambor, *Angew. Chem., Int. Ed. Engl.*, 1999, **38**, 1997.
- [96] A. Corma, M.-J. Díaz-Cabañas, J. Martínez-Triguero, F. Rey, and J. Rius, *Nature (London)*, 2002, **418**, 514.
- [97] P. A. Wright, R. H. Jones, S. Natarajan, R. G. Bell, J. Chen, M. B. Hursthouse, and J. M. Thomas, *J. Chem. Soc., Chem. Commun.*, 1993, p. 633.
- [98] G. W. Noble, P. A. Wright, P. Lightfoot, R. E. Morris, K. J. Hudson, Å. Kvik, and H. Graafsma, *Angew. Chem., Int. Ed. Engl.*, 1997, **36**, 81.
- [99] X. H. Bu, P. Y. Feng, and G. D. Stucky, *Science (Washington, D. C.)*, 1997, **278**, 2080.
- [100] M. A. Cambor, M.-J. Díaz-Cabañas, P. A. Cox, I. J. Shannon, P. A. Wright, and R. E. Morris, *Chem. Mater.*, 1999, **11**, 2878.
- [101] M. A. Cambor, A. Corma, P. Lightfoot, L. A. Villaescusa, and P. A. Wright, *Angew. Chem., Int. Ed. Engl.*, 1997, **36**, 2659.
- [102] K. Maeda, A. Tuel, S. Caldarelli, and C. Baerlocher, *Microporous Mesoporous Mater.*, 2000, **39**, 465.
- [103] V. Patinec, P. A. Wright, P. Lightfoot, R. A. Aitken, and P. A. Cox, *J. Chem. Soc., Dalton Trans.*, 1999, p. 3909.
- [104] K. J. Balkus Jr, A. Ramsaran, R. Szostak, and M. Mitchell In *Proceedings of the 12th International Zeolite Conference*, p. 1931, Warrendale, WA, 1999. Materials Research Society.
- [105] P. Wagner, Y. Nakagawa, G. S. Lee, M. E. Davis, S. Elomari, R. C. Medrud, and S. I. Zones, *J. Am. Chem. Soc.*, 2000, **122**, 263.
- [106] R. F. Lobo and M. E. Davis, *J. Am. Chem. Soc.*, 1995, **117**, 3766.
- [107] R. F. Lobo, S. I. Zones, and R. C. Medrud, *Chem. Mater.*, 1996, **8**, 2409.

- [108] S. T. Wilson, R. W. Broach, C. S. Blackwell, C. A. Bateman, N. K. McGuire, and R. M. Kirchner, *Microporous Mesoporous Mater.*, 1999, **28**, 125.
- [109] G. W. Noble, P. A. Wright, and Å. Kvik, *J. Chem. Soc., Dalton Trans.*, 1997, p. 4485.
- [110] G. W. Noble *Synthesis of New Microporous Solids by Template Design*, PhD thesis, University of St Andrews, 1998.
- [111] D. S. Wragg, G. B. Hix, and R. E. Morris, *J. Am. Chem. Soc.*, 1998, **120**, 6822.
- [112] L. Schreyeck, F. D'Agosto, J. Stumbe, P. Caullet, and J. C. Mougénel, *J. Chem. Soc., Chem. Commun.*, 1997, p. 1241.
- [113] P. A. Barrett, M.-J. Díaz-Cabañas, and M. A. Cambor, *Chem. Mater.*, 1999, **11**, 2919.
- [114] B. J. Campbell, G. Bellussi, L. Carluccio, G. Perego, A. K. Cheetham, D. E. Cox, and R. Millini, *J. Chem. Soc., Chem. Commun.*, 1998, p. 1725.
- [115] M. M. J. Treacy and J. B. Higgins, *Collection of Simulated XRD Powder Patterns for Zeolites*, Elsevier, Amsterdam, 4th ed., 2001.
- [116] Powder Diffraction File: Hanawalt Search Manual, Inorganic Phases, sets 1–47, JCPDS–International Center for Diffraction Data, Pennsylvania, 1997.
- [117] D. A. Fletcher, R. F. McMeeking, and D. J. Parkin, *Chem. Inf. Comput. Sci.*, 1996, **36**, 746.
- [118] J. March, *Advanced Organic Chemistry*, Wiley, New York, 1992.
- [119] Discover, v. 3.1, MSI, San Diego, 1993.
- [120] N. Ulagappan and V. Krishnasamy, *J. Chem. Soc., Chem. Commun.*, 1995, p. 373.
- [121] A. B. P. Lever, *Inorganic Electronic Spectroscopy*, Vol. 33 of *Studies in Physical and Theoretical Chemistry*, Elsevier, Amsterdam, 2nd ed., 1984.
- [122] R. García, E. F. Philp, A. M. Z. Slawin, P. A. Wright, and P. A. Cox, *J. Mater. Chem.*, 2001, **11**, 1421.

- [123] M. J. Maple, E. F. Philp, A. M. Z. Slawin, P. Lightfoot, P. A. Cox, and P. A. Wright, *J. Mater. Chem.*, 2001, **11**, 98.
- [124] teXsan Single Crystal Analysis Software, v. 1.6, Molecular Structure Corporation, TX, 1993.
- [125] J. M. Thomas, R. H. Jones, R. Xu, J. Chen, A. M. Chippindale, S. Natarajan, and A. K. Cheetham, *J. Chem. Soc., Chem. Commun.*, 1992, p. 929.
- [126] I. D. Williams, Q. Gao, J. Chen, L.-Y. Ngai, Z. Lin, and R. Xu, *J. Chem. Soc., Chem. Commun.*, 1996, p. 1781.
- [127] N. Simon, T. Loiseau, and G. Férey, *J. Chem. Soc., Dalton Trans.*, 1999, p. 1147.
- [128] E. J. P. Feijen, K. de Vadder, M. H. Bosschaerts, J. L. Lievens, J. A. Martens, P. J. Grobet, and P. A. Jacobs, *J. Am. Chem. Soc.*, 1994, **116**, 2950.
- [129] J. Li, J. Yu, K. Wang, G. Zhu, and R. Xu, *Inorg. Chem.*, 2001, **40**, 5812.
- [130] R. Szostak, *Handbook of Molecular Sieves*, Van Nostrand Reinhold, New York, 1992.
- [131] A. Corma, *Chem. Rev.*, 1995, **95**, 559.
- [132] J. M. Thomas, *J. Mol. Catal. A: Chem.*, 1999, **146**, 77.
- [133] I. Bull, L. A. Villaescusa, S. J. Teat, M. A. Cambor, P. A. Wright, P. Lightfoot, and R. E. Morris, *J. Am. Chem. Soc.*, 2000, **122**, 7128.
- [134] N. Herron, G. D. Stucky, and C. A. Tolman, *J. Chem. Soc., Chem. Commun.*, 1986, p. 1521.
- [135] J. C. Medina, N. Gabriunas, and E. Paez-Mozo, *J. Mol. Catal. A: Chem.*, 1997, **115**, 233.
- [136] M. J. Sabater, A. Corma, V. Fornes, and H. Garcia, *J. Chem. Soc., Chem. Commun.*, 1997, p. 1285.
- [137] ed. M. L. Duer, *Solid State NMR Spectroscopy: Principles and Applications*, Blackwell, Oxford, 2002.
- [138] R. D. Gougeon, E. B. Brouwer, P. R. Bodart, L. Delmotte, C. Marichal, J.-M. Chézeau, and R. K. Harris, *J. Phys. Chem.*, 2001, **105**, 12249.
- [139] P. J. Barrie and J. Klinkowski, *J. Phys. Chem.*, 1989, **93**, 5972.

- [140] F. Taulelle, M. Pruski, J. P. Amoureux, D. Lang, A. Bailly, C. Huguenard, M. Haouas, C. Gérardin, T. Loiseau, and G. Férey, *J. Am. Chem. Soc.*, 1999, **121**, 12148.
- [141] S. Qiu, W. Pang, H. Kessler, and J.-L. Guth, *Zeolites*, 1989, **9**, 440.
- [142] E. K. Barefield and F. Wagner, *Inorg. Chem.*, 1973, **12**, 2435.
- [143] M. Micheloni, A. Sabatini, and P. Paoletti, *J. Chem. Soc., Perkin Trans. 2*, 1978, p. 828.
- [144] M. Micheloni, P. Paoletti, and A. Vacca, *J. Chem. Soc., Perkin Trans. 2*, 1978, p. 945.
- [145] P. A. Wright, M. J. Maple, A. M. Z. Slawin, V. Patinec, R. A. Aitken, S. Welsh, and P. A. Cox, *J. Chem. Soc., Dalton Trans.*, 2000, p. 1243.
- [146] J. M. Bennett, J. M. Cohen, G. Artioli, J. J. Pluth, and J. V. Smith, *Inorg. Chem.*, 1985, **24**, 188.
- [147] G. M. Sheldrick, SHELX, University of Göttingen, 1986.
- [148] J.-H. Choy, J.-B. Yoon, and H. Jung, *J. Phys. Chem. B*, 2002, **106**, 11120.
- [149] V. J. Thom and R. D. Hancock, *J. Chem. Soc., Dalton Trans.*, 1985, p. 1977.
- [150] N. Binsted, EXCURV98, CCLRC Daresbury Laboratory, 1998.
- [151] P. A. Wright, C. Sayag, F. Rey, D. W. Lewis, J. D. Gale, S. Natarajan, and J. M. Thomas, *J. Chem. Soc., Faraday Trans.*, 1995, p. 3527.
- [152] K. P. Lillerud and D. Akporiaye, *Stud. Surf. Sci. Catal.*, 1994, **84**, 543.
- [153] R. D. Hancock, *J. Chem. Ed.*, 1992, **69**, 615.
- [154] E. Maimon, I. Zilbermann, G. Golub, A. Ellern, A. I. Shames, H. Cohen, and D. Meyerstein, *Inorg. Chim. Acta*, 2001, **324**, 65.
- [155] H. Irving and R. J. P. Williams, *J. Chem. Soc.*, 1953, p. 3192.
- [156] P. S. Wheatley and R. E. Morris, *J. Solid State Chem.*, 2002, **167**, 267.
- [157] Y. Hu, A. Navrotsky, C.-Y. Chen, and M. E. Davis, *Chem. Mater.*, 1995, **7**, 1816.

- [158] T. D. Coombs and P. A. Wright, Unpublished work, University of St Andrews, 2002.
- [159] J.-L. Paillaud, P. Caullet, L. Schreyeck, and B. Marler, *Microporous Mesoporous Mater.*, 2001, **42**, 177.
- [160] L. Schreyeck, P. Caullet, J. C. Mougénel, and B. Marler In *Proceedings of the 12th International Zeolite Conference*, p. 1733, Warrendale, WA, 1999. Materials Research Society.
- [161] T. A. Khan and J. A. Hriljac, *Inorg. Chim. Acta*, 1999, **294**, 179.
- [162] J. M. Thomas, *Angew. Chem., Int. Ed. Engl.*, 1999, **38**, 3588.
- [163] M. Stöcker, *Microporous Mesoporous Mater.*, 1999, **29**, 3.
- [164] T. Knott, *BP Review*, 2001, **33**, 7.
- [165] B. J. Miller and J. Drummond, *Petroleum Rev.*, 1981, p. 32.
- [166] F. J. Keil, *Microporous Mesoporous Mater.*, 1999, **29**, 49.
- [167] K. I. Zamaraev and J. M. Thomas, *Adv. Catal.*, 1996, **41**, 335.
- [168] I. M. Dahl and S. Kolboe, *J. Catal.*, 1994, **149**, 458.
- [169] I. M. Dahl and S. Kolboe, *J. Catal.*, 1996, **161**, 304.
- [170] M. Guisnet, *J. Mol. Catal. A: Chem.*, 2002, **182**, 367.
- [171] N. Y. Chen, W. E. Garwood, and F. G. Dwyer, *Chemical Industries*, Vol. 36, Marcel Dekker, New York, 1989.
- [172] D. H. Olson and W. O. Haag, *ACS Symp. Series*, 1984, **248**, 275.
- [173] A. V. Sapre, *Chem. Eng. Sci.*, 1997, **52**, 4615.
- [174] D. Chen, H. P. Rebo, A. Grønvold, K. Moljord, and A. Holmen, *Microporous Mesoporous Mater.*, 2000, **35–36**, 121.
- [175] J. Liang, H. Li, S. Zhao, W. Guo, R. Wang, and M. Ying, *Appl. Catal.*, 1990, **64**, 31.
- [176] L. Smith, A. K. Cheetham, L. Marchese, J. M. Thomas, P. A. Wright, J. Chen, and E. Gianotti, *Catal. Lett.*, 1996, **41**, 13.
- [177] H. Fu, W. Song, and J. F. Haw, *Catal. Lett.*, 2001, **76**, 1.
- [178] T. Inui and M. Kang, *Appl. Catal. A: General*, 1997, **164**, 211.

- [179] M.-J. Djieugoue and A. M. Prakash, *J. Phys. Chem. B*, 2000, **104**, 6452.
- [180] J. Chen, P. A. Wright, J. M. Thomas, S. Natarajan, L. Marchese, S. M. Bradley, G. Sankar, C. R. A. Catlow, P. L. Gai-Boyes, R. P. Townsend, and C. M. Lok, *J. Phys. Chem. B*, 1994, **98**, 10216.
- [181] R. García *In preparation*, PhD thesis, University of St Andrews, 2003.
- [182] ed. H. Robson, *Verified Syntheses of Zeolitic Materials*, Elsevier, Amsterdam, 2nd ed., 2001.
- [183] W. A. Dietz, *J. Gas Chromatog.*, 1967, **5**, 68.
- [184] B. Harji, CRD5000 Setup, Cambridge Reactor Design, Cambridge, 2001.
- [185] B. Harji, CRD5000 Run, Cambridge Reactor Design, Cambridge, 2001.
- [186] W. Song, J. F. Haw, J. B. Nicholas, and K. Heneghan, *J. Am. Chem. Soc.*, 2000, **122**, 10726.
- [187] W. Song, H. Fu, and J. F. Haw, *J. Am. Chem. Soc.*, 2001, **123**, 4749.
- [188] A. Corma, A. L. Agudo, and V. Fornes, *J. Chem. Soc., Chem. Commun.*, 1983, p. 942.
- [189] L. Marchese, J. Chen, P. A. Wright, and J. M. Thomas, *J. Phys. Chem.*, 1993, **97**, 8109.
- [190] K.-P. Schröder, J. Sauer, M. Leslie, C. R. A. Catlow, and J. M. Thomas, *Chem. Phys. Lett.*, 1992, **188**, 320.
- [191] J. B. Uytterhoeven, L. G. Christner, and W. K. Hall, *J. Phys. Chem.*, 1965, **69**, 2117.
- [192] W. J. Mortier, J. Sauer, J. A. Lercher, and H. Noller, *J. Phys. Chem.*, 1984, **88**, 905.
- [193] V. Gutmann, *The Donor–Acceptor Approach to Molecular Interactions*, Plenum, New York, 1978.
- [194] T. R. Hughes and H. M. White, *J. Phys. Chem.*, 1967, **71**, 2192.
- [195] J. Datka, A. M. Turek, J. M. Jehng, and I. E. Wachs, *J. Catal.*, 1993, **141**, 347.
- [196] A. Corma, P. J. Miguel, and A. V. Orchillés, *J. Catal.*, 1997, **172**, 355.

- [197] G. B. McVicker, G. M. Kramer, and J. J. Ziemiak, *J. Catal.*, 1983, **83**, 286.
- [198] C. J. A. Mota, L. Nogueira, and W. B. Kover, *J. Am. Chem. Soc.*, 1992, **114**, 1121.
- [199] P. A. Wright, Unpublished work, University of St Andrews, 1994.
- [200] A. C. Butler and C. P. Nicolaidis, *Catal. Today*, 1993, **18**, 443.
- [201] I. W. C. E. Arends and R. A. Sheldon, *Appl. Catal. A: General*, 2001, **212**, 175.
- [202] G. W. Parshall and S. D. Ittel, *Homogeneous Catalysis*, Wiley, New York, 2nd ed., 1992.
- [203] M. Hartmann and L. Kevan, *Chem. Rev.*, 1999, **99**, 635.
- [204] P. A. Barrett, G. Sankar, C. R. A. Catlow, and J. M. Thomas, *J. Phys. Chem.*, 1996, **100**, 8977.
- [205] I. Belkhir, A. Germanin, F. Fajula, and E. Fache, *J. Chem. Soc., Faraday Trans.*, 1998, p. 1761.
- [206] D. L. Vanoppen, D. E. DeVos, M. J. Genet, P. G. Rouxhet, and P. A. Jacobs, *Angew. Chem., Int. Ed. Engl.*, 1995, **34**, 560.
- [207] I. W. C. E. Arends, R. A. Sheldon, M. Wallau, and U. Schuchardt, *Angew. Chem., Int. Ed. Engl.*, 1997, **36**, 1144.
- [208] ed. C. L. Hill, *Activation and Functionalisation of Alkanes*, Wiley, Chichester, 1989.
- [209] A. A. Shteinman, *FEBS Lett.*, 1995, **362**, 5.
- [210] J. A. Kerr, *Chem. Rev.*, 1966, **66**, 465.
- [211] J. M. Thomas, R. Raja, G. Sankar, and R. G. Bell, *Nature (London)*, 1999, **398**, 227.
- [212] R. Raja and J. M. Thomas, *J. Chem. Soc., Chem. Commun.*, 1998, p. 1841.
- [213] R. Raja, G. Sankar, and J. M. Thomas, *J. Am. Chem. Soc.*, 1999, **121**, 11926.
- [214] J. Labinger, Unpublished work, California Institute of Technology, 1999.

- [215] J. Chen and J. M. Thomas, *J. Chem. Soc., Chem. Commun.*, 1994, p. 603.
- [216] P. A. Wright, Unpublished work, University of St Andrews, 2002.